Conference Proceedings of the Society for Experimental Mechanics Series

Gordon Shaw III · Barton C. Prorok
LaVern Starman · Cosme Furlong *Editors*

MEMS and Nanotechnology, Volume 5

Proceedings of the 2013 Annual Conference on Experimental and Applied Mechanics

Springer

Conference Proceedings of the Society for Experimental Mechanics Series

Series Editor
Tom Proulx
Society for Experimental Mechanics, Inc.,
Bethel, CT, USA

For further volumes:
http://www.springer.com/series/8922

Gordon Shaw III • Barton C. Prorok • LaVern Starman • Cosme Furlong
Editors

MEMS and Nanotechnology, Volume 5

Proceedings of the 2013 Annual Conference on Experimental and Applied Mechanics

Springer

Editors
Gordon Shaw III
NIST
Gaithersburg, MD
USA

Barton C. Prorok
Auburn University
Auburn, AL
USA

LaVern Starman
Air Force Research Laboratory
Wright-Patterson AFB, OH
USA

Cosme Furlong
Worcester Polytechnic Institute
Worcester, MA
USA

ISSN 2191-5644 ISSN 2191-5652 (electronic)
ISBN 978-3-319-00779-3 ISBN 978-3-319-00780-9 (eBook)
DOI 10.1007/978-3-319-00780-9
Springer Cham Heidelberg New York Dordrecht London

Library of Congress Control Number: 2013947472

© The Society for Experimental Mechanics, Inc. 2014
This work is subject to copyright. All rights are reserved by the Publisher, whether the whole or part of the material is concerned, specifically the rights of translation, reprinting, reuse of illustrations, recitation, broadcasting, reproduction on microfilms or in any other physical way, and transmission or information storage and retrieval, electronic adaptation, computer software, or by similar or dissimilar methodology now known or hereafter developed. Exempted from this legal reservation are brief excerpts in connection with reviews or scholarly analysis or material supplied specifically for the purpose of being entered and executed on a computer system, for exclusive use by the purchaser of the work. Duplication of this publication or parts thereof is permitted only under the provisions of the Copyright Law of the Publisher's location, in its current version, and permission for use must always be obtained from Springer. Permissions for use may be obtained through RightsLink at the Copyright Clearance Center. Violations are liable to prosecution under the respective Copyright Law.
The use of general descriptive names, registered names, trademarks, service marks, etc. in this publication does not imply, even in the absence of a specific statement, that such names are exempt from the relevant protective laws and regulations and therefore free for general use.
While the advice and information in this book are believed to be true and accurate at the date of publication, neither the authors nor the editors nor the publisher can accept any legal responsibility for any errors or omissions that may be made. The publisher makes no warranty, express or implied, with respect to the material contained herein.

Printed on acid-free paper

Springer is part of Springer Science+Business Media (www.springer.com)

Preface

MEMS and Nanotechnology, Volume 5: Proceedings of the 2013 Annual Conference on Experimental and Applied Mechanics represents one of eight volumes of technical papers presented at the SEM 2013 Annual Conference & Exposition on Experimental and Applied Mechanics organized by the Society for Experimental Mechanics and held in Lombard, IL, June 3–5, 2013. The complete Proceedings also includes volumes on: *Dynamic Behavior of Materials; Challenges in Mechanics of Time-Dependent Materials and Processes in Conventional and Multifunctional Materials; Advancement of Optical Methods in Experimental Mechanics; Mechanics of Biological Systems and Materials; Experimental Mechanics of Composite, Hybrid, and Multifunctional Materials; Fracture and Fatigue; Residual Stress, Thermomechanics & Infrared Imaging, Hybrid Techniques and Inverse Problems*.

Each collection presents early findings from experimental and computational investigations on an important area within Experimental Mechanics, MEMS and Nanotechnology being one of these areas.

Microelectromechanical systems (MEMS) and nanotechnology are revolutionary enabling technologies (ET). These technologies merge the functions of sensing, actuation, and controls with computation and communication to affect the way people and machines interact with the physical world. This is done by integrating advances in various multidisciplinary fields to produce very small devices that use very low power and operate in many different environments. Today, developments in MEMS and nanotechnology are being made at an unprecedented rate, driven by both technology and user requirements. These developments depend on micromechanical and nanomechanical analyses, and characterization of structures comprising nanophase materials.

To provide a forum for an up-to-date account of the advances in the field of MEMS and nanotechnology and to promote an alliance of governmental, industrial, and academic practitioners of ET, SEM initiated a *Symposium Series on MEMS and Nanotechnology*.

The 2013 Symposium is the fourteenth in the series and addresses pertinent issues relating to design, analysis, fabrication, testing, optimization, and applications of MEMS and nanotechnology, especially as these issues relate to experimental mechanics of microscale and nanoscale structures.

It is with deep gratitude that we thank the Organizing Committee, Session Chairs, Authors and Keynote Speakers, Participants, and SEM Staff for making the 13th-*ISMAN* a valuable and unforgettable experience.

Gaithersburg, MD, USA — Gordon Shaw III
Auburn, AL, USA — Barton C. Prorok
Wright-Patterson AFB, OH, USA — LaVern Starman
Worcester, MA, USA — Cosme Furlong

Contents

1 **Warpage Measurement of Simulated Electronic Packaging Assembly** 1
Ningning Du, George F. Raiser, and W. Carter Ralph

2 **Nanomechanical Characterization of Lead Free Solder Joints** 11
Md Hasnine, Muhannad Mustafa, Jeffrey C. Suhling, Barton C. Prorok, Michael J. Bozack, and Pradeep Lall

3 **In-Situ Surface Mount Process Characterization Using Digital Image Correlation** 23
Satyajit Walwadkar, Christopher Kovalchick, Wade Hezeltine, Frank Liang, and Alan McAllister

4 **Acoustic Waveform Energy as an Interconnect Damage Indicator** 33
W. Carter Ralph, Gregory L. Daspit, Andrew W. Cain, Elizabeth E. Benedetto, Randall S. Jenkins, Aileen M. Allen, and Keith Newman

5 **Shape Optimization of Cantilevered Piezoelectric Devices** 43
Naved A. Siddiqui, Seon-Bae Kim, Dong-Joo Kim, Ruel A. Overfelt, and Barton C. Prorok

6 **Unique Fabrication Method for Novel MEMS Micro-contact Structure** 49
Benjamin Toler, Brent Danner, Derrick Langley, and Ronald Coutu Jr.

7 **A Frequency Selective Surface Design Fabricated with Tunable RF Meta-Atoms** 57
Derrick Langley, Ronald A. Coutu Jr., and Peter J. Collins

8 **Stress Characterization in Si/SiO_2 Spherical Shells Used in Micro-robotics** 63
LaVern A. Starman and Vladimir Vasilyev

9 **MEMS Cantilever Sensor for Photoacoustic Detection of Terahertz Radiation** 73
Nathan E. Glauvitz, Ronald A. Coutu Jr., Michael Kistler, Ivan R. Medvedev, and Douglas T. Petkie

10 **In-Plane MEMS Acoustic Emission Sensors Development and Experimental Characterization** 81
Hossain Saboonchi and Didem Ozevin

11 **New Insight into Pile-up in Thin Film Indentation** 89
MariAnne Sullivan and Barton C. Prorok

12 **Mapping the Mechanical Properties of Alloyed Magnesium (AZ 61)** 97
Jennifer Hay and Phillip Agee

13 **Temperature Dependent Micromechanical Testing on the Formation of Cu/Sn Intermetallic Thin Films** 103
F.-C. Hsu, F.-C. Lu, C.-T. Huang, and M.-T. Lin

14 **Molecular Interactions on $In_xGa_{1-x}N$** 109
L.E. Bain, A.M. Hosalli, S.M. Bedair, T. Paskova, and A. Ivanisevic

15 Timoshenko Beam Model for Lateral Vibration of Liquid-Phase Microcantilever-Based Sensors 115
Joshua A. Schultz, Stephen M. Heinrich, Fabien Josse, Isabelle Dufour, Nicholas J. Nigro, Luke A. Beardslee, and Oliver Brand

16 Improvement in Uncertainty of Tuning Fork-Based Force Sensor Stiffness Calibration via the Indentation Method Using Direct Determination of Contact and Machine Compliance 125
Gordon A. Shaw

17 Flexible Terahertz Metamaterials for Frequency Selective Surfaces 129
J.A. Deibel, H.R. Jones, A. Fosnight, R. Shaver, E. Best, D. Langley, L.A. Starman, and R.A. Coutu

Chapter 1
Warpage Measurement of Simulated Electronic Packaging Assembly

Ningning Du, George F. Raiser, and W. Carter Ralph

Abstract Digital image correlation is an attractive displacement measurement method for thermo-mechanical characterization and simulation of electronic assemblies, but faces a number of challenges to implementation. In this paper, a batch reflow oven with a large window was used to allow for optical measurements of an assembly under simulated production reflow conditions, and the results were compared to those from a finite element model. The testing and modeling methods are described, and their results are compared.

Keywords Digital image correlation • Reflow • Electronic packaging • Assembly • Thermo-mechanical stress

1.1 Introduction

Failures associated with thermal-mechanical stress are common in electronics assemblies. Digital image correlation (DIC) is an attractive displacement measurement technique for addressing these issues, but it cannot be used inside of production reflow ovens or thermal cycling chambers due to space and temperature constraints of the hardware. One solution is to acquire images in a windowed thermal chamber that is able to replicate the thermal conditions of reflow and thermal cycling. Such a solution presents many challenges to the ability to replicate the rapid temperature changes of reflow while collecting sufficiently high quality images of the assemblies.

Digital image correlation is an optical displacement measurement technique that is attractive for a number of reasons. In particular, it is a full-field, non-contact, two- or three-dimensional measurement method with good spatial sensitivity. The full-field nature can reveal high-strain regions that are sometimes unanticipated and might be missed by strain gages. The non-contact nature of DIC reduces setup time and decreases the chance of measurement interference with specimen behavior. The three dimensional capability yields more data than most other displacement techniques, and is especially attractive for both electronic assembly manufacturing and thermal cycling, since problems are often due to multiple thermal expansion mismatches resulting in complex displacements and warpage. The data lends itself well to qualitative and quantitative comparisons to finite element analysis for model validation [1, 2], and may also be used for traditional engineering analyses.

DIC has been used extensively with thermal chambers to measure strains resulting from thermal expansion mismatches, but published work is primarily on the sub-component level or under isothermal conditions [3–8]. Measurement of entire assemblies requires a relatively large thermal chamber, and heating and cooling capacities must be sufficiently large to match the temperature ramp rates of typical reflow ovens. Furthermore, the chamber must have an optical port that allows images to be taken with low enough optical distortion that three-dimensional displacements can be calculated over the entire assembly throughout the range of thermal conditions.

N. Du • G.F. Raiser
Medtronic, Inc., 2343 W Medtronic Way, Tempe, AZ, USA

W.C. Ralph (✉)
Southern Research Institute, 757 Tom Martin Drive, Birmingham, AL, USA
e-mail: ralph@sri.org

G. Shaw III et al. (eds.), *MEMS and Nanotechnology, Volume 5: Proceedings of the 2013 Annual Conference on Experimental and Applied Mechanics*, Conference Proceedings of the Society for Experimental Mechanics Series,
DOI 10.1007/978-3-319-00780-9_1, © The Society for Experimental Mechanics, Inc. 2014

This paper presents a series of tests used to verify and test an electronics assembly under under simulated reflow conditions. A commercially-available batch reflow oven was modified to provide a more uniform temperature distribution and to reduce optical distortions, and test methods were developed to further improve thermal and optical performance. An electronic assembly was run through a temperature profile in three configurations, and a finite element model of one of the configurations was constructed. Two parts of an electronic assembly were then run through a simulated reflow profile in the batch oven in order to measure the warpage of the solder pads during assembly.

1.2 Test Hardware and Test Methods

The tests were performed using a thermal chamber and a commercial DIC system. The thermal chamber was a modified Bokar X-Reflow 306 LF batch reflow oven, shown in Fig. 1.1. The DIC system was an Aramis 5 M (5 megapixel) system with 50 mm lenses. The thermal chamber was modified to improve temperature uniformity by replacing the supply air vents at either end of the sample stage with ducts that distribute the heated air more evenly across the stage in both the horizontal and vertical directions, and by adding side frames along the stage to conduct the heated air across the sample stage to return vents in the middle of the stage. Thermally-induced optical distortions between the window panes were effectively eliminated by decreasing the spacing between the panes, which prevented convective air circulation from setting up. The oven lid guide was also replaced with one that allowed the lid to be opened to 90° in order to allow the DIC system to be calibrated through the window. Circular polarizing filters were used on both the lenses and lights on the DIC system to reduce reflections and glare [9].

In addition to the hardware modifications, several test methods were employed. Continuous supply air circulation was used to induce constant turbulent air flow across the sample stage, breaking up thermally-induced optical distortions. Likewise, an external fan was used to induce turbulent air flow across the outside of the window in order to break up thermally-induced distortions arising from the outside of the heated glass. Specimens were suspended vertically at the mid-plane of the specimen stage to allow the supply air to flow evenly across the top and bottom surfaces.

The hardware provides heating rates that can replicate typical production reflow ovens. An example heating and cooling profile is shown in Fig. 1.2, showing heating of the specimen stage from room temperature to 300 °C in 5 min. In a typical scenario, the specimen would be heated to the solder reflow temperature in several stages over about 5 min.

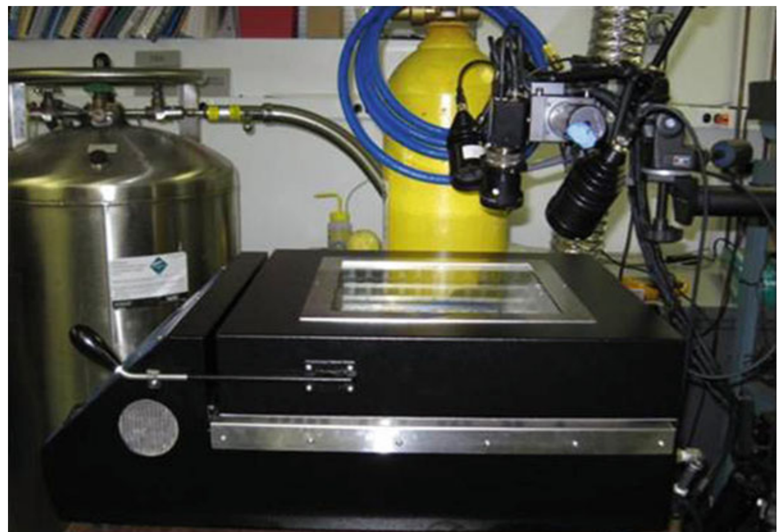

Fig. 1.1 Bokar X-Reflow 306 LF batch reflow oven and DIC system

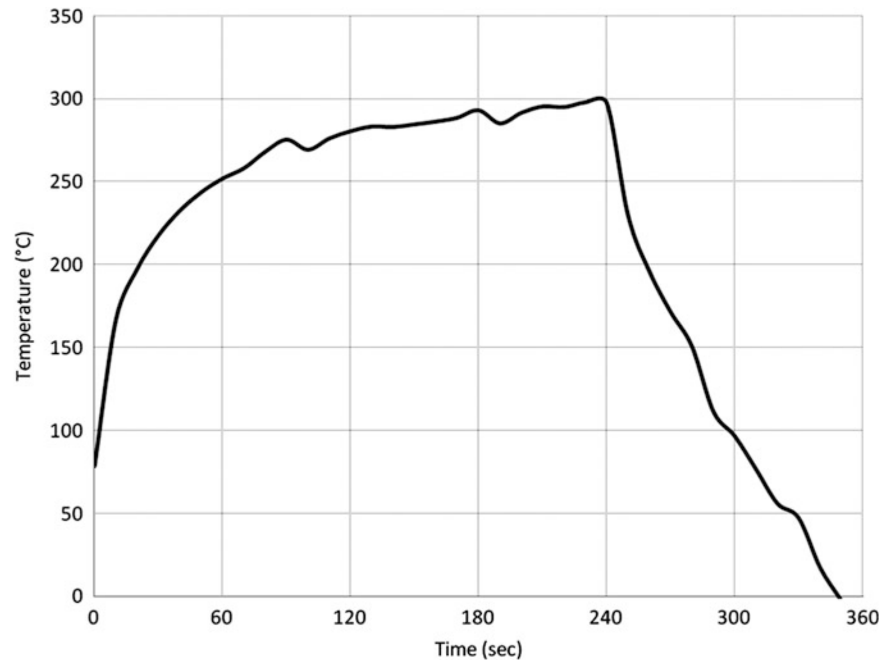

Fig. 1.2 Example heating and cooling profile

1.3 Low Rate Tests

In the first series of tests, warpage measurements were made during multiple temperature cycles on three specimen configurations. The purpose of the tests was to characterize the warpage of the specimens as a function of temperature. The first test configuration was a single overmolded package cycled to 220 °C five times. In the second configuration, the same overmolded package design was mounted to a daughter board, and two specimens were each cycled to 200 °C three times. The third configuration was similar to the second, except that the packages were underfilled, and two specimens were each cycled to 200 °C two times since no difference was observed between the second and third cycles in the first two configurations.

The specimens were speckled in the areas of interest, and were suspended above an aluminum holder with spring clips, as shown in Fig. 1.3. A thermocouple was attached to the underside of each specimen. For each test run the specimen was placed in the oven, the oven was heated to 5 °C above the target temperature, the specimen was heated until the thermocouple reached the target temperature, and then the heaters were turned off and the specimen was allowed to cool back down to room temperature (Fig. 1.4). The heating portion of each test required approximately 30 min, and each entire temperature cycle lasted about 2 h. DIC images were captured every 60 s during the tests. The coordinate system was set such that the x-y plane was coincident with three corners of the package. Rigid body motion was corrected for each image pair with a translation of a 6 degree of freedom best fit plane to that of the reference image at initial room temperature.

Warpage was defined as the displacement of the package center relative to the reference plane. In all tests the package warped downward when viewed from the overmolded side, so that the package center was lower than the corners as shown in Fig. 1.5. The warpage showed a difference between the heating and cooling legs as shown in Fig. 1.6. The difference between heating and cooling is most likely due to a temperature gradient in the package, and the response during the cooling phase is should more closely represent the isothermal behavior. The warpage of the package was −0.06 mm at initial and final room temperature, reached a maximum of −0.11 mm at 135 °C, and reached a minimum of −0.02 mm at 220 °C. The initial warpage before temperature cycling was −0.04 mm, which was different than the room temperature warpage after the first test and on subsequent tests, indicating that the difference is due to hysteresis in the materials that settles out after the first temperature cycle. An exception to this is that one of the non-underfilled specimens was cycled for third time approximately 3 days after the second cycle, and its warpage matched that of the first cycle.

The test results also showed significant part-to-part bias. When this bias was adjusted, the data yielded good repeatability. The warpage data for the non-underfilled tests are shown in the left-hand graph in Fig. 1.7, which shows significant scatter to the graph. When the final room temperature warpage is subtracted from the data and only the cool-down data are plotted, as in the right-hand graph of Fig. 1.7, the trends converge.

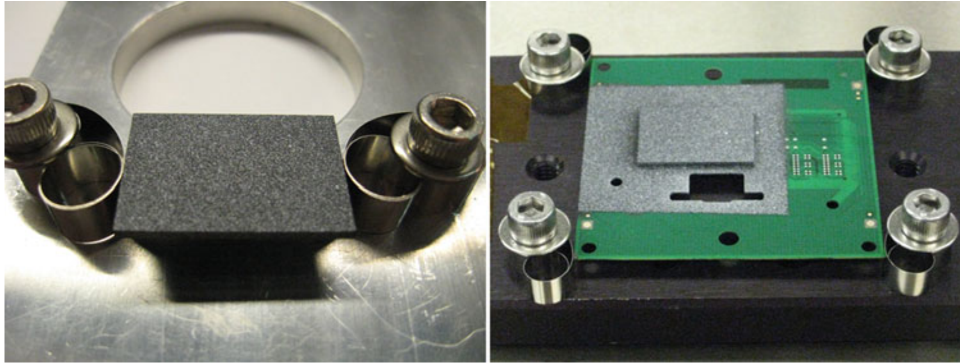

Fig. 1.3 Standalone (*left*) and mounted (*right*) test configurations

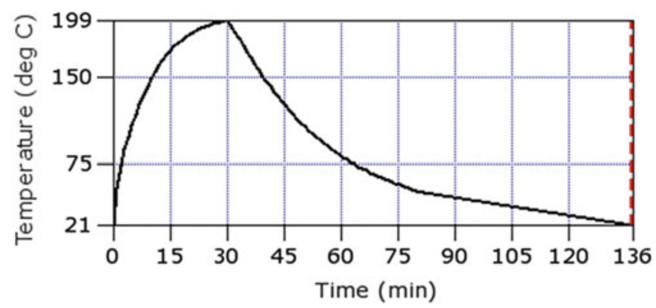

Fig. 1.4 Representative thermal cycle

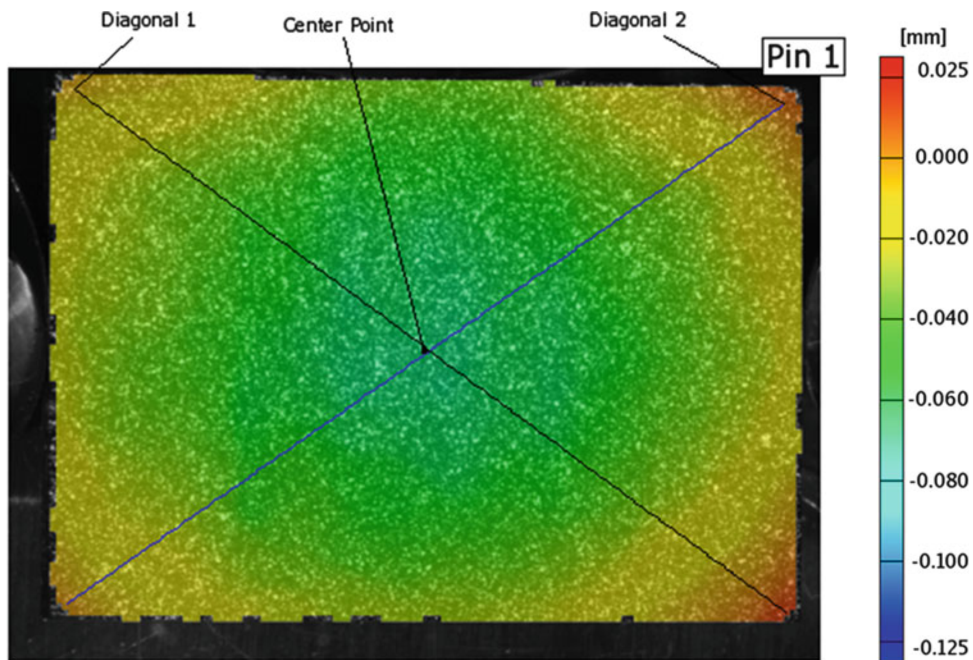

Fig. 1.5 Package warpage contour plot

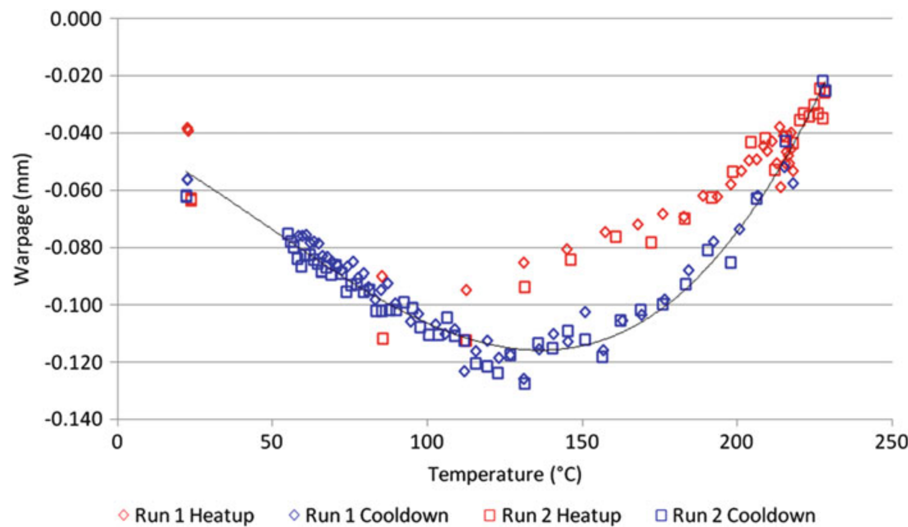

Fig. 1.6 Warpage of stand-alone package for first two cycles

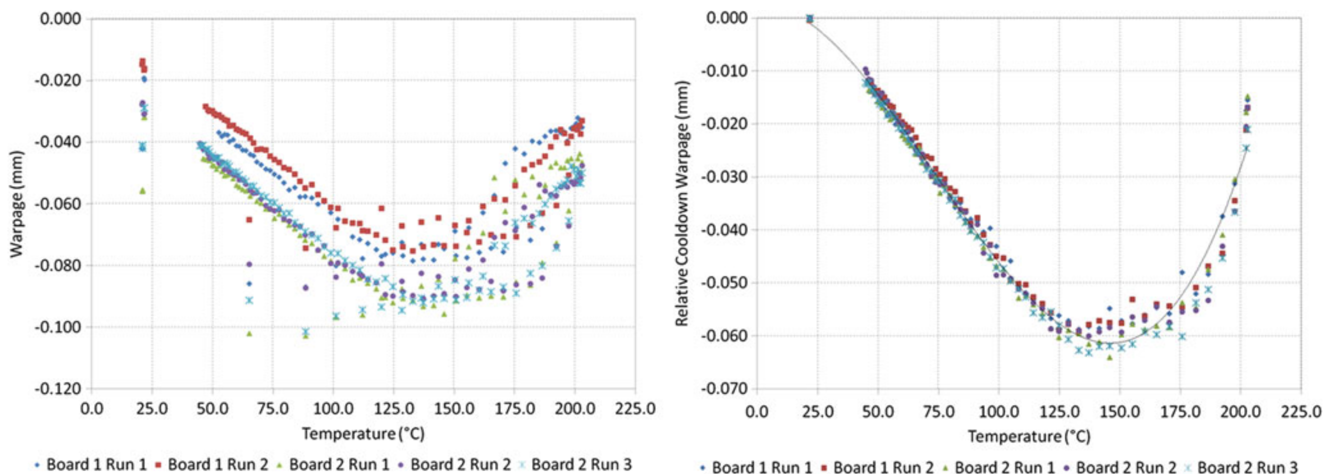

Fig. 1.7 Complete (*left*) and adjusted (*right*) warpage for non-underfilled tests

1.4 FEA Model Calibration and Validation

A FEA model was built to calculate the stresses within the package due to thermal-mechanical loading under its manufacturing and use conditions, and to optimize the design for reliability. The first step was to construct a model of the stand-alone module and validate it against the experimental measurements. This section describes the model and the method used for model calibration and validation with DIC data.

Figure 1.8 shows the mesh of the standalone module with and without the mold cap. Quadratic cubic and tetrahedral elements were used in order to avoid shear lock and accurately calculate the deformation. Since the temperature range of interest encompasses the glass transition temperature of the overmold epoxy, it is important to capture the time and temperature dependence of this material in the model. Viscoelastic material properties of the overmold epoxy was measured with DMA (Dynamic Mechanical Analysis) and used in the model. The cure shrinkage of the overmold epoxy was also included in the material model in order to capture the cross-linkage of the polymer at the cure temperature (175 C) of the epoxy. Typically the printed circuit board (PWB) can also exhibit some viscoelastic behaviors. However due to its relatively higher glass transition temperature, in this model the PWB is modeled as a transversely isotropic elastic material. The material properties that were used are listed in Table 1.1 and plotted in Fig. 1.9.

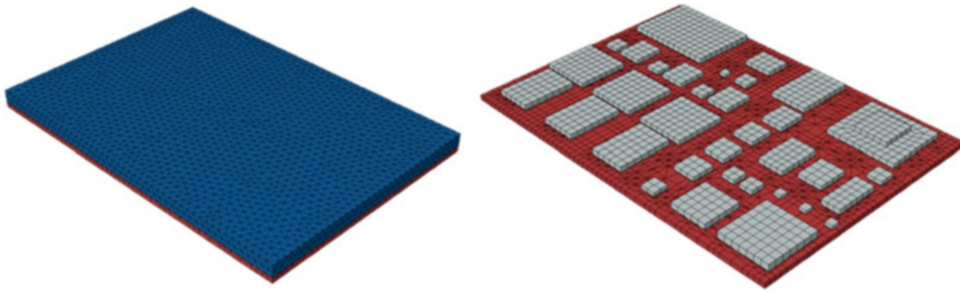

Fig. 1.8 Finite element mesh of the module package with and without the mold cap

Table 1.1 Material properties used in the FEA model

Material	Constitutive model
PWB	Transversely isotropic linear elastic In plane: E = 30 GPa, CTE = 11–14 ppm/°C
Die Attach	Temperature dependent linear elastic Tg = 83 °C Above Tg, CTE = 151 ppm/°C Below Tg, CTE = 65 ppm/°C
Overmold epoxy	Viscoelastic, master curve see Fig. 1.5 Tg = 135 °C Above Tg, CTE = 31 ppm/°C Below Tg, CTE = 7 ppm/°C Cure shrinkage, ~0.16 %
Die	Linear elastic, E = 131 GPa, CTE = 2.6 ppm/°C

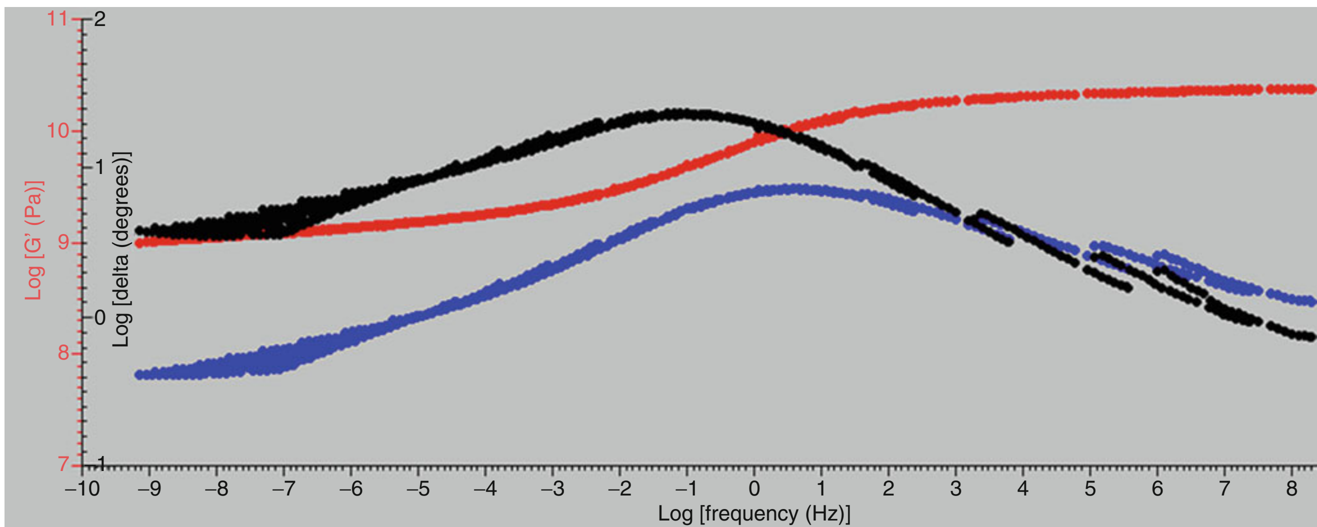

Fig. 1.9 Master curves of the overmold epoxy viscoelastic properties

In order to capture the initial warpage of the lab samples at room temperature prior to the DIC measurements, the thermal history of the manufacturing processes was considered in the model. Here the model assumes that at the time of overmolding of the package, the warpage of the module and all of its components is zero. Overmold epoxy cure and the subsequent cooling process were modeled to calculate the initial room temperature warpage. A subsequent step that used the same temperature history as the DIC tests was also included. Figure 1.10 shows the entire temperature history modeled.

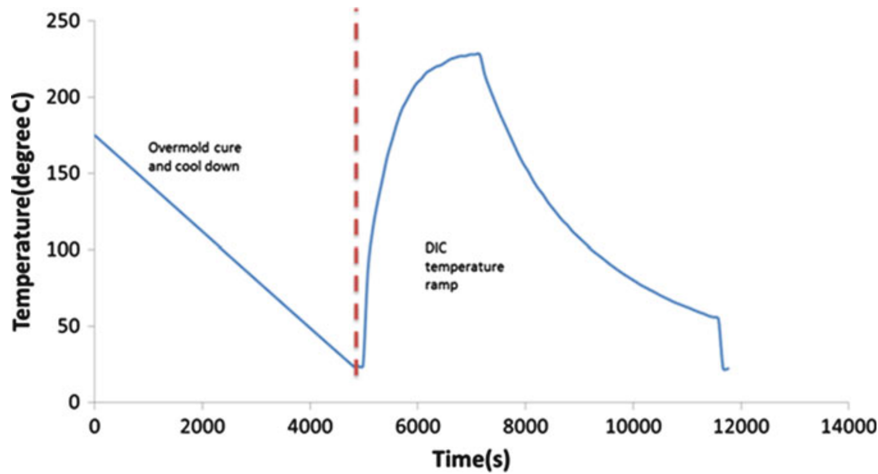

Fig. 1.10 Temperature history used in the FEA model

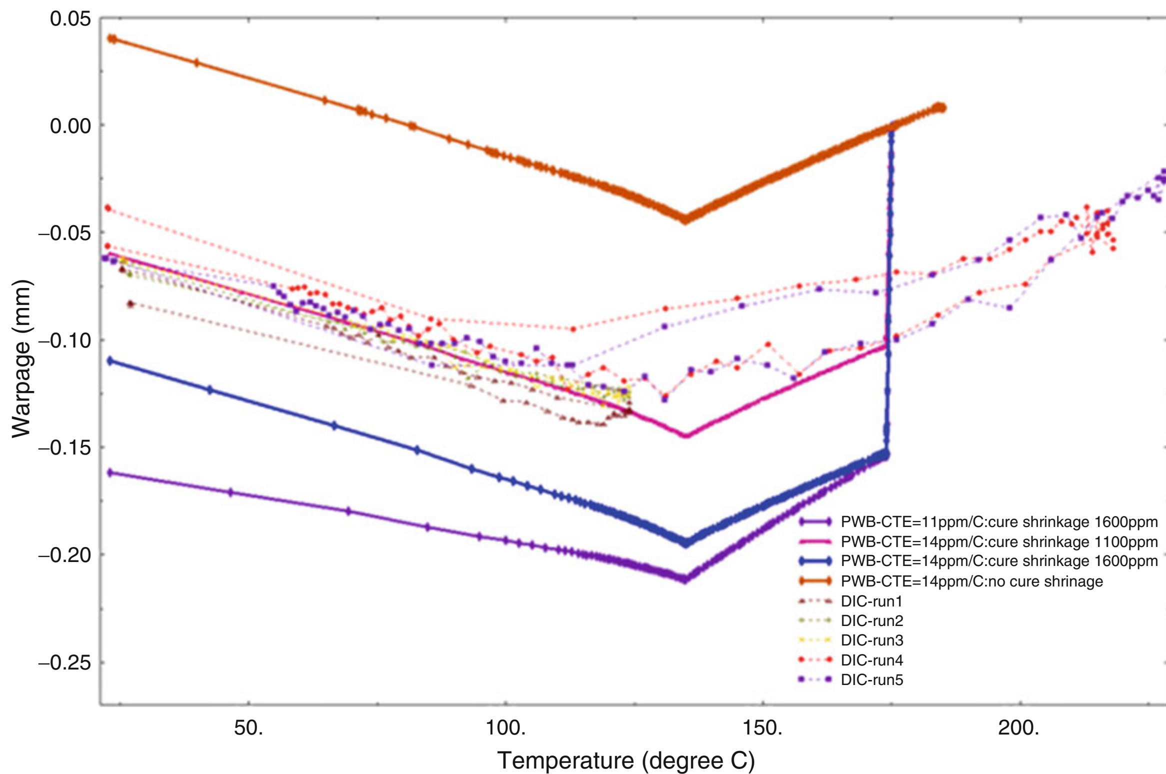

Fig. 1.11 Comparison of the warpage of the module from DIC and FEA

Several simulations with variations in the CTE of PWB and overmold cure shrinkage values were conducted and the results are compared to the DIC measurements (Fig. 1.11). First, all simulations were able to capture the change of warpage trend at around 135 °C. The change in the trend of the warpage-temperature curve is mainly due to the rapid change of the overmold epoxy material properties around its glass transition temperature, and the constitutive model of the overmold epoxy was able to reflect this change. Second, the stand-alone modules at room temperature prior to any DIC measurements have a warpage value around 0.06 mm; in simulation, this value was determined by two critical parts – the cure shrinkage amount of the overmold epoxy, and the relative thermal expansion mismatch of the overmold and the PWB during the cool down. The latter also determines the slopes of the warpage-temperature curve. By comparing the DIC data and the FEA simulation results, it is evident that the cure shrinkage needed to be included in order to correctly model the deformation of the package.

A final observation is that during the entire temperature history, the warpage results from FEA showed little time history dependency. In contrast the DIC data showed some hysteresis of the samples, with this effect more pronounced in the standalone modules and non-underfilled parts. This discrepancy could be caused by the neglecting the viscoelastic effect in other polymer materials such as PWB in the package, and needs to be further investigated.

1.5 Reflow Simulation Tests

In the second set of tests, the objective was to compare the displacements of pads on a circuit board to those of corresponding pads on a surface mount component. The air temperature profile of the production reflow oven was measured, and the batch reflow oven was programmed to provide a reasonable match, as shown in Fig. 1.7, with cool-down accelerated by opening the lid 30° and forcing ambient air across the stage. The circuit boards were composed of multiple daughter boards that were manufactured and assembled in one piece and singulated after assembly, and both bare and over-molded board configurations were tested. Each daughter board was speckled in the area of interest, a thermocouple was adhered to the board near the location of the surface mount component, and the boards were placed in their reflow carrier trays for testing. Three components were similarly prepared, except that they were placed upside down on a quartz stand so that the surface mount pads were facing the cameras. The DIC system was calibrated through the window. The specimens were run through the reflow profile and images were acquired at 10 s intervals during heating and 20 s intervals during cooling (Fig. 1.12).

Rigid body motion was corrected post-test, and out-of-plane displacement data were reduced for specific points on each pad. Example contour plots of the data are shown in Fig. 1.13. The test data yielded good part-to-part and test-to-test consistency. The warpage was modeled for the bare board configuration and the finite element and experimental results showed matching behavior.

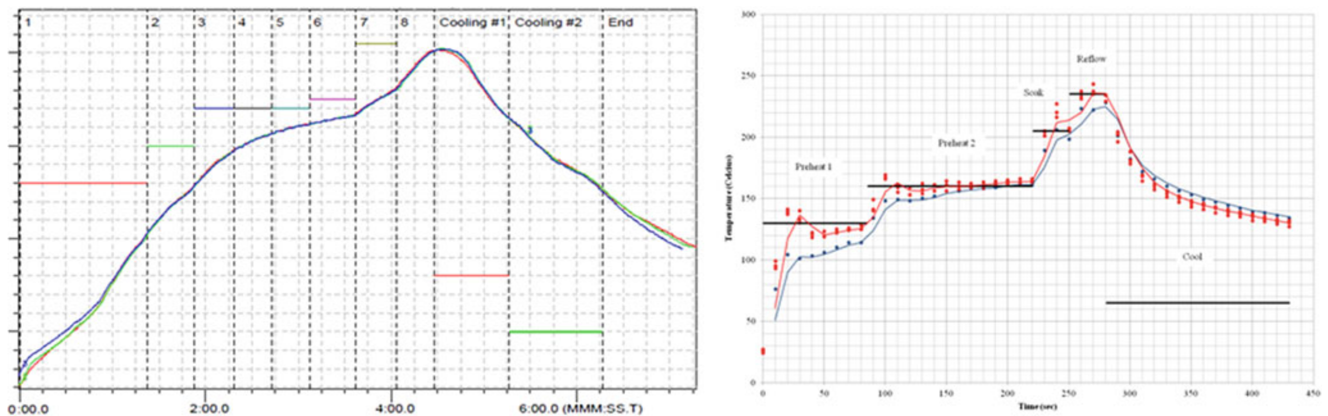

Fig. 1.12 Comparison of production (*left*) and test (*right*) temperature profiles

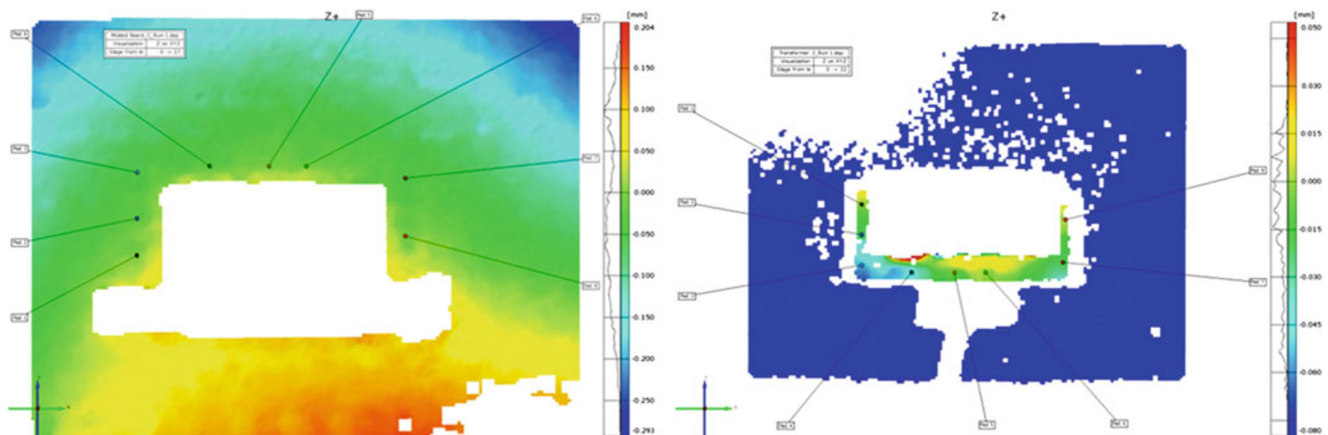

Fig. 1.13 Example contour plots of daughter board (*left*) and component (*right*)

1.6 Conclusions

A series of low heating rate tests was conducted on parts with three configurations. The results appear to show a heating rate effect, part-to-part variability, and a hysteresis between the first and second heating cycles. When adjusted for part-to-part bias and hysteresis, the results showed good repeatability.

A finite element model of the stand-alone configuration was constructed and compared to the experimental results. The model included the entire thermal history of assembly, cure shrinkage of the overmold epoxy, and the thermal expansion mismatches of the overmold and substrate. The model reflected the experimental results, including the warpage peak at about 140 °C, but did not show the hysteresis between the first and second temperature cycles.

A second series of tests was performed on a daughter board and a surface mount component under simulated reflow conditions. The test hardware was able to provide a reasonable match to the production reflow profile. The response of the thin daughter board matched modeled behavior. The test was used to quantify the warpage difference between board and component solder pads under simulated manufacturing conditions.

Acknowledgements Thanks to Wade Hezeltine at Intel Corporation's SMTD laboratory in Hillsboro, Oregon, for his idea to decrease the spacing of the window panes to reduce optical distortions.

References

1. Chu TC (1985) Applications of digital-image-correlation techniques to experimental mechanics. Exp Mech 25:232–245
2. Sutton MA (2009) Image correlation for shape, motion and deformation measurements. Springer, New York
3. Zhang J, Li M, Xiong CY, Fang J, Yi S (2005) Thermal deformation analysis of BGA package by digital image correlation technique. Microelectron Int 22(1):34–42
4. Lu H (1998) Experimental evaluation of solder joint thermal strain in a CSP using digital speckle correlation. ITHERM '98, Seattle, WA, pp 241–245, 27–30 May 1998
5. Sun SY (2006) Thermal deformation measurement by digital image correlation method. ITHERM '06, San Diego, CA, pp 921–927, 30 May–2 June 2006
6. Sun Y (2008) Digital image correlation for solder joint fatigue reliability in microelectronics packages. Microelectron Reliab 48(2):310–318
7. Eitner U (2010) Use of digital image correlation technique to determine thermomechanical deformations in photovoltaic laminates. 94(8):1346–1351
8. Pendse RD (2002) Methodology for predicting solder joint reliability in semiconductor packages. Microelectron Reliab 42(2):301–305
9. Ralph W (2013) Assembly level digital image correlation under reflow and thermal cycling conditions. ECTC '13, Las Vegas, NV, pp 2223–2227, 28–31 May 2013

Chapter 2
Nanomechanical Characterization of Lead Free Solder Joints

Md Hasnine, Muhannad Mustafa, Jeffrey C. Suhling, Barton C. Prorok, Michael J. Bozack, and Pradeep Lall

Abstract The mechanical properties of a lead free solder are strongly influenced by its microstructure, which is controlled by its thermal history including solidification rate and thermal aging after solidification. In our ongoing research, we are exploring aging effects in lead free solder joints, and correlating the results to measured behavior from miniature bulk tensile samples. As a part of these efforts, the mechanical properties and creep behavior of lead free solders are being characterized by nano-mechanical testing of single SAC305 solder joints extracted from PBGA assemblies. Using nanoindentation techniques, the stress–strain and creep behavior of the SAC solder materials have been explored at the joint scale. Mechanical properties characterized included the elastic modulus, hardness, and yield stress. The test results show that the mechanical properties (modulus, hardness) of single grain SAC305 joints were dependent on the crystal orientation. Using a constant force at max indentation, the creep response of the solder joint materials has also been measured as a function of the applied stress level. An approach has been developed to estimate tensile creep strain rates for low stress levels using nanoindentation creep data measured at very high compressive stress levels.

Keywords Nanoindentation • Lead free solder • SAC alloy • Modulus • Hardness • Creep

2.1 Introduction

The ongoing transition to lead free soldering has been motivated by environmental concerns, legislative mandates, and market differentiation. Although no clear solution has been identified for all applications; Sn-Ag, Sn-Ag-Cu (SAC), and other alloys involving elements such as Sn, Ag, Cu, Bi, In, and Zn have been identified as potential replacements for standard 63Sn-37Pb eutectic solder. Several SAC alloys, such as 96.5Sn-3.0Ag-0.5Cu (SAC305), 95.5Sn-3.8Ag-0.7Cu (SAC387), 95.5Sn-3.9Ag-0.6Cu (SAC396) and 95.5Sn-4.0Ag-0.5Cu (SAC405), have been the proposed by various user groups and industry experts. For enhanced reliability of portable electronic devices during shock/drop loading (e.g. high strain rates), SAC alloys with low silver content have been recommended including 98.5Sn-1.0Ag-0.5Cu (SAC105). The main benefits of the various SAC alloy systems are their relatively low melting temperatures compared with the Sn-Ag binary eutectic alloy, as well as their higher strength, superior resistance to creep and thermal fatigue and solderability when compared to other lead free solders.

Solder joint fatigue is one of the predominant failure mechanisms in lead free electronic assemblies exposed to thermal cycling. Thus, accurate mechanical properties and constitutive equations for solder materials are needed for use in mechanical design, reliability assessment, and process optimization. Ma et al. [1] have reviewed the literature on the mechanical behavior of lead free solders. The mechanical properties of a lead free solder are strongly influenced by its microstructure, which is controlled by its thermal history including solidification rate and thermal aging after solidification. Due to aging phenomena, the microstructure, mechanical response, and failure behavior of lead free solder joints in electronic assemblies are constantly evolving when exposed to isothermal aging and/or thermal cycling environments.

Md. Hasnine • M. Mustafa • J.C. Suhling (✉) • B.C. Prorok • M.J. Bozack • P. Lall
Department of Mechanical Engineering, and Center for Advanced Vehicle and Extreme Environment Electronics (CAVE^3), Auburn University, Auburn, AL 36849, USA
e-mail: jsuhling@auburn.edu

G. Shaw III et al. (eds.), *MEMS and Nanotechnology, Volume 5: Proceedings of the 2013 Annual Conference on Experimental and Applied Mechanics*, Conference Proceedings of the Society for Experimental Mechanics Series,
DOI 10.1007/978-3-319-00780-9_2, © The Society for Experimental Mechanics, Inc. 2014

Such aging effects are greatly exacerbated at higher temperatures typical of thermal cycling qualification tests. However, significant changes occur even with aging at room temperature.

In our prior papers on elevated temperature aging effects [2–9], we have demonstrated that the observed material behavior variations of SACN05 (N = 1, 2, 3, 4) lead free solders during isothermal aging at a variety of elevated temperatures (e.g. 25 C, 50 C, 75 C, 100 C, and 125 C) were unexpectedly large and universally detrimental to reliability. The measured stress–strain data demonstrated large reductions in stiffness, yield stress, ultimate strength, and strain to failure (up to 50 %) during the first 6 months after reflow solidification. After approximately 10–20 days of aging, the lead free solder joint material properties were observed to degrade at a slow but constant rate. In addition, even more dramatic evolution was observed in the creep response of aged solders, where up to 10,000× increases in the secondary creep rates were observed for aging up to 6 months. The aged solder materials were also found to enter the tertiary creep range (imminent failure) at much lower strain levels than virgin solders (non-aged, tested immediately after reflow solidification). In our most recent studies [7, 8], we have investigated the effects of aging on the parameters in the Anand viscoplastic constitutive model and the fatigue life of lead free solders.

All of our prior work has been based on uniaxial testing of miniature bulk solder tensile specimens. These samples were solidified in glass tubes under a controlled temperature profile in an effort to accurately match the microstructure of actual solder joints. Complementary studies by other research groups have verified aging induced degradations of SAC mechanical properties. In those investigations, mechanical testing was performed on a variety of sample geometries including lap shear specimens, Iosipescu shear specimens, and custom solder ball array shear specimens.

There have been limited prior mechanical loading studies on aging effects in actual solder joints extracted from area array assemblies (e.g. PBGA or flip chip) [10–13]. This is due to the extremely small size of the individual joints, and the difficulty in gripping them and applying controlled loadings (tension, compression, or shear). Pang et al. [10] have measured microstructure changes, intermetallic layer growth, and shear strength degradation in custom SAC single ball joint lap shear specimens subjected to elevated temperature aging. Darveaux [11] performed an extensive experimental study on the stress–strain and creep behavior of solder using specially constructed double lap shear specimens with a 10 × 10 area array solder balls. He found that aging for 1 day at 125 C caused significant effects on the stress–strain and creep behavior. For example, aged specimens were found to creep much faster than non-aged specimens by a factor of up to 20 times for both SAC305 and SAC405 solder alloys. Wiese, et al. [12] also studied the effects of aging on solder joint creep using custom assemblies with four flip chip solder balls, and found highly accelerated creep rates after aging at 125 C. Finally, Dutta and coworkers [13] used an impression creep technique with a cylindrical punch to study creep in PBGA solder balls that had been subjected to thermal-mechanical cycling.

Nanoindentation techniques have been widely used to probe the mechanical properties and deformation behavior of extremely small material samples [14]. Over the past decade, it has been applied by several investigators to characterize lead free solder joints and intermetallic compounds (IMC) in lead free solder joints [15–29]. In early studies by Rhee et al. [15, 16], Chromik et al. [17], and Deng and coworkers [18, 19], the elastic modulus E and hardness H of various regions in Sn-Ag and SAC lead free solder joints were explored by nanoindentation. In particular, the properties for the Sn-rich phase (β-tin) and the eutectic phase (containing β-tin and a mix of Sn-Ag and Sn-Cu intermetallics) were explored. Attempts were also made to indent individual Sn-Ag and Sn-Cu intermetallic particles [17–19], and then to compare the properties of the IMCs to those for the solder joint phases. Rhee et al. [15] also measured changes in the mechanical properties after the joints were subjected to thermal-mechanical cycling.

Gao et al. [20, 21] have used nanoindentation to characterize the effects of loading rate on the modulus and hardness of Sn-Ag lead free solders. They also performed creep experiments for two different microstructures (bulk cast and reflowed), and examined the effects of elevated temperature aging on the hardness. Indentation experiments with a heated stage to control the solder sample temperature have been performed by Sun et al. [22], Liu et al. [23], Gao et al. [24], and Han and coworkers [25]. The alloys tested in these studies included SAC387, 80Au-20Sn, SAC305, and SAC357, respectively. In all of these investigations, the temperature dependencies of the mechanical properties (E, H) of the solder matrix or individual solder phases were characterized. In addition, the sensitivity of the creep response of lead free solder to temperature has also been examined [23–25]. Han et al. [26] have studied the indentation size effect on the creep behavior of SAC357 lead free solder.

The effect of thermal aging on the mechanical properties of intermetallic compounds at SAC solder joint interfaces have been explored using nanoindentation by Xu and Pang [27, 28] and Song et al. [29]. Significant drops in both the modulus and hardness were recorded for aged samples relative to non-aged samples. Xu and Pang [27] also characterized the mechanical properties of the various phases and IMCs in a SAC387 solder joint. Venkatadri et al. [30] have studied the effects of aging on lead free solder joints using a micro-hardness test to perform single idents on joints.

As discussed above, there is an extensive literature that documents the large changes in the microstructure and mechanical behavior that occur in bulk lead free solder specimens during isothermal aging. There have also been some

limited investigations on the effects of aging on mechanical properties and creep behavior of solder joint arrays. In addition, nanoindentation has been utilized to study aging induced changes in the mechanical properties of intermetallic compound layers in solder joints. However, there has been little work on aging effects on mechanical properties and creep behavior in individual solder joints. Such knowledge is crucial for the optimizing the design, manufacturing, and reliability of microelectronic packages. Characterization of individual joints is quite challenging because of their extremely small size, and the difficulty in gripping them and applying controlled loadings.

In our ongoing research, we are exploring aging effects in lead free solder joints, and correlating the results to measured behavior from miniature bulk tensile samples. As a part of these efforts, the mechanical properties and creep behavior of lead free solders are being characterized by nano-mechanical testing of single SAC305 solder joints extracted from PBGA assemblies. Using nanoindentation techniques, the stress–strain and creep behavior of the SAC solder materials have been explored at the joint scale. Mechanical properties characterized included the elastic modulus, hardness, and yield stress. The test results show that the mechanical properties (modulus, hardness) of single grain SAC305 joints were highly dependent on the crystal orientation. Using a constant force at max indentation, the creep response of the solder joint materials has also been measured as a function of the applied stress level. An approach has been developed to estimate tensile creep strain rates for low stress levels using nanoindentation creep data measured at very high compressive stress levels.

2.2 Experimental Procedure

2.2.1 Solder Joint Samples

Lead free solder joints were extracted from PBGA assemblies (Amkor CABGA, 14 × 14 mm, 192 balls, 0.8 mm ball pitch, 0.46 mm ball diameter). The test boards were assembled as part of the iNEMI Characterization of Pb-Free Alloy Alternatives Project [31], and a variety of samples with 14 different solder joint alloys are being studied. In this paper, we concentrate on presenting results for SAC305 (96.5Sn-3.0Ag-0.5Cu) solder joints. These joints were extracted from test boards where the original components had SAC305 solder balls, the bare test boards had ENIG surface finish, and where SAC305 solder paste was used in the surface mount assembly process. The assembled PBGA components were cut out from the test boards and then cross-sectioned into samples of four joints each. These samples were mounted in an epoxy molding compound suitable for SEM microscopy, and then polished to a level appropriate for nanoindentation. Details of the sample preparation process include mechanical grinding with several SiC papers (#320 to #400, #600, #800 and #1200), and then final polishing with 1 μm diamond paste followed by 0.05 μm colloidal silica suspensions. This resulted in mirror finish samples suitable for nanoindentation tests and SEM microscopy.

2.2.2 Nanoindentation System and Test Procedures

The nanoindentation tests were conducted using an instrumented MTS Nanoindenter XP system with a Berkovich tip indenter. The load versus indentation displacement normal to the cross-section surface was measured during each indentation experiment, and the elastic modulus could then be extracted using the approach proposed by Oliver and Pharr [32, 33] to process the measured slope of the load–displacement curve in the unloading phase. In addition, the Continuous Stiffness Measurement (CSM) technique [33, 34] was also used in all experiments to extract elastic modulus and hardness as a function of the distance from the surface (indentation depth).

A typical cross-sectioned lead free solder ball sample after nanoindentation testing is shown in Fig. 2.1, and a close-up view of an example permanent indentation mark is shown in Fig. 2.2. For each set of experimental test conditions, an array of several indents spaced 30 μm apart were made (e.g. 2 × 3 array as shown in Fig. 2.1), and the individual indent test values were averaged to obtain statistically relevant results and consistency of inspection. All tests were performed on single grain (Sn crystal) solder balls, so that there were no orientation effects caused by an indentation array covering two or more grain boundaries of grains with significantly different crystal orientation (different material properties).

A maximum load of 30 mN was selected for the tests so that the indentation marks were large enough to cover all the phases of SAC305 solder material (see Fig. 2.2). Thus, the nanoindentation tests characterized the global mechanical

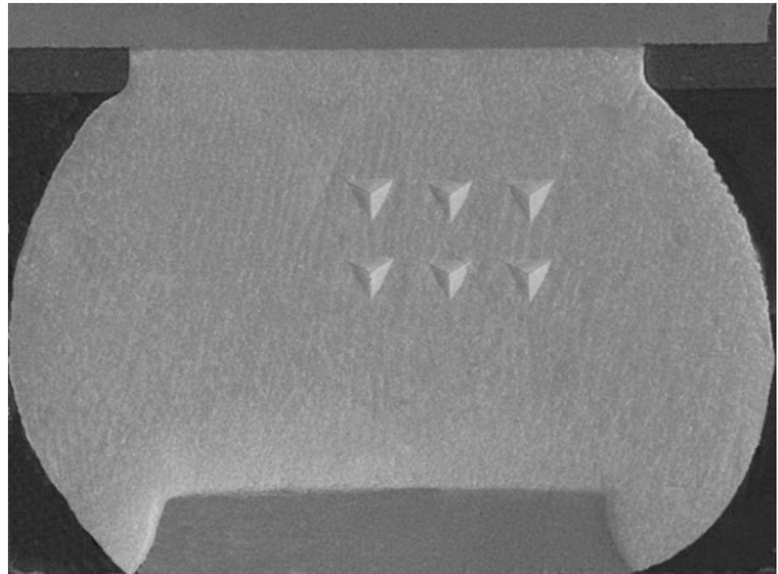

Fig. 2.1 Solder ball after nanoindentation testing

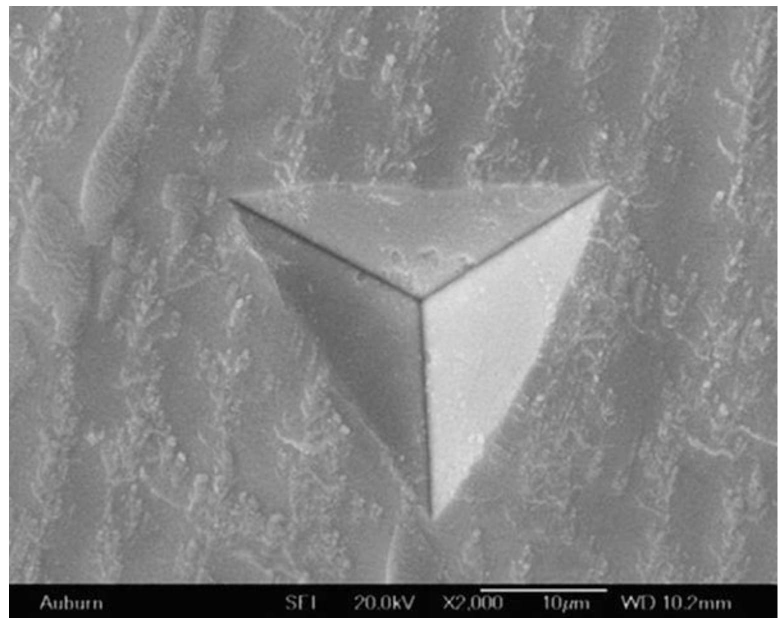

Fig. 2.2 Permanent indentation after testing

properties of the solder joints, rather than the localized properties in the β-Sn phases (Sn-rich dendrites) or in the eutectic phases between dendrites that contain Sn-Ag and Sn-Cu intermetallics. Indentation experiments were conducted at constant indentation displacement rate of 10 nm/s, corresponding to an effective strain rate of 0.05 s^{-1}. Calibration of the load and hardness measurements was performed on fused silica.

Indentation creep tests were performed holding the load constant at its maximum value of 30 mN for 500–1,000 s. After this dwell, the sample was unloaded at the same 10 nm/s displacement rate used during loading. There was also a holding period of 60 s after 90 % unloading to allow for thermal drift correction. In our work, the thermal drifts were kept smaller than 0.05 nm/s, and the thermal drift effects were excluded from the resulting displacement data.

2.3 Indentation Procedure for Lead Free Solder Joints

2.3.1 *Measurement of Elastic Modulus and Hardness*

A typical nanoindentation load versus displacement (P vs. h) curve for one of the SAC305 solder joint samples is shown in Fig. 2.3. During indentation, continuous load–displacement data are recorded. The measured response consists of three segments: (1) loading at constant deformation rate (10 nm/s) to the indentation force reaches its prescribed maximum value of 30 mN; (2) dwell (creep) for 500 s at maximum load of 30 mN; and (3) unloading at the same constant deformation rate (10 nm/s). The loading curve is a function of loading rate. The slope $S = dP/dh$ of the unloading region at maximum load is called the unloading stiffness, and can be used to calculate the elastic modulus E and hardness H at the point of maximum indentation using the Oliver and Pharr method [32, 33]. In addition to S, the procedures to calculate E and H (see below) require the values of P_{max}, h_{max}, v (Poisson's ration of the indented material), and several geometrical parameters and materials constants for the indentor tip.

In nanoindentation testing, the hardness (Meyer hardness) H is defined as maximum load divided by projected contact area A of the indentation at maximum load:

$$H = \frac{P_{max}}{A} \tag{2.1}$$

The hardness is thought of as a material flow resistance or resistance to plastic deformation. For many metals, the hardness and yield stress can be related by the approximation

$$H \approx 3\sigma_Y \quad \text{or} \quad \sigma_Y \approx \frac{H}{3} \tag{2.2}$$

This empirical expression is often referred to as the Tabor relationship [35, 36].

For the Berkovich indentor tip used in the work, the projected contact area at maximum load is given by:

$$A = 24.5h_c^2 + Ch_c \tag{2.3}$$

where h_c is the vertical distance in which the contact is made, and C is a geometrical factor that is approximately 150 nm [34]. The distance h_c can be related to the measured indentation displacement using theory of elasticity based contact mechanics:

$$h_c = h_{max} - h_s = h_{max} - \varepsilon\frac{P_{max}}{S} \tag{2.4}$$

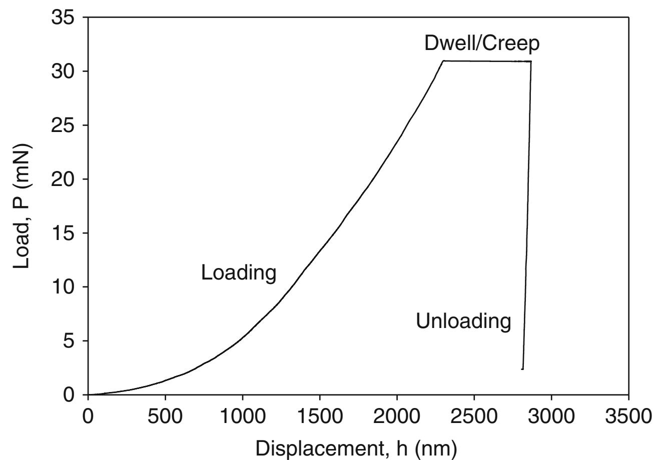

Fig. 2.3 Typical nanoindentation load–displacement curve for a SAC305 solder joint

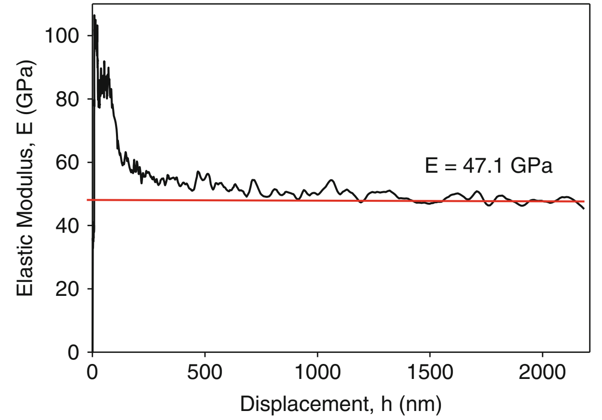

Fig. 2.4 Nanoindentation elastic modulus of SAC305 solder as a function of indentation depth

where h_{max} is the measured maximum indentation displacement from the P vs. h curve, h_s is the displacement of the surface of the material at the perimeter of the indentor contact, and $\varepsilon \approx 0.75$ is a geometrical constant for the Berkovich indentor tip [33]. Combining Eqs. 2.1, 2.2, 2.3 and 2.4, the hardness H and projected contact area A can be related to P_{max}, h_{max}, and S measured from the nanoindentation P vs. h curve. Equation 2.2 can then be used to estimate the yield stress of the indented material from the measured hardness.

Using the assumption that the contact area remains constant during withdrawal of the indentor tip and theory of elasticity solutions for contact of a material with a rigid punch, it can be established that the unloading stiffness from the recorded nanoindentation curve is given by:

$$S = \frac{dP}{dh} = \frac{2\beta\sqrt{A}}{\sqrt{\pi}} E_r \quad \text{or} \quad \frac{1}{E_r} = \frac{2\beta\sqrt{A}}{\sqrt{\pi}\,S} \tag{2.5}$$

where $\beta \approx 1$ is a geometrical factor for the chosen indentor tip and E_r is the reduced modulus [32, 33]. The desired elastic modulus E of the material being indented is related to the reduced modulus using

$$E = \frac{1 - \nu^2}{\left[\frac{1}{E_r}\right] - \left[\frac{1-\nu_i^2}{E_i}\right]} \tag{2.6}$$

where ν is the Poisson's ratio of the indented material (usually assumed to be 0.3 if unknown), ν_i is the known Poisson's ratio of the indentor tip material, and E_i is the known elastic modulus of the indentor tip material [14, 32, 33]. Combining Eqs. 2.3, 2.4, 2.5 and 2.6, the elastic modulus E can be related to P_{max}, h_{max}, and S measured from the nanoindentation P vs. h curve.

In the Continuous Stiffness Measurement (CSM) method, the procedure above is modified by measuring the unloading stiffness dP/dh continuously along the load–displacement nanoindentation curve (P vs h curve). This is accomplished by superimposing a small harmonic oscillating force on top of the normal force vs. time curve obtained by application of the constant indentation rate [32, 34]. The value of S in this case is:

$$S = \frac{dP}{dh} = \left[\frac{1}{\frac{P_{os}}{h(\omega)}\cos\phi - (K_s - m\omega^2)} - K_f^{-1}\right] \tag{2.7}$$

where, P_{os} is the peak value of the applied harmonic force with frequency ω, h(ω) is the magnitude of the indenter displacement when the harmonic force is applied, p is the phase angle between the force and displacement, m is the mass of indenter, K_s is the spring constant of leaf spring supporting indenter, and K_f is stiffness of the indenter [33, 34]. The values of E and H can then be evaluated continuously as a function of the indentation depth h during the nanoindentation test by using Eqs. 2.1, 2.2, 2.3, 2.4, 2.5, and 2.6 and the values of dP/dh, P, h recorded at each point along the nanoindentation curve.

Typical CSM results for the hardness and elastic modulus as a function of indentation depth for a single indent in a SAC305 solder joint are shown in Figs. 2.4 and 2.5, respectively.

The results were found to stabilize and be independent of depth after approximately 1,500 nm of indentation depth. Thus, we have determined the E and H values in this work by finding the average the values of the CSM response curves for

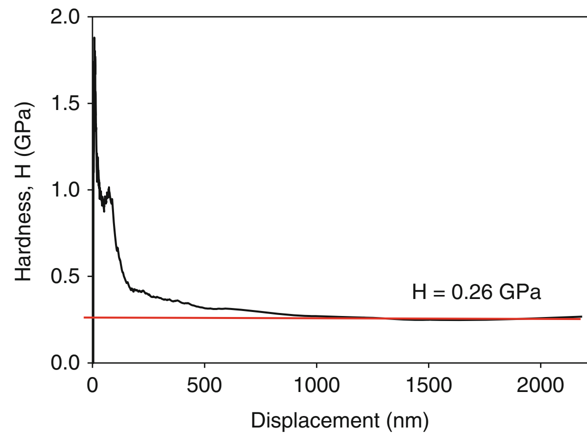

Fig. 2.5 Nanoindentation hardness of SAC305 solder as a function of indentation depth

Fig. 2.6 SAC305 solder ball mechanical properties

Property	Joint #1	Joint #2	Joint #3
Elastic Modulus (GPa)	47.10	50.25	55.59
Hardness (GPa)	0.260	0.310	0.340

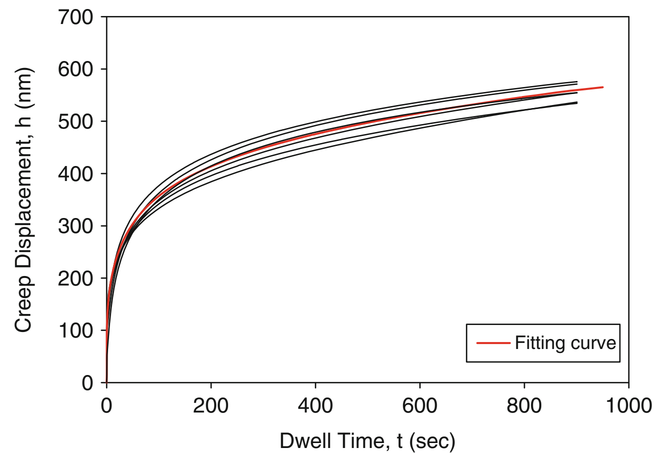

Fig. 2.7 Creep displacement data for SAC305 solder

h > 1,500 nm. For the indentation test data in Figs. 2.4 and 2.5, the extracted values were E = 47.1 GPa and H = 0.26 GPa for this solder joint. Thus, the compressive yield stress can be estimated by $\sigma_Y = H/3 = 86.7$ MPa. Values for other joints are tabulated in Fig. 2.6. The variations from joint to joint are due to the anisotropy of the β-Sn matrix of the SAC solder [37–40]

2.3.2 *Measurement of Creep Behavior*

Nanoindentation creep testing was performed during the hold/dwell at the peak load of 30 mN as shown in Fig. 2.3. Dwell times of 500–1,000 s were considered in this work. The total displacements were measured continuously, and the creep displacement data (change in displacement) during the constant load period were extracted. For example, Fig. 2.7 illustrates the measured creep displacement vs. time response for an array of six indents performed a single solder joint under similar conditions. The creep displacement data can be fit well with a variety of empirical models. In this work, we have chosen to use a log hyperbolic tangent model [41]

$$h = C_1 \ln(1 + t) + C_2 \tanh(C_3 t) + C_4 t + C_5 \tag{2.8}$$

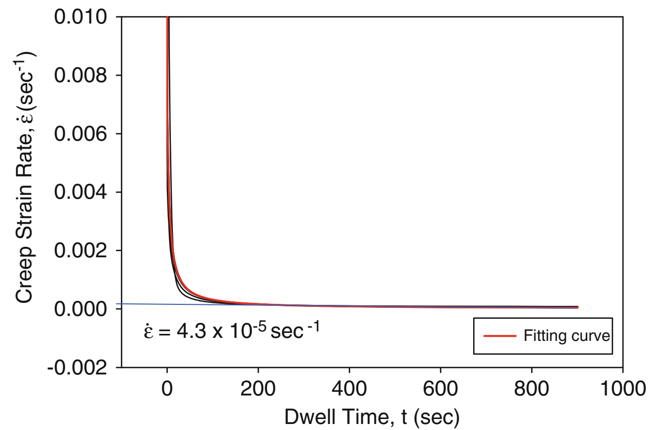

Fig. 2.8 Creep strain rate versus time for SAC305 solder

where C_1, C_2, C_3, C_4 and C_5 are fitting constants. The red curve in Fig. 2.6 is the fit of Eq. 2.8 to the creep data from the six individual indent curves.

The creep rate (creep deformation rate) is determined by taking the derivative of the creep displacement vs. time response:

$$\dot{h} = \frac{dh}{dt} \tag{2.9}$$

Using the fitting curve in Eq. 2.8, the creep rate can be easily evaluated as a function of time. The concept of indentation creep strain rate was developed by Mayo and Nix [42, 43], and is defined by dividing the creep deformation rate by the instantaneous creep deformation at each time:

$$\dot{\varepsilon} = \frac{1}{h}\frac{dh}{dt} \tag{2.10}$$

By again using the fitting curve in Eq. 2.8, the creep rate can be easily evaluated as a function of time. For the creep deformation data in Fig. 2.7, the creep strain rate vs. time response is plotted in Fig. 2.8, and a nearly constant strain rate value of $4.3 \times 10^{-5}\ s^{-1}$ was obtained for a long creep time of 900 s.

The nanoindentation creep response never actually achieves a constant strain rate due to the fact that the projected contact area A of the indentation continues to grow during the creep deformation period (constant load region). For example, evolution of the hardness H for the responses in Fig. 2.7 were calculated using the applied constant load of $P_{max} = 30$ mN, and the time evolving contact area calculated from the measured the creep deformations and Eqs. 2.3 and 2.4. Figure 2.9 illustrates the hardness vs. time response for the six individual indents and the fitting curve from Fig. 2.7. Using the Tabor relation in Eq. 2.2, the applied compressive creep stress vs. time can be estimated using $\sigma = H/3$, and Fig. 2.10 shows the stress vs. time response for the individual six individual indents and the fitting curve from Fig. 2.7. It is seen from Figs. 2.9 and 2.10 that the creep stress becomes fairly constant ($\sigma = 54$ MPa) after 900–1,000 s of constant load application. Thus, the asymptotic strain rate extracted from Fig. 2.8 can be estimated to be steady state strain rate for this stress level.

The entire strain rate vs. applied stress response for the SAC305 solder can be estimated by extracting the creep rate from the fitting curve in Fig. 2.8 and the applied stress from the fitting curve in Fig. 2.10 for each time, and then replotting the results to eliminate time as shown in Fig. 2.11. With this approach, a single nanoindentation experiment can be used to generate the complete creep strain rate vs. stress response of the material. The first point on the curve in Fig. 2.11 has the coordinates $\dot{\varepsilon} = 4.3 \times 10^{-5}\ s^{-1}$ and $\sigma = 54$ MPa, and are the values obtained for the long dwell time of 900 s. Since the nanoindentation tests are compressive in nature, the applied stress levels in Fig. 2.11 ($\sigma > 54$ MPa) possible via nanoindentation are well above those that are normally possible and of interest for lead free solders in tension or shear. For example, the tensile stress levels typically used in tensile creep testing are in the range of 10–30 MPa [2–6]. The low stress creep response can be extrapolated from the nanoindentation measured compressive creep response by nonlinear regression fitting of the data in Fig. 2.11 using one of the popular creep models for lead free solders such as the exponential model

$$\dot{\varepsilon} = C_1 e^{C_2 \sigma} \tag{2.11}$$

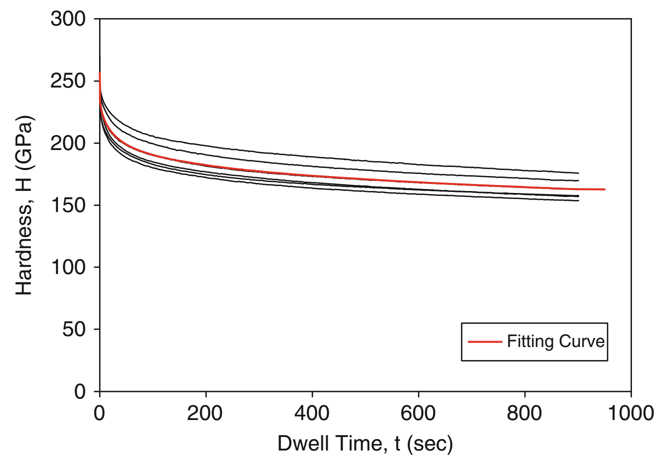

Fig. 2.9 Hardness versus time for SAC305 solder during the nanoindentation creep loading

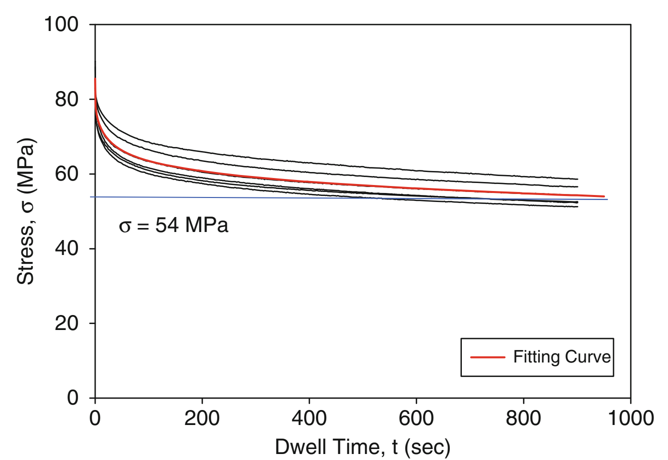

Fig. 2.10 Stress versus time for SAC305 solder during the nanoindentation creep loading

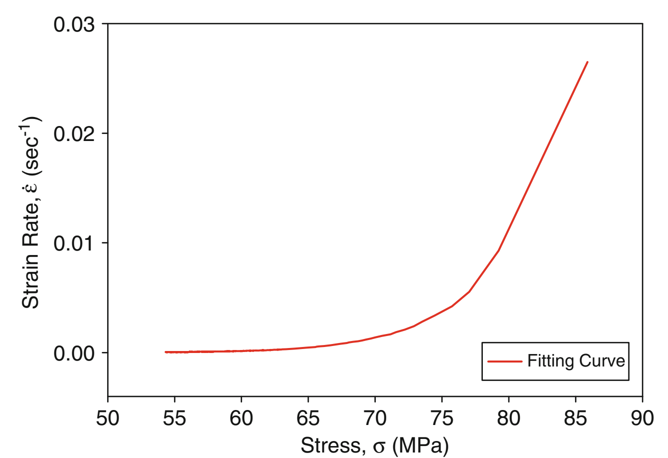

Fig. 2.11 Creep strain rate versus stress for SAC305 solder extracted from the nanoindentation creep data

or the Garofalo model

$$\dot{\varepsilon} = C_1[\sinh(C_2\sigma)]^{C_3}e^{-C_4/T} \tag{2.12}$$

where the C_i ($i = 1, 2, 3, 4$) are fitting constants. These calculations have performed and the results are illustrated in the log-log plots in Figs. 2.12 and 2.13. In each of these graphs, the red curve is the measured nanoindentation creep response

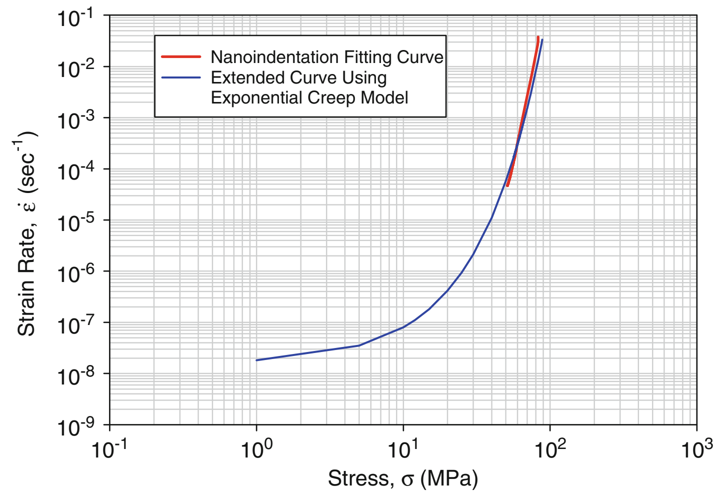

Fig. 2.12 Creep strain rate versus stress for SAC305 solder using the exponential creep model

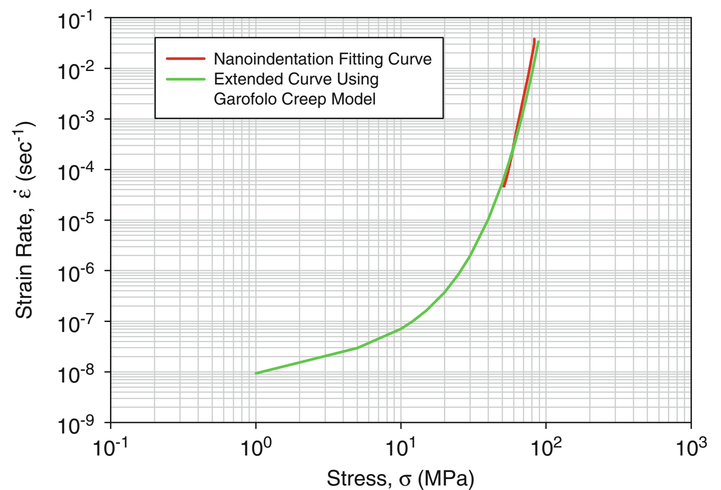

Fig. 2.13 Creep strain rate versus stress for SAC305 solder using the Garofalo creep model

from Fig. 2.10, while the blue and green curves are the regression fitting results using the exponential and Garofalo models, respectively. Both creep models are able to fit the nanoindentation creep results equally well, and both give nearly the same results when extrapolated to lower stress levels.

2.4 Summary and Conclusions

In the current paper, the mechanical properties and creep behavior of lead free solders have been characterized by nano-mechanical testing of single SAC305 solder joints extracted from PBGA assemblies. Using nanoindentation techniques, the stress–strain and creep behavior of the SAC solder materials have been explored at the joint scale. Mechanical properties characterized included the elastic modulus, hardness, and yield stress. The test results show that the mechanical properties (modulus, hardness) of single grain SAC305 joints were dependent on the crystal orientation. Using a constant force at max indentation, the creep response of the solder joint materials has also been measured as a function of the applied stress level. An approach has been developed to estimate tensile creep strain rates for low stress levels using nanoindentation creep data measured at very high compressive stress levels.

Acknowledgments This work was supported by Center for Advanced Vehicle Electronics and Extreme Environment (CAVE^3). We thank the members of iNEMI for providing the joint samples tested in this work.

References

1. Ma H, Suhling JC (2009) A review of mechanical properties of lead-free solders for electronic packaging. J Mater Sci 44:1141–1158
2. Ma H, Suhling JC, Lall P, Bozack MJ (2006) Reliability of the aging lead-free solder joint. In: Proceedings of the 56th electronic components and technology conference, San Diego, pp 849–864
3. Ma H, Suhling JC, Zhang Y, Lall P, Bozack MJ (2007) The influence of elevated temperature aging on reliability of lead free solder joints. In: Proceedings of the 57th IEEE electronic components and technology conference, Reno, pp 653–668
4. Zhang Y, Cai Z, Suhling JC, Lall P, Bozack MJ (2008) The effects of aging temperature on SAC solder joint material behavior and reliability. In: Proceedings of the 58th IEEE electronic components and technology conference, Orlando, pp 99–112
5. Zhang Y, Cai Z, Suhling JC, Lall P, Bozack MJ (2009) The effects of SAC alloy composition on aging resistance and reliability. In: Proceedings of the 59th IEEE electronic components and technology conference, San Diego, pp 370–389
6. Cai Z, Zhang Y, Suhling JC, Lall P, Johnson RW, Bozack MJ (2010) Reduction of lead free solder aging effects using doped SAC alloys. In: Proceedings of the 60th electronic components and technology conference, Las Vegas, pp 1493–1511
7. Mustafa M, Cai Z, Suhling J, Lall P (2011) The effects of aging on the cyclic stress–strain behavior and hysteresis loop evolution of lead free solders. In: Proceedings of the 61st electronic components and technology conference, Orlando, pp 927–939
8. Motalab M, Cai Z, Suhling JC, Zhang J, Evans JL, Bozack MJ, Lall P (2012) Improved predictions of lead free solder joint reliability that include aging effects. In: Proceedings of 62nd electronic components and technology conference, San Diego, pp 513–531
9. Zhang J, Thirugnanasambandam S, Evans JL, Bozack MJ, Zhang Y, Suhling JC (2012) Correlation of aging effects on the creep rate and reliability in lead free solder joints. SMTA J 25(3):19–28
10. Pang JHL, Low TH, Xiong BS, Xu L, Neo CC (2004) Thermal cycling aging effects on Sn–Ag–Cu solder joint microstructure, IMC and strength. Thin Solid Films 462–463:370–375
11. Darveaux R (2005) Shear deformation of lead free solder joints. In: Proceedings of the 55th IEEE electronic components and technology conference, Lake Buena Vista, FL, pp 882–893
12. Wiese S, Wolter KJ (2007) Creep of thermally aged SnAgCu solder joints. Microelectron Reliab 47:223–232
13. Dutta I, Pan D, Marks RA, Jadhav SG (2005) Effect of thermo-mechanically induced microstructural coarsening on the evolution of creep response of SnAg-based microelectronic solders. Mater Sci Eng A 410–411:48–52
14. Fischer-Cripps AC (2011) Nanoindentation, 3rd edn. Springer, New York, NY, USA
15. Rhee H, Lucas JP, Subramanian KN (2002) Micromechanical characterization of thermo-mechanically fatigued lead-free solder joints. J Mater Sci Mater Electron 13:477–484
16. Lucas JP, Rhee H, Guo F, Subramanian KN (2003) Mechanical properties of intermetallic compounds associated with Pb-free solder joints using nanoindentation. J Electron Mater 32(12):1375–1383
17. Chromik RR, Vinci RP, Allen SL, Notis MR (2003) Measuring the mechanical properties of lead free solder and Sn-based intermetallics by nanoindentation. J Met 55(6):66–69
18. Deng X, Chawla N, Chawla KK, Koopman M (2004) Deformation behavior of (Cu, Ag)-Sn intemetallics by nanoindentation. Acta Mater 52:4291–4303
19. Deng X, Chawla N, Chawla KK, Koopman M (2004) Young modulus of (Cu, Ag)-Sn intemetallics by nanoindentation. Mater Sci Eng A 364:240–243
20. Gao F, Taekmoto T (2006) Mechanical properties evolution of Sn-3.5Ag based lead free solders by nanoindentation. Mater Lett 60:2315–2318
21. Gao F, Nishikawa H, Takemoto T (2007) Nanoscale mechanical response of Sn-Ag based lead free solders. In: Proceedings of the IEEE electronic components and technology conference, Reno, NV, pp 206–210
22. Sun Y, Liang J, Xu JH, Wang G, Li X (2008) Nanoindentation for measuring individual phase mechanical properties of lead free solder alloy. J Mater Sci Mater Electron 19:514–521
23. Liu YC, Teo JWR, Tung SK, Lam KH (2008) High temperature creep and hardness of eutectic 80Au/20Sn solder. J Alloys Compd 448:340–343
24. Gao F, Nishikawa H, Takemoto T, Qu J (2009) Mechanical properties versus temperature relation of individual phase in Sn-3.0Ag-0.5Cu lead free solder alloy. Microelectron Reliab 49:296–302
25. Han YD, Jing HY, Nai SML, Xu LY, Tan CM, Wei J (2010) Indentation size effect on the creep behavior of SnAgCu solder. Int J Mod Phys B 24(1–2):267–275
26. Han YD, Jing HY, Nai SML, Xu LY, Tan CM, Wei J (2010) Temperature dependence of creep and hardness of Sn-Ag-Cu lead free solders. J Electron Mater 39(2):223–229
27. Xu L, Pang JHL (2006) Nanoindentation on SnAgCu solder joints and analysis. J Electron Mater 35(12):2107–2115
28. Xu L, Pang JHL (2006) Nanoindentation characterization of Ni-Cu-Sn IMC layer subjected to isothermal aging. Thin Solid Films 504:362–366
29. Song JM, Huang BR, Liu CY, Lai YS, Chiu YT, Huang TW (2012) Nanomechanical response of intermetallic phase at the solder joint interface-crystal orientation and metallurgical effects. Mater Sci Eng A 534:53–59
30. Venkatadri V, Yin L, Xing Y, Cotts E, Srihari K, Borgesen P (2009) Accelerating the effects of aging on reliability of lead free solder joints in a quantitative fashion. In: Proceedings of the IEEE electronic components and technology conference, San Diego, CA, pp 398–405
31. Henshall G (2009) iNEMI lead-free alloy alternatives project report: thermal fatigue experiments and alloy test requirements. In: Proceedings of the SMTAI, San Diego, CA, pp 317–324
32. Pharr GM, Oliver WC, Brotzen FR (1992) On the generality of the relationship among contact stiffness, contact area, and elastic modulus during indentation. J Mater Res 7(3):613–617
33. Oliver WC, Pharr GM (1992) An improved technique for determining hardness and elastic modulus using load and displacement sensing indentation experiments. J Mater Res 7(6):1564–1583
34. Hay J, Agee P, Herbert E (2010) Continuous stiffness measurement during instrumented indentation testing. Exp Tech 34(3):86–94
35. Tabor D (1951) Hardness of metals. Oxford University Press, Oxford, UK
36. Zhang P, Li SX, Zhang ZF (2011) General relationship between strength and hardness. Mater Sci Eng A 529:62–73

37. Lee BZ, Lee DN (1998) Spontaneous growth mechanism of tin whiskers. Acta Mater 46(10):3701–3714
38. Bieler TR, Jiang H, Lehman LP, Kirkpatrick T, Cotts EJ, Nandagopal B (2008) Influence of Sn grain size and orientation in the thermomechanical response and reliability of Pb-free solder joints. IEEE Trans Compon Pack Technol 31(2):370–381
39. Telang TU, Bieler TR (2005) The orientation imaging microscopy of lead free Sn-Ag solder joints. J Met 57(6):44–49
40. Yang S, Tian Y, Wang C (2010) Investigation on Sn grain number and crystal orientation in the Sn-Ag-Cu/Cu solder joints of different sizes. J Mater Sci Mater Electron 21:1174–1180
41. Chhanda N, Suhling JC, Lall P (2011) Experimental characterization and viscoplastic modeling of the temperature dependent material behavior of underfill encapsulants. In: Proceedings of InterPACK 2011, ASME, Paper no. IPACK2011-52209, pp 1–13
42. Mayo MJ, Nix WD (1988) A micro-indentation study of superplasticity in Pb, Sn and Sn-38 wt%Pb. Acta Mater 36(8):2183–2192
43. Mayo MJ, Nix WD (1990) Mechanical properties of nanophase TiO2 as determined by nanoindentation. J Mater Res 5(5):1073–1082

Chapter 3
In-Situ Surface Mount Process Characterization Using Digital Image Correlation

Satyajit Walwadkar, Christopher Kovalchick, Wade Hezeltine, Frank Liang, and Alan McAllister

Abstract Surface mount technologies (SMT) are widely used in the electronic industry to mount integrated circuit (IC) component packages onto printed circuit boards (PCB). Increasing miniaturization and form factor reduction drives the need for improved tools and techniques to better understand and quantify the fundamentals of the surface mount process A novel application of the digital image correlation (DIC) method, a non-contact, full-field optical measuring technique for quantifying displacements and strains on a surface of interest, is employed for in-situ lab-based SMT investigations to characterize solder joint collapse. A case study is presented to examine key phenomena during the SMT process illustrating the effect of package tilt on solder joint collapse as a result of asymmetric solder ball array pattern on BGA.

Keywords DIC • Surface mount process • In-situ reflow • Printed circuit board (PCB) • Ball grid array (BGA) package

3.1 Introduction

The electronic industry widely uses combinations of ball grid array (BGA) devices and composite printed circuit boards (PCBs) to establish an electrical and mechanical platform for the devices to function. As the soldering process involves changes from room temperature to reflow temperature, understanding the warpage behavior of both the BGA and PCB is important to ensure good solder joint quality. Warpage is nothing but out-of-plane deformation (normal to the (x,y) orientation) induced in components under the application of a load, such as an applied force or exposure to change in temperature. Warpage occurs at both room and elevated temperature in different modes of which the most common are either convex or concave in shape, as shown in Fig. 3.1.

PCBs are composite structures made up of one or more layers of metal, bonded onto insulating substrates that are fabricated from the glass-fiber-reinforced thermosetting resin. There have been numerous attempts to reduce thermal warpage in PCB's by balancing the copper amounts through layers placed on the opposite sides of the center core, however, warpage still continues to daunt the PCBs [1]. PCBs in particular are prone to warp in either direction altering the gap between the BGA package and the PCB during reflow. As a byproduct of this altered gap, different failure modes such as solder ball bridging (SBB), non wet open (NWO), head on pillow (HoP) and head on pillow open (HoP – open) (aka non-contact open -NCO) as shown in Fig. 3.2, can arise in components affecting their functionality [2]. Practically, it becomes very important to study the warpage interactions that take place between components during assembly to quickly develop mitigation strategies.

This paper focuses mainly on developing a method to control warpage in PCBs using fixtures and advanced imaging techniques such as digital imaging correlation technique (DIC) and projection moiré for conducting in-situ SMT studies on controlled PCB warpage fixtures. The method described in this paper is capable of capturing the dynamic warpage interactions that happen between a BGA package and a PCB during the reflow process, thereby providing deep understanding of the mechanisms that lead to formation of SMT defects. Insights gained using this technique can help early detection and retention of SMT issues, thereby helping to improve product yields.

S. Walwadkar (✉) • C. Kovalchick • W. Hezeltine • F. Liang • A. McAllister
Mechanical Core Competency, Assembly Test and Technology Development, Intel Corporation, 5200 Elam Young Parkway, 97124 Hillsboro, OR, USA
e-mail: satyajit.s.walwadkar@intel.com

G. Shaw III et al. (eds.), *MEMS and Nanotechnology, Volume 5: Proceedings of the 2013 Annual Conference on Experimental and Applied Mechanics*, Conference Proceedings of the Society for Experimental Mechanics Series,
DOI 10.1007/978-3-319-00780-9_3, © The Society for Experimental Mechanics, Inc. 2014

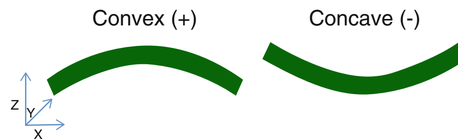

Fig. 3.1 Schematic showing component warpage shapes

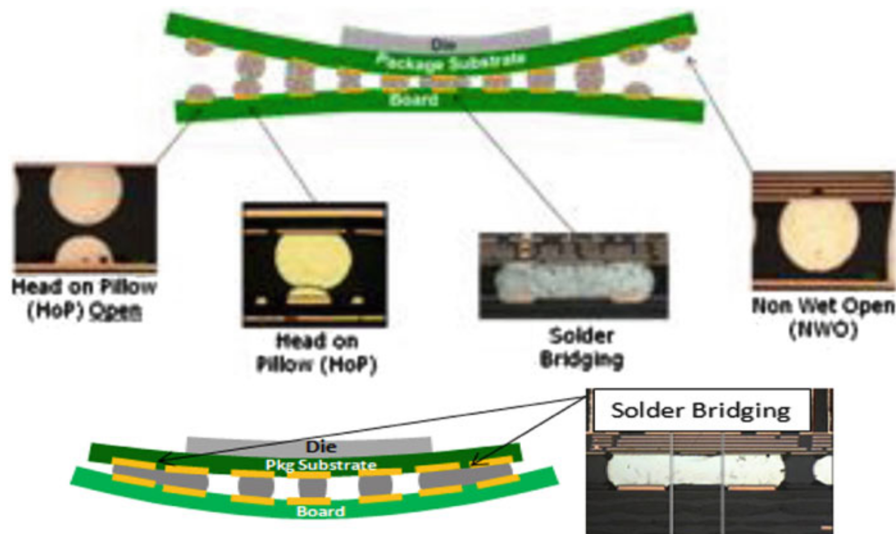

Fig. 3.2 Various soldering defects observed due to PCB warpage

3.2 SMT Study Using Controlled Fixtures

While it is common for PCBs to warp as they go through the reflow soldering process, it is challenging to control the magnitude of warpage. Controlling the magnitude of PCB warpage helps to study this impact by incorporating all sources of variation experienced in the field without the need for extensive testing. This aspect is extremely beneficial for finding warpage cliffs for product margin assessments.

To study the impact of PCB warpage on SMT yield, a novel method was developed at Intel to consistently produce a set level of PCB warpage. With the help of adjustable fixtures, PCBs were put under constraints to exhibit varying levels of convex and concave warpage. For the convex fixture, a rib – screw combination was used to impose a deflection underneath the component region of the PCB whereas for the concave fixture, diagonal inward motion of the four edge support clamps was used to bow the center of the PCB. The magnitude and stability of the fixture induced PCB warpage both at room and elevated temperature was confirmed using a non-contact full-field optical shadow moiré technique, shown in Fig. 3.3.

Due to the interaction of BGA package warpage and fixture-induced PCB warpage in either direction, it was possible to generate defects during SMT. SMT assembly builds were performed by dialing different PCB warpage levels, from low to high categorized in three different levels by altering the fixture settings. The defect levels generated during SMT due to different PCB warpage were calculated by prying the components off the PCBs and counting the number of defective joints (in the case of a convex fixture) and x-ray and cross-sectioning the assembled PCBs in case of concave fixture. Figure 3.4a shows the plot of defect density obtained for different PCB warpage levels using convex fixture. Images of various defect modes observed are also shown with the results. It is observed that as the PCB warpage increases, the solder joint defect density increases. On the other hand, Fig. 3.4b shows solder joint height maps obtained through cross-section for different PCB warpage levels using the concave fixture. It is observed that as the PCB warpage increases, the solder joints at the package edges become compressed whereas those in the center are stretched. Solder bridging defects were observed at the package corners for the highest level of concave PCB warpage.

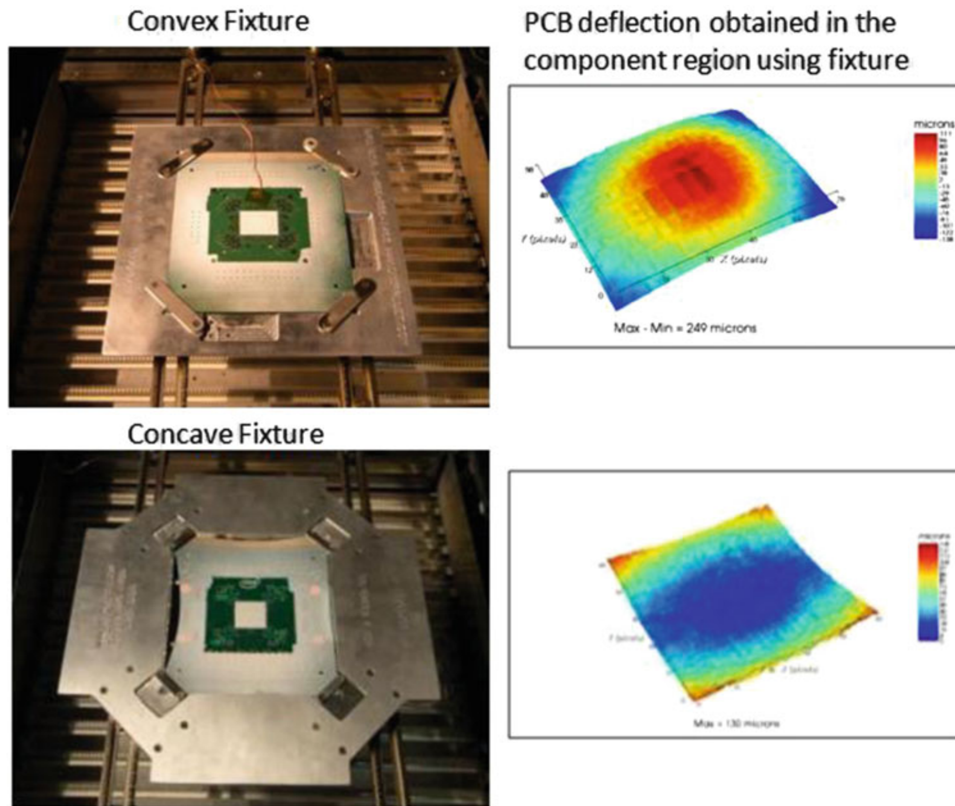

Fig. 3.3 Convex and concave fixtures used in SMT study for controlling PCB warpage

A cumulative defect map developed by overlaying defective joints from all PCBs tested using the convex fixture at the highest settings showed that defects were observed at all of the corners except the A1 corner, as shown in Fig. 3.5. The defects were heavily distributed on one side of the BGA package compared to the other side along *y* direction. This asymmetric distribution of the defects had some bearing on the BGA cavity offset, since the edge that was closer to the cavity had a higher density of defects. A detailed investigation of this effect was studied using advanced in-situ techniques discussed in the next section of the paper.

3.3 Advanced Techniques for In-Situ Warpage Characterization

For investigating the cause of the asymmetric defect distribution on BGA packages, two separate experimental techniques were employed. These techniques make use of in-situ lab-based SMT to characterize solder joint collapse, and to study BGA package and PCB warpage interactions that happen during reflow. These studies were conducted with identical boundary and use conditions as seen during the SMT assembly process using a newly-developed experimental setup consisting of a modified Bomir reflow oven and two separate imaging techniques: digital image correlation (DIC) and projection moiré. The advantage to conducting such lab-based experiments is that it enables a range of variables to be altered to investigative fundamental studies which limits line time away from the factory floor and allows for advanced insight for new products prior to running a large number of samples through SMT.

3.3.1 DIC and Projection Moiré Technique for Warpage characterization

Digital image correlation (DIC) is a non-contact, full-field optical measurement technique used for quantifying displacements on a sample of interest in the *x*, *y*, and *z* directions. A stochastic speckle pattern with light – dark contrast is applied to the sample prior to testing. The sample is imaged in the initial, undeformed reference configuration using a pair

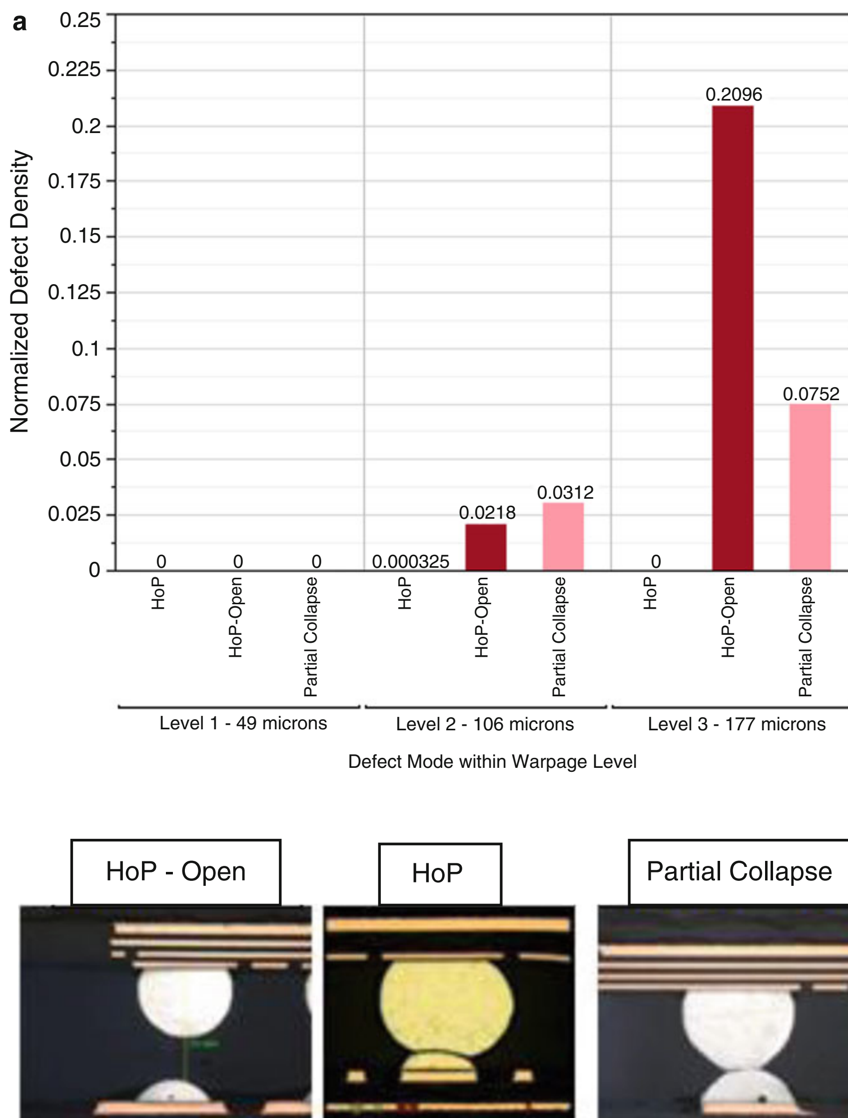

Fig. 3.4 (**a**) Solder joint defect density as function of PCB warpage for the convex fixture. (**b**) Solder joint height maps for different levels of PCB warpage for the concave fixture

of CCD cameras oriented at a fixed angle and distance away from the sample. The sample is then deformed through some loading condition (e.g. applied force, temperature, or humidity exposure) and a second image is acquired. Using a least-squares correlation algorithm to track subsets of the pattern from the reference to the deformed image, the displacement is determined in each direction for every pixel in the image field-of-view [3]. DIC, which allows for measurement of the displacement for every point in the array, should not be confused with a particle tracking method which only provides the displacement for a single point. . . The DIC technique employed here is capable of measuring the relative change in shape between two configurations, such as package displacement between 180 C and 220 C, to 11 μm. However, to measure the shape of a sample in a single fixed condition, a second methodology must be introduced.

Projection moiré is a non-contact, optical metrology for measuring out-of-plane deformation (height and surface topography) of a sample in the z direction [4]. Its sensitivity and large fields of view and depth of field make projection moiré useful for measuring the warpage of electronic packages at elevated temperature, particularly parts which are populated with components or have large surface height variation (for this specific projection moire tool, as much as 25 mm) such as the step height between the package and board in a post-SMT assembly. A series of striped patterns of known spacing are projected on the sample from a white light LCD projector at a known angle incident to the surface. An initial striped pattern is projected down on the sample, and then the striped pattern is stepped a known distance. Both patterns are captured by a CCD camera positioned normal to the sample surface, and are interfered digitally to form a fringe pattern which contains sample height and topography information.

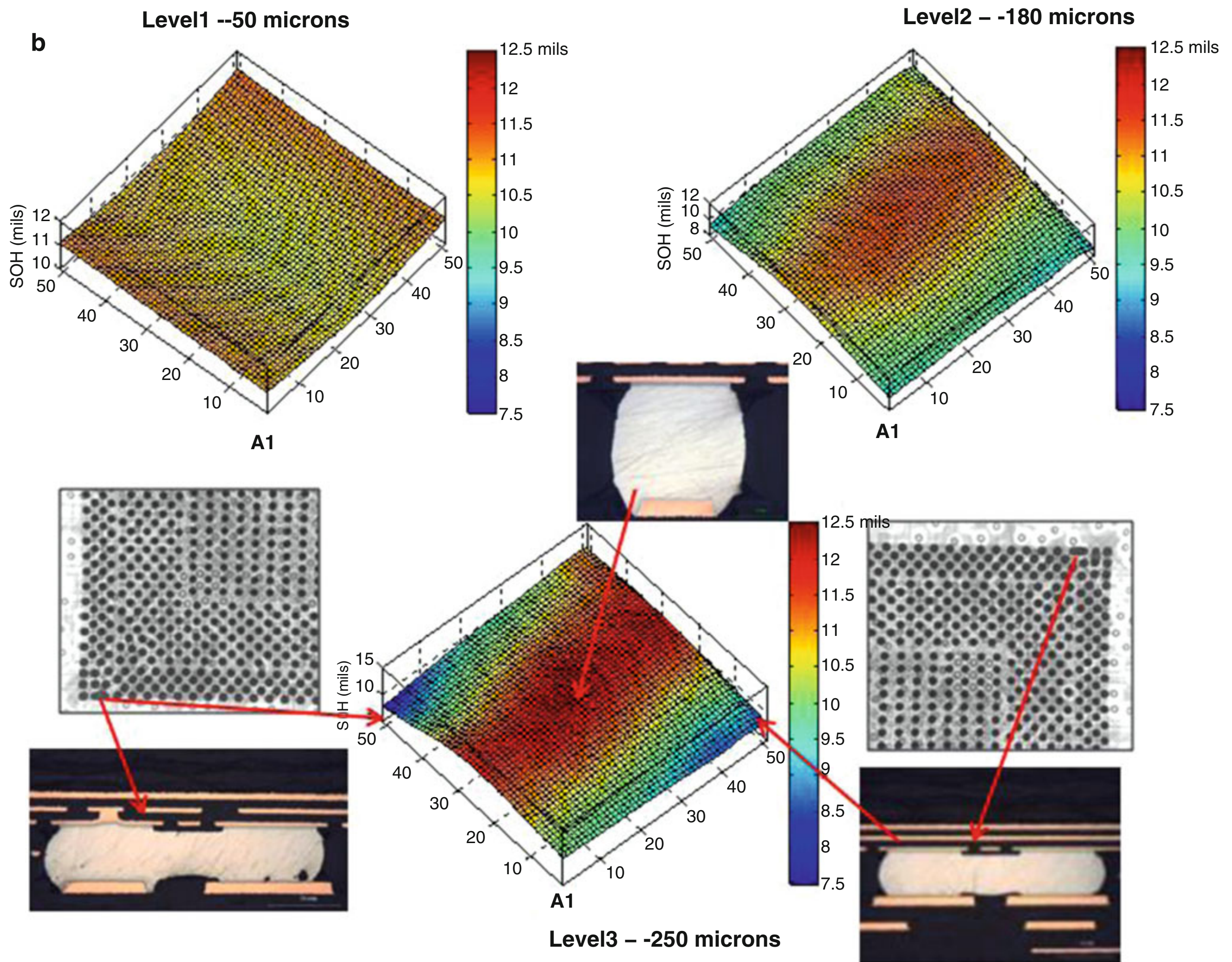

Fig. 3.4 (continued)

3.3.2 Understanding of Defect Mechanism on BGA Packages Using DIC and Projection Moiré Set-up

The study here was conducted to examine the effect of BGA package tilt in addition to warpage on solder joint collapse during a reflow temperature profile. The BGA package was placed on a PCB bent in the convex fixture to 120 μm prior to SMT. Since the BGA package had a offset cavity away from the A1 pin location more in the *y* direction, the hypothesis is that the BGA package will tilt preferentially in one direction as the component changes shape as it goes through the SMT temperature cycle. On the side of the BGA package that moves away from the PCB in the *z* direction, this tilt will create solder joint defects, such as NWO and HoP, which ultimately cause product failures.

Results are shown for a single SMT run using the in-situ method described here. As all runs show agreement within 10 μm for out-of-plane deformations (*z* direction), the test shown here is representative of all the tests run in this study. The progression in warpage through a simulated SMT temperature reflow profile is shown in Fig. 3.6a–d. The color bar scale represents contours of constant height, with red and purple indicating the high and low points, respectively. The initial room temperature (RT) condition shows that the BGA package is slightly concave, but symmetric about the center of the package. However, as the BGA package-PCB assembly is heated to the reflow solder collapse temperature of 220 C, the warpage increases and the component tilts upwards in y direction on the left side of the package. The reference plane in this plot is fixed with respect to the PCB to allow comparison of the BGA package tilt behavior at different temperatures. The degree of

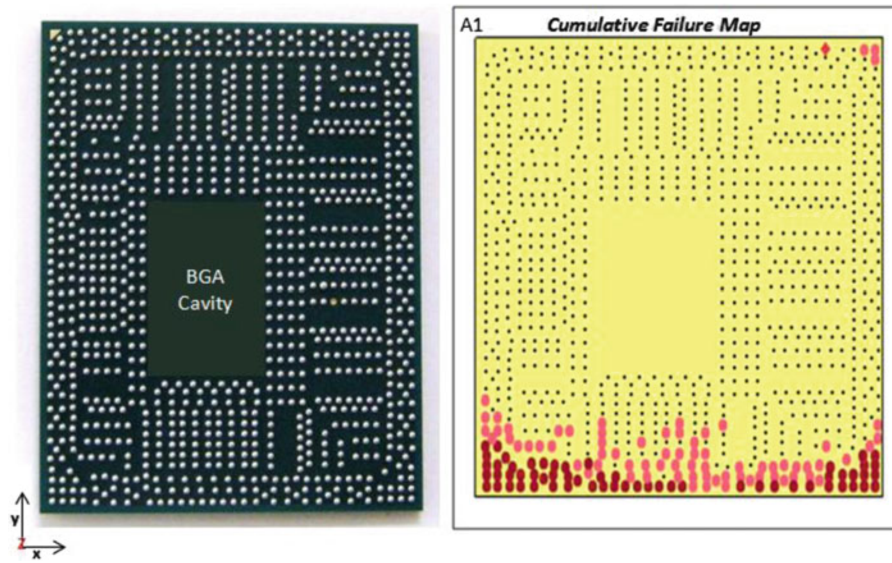

Fig. 3.5 SMT defect failure map assessment of the convex shape fixture outlining the warpage impact on defect location The *pink* and *red outlines* indicate solder joint locations where a defect was present

Fig. 3.6 (**a–d**) Relative change in shape in the *z* direction of a cavity grid array package-PCB assembly using digital image correlation through a reflow profile

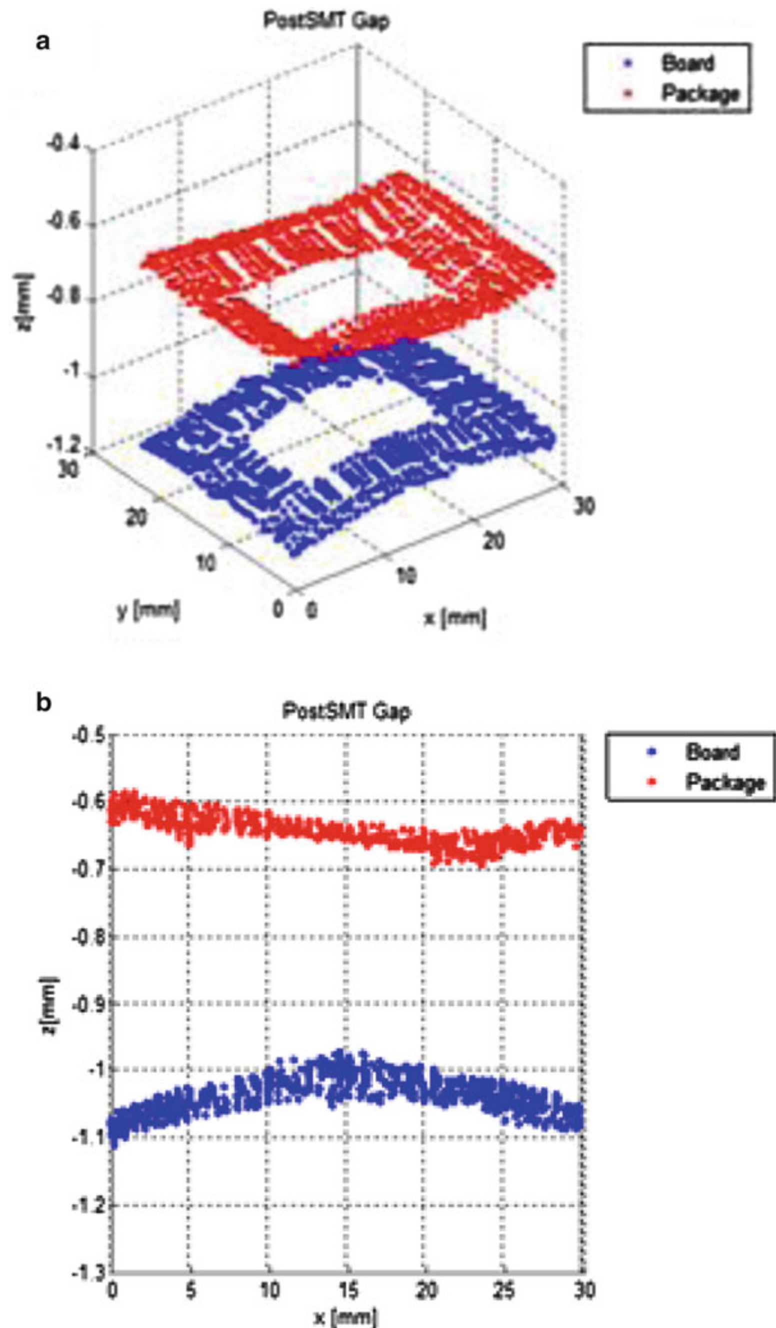

Fig. 3.7 (**a**, **b**) Post-SMT shape of a cavity grid array package-PCB assembly using projection moiré

tilt decreases slightly upon cooling after reflow collapse at 225 C, but remains the same through the end of the cooling cycle at 25 C Thus, it is seen directly here that the package is tilting up during reflow, causing an asymmetric warpage distribution that remains post-SMT.

To verify the permanent set of asymmetric package tilt during reflow, the assembly was measured post-SMT using projection moiré. Two separate measurements were acquired in this condition: one from the top side of the assembly to quantify BGA package warpage, and one from the bottom side of the PCB to quantify PCB warpage underneath the BGA package footprint region. Using a fixed common reference plane, the solder joint stand-off height in the z-direction for each pin location in the BGA package array was calculated. The BGA package and PCB shape are shown at each solder joint relative to each other in Fig. 3.7a, with a 2D cross-section of the same plot along the length of the cavity grid array package as shown in Fig. 3.7b.

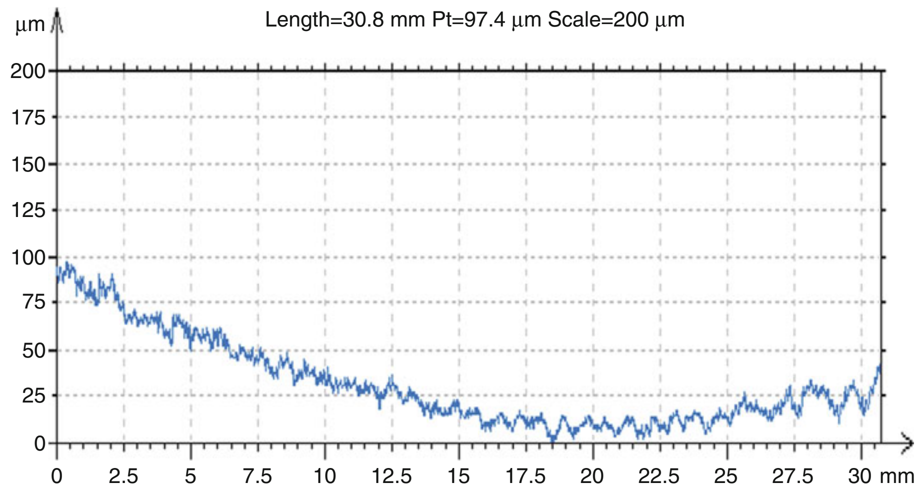

Fig. 3.8 *Z*-height of the cavity grid array package post-SMT using projection moiré

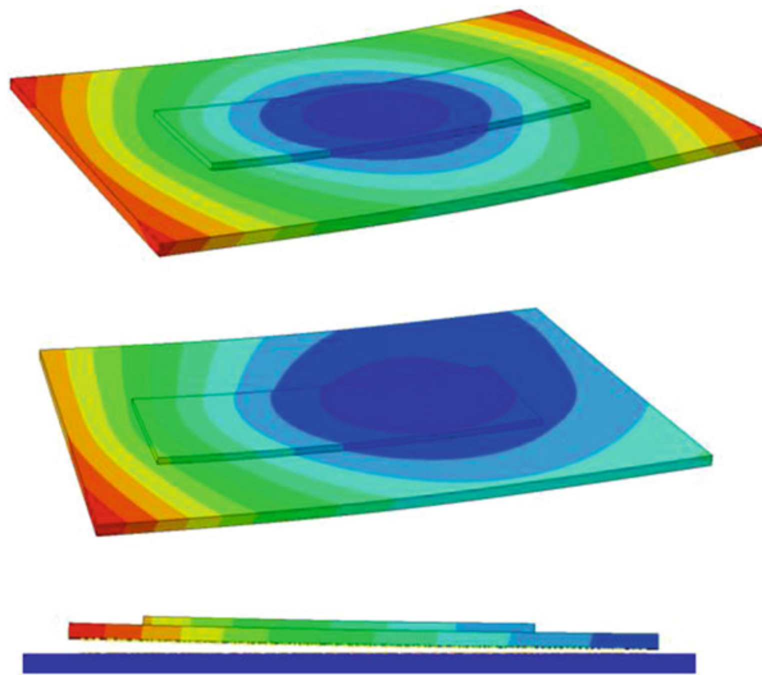

Fig. 3.9 FEA model study showing asymmetric and symmetric warrpage in BGA package due to offset in BGA

Figure 3.7b shows that, the PCB warpage is symmetrical under the BGA package footprint region. However, the BGA package exhibits the same asymmetric warpage as measured with DIC, with the left end of the package (away from the A1 pin) along the y direction tilting up with respect to the PCB. The *z*-heights of the pins along the top row of the package are plotted in Fig. 3.8, showing a tilt of approximately 75 μm from the right to left edge of the BGA package.

Using advanced in-situ lab based techniques; BGA package tilt behavior in addition to warpage at elevated temperature was confirmed. Asymmetric offset in BGA package cavity causes the BGA package to tilt as it goes through SMT assembly process causing uneven solder ball collapse. The BGA package tilt behavior at elevated temperatures can be potentially corrected by removing the BGA cavity offset or by offsetting the array of solder balls to compensate for the BGA cavity offset so that even collapse is achieved across the entire BGA package. A quick FEA model study was undertaken to confirm former case by removing the offset in the BGA cavity by moving it to the center of the BGA package. Having the BGA cavity in the center of the BGA package causes symmetric warpage in BGA package during reflow creating symmetric distribution of the defects around the BGA package as shown in Fig. 3.9.

3.4 Summary

In this paper, the approach of using novel fixtures to control the warpage in PCBs is explored. Two separate fixtures for achieving worst case PCB warpage i.e. convex and concave were built. Both the fixtures offer flexibility to set desired magnitudes of convex and concave warpage in PCBs. By tuning the desired PCB warpage magnitude levels it is possible to study the in-situ warpage interactions that take place between components during reflow with help of in-situ DIC method. This method has made it possible to evaluate the impact of warpage magnitude and shape on the formation of solder joint defects. Experiments using these fixture designs and new simulation and in-situ measurement techniques have taken roots in development of products based on the defects and will help in early identification and mitigation SMT assembly risks for future BGA products.

Acknowledgments The authors would like to acknowledge the following people whose work in research, design allowed the publication of this paper: Srini Aravamudhan, Dudi Amir, Chang Lin, Rick Canham, and Do Nguyen

References

1. Ming Ying, Yew Choon Chia, Arman Mohtar, Tiang Fee Yin, Sai Poh Chauh (2006) Thermal induced warpage characterization for printed circuit boards for shadow moire system. Electronics packaging technology conference, Singapore, pp 265–270
2. Shan Gao, Jupyo Hong, Jungho Hyun, Seogmoon Choi, Sung Yi (2007) Warpage control of wireless LAN SiP during manufacturing process. Electronic materials and packaging, EMAP 2007. International conference on 2007, Daejeon, Korea (South), pp 1–4
3. Sutton MA, Wolters WJ, Peters WH, Ranson WF, McNeill SR (1983) Determination of displacements using an improved digital correlation method. Image Vis Comput 1(3):133–139
4. Ding H, Powell RE, Hanna CR, Ume IC (2002) Warpage measurement comparison using shadow moiré and projection moiré methods. IEEE electronic components and technology conference, San Diego, pp 176–182

Chapter 4
Acoustic Waveform Energy as an Interconnect Damage Indicator

W. Carter Ralph, Gregory L. Daspit, Andrew W. Cain, Elizabeth E. Benedetto, Randall S. Jenkins, Aileen M. Allen, and Keith Newman

Abstract The industry standard process for determining safe assembly bending levels uses failure analysis following destructive stress testing to determine solder joint damage – a time-consuming and expensive process. Modal acoustic emission detection has been used to indicate the initiation of interconnect damage based on the energy of the waveforms, where a sudden increase in energy was observed at strain levels corresponding to interconnect damage. The test method and results are presented, and the use of event waveform energy is discussed.

Keywords Electronics packaging • Acoustic emission • Spherical bend • Second level interconnect • Assembly

4.1 Introduction

Interconnect damage during system assembly is a concern for manufacturers because it can result in production losses and decreased long-term reliability. The industry standard method for determining safe bending levels for assembly uses failure analysis to determine whether cracks have been induced by bending specially-designed test boards to one or more levels of strain, as measured by strain gauges mounted at the corners of a component [1]. This method is slow and expensive due to the amount of failure analysis required. Furthermore, the precision of the bending level determined to be safe depends on the number of bending levels that are tested, and how close those levels are to a point at which detectable damage initiates. The strain gauges and daisy-chain continuity networks in the test method provide a general indication of damage, but are not precise – discontinuity occurs only after the damage has progressed enough to completely sever the chain, and strain gauge non-linearity is imprecise and inaccurate. Modal acoustic emission has been used in a prior study to detect the magnitude and location of fracture events during bend testing of boards made from two laminate materials, and the results compared well to failure analysis. This study provides further analysis of event energy as a metric for damage at the interconnections.

The industry standard test method for determining safe assembly bending levels is detailed in IPC-JEDEC 9707. The test method uses a bending mode called spherical bend to flex specially-designed test boards. Spherical bend is like a three-dimensional version of three-point bend in which the component side of the board rests on a circle of eight support points and is loaded from the back side of the board at the middle of the component. A spherical bend test fixture is shown in Fig. 4.1. This bending mode induces stress on BGA interconnects that is considered to be the worst case for assembly conditions [2]. The amount of bending is measured by strain gauge rosettes mounted near the corners of the BGA, and the diagonal strain metric is used to report strain. Daisy-chain networks are typically designed into the test boards to detect electrical continuity through the interconnections. First, several test specimens are bent to electrical open and the strain responses are used to

W.C. Ralph (✉) • G.L. Daspit • A.W. Cain • R.S. Jenkins
Southern Research Institute, 757 Tom Martin Drive, Birmingham, AL, USA
e-mail: ralph@southernresearch.org

E.E. Benedetto
Hewlett-Packard, 11445 Compaq Center Dr W, Houston, TX, USA

A.M. Allen • K. Newman
Hewlett-Packard, 1501 Page Mill Rd, Palo Alto, CA, USA

G. Shaw III et al. (eds.), *MEMS and Nanotechnology, Volume 5: Proceedings of the 2013 Annual Conference on Experimental and Applied Mechanics*, Conference Proceedings of the Society for Experimental Mechanics Series,
DOI 10.1007/978-3-319-00780-9_4, © The Society for Experimental Mechanics, Inc. 2014

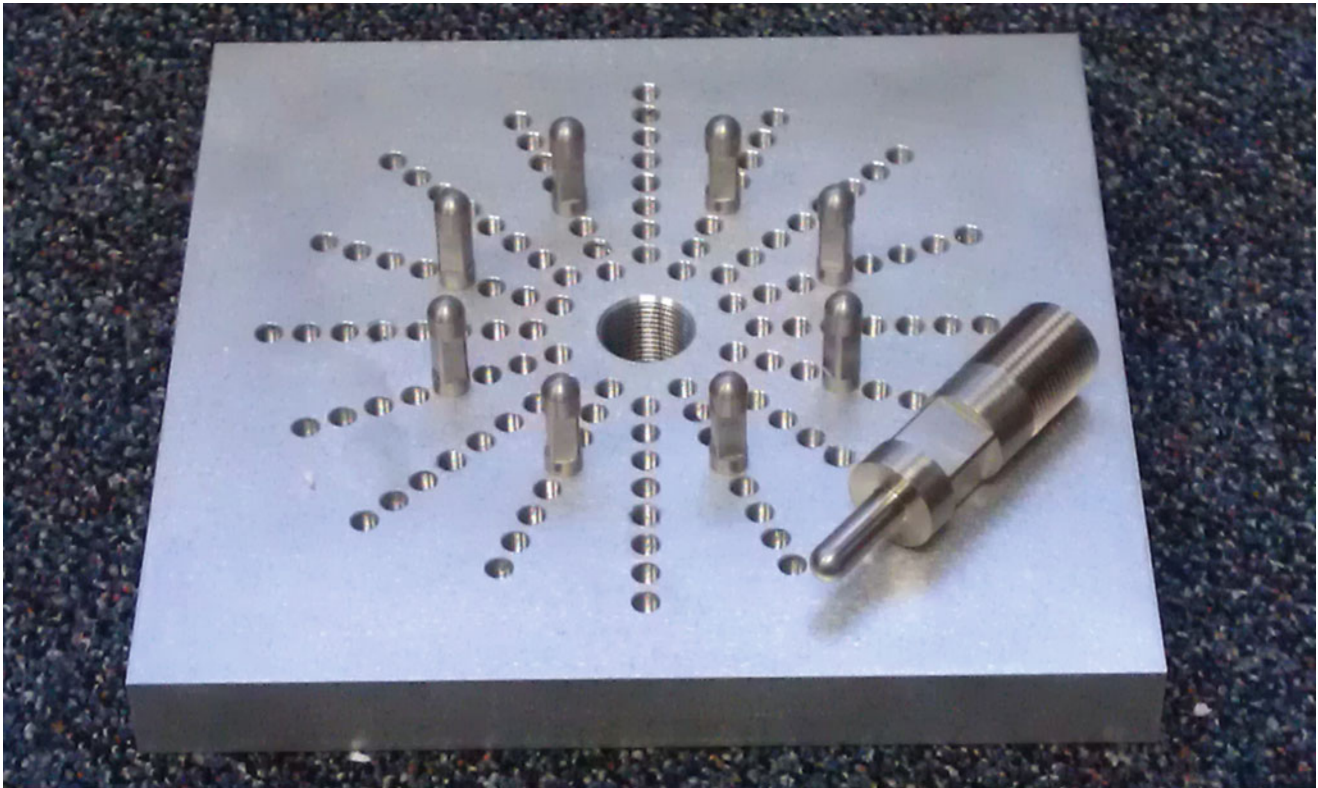

Fig. 4.1 Spherical bend test fixture

estimate the point at which damage initiates. Then a set of test boards are bent to one or more target strain levels and are inspected for interconnect damage. The safe level is the highest tested level that does not produce failing results.

Modal acoustic emission (MAE) is a technique in which acoustic events trigger recording of the event waveform at several transducers. This is similar to traditional acoustic emission, in which a digital signal is recorded whenever a wave passes a threshold on a transducer, except that the modal technique records the entire waveform, much like a oscilloscope. This provides all of the capabilities of traditional AE and allows for post-test analysis of the waveforms and post-test reprocessing of the data [3].

MAE was used in a prior study to detect solder joint failures in spherical bend. Test boards made from two laminates were bent to daisy-chain open and to four levels of strain. Dye and pry was performed on the boards to identify the extent and mode of failure. The tests to electrical open consistently had relatively few low-magnitude events over the early part of the test, followed by a sudden increase in the number and magnitude of events preceding electrical open. The tests at different strain levels showed dye stain in one corner of one board and the MAE detected two large magnitude events originating from the same corner of the same board, but no other dye stain or large events were observed in the other tests. The strain at which the sudden increase occurred in all of the tests was consistent, and all failures were of the same mode. The acoustic behavior and failure mode did not change over the range of strain rates tested, which were between 30 and 300 $\mu\varepsilon$/s [4].

This study describes the test methods and results. The energy calculation is presented, and the limitations of the calculation are discussed. The use of the energy metric for data interpretation is illustrated. Further development work is proposed.

4.2 Test Methods

The test method involved loading specimens in spherical bend while recording mechanical, electrical, and acoustic data. Specimens were then inspected for damage using dye and pry. The data was analyzed post-test in order to determine the point at which observable interconnect damage initiated.

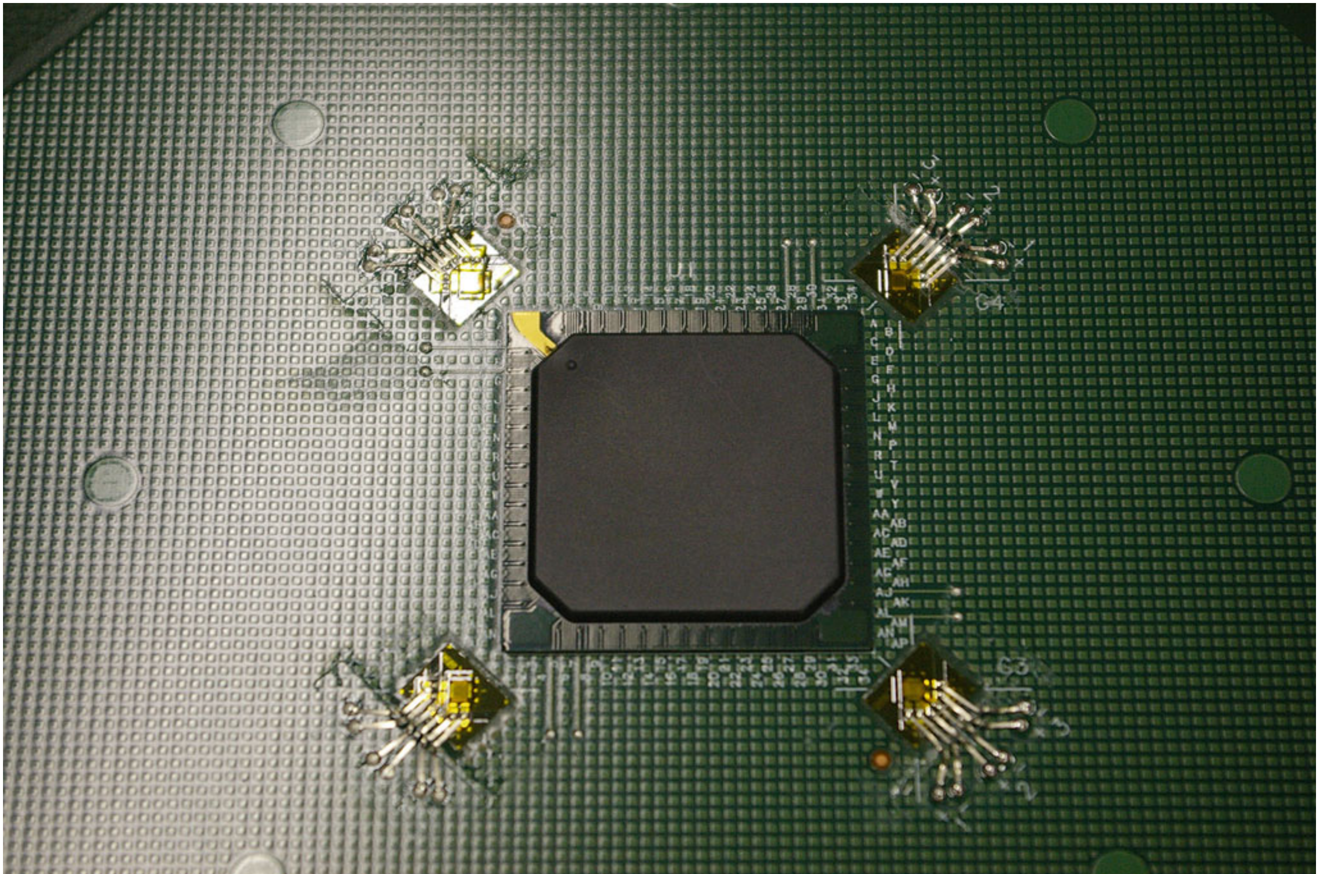

Fig. 4.2 Test specimen

The specimens were PBGA packages reflowed onto a test board as shown in Fig. 4.2. The packages were 35 × 35 mm and incorporated organic substrates with fully-encapsulated die. The packages were mounted to the boards with 1 mm pitch SAC305 solder balls on metal-defined pads. The pads were connected to plated through holes in a dogbone configuration, with the plated through-holes (PTH) positioned to the lower left – in the direction of corner 1 – as shown in Fig. 4.3. The circuit boards were 160 × 160 mm, 1.6 mm thick, eight layers, with two different FR-4 laminate materials. Daisy-chain networks and strain gauge lead soldering points were designed into the boards and specimens at each corner. The daisy-chains and strain gauges were routed out to pins at the corners of the boards where they were connected to cables leading to the data acquisition system. The specimens were fabricated for a previous study and were 2 years old when tested. Specimens from the same lot had been tested in the prior evaluation in accordance with industry standard IPC/JEDEC-9707. That unpublished study found that interconnections in Corner 3 were damaged at lower strain levels than the other three corners, and that the boards made from Laminate B were damaged at lower strain as compared to Laminate A.

Load was applied to the specimens with a United FM-20AE screw-driven test frame using a spherical bend test fixture. The testing equipment was run in displacement control. The span radius of the reaction pins was 55 mm. Specimens were centered on the reaction pins and kept in position with metal brackets at the corners that were positioned so that the board could bend freely, but could not translate more than about 1 mm or rotate more than a few degrees. Displacement, load, strain, and daisy-chain continuity were measured at 50 Hz with a 25 Hz Bessel filter by an HBM digital data acquisition system. The daisy-chains were combined into a single chain for the purposes of these tests. Stacked strain gauge rosettes (Vishay C2A-06-062WW-350) were placed at each corner in accordance with the recommended strain gauge placement for area array devices in IPC/JEDEC-9704.

Four broadband piezoelectric acoustic transducers were located along the package centerline 39 mm from the package center, as shown in Fig. 4.4, and the locations were entered into the analysis software. The transducers were coupled to the board with vacuum grease and were held in place with spring clips. The input signals were amplified by 54 dB, while the trigger signals were amplified by 45 dB. When any channel triggered, waveforms on all four channels were recorded for

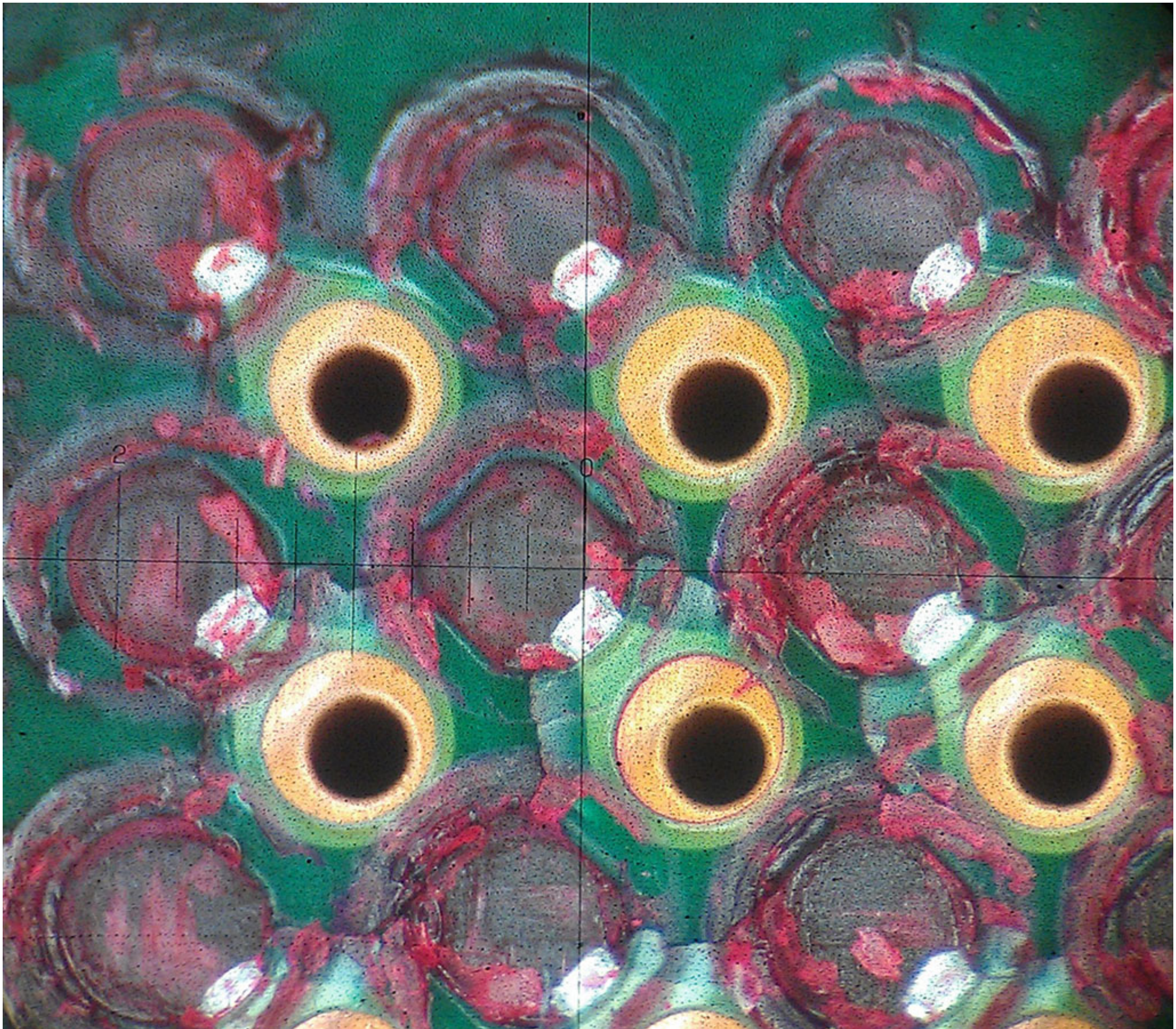

Fig. 4.3 Solder pad design

200 μs. A cable was connected between the primary data acquisition system and the MAE system to provide a voltage signal corresponding to load so that the mechanical data could be correlated with the MAE data in post-processing.

The first step in the test procedure was to mark the transducer locations on the test specimen, mount the transducers, and connect the strain gauge and daisy-chain leads. The specimen was then placed on the test fixture, the load cell was zeroed, the load pin was lowered slowly until load was detected, and then the load pin was reversed slowly until load was relieved. At this point, displacement and strain were zeroed and pencil lead breaks (PLB) were performed in accordance with ASTM Standard E976. PLBs were performed at the package corners, transducer edges, and board edges in order to check the operation of the transducers and calculate the sonic velocity, and also as a geometric reference post-test. The data acquisition systems were started and the specimens were loaded to the target level and unloaded.

The first round of testing was a "cliff test" in which two boards of each laminate were bent at a variety of strain rates to daisy-chain open in order to survey the general mechanical and acoustic event behavior. In the second round of testing, boards were bent at a low strain rate of 60 με/s (10^{-6} cm/cm per second) until five acoustic events were detected in order to determine the level of acoustic signal amplification that would trigger waveform capture of low energy events without triggering due to background noise. In the third round of testing one board of each laminate was bent until the first strain gauge reached either 400, 500, 600, or 700 με at 50 με/s, unloaded, then dyed and pried to check for solder joint damage in

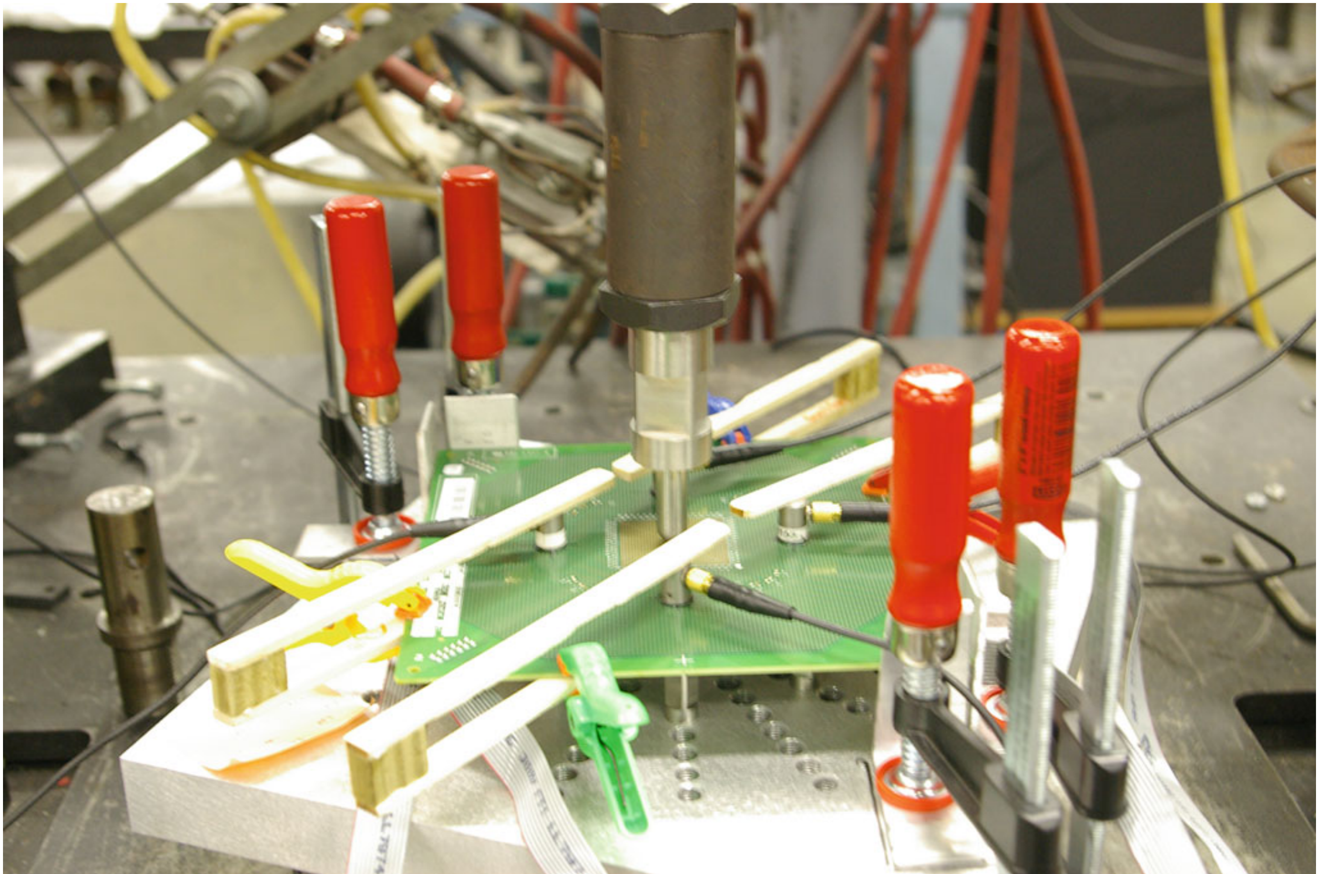

Fig. 4.4 Test setup

order to determine the level at which damage initiated. The final round of testing was another cliff test on one board of each laminate type at either 30 or 300 με/s to daisy-chain open. The test frame prevented evaluation at higher strain rates, such as the 5,000 με/s that is recommended in IPC/JEDEC-9707. These tests were conducted to evaluate the acoustic event behavior with the adjusted signal amplification on tests with a high level of board bending, and over a range of strain rates.

Post-test failure analysis consisted solely of dye and pry. The failure mode was consistent, and since the goal was to determine the extent of damage, cross-section was not performed.

4.3 Waveform Effective Energy

The effective energy of each event can be calculated from the waveform. This value is not the energy of the event, but of the waveform as it is recorded by the data acquisition system. This section discusses the calculation of the effective energy and factors that influence the magnitude of the value.

A typical PLB waveform is shown in Fig. 4.5. The waveform is made up of two waves: a lower energy, higher velocity, and higher frequency extensional wave arriving first and passing the threshold at the vertical line; and a higher energy, lower velocity, and lower frequency flexural wave that is overlaid by the extensional wave. Effective waveform energy is calculated for each transducer by integrating the absolute value of the entire recorded wave, yielding units of $V^2/\mu s$. Noise events, such as the one in Fig. 4.6, typically yield much shorter waveforms compared to fracture events, so their effective energies are correspondingly low, allowing noise events to be eliminated from the data set by excluding events below a certain energy value.

The effective energy is highly dependent on the amplification of the transducers. Increasing the amplification proportionately increases the magnitude of the waveforms for all transducers. Therefore, tests that are performed at different

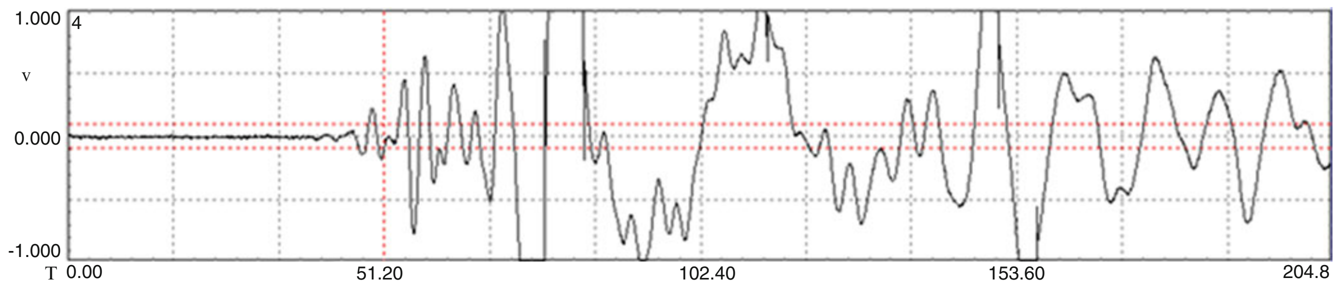

Fig. 4.5 PLB waveform

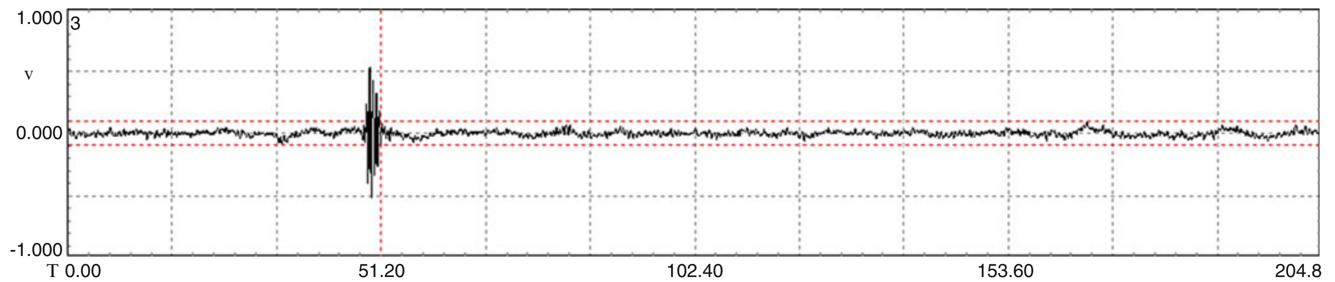

Fig. 4.6 Interference waveform

amplifications would have to be scaled in order to make direct comparisons of the energy values. Excessive amplification may result in saturating the data acquisition system and clipping the peaks of the waves, as can be seen in the largest wave in Fig. 4.5, which will artificially decrease the effective energy of the event. Insufficient amplification may cause some events of interest to not be recorded if none of the waves exceed the threshold.

Attenuation of the waveform will decrease the effective energy. Wave energy dissipation follows a power law function of distance, frequency, and material [5]. The anisotropy of the PCB laminate will result in different levels of attenuation based on the direction of travel. Since events are likely to be different distances and directions from each transducer, the energy of the waveform will be different for each. Therefore, the effective energy of each event depends on how the effective energy values from each of the multiple transducers are used. For example, the effective energy value at the transducer of first incidence may be less than the value at the second transducer, so in this case the first, maximum, and average effective energies would each produce different results.

The length of the capture time will affect the effective energy, depending on the length of capture relative to the length of the waveforms. The data acquisition system is set before the test to record for a certain length of time whenever a wave exceeds the threshold. If the length of capture is shorter than the duration of a waveform, the waveform will be cropped and the effective energy will be artificially decreased. If the length of capture is longer than the duration of the waveform, the effective energy will be slightly increased by the integration of the noise.

Multiple simultaneous waveforms would increase the effective energy. This could happen if multiple events occur within the capture time, or if a reflected wave is incipient on a transducer during the capture of a different event. The data acquisition system would not distinguish between multiple events, and would calculate the energy for the entire capture time.

Transducer sensitivity has a random effect on the effective energy. The transducers have not been calibrated to give the same magnitude, so there is a natural variation in sensitivity. The variation between transducers is assumed to be small.

4.4 Results

Strain response of one of the cliff tests on Laminate A is shown in Fig. 4.7, with strain from each of the four corners plotted as a function of time and daisy-chain open shown as a vertical line. The strain response of the board became nonlinear at approximately 600 $\mu\varepsilon$ for Laminate A, and 500 $\mu\varepsilon$ for Laminate B; peak strain occurred near 1,000 $\mu\varepsilon$. Electrical discontinuity occurred late in the tests after severe damage had apparently been induced. This behavior did not change

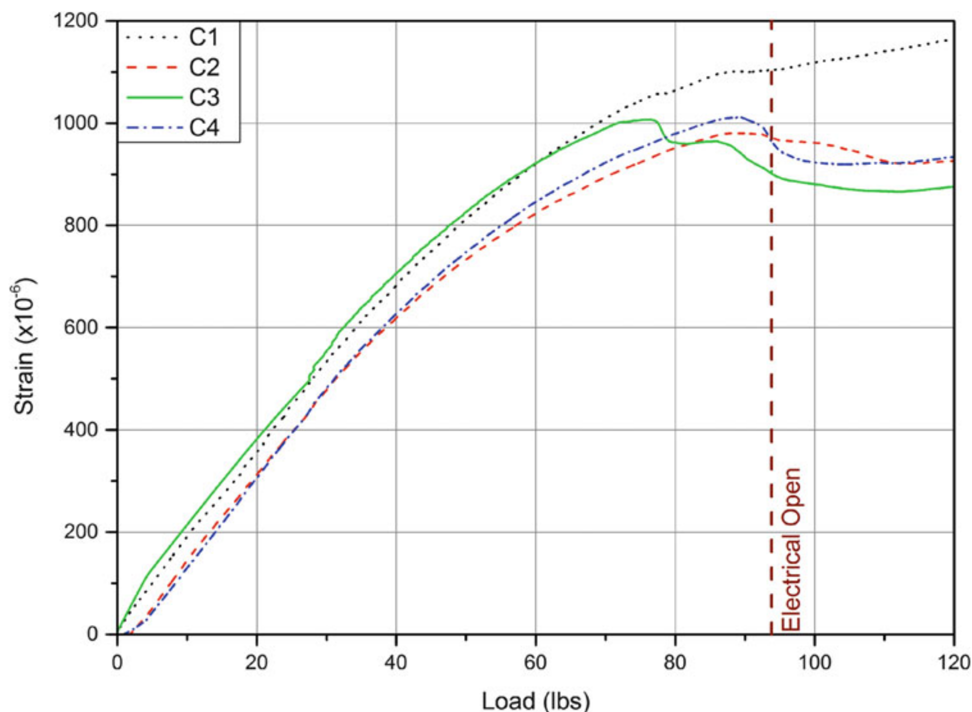

Fig. 4.7 Bend test to electrical open

for the range of bending rates that were tested. Dye and pry of the cliff test boards yielded pad craters for all test failures, regardless of bending rate. Among the boards that were bent to 400, 500, 600, and 700 με, dye stain at pad craters was only found on the Laminate A board that was bent to 700 με. On that board, dye stain was found in the pad craters of five solder joints at corner 3.

The acoustic event histories of the tests show that a number of low energy events occur early in the test, followed by a period of relative quiet, and then a sudden increase in both the number and energy of events. Figure 4.8 shows a typical test in which the cumulative effective event energy is plotted as a function of strain, where effective energy is the average calculated waveform energy of the two transducers equidistant from the corner. The events are separated by the quadrant in which they were located and plotted against the strain measured at that quadrant's corner in order to account for differences in strain at each corner. The size of each marker is relative to the effective energy of that event.

Similarly, Fig. 4.9 shows the individual event effective energy as a function of strain, separated by quadrant. The Laminate A board that was tested to 700 με showed a sudden ramp with two large events in corner 3 at 678 and 712 με, indicating that damage initiated in the historically weak corner at this strain level, as shown in Fig. 4.10. This is the same corner of the same board that subsequently showed dye stain on several solder joints. There were no high energy events recorded on any of the other specimens tested to specific strain levels, nor was any dye stain later observed under the solder joints. This indicates that the high energy events in the 700 με Laminate A board correspond to fracture at the interconnections. There was no significant change in behavior for the two different strain rates. Figure 4.11 shows the cumulative energy as a function of strain for each corner of the two Laminate A boards tested at 30 and 300 με/s, and shows similar trends between the two boards.

4.5 Conclusion

The tests show a consistent trend of relatively few low energy acoustic events at lower strain levels followed by a sudden increase in the number and energy of events at about the point where observable solder joint damage is expected to begin. The data present several potential acoustic damage indicators: a threshold for individual event effective energy, and the inflection in cumulative effective energy. An acoustic damage indicator has at least three important advantages to this test.

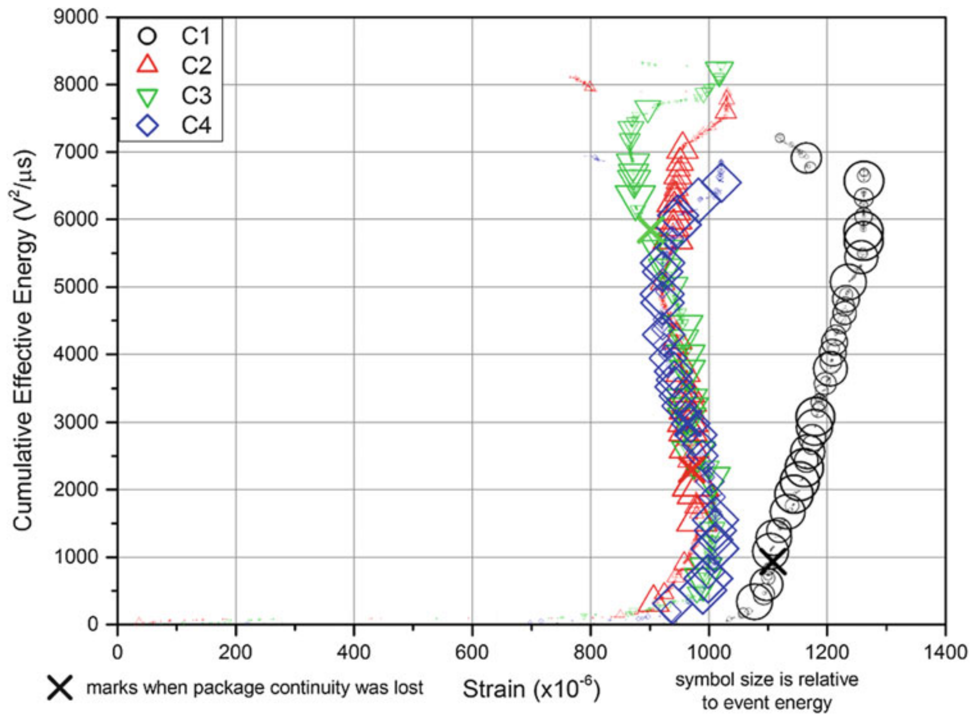

Fig. 4.8 Representative cumulative energy history

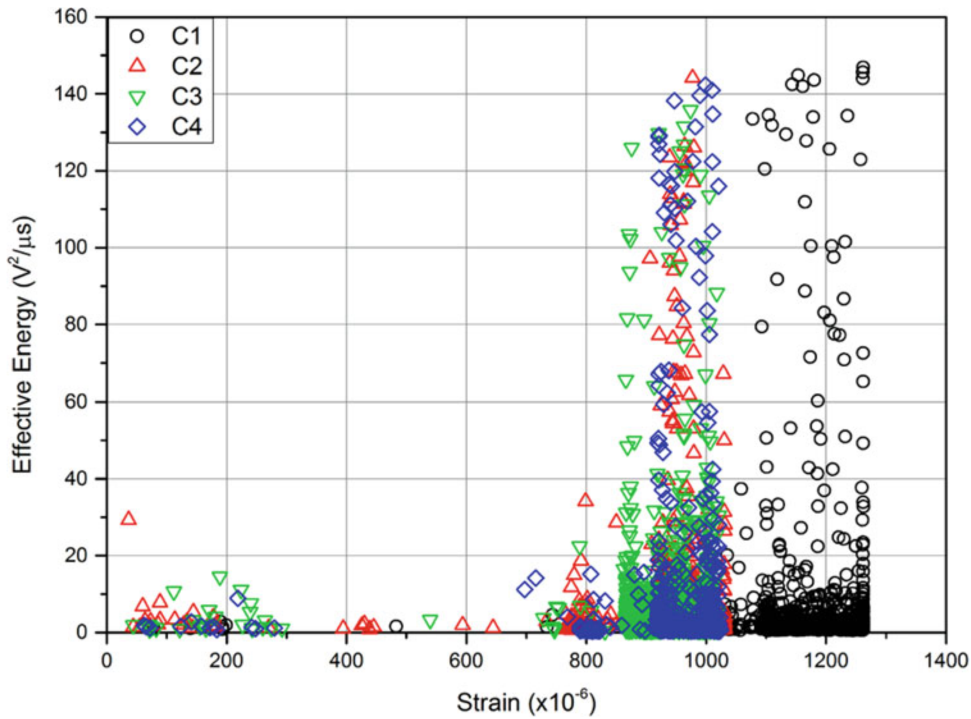

Fig. 4.9 Representative event energy history

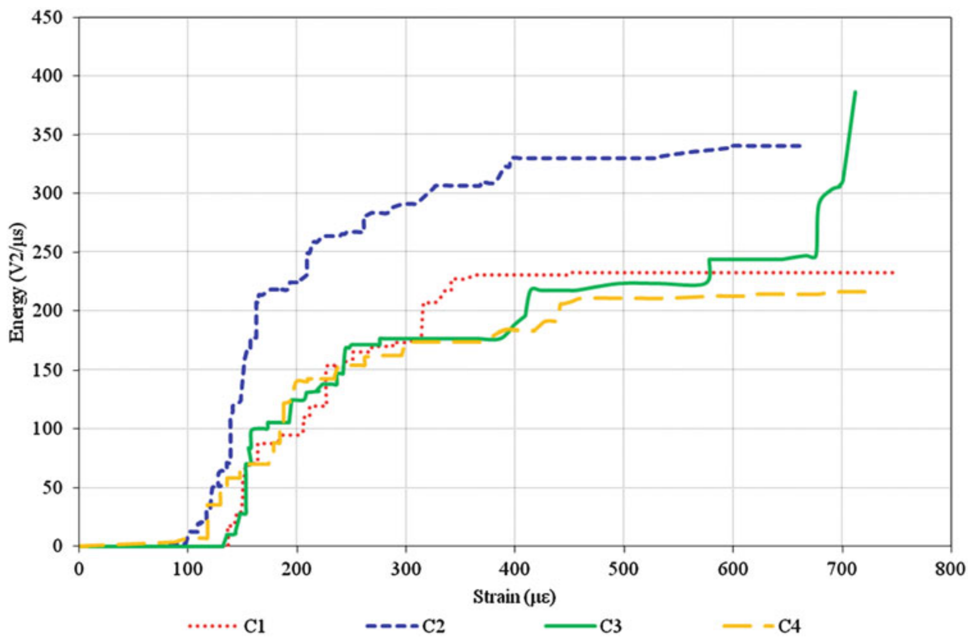

Fig. 4.10 Event history of laminate a board tested to 700 με

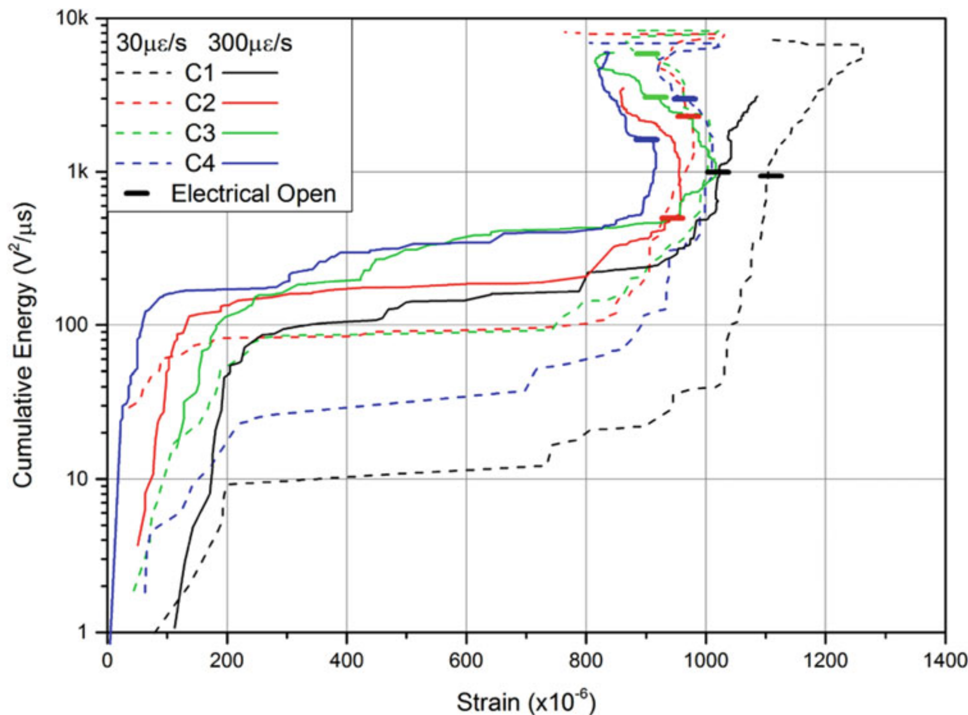

Fig. 4.11 Cumulative energy (log) history of boards tested at 30 and 300 με/s

First, failure strain could be precisely determined for each corner of each test specimen, yielding more data with fewer tests and allowing the safe level to be set through a statistical evaluation of the data rather than by failure analysis. Second, failure analysis could be greatly reduced, saving significant time and money. Third, the test could be performed on production assemblies, yielding more representative data and eliminating the need for a dedicated test board for each component.

The low energy events that occur early in the test may indicate low level damage occurring in the board. These events are scattered around the vicinity of the package and begin to occur very early in the test. Visual analysis of the waveforms

indicates that they are mechanically induced. It is thought that these events might be caused by micro-cracking within the laminate or the glass weave.

Tests were performed at relatively low rates compared to the range of loading rates observed in assembly. Tests were performed at rates between about 30 and 300 με/s, which is about one to two orders of magnitude lower than the upper range of assembly-related strain rates. All failure modes were pad cratering, which is consistent with failures observed in previous tests on the same board design at higher strain rates. The acoustic event history did not show a conclusive trend between the two rates that were tested. This indicates that failure may not be sensitive to loading rate in the range of rates used for this study. This is important if the test is to be stopped based on an event energy threshold in order to check for damage resulting from those events.

These results are promising, but are based on a limited number of tests using a single board design. Additional tests need to be performed to validate that damage initiation coincides with an increase in acoustic activity. Additional work should be done to improve the waveform energy metric. For these specific tests, the amplification should be decreased to avoid saturating the data acquisition system on the larger magnitude events of interest, and the capture time should be optimized to capture the entire waveform while avoiding multiple events. Ultimately, it would be ideal to calculate the energy of the event based on the distance of the event from the transducers, the loss coefficient of the material as a function of direction of transmission through the laminate, and the frequencies of the waveform.

References

1. Reinosa R (2010) Characterizing mechanical performance of board level interconnects for in-circuit test. In test conference (ITC), Austin, 2–4 Nov 2010
2. Hsieh G (2005) Flip chip ball grid array component testing under board flexure. ECTC ’05, Orlando, FL, pp 937–944, 31 May–3 June, 2005
3. Morscher G (1998) Modal acoustic emission of damage accumulation in a woven SiC/SiC composite. Compos Sci Technol 59(1999):687–697
4. Ralph W (2013) Acoustic emission detection of BGA components in spherical bend. ECTC ’13, Las Vegas, pp 208–213, NV, 28–31 May 2013
5. Szabo T (1994) Time domain wave equations for lossy media obeying a frequency power law. J Acoust Soc Am 96(1):491–500

Chapter 5
Shape Optimization of Cantilevered Piezoelectric Devices

Naved A. Siddiqui, Seon-Bae Kim, Dong-Joo Kim, Ruel A. Overfelt, and Barton C. Prorok

Abstract Energy harvesting using piezoelectric devices has received considerable attention in the past few years. The most commonly used devices have been cantilevered bimorphs with a large proof mass attached to it. The goal of this paper is to discuss the effects of varying geometry to enhance the average strain through a material via shape optimization into triangular type geometries from a quantitative point of view, while studying the internal strain energy and the stress distribution over the surface when a cantilevered device is loaded. When a triangular cantilever is compared to a rectangular counterpart with the same volume, the stress over its surface is linear, as it has a more constant radius of curvature, and its loading capacity effectively doubles. These concepts are explored numerically using ANSYS. The concept of internal strain energy per unit area over the length span of the beam is used to evaluate the amount of average energy stored in the material over the surface, and shows that regardless of geometry, the value is strictly a function of volume of the device. The linear stress distribution over the length of triangular beams, and their relations with the volume when compared to a rectangular cantilever is the standout property that would allow much more reliable operation of cantilevered brittle piezoelectric ceramic devices.

Keywords Shape-optimization • Quasi-static • Energy-harvesting • Piezoelectric • Cantilever

5.1 Introduction

In recent years, there has been a quest for finding a source of localized energy for wireless sensor nodes, and the development of various portable systems such as MEMS devices for low power applications. These sensor nodes or devices could utilize traditional batteries; however since batteries have a finite life [1], and in certain applications where these sensors might be placed in locations that are not easily accessible, the replacement of a battery might become a difficult task. Cook-Chennault et al. reviewed [2] various types of non-regenerative sources that may be viable such as micro-batteries, micro-fuel cells, micro-heat engines, but some of these require a fuel, or might not have the desired efficiency, or may be expensive and cumbersome. Therefore, there has been much interest in searching for a source from where energy is regenerative, and can be harvested from ambient conditions.

Some of the sources for energy harvesting technologies that have been researched in the past few years include solar, thermoelectric, electromagnetic, electrostatic, and piezoelectric [2–6]. Of these mechanisms, and sources of energies, piezoelectric devices offer the greatest range of power density, as indicated in the review by Cook-Chennault et al. [2]. Electrostatic devices greatly suffer from due to high impedance and output voltages, and therefore do not fit in the chart in Fig. 5.1. Therefore, there is a great potential for using the piezoelectric effect to obtain harvested energy from a potential mechanical source and converting it into electrical energy. One of the major sources of such potential energies that can be utilized are ambient vibrations that are present in numerous mechanical systems and structures, that can invoke a charge in a piezoelectric device when it is strained.

The phenomenon of piezoelectricity was famously found by the Curie family, and it has been widely reported that there are two possible mechanisms for the operation of piezoelectric devices. One is the direct piezoelectric effect, which is where

N.A. Siddiqui • S.-B. Kim • D.-J. Kim • R.A. Overfelt • B.C. Prorok (✉)
275 Wilmore Laboratories, Materials Engineering, Auburn University, Auburn, AL 36849, USA
e-mail: prorok@auburn.edu

G. Shaw III et al. (eds.), *MEMS and Nanotechnology, Volume 5: Proceedings of the 2013 Annual Conference on Experimental and Applied Mechanics*, Conference Proceedings of the Society for Experimental Mechanics Series,
DOI 10.1007/978-3-319-00780-9_5, © The Society for Experimental Mechanics, Inc. 2014

a material is strained and in return a charge is generated, and the converse effect is vice versa. The constitutive equations for the piezoelectric effect are as follows [7]:

$$S_{ij} = s^{E}_{ijkl} T_{kl} + d_{kij} E_k$$

$$D_i = d_{ikl} T_{kl} + \varepsilon^{T}_{ik} E_k$$

where, S is strain, s^E is elastic compliance at constant electric field, T is stress, d is piezoelectric constant, E is the electric field, D is dielectric displacement component, and ε^T is the permittivity of the material at constant stress. The subscripts indicate the tensor notation. The reduced form of the equation when $E_1 = E_2 = 0$, and $E_3 \neq 0$, indicates that the strain is directly related to the charge output and the piezoelectric coefficient in addition to the elastic compliance multiplied by stress.

One of the most important properties is the piezoelectric coefficient, and is often used to describe the mode of operation. Often times, in energy harvesting applications, the piezoelectric material is used in the d_{31} mode, which in commonly used Cartesian coordinates indicates that the charge is developed in the transversal (one direction) when the strain is applied in the longitudinal direction. This d_{31} mode is most commonly exploited using a cantilevered bimorph as indicated by Roundy [5] and followed up by several researchers. Piezoelectric bimorphs are devices that contain two thin piezoelectric layers that sandwich a metallic layer meant for structural rigidity, and the cantilever boundary conditions give the opportunity of producing the largest possible deflections in a beam [6], and hence the greatest amount of strains, which are directly related to the power generated by the piezoelectric device. Due to the fact that strain and stress are directly related, which dictate the amount of possible charge generation; it becomes imperative to study the bending of a cantilevered bimorph. The aim of this paper is to show how these stresses and strains in a beam can be enhanced by changing the geometry of a cantilevered device in order to improve power generation efficiency from a cantilevered device. Various researchers [8–13] explored the concept of changing geometry of a cantilevered beam from a simple rectangular shape to a trapezoidal to an increasingly triangular shape, and confirm that there is a definite improvement of power output when the geometries are changed. However, the goal of this paper is to present an insight into the bending of beams with these changing geometries in a systematic fashion, and understand the characteristics that may lead to enhanced power output, which can serve as a way to predict improved geometries. The concept of internal strain energy per unit area is presented which helps us better understand the mechanical response when a beam is deflected under an external load.

5.2 Methodology

The numerical package ANSYS 13.0 Mechanical APDL is utilized for generating the energy harvester devices and evaluating their characteristics. A simple quasi-static analysis is performed for each structure. The cantilever beams that are generated in the software have dimensions adopted from commercially available piezoelectric bimorphs from Piezo Inc. The adopted rectangular beam is 31.8 mm in length, 12.7 mm in width and overall thickness is 0.51 mm. Triangular beams that have been generated maintain the same length and thickness as the rectangular cantilevers, which the width at the base is altered to study the beams. The material properties applied utilize the d_{31} directional properties of PZT-5A from Piezo Inc. The Young's modulus is 62 GPa, Poisson's ratio of 0.31, and mass density of 7,750 kg m^{-3}.

The geometry is constructed, using the 20 node SOLID186 element, and applying a brick shaped mesh, while maintaining an elemental aspect ratio of 1:1. The back of the beam is fixed by setting displacements at the prescribed fixed end to zero. Point load of 0.5 N is applied at the free end; as a distributed load in the case of the rectangular cantilever, and a simple point load at the free end of the triangular cantilevers. Quasi-static analyses are performed, and nodal displacements, transversal stresses and strains along the mid-span (i.e. length at the center) on the surface are extracted from the numerical package and plotted and evaluated.

Three of the explored geometries, along with their meshes, load and boundary conditions are presented in Fig. 5.1. Figure 5.1a shows the rectangular beam with the above mentioned dimensions. Figure 5.1b (Triangle 1) is a triangular cutout from the rectangular geometry while maintaining the base width, and Fig. 5.1c (Triangle 2) is a triangular beam which has twice the base width of the Rectangular beam and Triangle 1.

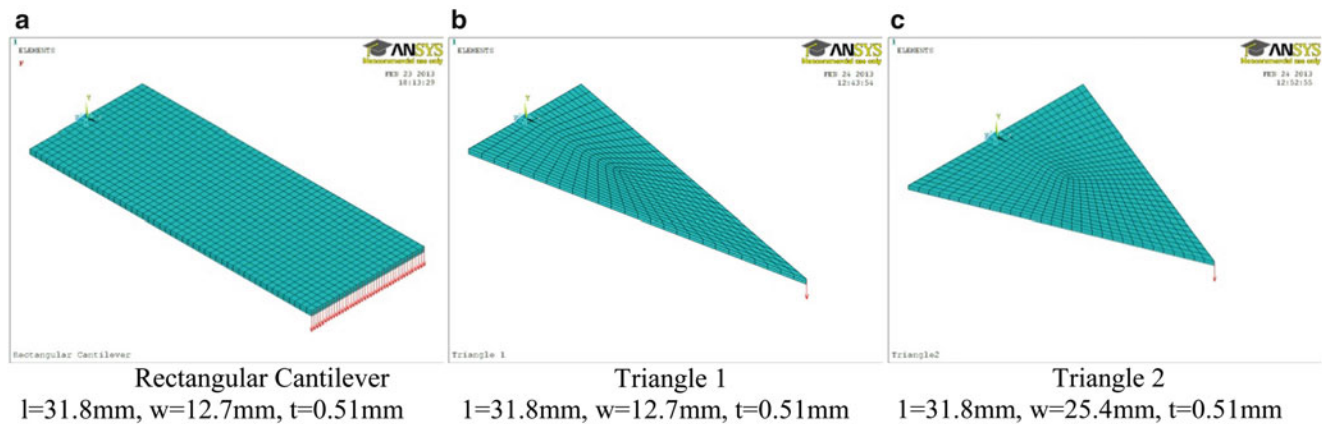

Fig. 5.1 Geometric considerations for cantilevered devices

5.3 Results and Discussion

As the geometries mentioned above were constructed and meshed, the boundary conditions were applied to cantilever the structures, and the loads were applied. Static mode analyses were carried out in ANSYS, and the main parameters that were extracted include longitudinal deflection (y-direction), and transversal stresses (x-direction). These parameters are shown in Figs. 5.2, 5.3 and 5.4, where Fig. 5.2 gives an illustration of the deflection contour plots, and Fig. 5.3 provides the numerical deflection data of the three structures. Similarly Figs. 5.3 and 5.4 provide the transversal stress contours and numerical data respectively.

It is very interesting to notice some of the subtle differences between the three cantilevered devices, indicative upon close inspection of Fig. 5.3. As expected, the overall magnitude of deflection of Triangle 1 (0.92 mm) is about 54 % of the Rectangular cantilever (0.59 mm), since it has half the volume by comparison, and thus less amount of material to provide resistance to deformation. However, when comparing the rectangular cantilever, and Triangle 2, the tip deflection of Triangle 2 is 21 % less (0.47 mm) than the Rectangular cantilever, even though they have the same volume, and the same surface area. This is a direct effect of the changing geometry wherein the tapering in the triangular cantilevers provides a linear decrease in the area moment of inertia from the fixed end to the free end. An effect of this can also be again noticed in Fig. 5.3, where it can be seen that the slope of the curve is somewhat linear in the second half of deflection of the beam, whereas the slope of deflection is more radial in the case of the triangular cantilevers; i.e. bending has a more constant radius of curvature. This behavior is further discussed upon inspection of the next two figures.

The drive towards the changing geometry was to be able to obtain a more constant transversal stress. This behavior is successfully obtained as can be noticed in the contour plots of transversal stresses in Fig. 5.4, which are plotted in terms of numerical data in Fig. 5.5.

Figure 5.4 is an important visual aid in understanding the stress distribution over the surface of the cantilevered devices. It can be seen that the rectangular beams have areas of high stress concentration near the fixed end of the beam, which keep on decreasing along the length towards the free end. This aspect is however not as pronounced in the triangular cantilevers, which have a small area of high stress concentration near the fixed end for a length of about 10 % of the total length of the beam, but then are steady through the rest of the length. This behavior is depicted in Fig. 5.5.

Figure 5.5 shows the transversal stress (x-direction) through the mid-span, along the length, on the surface of the cantilevered device. In the case of the rectangular cantilever, it can be clearly seen that the stress along the length of the beam decreases linearly, while in the case of the triangular cantilevers, it remains constant for 90 % of the length span. It is also important to notice the magnitudes of the stresses with the given geometries. The maximum stress on the rectangular cantilever is 34.6 MPa, and the minimum is 78.4 kPa, a two order of magnitude decrease over the length. However, when compared to Triangle 1, the maximum stress is 37.1 MPa, but in the linear region, the stress is 29.0 MPa in the linear region, which is only a 20 % decrease and that too within a 10 % length span. Hence, the average stress can be considered to be 29.0 MPa for Triangle 1. Therefore, Triangle 1, which has half the volume of the rectangular cantilever is stressed to the same level of stress over the entirety of the surface, as of the rectangular cantilever with the same applied load. In the case of triangular cantilever 2, the maximum stress and average stress are very similar, which is about 14.60 MPa. This stress is

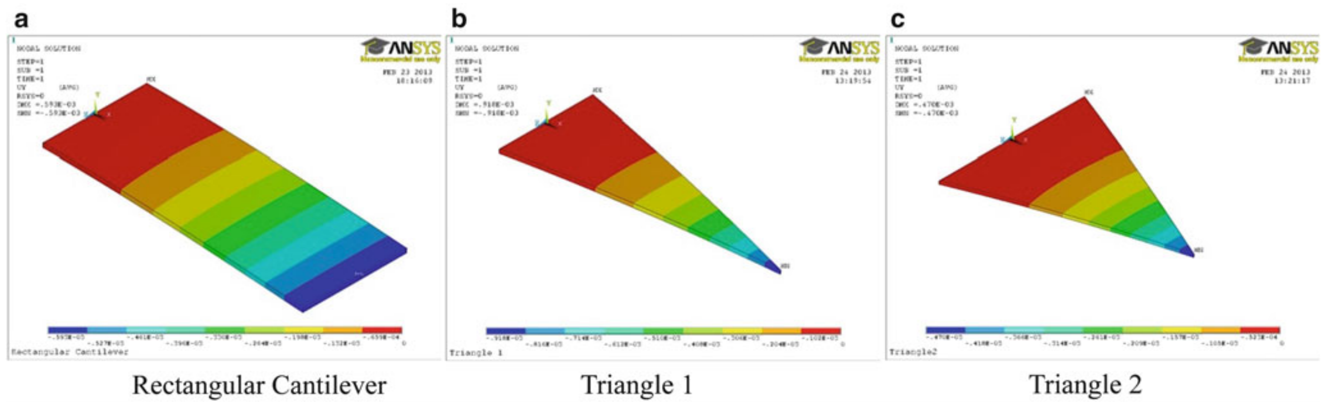

Fig. 5.2 Deflection contours of cantilevered devices

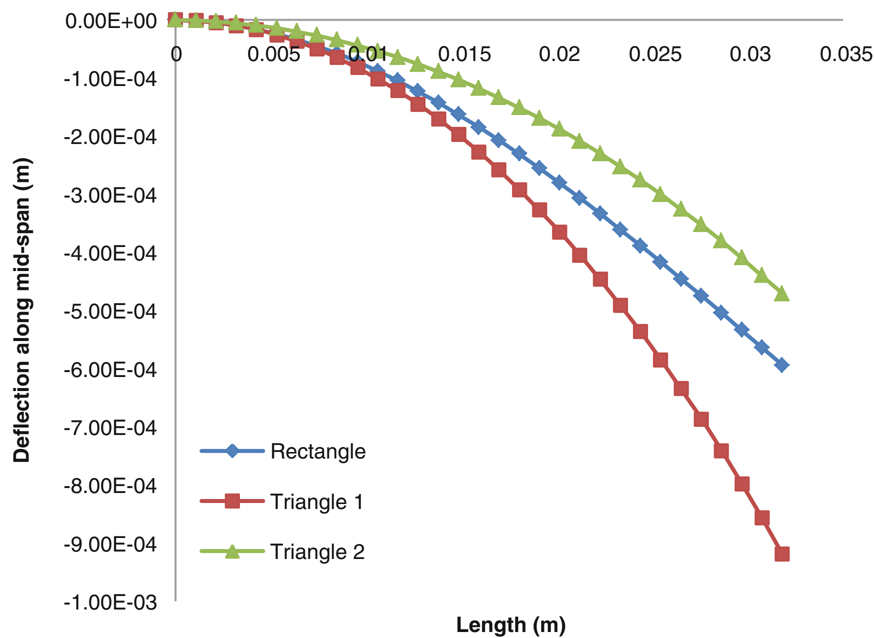

Fig. 5.3 Deflection along mid-span of cantilevered devices

about half the average stress of Triangle 1 and maximum stress of the rectangular cantilever, with the same applied load. Therefore, in essence, changing the geometry of the rectangular cantilever to a triangular cantilever while maintaining the length and thickness, and varying the base (Triangle 2), in essence the loading capacity can be doubled, which would allow for a much greater strain on the device and at least double the power output with the same given area from a quasi-static – mechanical standpoint.

In order to further scrutinize Fig. 5.5, the area under the stress-length curve for each device was integrated to find units of N/m^2 times meter. This in effect is a unit of energy per area, which can be called as an internal strain energy per surface area of the device, which can give a figure of merit of stress over the surface of a device. Values for internal strain energy per unit area for the three devices are presented in Table 5.1. With the same load of 0.5 N for the three devices, it can be seen that the Rectangle and Triangle 2, which have the same volume have a very similar internal strain energy, i.e. the area under their curves is almost equal. This indicates that Triangle 2, which has the same volume as the rectangular cantilever is taking the same load as the rectangular cantilever, but is able to distribute is more efficiently and more evenly over its surface. This behavior would be very desirable for an energy harvesting device as the power generation would be more efficient over a

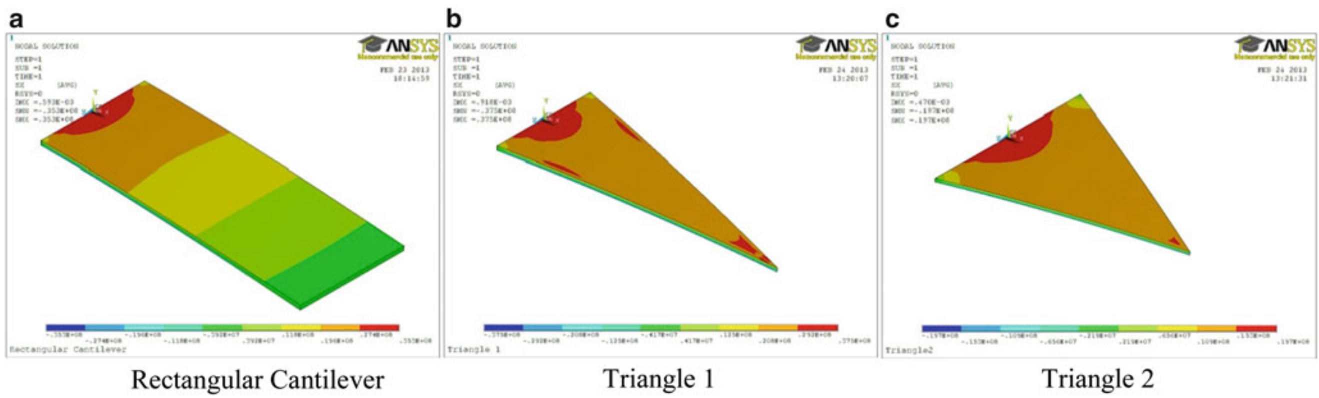

Fig. 5.4 Transversal stress contours on cantilevered devices

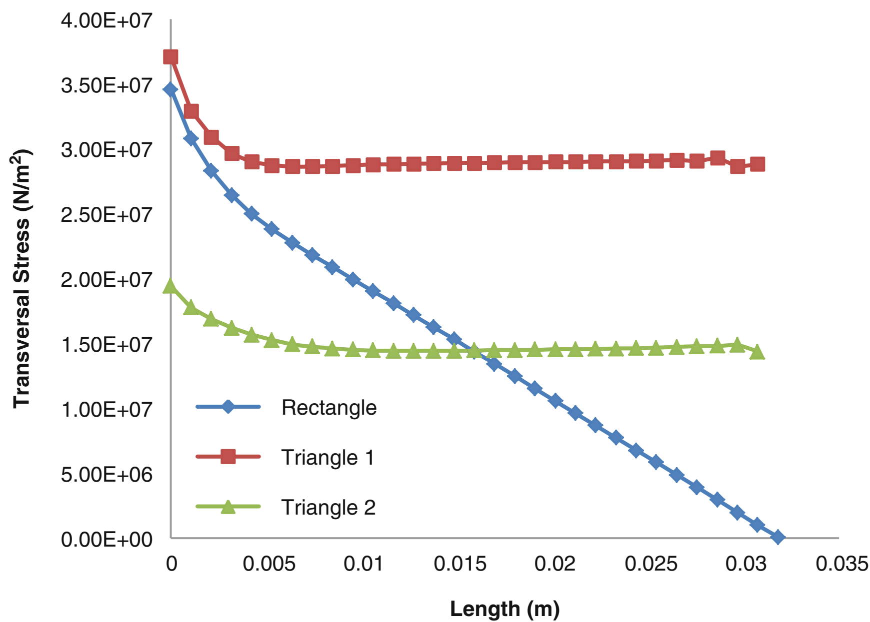

Fig. 5.5 Transversal stresses along the length over the mid-span of the cantilevered devices

Table 5.1 Summary of characteristics of the stressed cantilevered devices

	Max deflection (mm)	Average stress (MPa)	Internal strain energy per area (Nm/m^2)
Rectangle	0.59	Linear decrease	467,946.25
Triangle 1	0.92	29.00	928,223.20
Triangle 2	0.47	14.60	475,491.27

device, which would not be the case for a rectangular cantilever. The internal strain energy of the Triangle 1, which is double the value of the other two devices, is indicative of double the amount of stress it is experiencing.

In order to utilize this concept of internal strain energy per unit area for evaluating a variety of cantilevered devices, multiple simulations were performed for various triangular and rectangular beams having the same length and thickness, and varying base widths. It was found that regardless of geometry, the area under the stress-length curve gives an indication of the amount of load applied. However, the true characteristic that is of importance is the behavior of the stress versus beam length curve.

5.4 Conclusions

This paper strictly evaluates the effect of constrained design parameters for a cantilevered device for energy harvesting. Energy harvesting using piezoelectric devices is a complex problem where the electro-mechanical coupling and the type of applied force has adverse effects on the power generation of a piezoelectric cantilever, but in order to fully exploit the d_{31} mode of operation, where a piezoelectric device is cantilevered, it is important to evaluate the bending characteristics of a beam. It is seen that when a force is applied on the tip of a rectangular beam, the deflection does not have a constant radius of curvature, and have a linear decrease in the stress over the surface from the fixed end. When the geometry is modified to a triangular shape, the stresses (and hence the strain) produced in the device is far more linear, over the length of the beam. The internal strain energy per unit area gives an account of how much the cantilever beam is stressed, and can indicate a design parameter for the maximum stress over a beam, but it is the bending characteristic of a tapered beam that gives us a constant radius of curvature and linear stress over its surface that would be desirable for piezoelectric energy harvesting from an applied mechanical load such as vibrations or quasi-static loading that would allow the device to operate more reliably with lower levels of stress. Ongoing research includes evaluation of shaped devices for power generation from these devices.

References

1. Sodano HA, Inman DJ, Park G (2004) A review of power harvesting from vibration using piezoelectric materials. The Shock Vib Dig 36:197–205
2. Cook-Chennault KA, Thambi N, Sastry AM (2008) Powering MEMS portable devices – a review of non-regenerative and regenerative power supply systems with special emphasis on piezoelectric energy harvesting systems. Smart Mater Struct 17:043001
3. Priya S (2007) Advances in energy harvesting using low profile piezoelectric transducers. J Electroceram 19:167–184
4. Beeby SP, Tudor MJ, White NM (2006) Energy harvesting vibration sources for microsystems applications. Meas Sci Technol 17:R175–R195
5. Roundy S, Wright PK, Rabaey J (2003) A study of low level vibrations as a power source for wireless sensor nodes. Comput Commun 26:1131–1144
6. Roundy S, Wright PK, Rabaey JM (2004) Energy scavenging for wireless sensor networks: with special focus on vibrations. Kluwer, Boston
7. Ikeda TO (1990) Fundamentals of piezoelectricity. Oxford University Press, New York
8. Roundy S, Leland ES, Baker J, Carleton E, Reilly E, Lai E, Otis B, Rabaey JM, Wright PK, Sundararajan V (2005) Improving power output for vibration-based energy scavengers. Pervas Comput IEEE 4:28–36
9. Goldschmidtboeing F, Woias P (2008) Characterization of different beam shapes for piezoelectric energy harvesting. J Micromech Microeng 18:104013
10. Benasciutti D, Moro L, Zelenika S, Brusa E (2009) Vibration energy scavenging via piezoelectric bimorphs of optimized shapes. Microsyst Technol 16:657–668
11. Park JH, Kang J, Ahn H, Kim SB, Liu D, Kim DJ (2010) Analysis of stress distribution in piezoelectric MEMS energy harvester using shaped cantilever structure. Ferroelectrics 409:55–61
12. Paquin S, St-Amant Y (2010) Improving the performance of a piezoelectric energy harvester using a variable thickness beam. Smart Mater Struct 19:105020
13. Park J, Lee S, Kwak BM (2012) Design optimization of piezoelectric energy harvester subject to tip excitation. J Mech Sci Technol 26:137–143

Chapter 6
Unique Fabrication Method for Novel MEMS Micro-contact Structure

Benjamin Toler, Brent Danner, Derrick Langley, and Ronald Coutu Jr.

Abstract Microelectromechanical systems (MEMS) switch reliability is a major obstacle for large-volume commercial applications despite offering lower power consumption, better isolation, and lower insertion loss compared to conventional field-effect transistors and PIN diodes (Yang et al. IEEE J Microelectromech Syst 18(2): 287–295, 2009). To enhance reliability and performance, MEMS researchers focus on the micro-contact lifecycle evolution based on material choice and design of the micro-contact. In order to examine the micro-contact phenomena and physics, a novel DC MEMS micro-contact structure has been developed. The structure is composed of a Gold contact pad and a layered Gold beam. The reliability and performance of a micro-contact is directly influenced by its ability to make and break its electrical connection. Its ability to separate from the contact area is a function of applied force, adhesion forces, and the restoring force. The layered Gold micro-contact structure was fabricated and the processing steps, performance, and experimental results of the device reliability of the device are presented.

Keywords Micro-contacts • Processing • Fabrication • Reliability • MEMS

6.1 Introduction

This paper presents a fabrication method for a novel MEMS structure which supports the study of micro-contacts. Many researchers like Poulain et al. and Bromley et al. use cantilever based designs for studying the evolution of micro-contact physics [1]. Unfortunately, a drawback to cantilever based designs are the increased opportunity for structural fatigue and other failure modes which are not considered a failure of the micro-contact itself. Also, cantilever designs are commonly electrostatically actuated. Electrostatic actuation requires researchers to comb through the data and back out the values for contact force. Rather than backing out values for contact force, the device presented is for use with an externally calibrated applied force. Both contact force and temperature are integral components which greatly influence the performance and reliability of micro-contacts [2, 3]. The device presented in this paper was specifically designed to allow for the study of micro-contact interface evolution. The fixed-fixed beam design promotes the study of purely micro-contact failure modes by provided better countermeasures against stiction and mechanical failures such as structural fatigue. This design essentially limits the failure of the device to the evolution of the contact interface. A recreation of Holm's crossed bar experiment, the device's design is configured for a four wire measurement [4]. The fabrication method is described and the novel device is characterized.

Disclaimer: The views expressed in this article are those of the authors and do not reflect the official policy or position of the United States Air Force, Department of Defense, or the U.S. Government.

B. Toler • B. Danner • D. Langley • R. Coutu Jr. (✉)
Air Force Institute of Technology, 2950 Hobson Way, WPAFB, OH 45433, USA
e-mail: ronald.coutu@afit.edu

G. Shaw III et al. (eds.), *MEMS and Nanotechnology, Volume 5: Proceedings of the 2013 Annual Conference on Experimental and Applied Mechanics*, Conference Proceedings of the Society for Experimental Mechanics Series,
DOI 10.1007/978-3-319-00780-9_6, © The Society for Experimental Mechanics, Inc. 2014

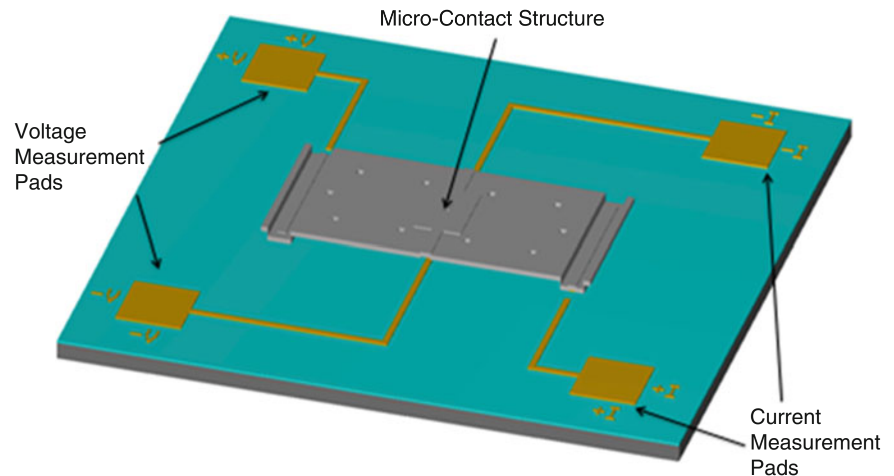

Fig. 6.1 Fixed-fixed beam micro-contact support structure

6.2 Device Design Concept

Figure 6.1 illustrates the fixed-fixed beam micro-contact support structure concept. The fixed-fixed beam micro-contact structure emulates Holm's crossed bar experiment on the micro-scale by allowing a four wire measurement which will measure the resistance of the micro-contact interface at contact make. Voltage is then measured across the micro-contact via gold traces connected to the anchor of the beam and micro-contact area. The structure is designed for studying micro-contact failure modes using an externally calibrated applied force. The bottom metal layer consists of the measurement pads and planar micro-contact area underneath the micro-contact support structure. The underside of the support structure has a micro-contact 'bump' to create a hemisphere-to-planar surface contact. Based on the idea of testing multiple micro-contact materials as well as investigating modified structural or electrical layers, the device can be considered 'modular'. For example, the electroplated gold structural layer (described in the next section) could be replaced by another material with greater thermal conductivity in order to examine the effect of material choice and proximity to micro-contact on micro-contact temperature and longevity.

6.3 Fabrication Process

The fixed-fixed beam micro-contact support structure is fabricated using surface micromachining processes at the Air Force Institute of Technology. Surface micromachining involves depositing, patterning, and etching sacrificial and structural layers. This method of fabrication was chosen in order to allow changes in the choice of materials for the contact or structural layer(s) and for precise dimensional control in the vertical and horizontal direction. A disadvantage of surface micromachining is the limitation of using thin-films; which properties are usually unknown and must be measured. A device made via surface micromachining is released when sacrificial layers are removed and the structural layers remain. Figure 6.2 shows the surface micromachining process used to fabricate the fixed-fixed beam micro-contact structure.

Beginning with (a), a silicon substrate is cleaned before a layer of nitride is deposited (b). The nitride layer acts as an electrical isolation layer. In (c) and (d), a layer of SF-11 photoresist and 1805 photoresist is established on the surface of the nitride coated wafer. The 1805 serves as a mask for patterning the layer of SF-11. In (e), the 1805 photoresist is patterned by a mask and exposed to ultraviolet light. The ultraviolet light breaks the chemical bonds of the photoresist in the exposed areas and allows the exposed 1805 to be developed away (f). After the 1805 is developed, the exposed SF-11 is subjected to deep ultra violet light (DUV) which, similar to the 1805, breaks the chemical bonds of the exposed SF-11 and allows the exposed area to be removed. A gold layer is then deposited in (g). Following deposition, the remaining gold is lifted off and all photo resist is removed (h). What remains in (h) is the bottom metal layer of the fixed-fixed beam micro-contact support structure.

For the mechanical layer of the fixed-fixed beam micro-contact support structure, two layers of SF-11 and a layer of 1805 are coated on the wafer. The 1805 is patterned and developed in (j) and (k) and then the SF-11 is exposed to DUV and developed away (l). The 1805 is then removed in (m) and 1805 is placed on the wafer in (n). This allows for the patterning of the micro-contact bump. The 1805 is patterned and developed and the exposed SF-11 is exposed to a partial DUV to

(a) Clean Si Substrate
(b) Nitride Deposition
(c) SF-11 Photoresist
(d) 1805 Photoresist
(e) UV Exposure (patterning)
(f) 1805 Developed SF-11Exposed to DUV SF-11Developed
(g) Gold Deposition
(h) Lift-Off and Photoresist Removal
(i) Two layers of SF-11 and 1805 Photoresist
(j) UV Exposure
(k) 1805 Developed
(l) SF-11Exposed to DUV SF-11 Developed
(m) 1805 Removal
(n) 1805 Photoresist
(o) UV Exposure
(p) 1805 Developed
(q) 1805 Removal
(r) Gold Deposition
(s) AZ 3350 Photoresist
(t) UV Exposure
(u) AZ 3350 Developed
(v) Gold Electroplate
(w) AZ 3350 Removal
(x) Gold Etch
(y) Release

Fig. 6.2 Surface micromachining process for fixed-fixed beam micro-contact support structure

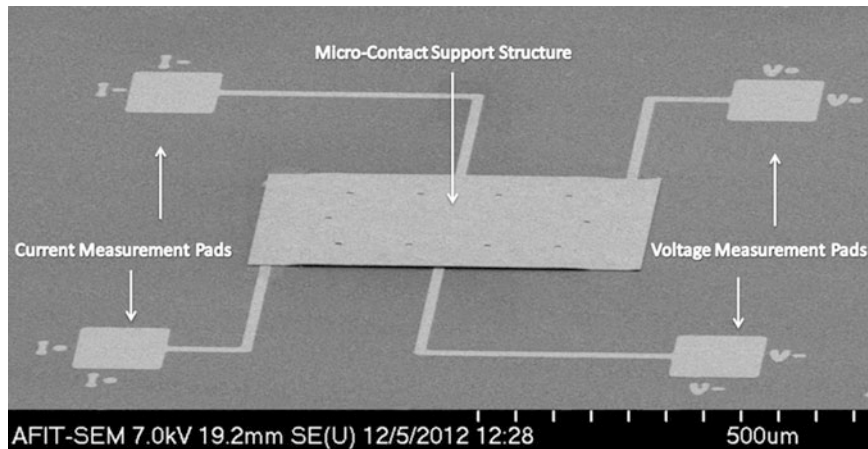

Fig. 6.3 Fabricated device

establish the micro-contact bump ((o) and (p)). The layers of SF-11 are sacrificial layers which, in addition to the contact bump exposure, determine the gap between the hemispheric contact bump and planar lower contact. In (q), the 1805 is removed and Au is sputtered in (r) as a seed layer for electroplating. AZ 3350 photoresist is applied in (s) and patterned (t) and developed (u) for electroplating (v). Once the desired amount of Au has been electroplated, the AZ 3350 is removed (w). To remove the seed layer, an Au etch is performed (x). To release the device, the sacrificial SF-11 is removed (y). Figure 6.3 shows an SEM image of the fabricated device.

6.4 Contact Force and Micro-contact Resistance Modeling

In order to determine the force required to make contact using the fixed-fixed beam micro-contact support structure, the micro-contact support structure is modeled as a simple fixed-end beam with a concentrated load F at the midpoint. Figure 6.4 shows the simplified beam's moment diagram.

Because of beam symmetry and the applied load F in the vertical direction, the moments on either end of the beam are equivalent and lead to:

$$M = \frac{Fx}{2} - M_1 \quad \left(0 \le x \le \frac{L}{2}\right) \tag{6.1}$$

Mohr's theorems provide the relationship between the moment M, Young's modulus E, inertia I, and rate of change for deflection δ''

$$EI\delta'' = M = \frac{Fx}{2} - M_1 \quad \left(0 \le x \le \frac{L}{2}\right) \tag{6.2}$$

Integrating Eq. 6.2 twice to obtain deflection δ gives:

$$EI\delta = \frac{Fx^3}{12} - \frac{M_1 x^2}{2} + C_1 x + C_2 \quad \left(0 \le x \le \frac{L}{2}\right) \tag{6.3}$$

Boundary conditions and symmetry reveal:

$$C_1 = C_2 = 0 \tag{6.4}$$

$$M_1 = \frac{FL}{8} = M_2 \tag{6.5}$$

Substitution of Eqs. 6.4 and 6.5 into Eq. 6.2 provides the deflection equation:

$$\delta = -\frac{Fx^2}{48EI}(3L - 4x) \quad \left(0 \le x \le \frac{L}{2}\right) \tag{6.6}$$

Maximum deflection is found at $x = \left(\frac{L}{2}\right)$, which reveals:

$$\delta = \frac{FL^3}{192EI} \tag{6.7}$$

where δ is deflection, F the applied center load, L the length of the beam, E the Young's modulus of the beam material, and I is the moment of inertia [5]. The moment of inertia is given by:

$$I = \frac{wt^3}{12} \tag{6.8}$$

where w is the width of the beam and t is the thickness of the beam [5].

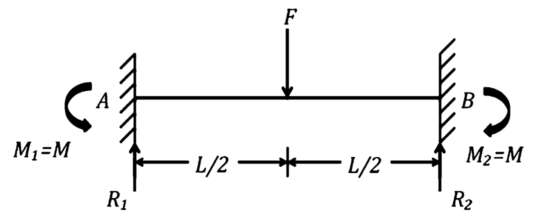

Fig. 6.4 Fixed-fixed beam moment diagram

As previously mentioned, the micro-contact resistance is the parameter being used to characterize the evolution of the performance of the micro-contact over its lifetime. Micro-contact resistance is used due to its fundamental factors which are effective contact area, material hardness, and underlying physics of conduction. Small ‘peaks’ of material, known as asperities or ‘a-spots’, on the surface of two materials are the first to make initial contact and allow current to flow through the micro-contact. As more a-spots mate at the contact interface, more conduction paths are created and resistance begins to decline. The sum of all of the a-spot areas in contact is considered the effective contact area. For simplified contact resistance calculations, the effective contact radius is used. The effective contact radius changes based on elastic, elastic–plastic, and plastic deformations caused by the applied force. The hardness of the contact material determines its susceptibility to the aforementioned deformation modes under applied loads. For micro-contacts, consideration of the electron’s elastic mean free path l_e compared to the effective radius r_{eff} is important for determining the appropriate analytical contact resistance equation. From Ohm’s Law, the resistance of a conductor scales proportionally to its length [6]. However, if the elastic mean free path is greater than the effective contact radius, $l_e > r_{eff}$ then electrons are transported ballistically through the contact materials and quantum effects must be considered [6]. If electrons are moving through a conductor ballistically, then resistance becomes independent of the conductor length and the wave nature of the electrons in the conductor are necessary for an appropriate description of resistance [6]. Alternatively, if $l_e \ll r_{eff}$ then electrons are transported diffusively [6]. For an analytical prediction of contact resistance as a function of force, both micro-contact structures have effective contact areas much greater than the elastic mean free path, therefore, Holm’s contact resistance for elastic deformation and diffusive electron transport is used.

$$R_{cDE} = \frac{\rho^3}{2}\sqrt{\frac{4E'}{3F_cR}} \tag{6.9}$$

where ρ is the resistivity of the conducting material, E′ is the Hertzian modulus, R is the asperity peak radius of curvature.

6.5 Measured Results and Discussion

The fabricated device was tested in a nitrogen environment to reduce the risk of adsorbing unwanted contaminants. The device was placed in parallel with 750 Ω resistor to protect against in-rush current. Figure 6.5 shows a schematic diagram of the test setup used. Two Agilent 34410A multi-meters were used to measure the current and voltage across the micro-contact. An Agilent U3606A current source was required to apply current to the micro-contact structure. A Femto Tools FT-S270 force sensor was used to determine the amount of force applied to the micro-contact test structure. In order to apply force to the micro-contact, a Thorlabs BPC301 piezo motor and controller was needed to move the sensor away and to the micro-contact test structure. An Agilent 33250A waveform generator was programmed to supply the driving signal to

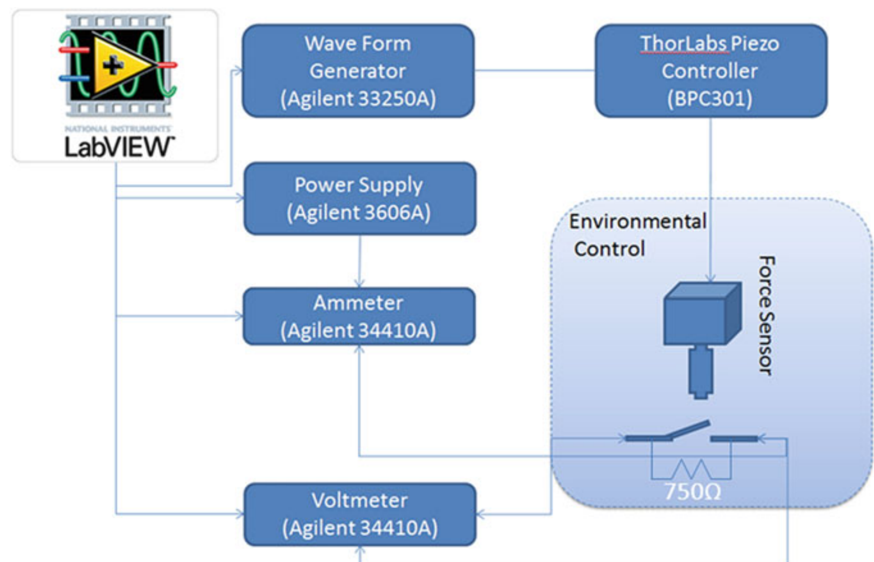

Fig. 6.5 Schematic diagram of test setup

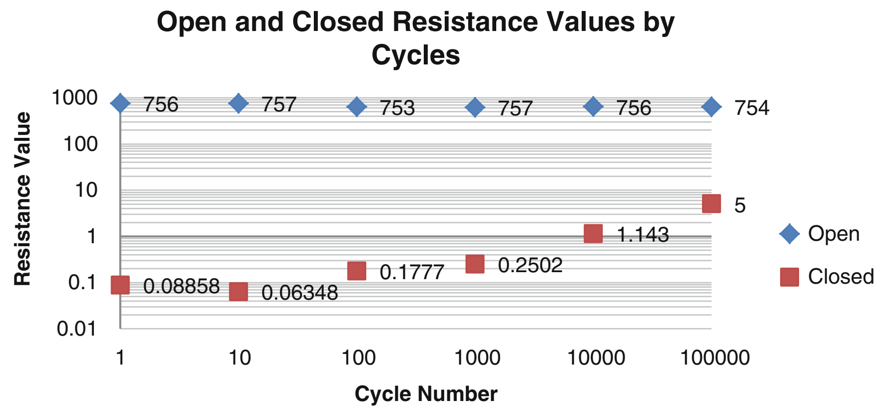

Fig. 6.6 Open and closed resistance values by cycles

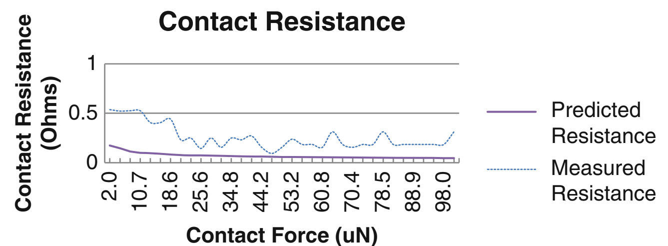

Fig. 6.7 Measured resistance and predicted resistance plot

the piezo actuator for high cycle rate testing. In addition, the micro-contact test structure, which is on a silicon wafer, is placed on a carrier and fixed into place to allow for proper alignment and testing with the force sensor. To integrate these components into one system, a computer with Lab View and a GPIB interface is used.

Figure 6.6 shows lifetime evolution of micro-contact tested by showing the open and closed resistance values for the micro-contact. When in the open state, the 750 Ω resistor is all that is measured. Upon metal to metal contact, i.e. the contact bump and lower planar contact area meet, the micro-contact resistance is recorded. As can be seen by the figure, the resistance of the interface began to increase with repeated actuation; indicating a failure of the micro-contact interface. To cold-switch the device, the test was performed by applying 3 mA of current at only when metal to metal contact was achieved. A common assumption for failure of the micro-contact is assumed to be when the contact resistance becomes greater than 5 Ω, which, for an RF micro-switch, results in an insertion loss of −0.5 dB [7]. An externally calibrated load applied 100μN's of contact force for each actuation.

Figure 6.7 shows the measured resistance against the predicted resistance using Eq. 6.9. The measured resistance is in close agreement with the predicted resistance when considering the resolution of the voltmeter, ammeter, and data acquisition system. Aside from the resolution, variations in measured resistance can be caused by the output accuracy of the current source employed; which can vary from the programmed output by 15 %. To improve the measurements, a dedicate current source which can operate in the nA to mA range with better output precision should be employed.

6.6 Conclusions

The purpose of this work was to present the fabrication method for a novel micro-contact support structure. The performance of the device matched closely to predicted results. The contact was cycled 100,000 times before contact resistance increased to 5 Ω. The reliability of the device is characterized and the feasibility of the device for use to study the physics of micro-contact evolution is successfully demonstrated.

Acknowledgements The authors would like to thank Lt Col L. Starman for his support and assistance with theory and analysis. The authors would also like to extend gratitude to AFIT technicians, Mr. Rich Johnston and Mr. Tom Stephenson for their work.

References

1. Poulain C, Peschot A, Vincent M, Bonifaci N (2011) A nano-scale investigation of material transfer phenomena at make in a MEMS switch. In: Proceedings of the IEEE 57th Holm conference on electrical contacts, Minneapolis, MN, USA
2. Broue A (2010) Multi-physical characterization of micro-contact materials for MEMS switches. In: Proceedings of the 56th IEEE Holm conference on electrical contacts, Charleston, SC, USA
3. Coutu R, Reid J, Cortez R, Strawser R, Kladitis P (2006) Microswitches with sputtered Au, AuPd, Au-on-AuPt, and AuPtCu alloy electrical contacts. IEEE Trans Compon Packag Technol 29(2):341–349
4. Holm R (1967) Electric contacts: theory and applications, 4th edn. Springer, Berlin
5. Gere J, Timoshenko S, Thornes S (1999) Mechanics of materials, 4th SI edn, Nelson Thornes, Cheltenham, UK
6. Agrait N, Yeyati A, Ruitenbeek J (2003) Quantum properties of atom-sized conductors. Phys Rep 377:81–279
7. Rebeiz G (2004) RF MEMS, theory, design, and technology. Wiley, Hoboken

Chapter 7
A Frequency Selective Surface Design Fabricated with Tunable RF Meta-Atoms

Derrick Langley, Ronald A. Coutu Jr., and Peter J. Collins

Abstract Frequency selective surfaces are being used in applications from RF to optical systems. Current applications involve beam steering or blocking transmission for electromagnetic signals. The RF Meta-atom is an excellent and novel component for frequency selective surfaces which alter or block propagating RF signals. Based on research into the tunable RF meta-atoms, a frequency selective surface has been developed that effects the propagation of RF signals. Integrating RF meta-atoms with microelectromechanical systems varactors provides a tunable method for frequency selective surfaces. Optimization of the frequency selective surface is performed through design, modeling, simulation and experimental testing for controlling propagating electromagnetic signals. To test the design concept, an RF meta-atom array was fabricated using surface micromachining fabrication methods. The RF meta-atom array was placed into RF strip-line to experimentally show the transmission and reflection response of propagating electromagnetic signals impending onto the array. The experimental results show that the resonant null at 4.85 GHz decreases from a transmission magnitude of 0.51 at 0 VDC to 0.14 at 70 VDC. This investigation shows results on how RF meta-atoms integrated with MEMS varactors can be arrayed for frequency selective surfaces.

Keywords Metamaterials • Frequency selective surface • MEMS • Reconfigurable • Meta-atom

7.1 Introduction

Frequency selective surfaces (FSS) are built to react with electromagnetic fields that impend on the structural surface [1]. The ability to react with electromagnetic fields provides several useful applications for these FSS. Using metamaterials, specifically the RF meta-atom, a design is investigated to implement a tunable FSS as a way to build it into a useful application. The first potential application consists of reconfigurable frequency selective surfaces. This application can be used for multiband response, angular stability and size reduction for systems. A second potential application consists of electromagnetic bandgap FSS for absorbers. This application focuses on the size reduction for absorbers in RF systems. Applying tunable RF meta-atoms as a method to build a FSS will be the research focus as a possible structure based on this investigation. The tunable RF meta-atoms are designed to produce a resonance between 0 and 5 GHz. The RF meta-atom will be built based on tunable RF meta-atoms built in previous research [2–4]. The RF meta-atom will be fabricated and characterized prior to building it into a metamaterial design. To characterize the metamaterial structure, testing will consist of inserting the design into a local testing apparatus to observe the performance. This testing apparatus is a compound design composed of two existing measurement systems. The apparatus combines the testing capabilities of a focused beam system and a movable-plate parallel-plate transmission system.

D. Langley (✉) • R.A. Coutu Jr. • P.J. Collins
Air Force Institute of Technology, 2950 Hobson Way, Wright-Patterson Air Force Base, OH 45433, USA
e-mail: Derrick.Langley@afit.edu

G. Shaw III et al. (eds.), *MEMS and Nanotechnology, Volume 5: Proceedings of the 2013 Annual Conference on Experimental and Applied Mechanics*, Conference Proceedings of the Society for Experimental Mechanics Series,
DOI 10.1007/978-3-319-00780-9_7, © The Society for Experimental Mechanics, Inc. 2014

7.2 Design

The tunable RF meta-atom is a combination of MEMS varactor, split ring resonators and metal traces. The split ring resonators and metal traces provide the fundamental structure to create a resonant null when interacting with propagating

Disclaimer: The views expressed in this article are those of the authors and do not reflect the official policy or position of the United States Air Force, Department of Defense, or the U.S. Government.

Electromagnetic fields. The MEMS varactor provides the ability to tune the meta-atom across a frequency range by varying the capacitance. Figure 7.1 shows three meta-atom designs built with MEMS varactors. Each MEMS varactor is constructed with an electrostatic actuated cantilever. The electrostatic cantilever is controlled by a metal actuation pad located directly

Underneath the overlapping cantilever. Dielectric material and an air gap electrically isolate the actuation pad from the cantilever. In addition, the dielectric material can isolate the path for the RF signal propagating around the split ring resonators. The cantilever is the main element that allows tuning or changes to capacitance for the MEMS varactor. The principle of electrostatic actuation allows the varactor to change the capacitance based on mechanical movement of the device. From the capacitance change, the meta-atom resonant frequency shifts based on the amount of effective capacitance built up on the meta-atom. The analytical model for the resonant frequency is given below,

$$\omega_{res} = \frac{1}{\sqrt{\frac{1}{\frac{1}{L_{Outer}} + \frac{1}{L_{Inner}}}\left(2C_{Side_A} + C_{Side_B} + C_{Side_C} + C_{Rods}\right)}} \tag{7.1}$$

where, L_{Outer} represents the inductance of the outer resonator ring, L_{Inner} is the inductance of the inner resonator ring. Capacitance is determined by dividing the meta-atom into four sections. Capacitance for section A (C_{Side_A}) is the capacitance between the outer resonator ring and inner resonator ring section divided into the section. For C_{Side_B}, C_{Side_C} and C_{Rods} the capacitance is based on the metal structures and spacing of the elements in the section. The area which defines the sections is identified in the Fig. 7.1a. The various design changes were determined based on the ability for tuning the RF meta-atom.

All the designs are fabricated with gold to insure high conductivity, ability to work with surface micromachining fabrication processes and remove issues of oxidation of the material. A quartz substrate is used to support the RF meta-atom design and keep the elements electrically isolated. From these initial properties, each design has a slight modification to its structure. Each design modification looks at the actuation properties of the cantilevers and the overall capacitance shift.

The first design, shown in Fig. 7.1a, integrates the MEMS varactor into the gap of the split ring resonator changing the capacitance in section B of the RF meta-atom. The gap in the Outer Split Ring Resonator is used to incorporate the MEMS varactor as a position to tune the capacitance. The electrostatic cantilever of the MEMS varactor is electrically isolated from one side of the split ring by dielectric material. The metallic layer of the split ring, dielectric material and the air gap of the cantilever form a variable capacitor. The air gap can be removed by electrostatic actuation on the cantilever. The maximum capacitance depends on the thickness of the dielectric material and minimum air gap spacing. The capacitance is used to determine the resonant frequency location and effective parameters of the overall meta-atom design.

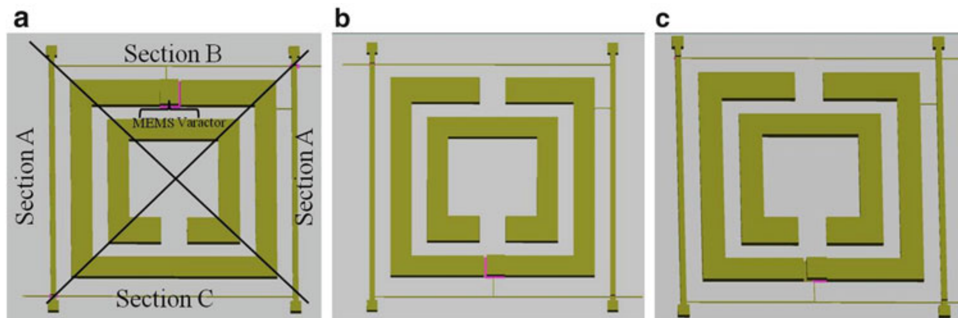

Fig. 7.1 RF meta-atom designs incorporating the MEMS varactors at various locations. In (**a**), the *two dark lines divide* the RF meta-atom into four sections for modeling the structure

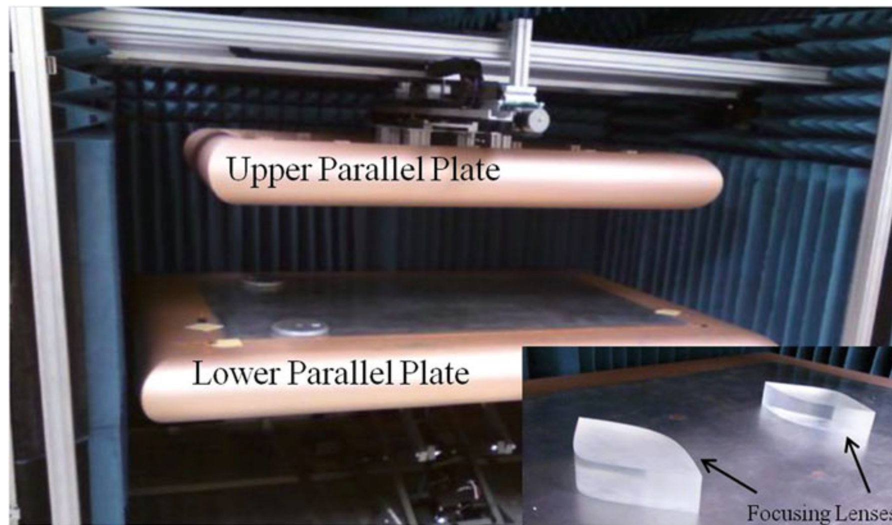

Fig. 7.2 Metamaterial testing system assembled with the *upper* and *lower parallel plates*. The inset shows the focusing lens used to direct the RF electromagnetic waves

The second and third designs are shown in Fig. 7.1b, c, respectively. These designs incorporate the MEMS varactors into the ring of the outer split ring resonator. There are two differences in the electrostatic cantilevers on the area that overlaps the metal on the ring. Design B uses dielectric material to isolate the ring at the MEMS varactor. Design C allows the cantilever to make a direct contact to the adjacent side of the ring.

Based on the modeling, simulation and experimental testing conducted on the three RF meta-atom designs. One will be chosen to fabricate the metamaterial structure. With a metamaterial structure fabricated, the design will be placed into a testing apparatus to collect data on the performance of the metamaterial design exposed to RF signals. The testing apparatus was developed at AFIT as a method to characterize radar frequency materials for electromagnetic properties [5]. With this system, data can be collected for scattering parameters (S-parameters) and near field electric distributions. Figure 7.2 shows the testing system with the upper and lower parallel plates. Monopole antennas will be used to transmit and receive the propagating RF signals. The focusing lenses, made from acrylic, rest on the lower parallel plate and help direct the RF signals toward the receiving antenna as a propagating plane wave. The lower plate is raised to reduce the air gap between the parallel plates. The inset in Fig. 7.2 shows the acrylic lenses use to focus the RF electromagnetic wave in the hybridized testing system.

In the next sections, the RF meta-atom modeling and experimental testing for the designs are covered leading to the decision on which design will be fabricated into a metamaterial structure. The experimental testing on the metamaterial structure will be presented in future work demonstrating the testing performed with the system.

7.3 Modeling

RF meta-atoms were modeled to simulate the performance of the three designs prior to fabrication and experimental testing with the RF strip-line system. The RF meta-atoms were simulated with CoventorWare® to compare the results against analytical models and the expected experimental results [6]. The benefit of using the CoventorWare® simulations is to generate the capacitance and inductance parameter values for the various designs before any fabrication and experimental testing is started. This saves time by determining the type of RF meta-atoms to fabricate based on the estimated change in the resonant frequency response for the designs. Another benefit to simulations is the ability to change design dimension before fabrication steps are attempted seeing how it changes the response. Using CoventorWare®, the capacitance and inductance parameters for three designs were generated and compared to the analytical modeling results. For each design, the parameter values were used in the resonant frequency equation to determine the resonant frequency response. Table 7.1 provides the simulated responses for each RF meta-atom design along with the resonant null frequencies. Because the designs incorporate the MEMS varactors, the resonant response for the RF meta-atoms are estimated with the change in capacitance based on the cantilevers being in the open and close positions. These modeling results are included in Table 7.1 to show the expected shift in the resonant frequency.

Table 7.1 Parameters based on CoventorWare® simulations

RF meta-atom design	Total inductance (nH)	Total capacitance (pF)	Resonant frequency response (GHz)
Design A with MEMS varactor open	4.53	0.318	4.21
Design A with MEMS varactor closed	4.53	0.325	4.15
Design B with MEMS varactor open	4.53	0.30	4.3
Design B with MEMS varactor closed	4.53	0.323	4.16
Design C with MEMS varactor open	4.53	0.308	4.26
Design C with MEMS varactor closed	4.53	0.325	4.15

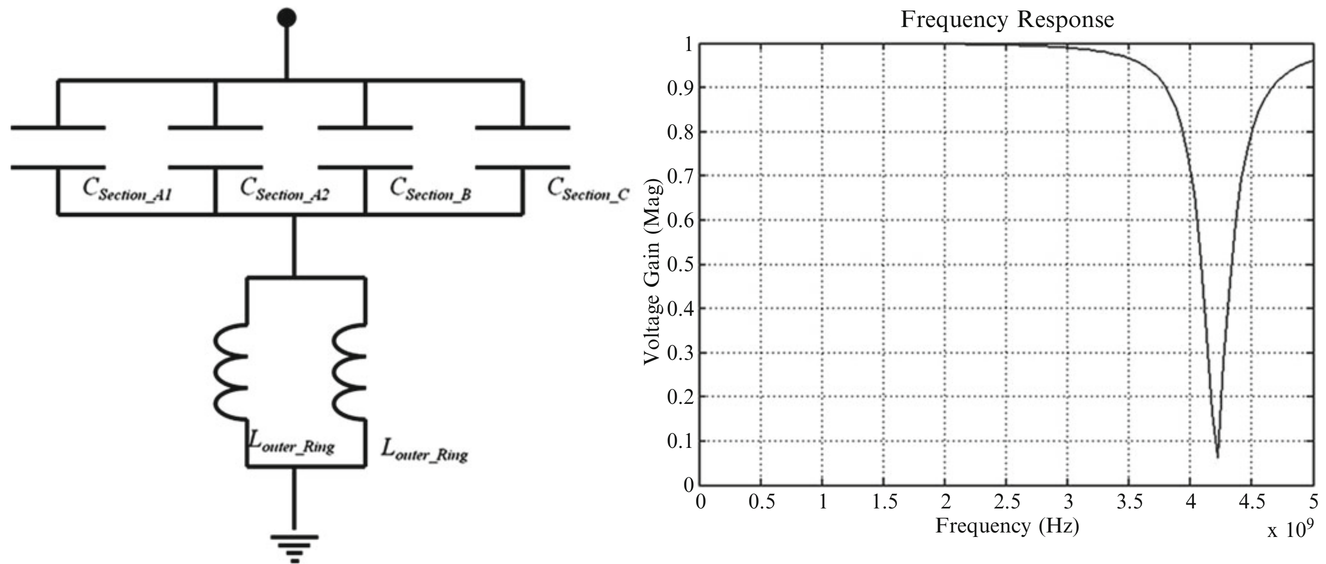

Fig. 7.3 Equivalent circuit model with simulated results

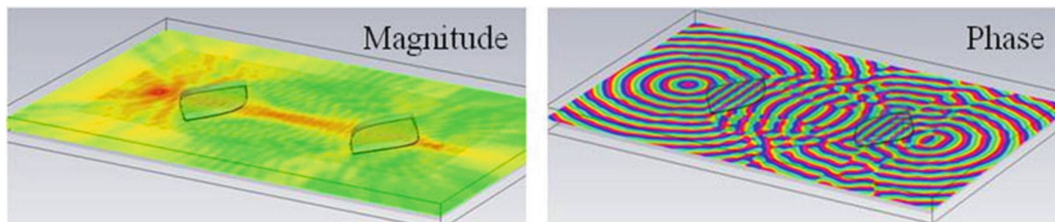

Fig. 7.4 Simulated RF magnitude and phase response for the combined testing system at 4 GHz

Using the resonant frequency parameters, small signal analysis can be performed based on the capacitance and inductance parameters. Simulink is an analysis tool used to simulate the bandstop filter response generated by the RF meta-atom on the propagating electromagnetic RF signals. Using one of the RF meta-atoms and it parameters generated from the analytical and simulated responses, the parameters are placed into the small signal analysis over a 0–5 GHz frequency range to show the bandstop response. Figure 7.3 shows the bandstop filter equivalent circuit model and the simulated results for the parameters of the RF meta-atom with the MEMS Varactor made into the outer split ring resonator.

The combined testing system was simulated using CST Microwave Studio to estimate its RF properties [5]. The measurement system was simulated in two design increments. The first simulation was for modeling the system as a parallel plate wave guide. And second simulation consists of modeling the system with the focusing lenses inserted in the model. Figure 7.1 shows the simulation results for the system with the focusing lenses inserted. The modeling provides a method to describe the expected experimental values [5]. Figure 7.4 illustrates the RF magnitude and phase response of the system at 4 GHz.

7.4 Testing

The RF meta-atom designs were fabricated using surface micromachining processes and prepared for experimental testing. Testing will be accomplished in two phases. The first phase consisted of inserting the different designs into an RF strip-line. The RF strip-line is used to determine the effective resonant frequency response. Additionally, it is used to experimentally determine which design has the largest shift in the resonant frequency. The RF strip-line allows for testing one or several rows of the RF meta-atoms arrayed on a quartz substrate that can be inserted within the system. It provides a method to collect the transmission and reflection response which are provided as scattering parameters (s-parameters). The second testing phase will be accomplished once the metamaterial design is completed.

Measurements for the RF testing system are used to show the performance of the system with and without the metamaterial design inserted for radio frequency material testing. Initial testing has provided excellent results for the system both as a parallel plate wave guide and a focused beam system. The system has performed as expected based comparison of the experimental results with the simulation modeling.

7.5 Results

The three RF meta-atom designs were fabricated into a row consisting of four meta-atoms. The designs were placed in the RF stripline to measure the response to propagating electromagnetic fields. The RF meta-atom showing the best results came from Design B, the meta-atom with MEMS varactor inserted into the outer split ring resonator. This design has silicon nitride coated on the split ring resonator section under the cantilever tip. This prevents the cantilever tip from contacting the other side of the ring providing continuous isolation. As the MEMS varactor is pulled in by the actuation voltage, the capacitance changes based on the separation gap. The results are shown in Fig. 7.5. Compared to the modeling results, the meta-atoms response is at a higher frequency than the simulated results. This is attributable to the connections made to the RF meta-atoms necessary to provide the DC voltage bias lines to the MEMS Varactors. The resonant nulls changes significantly based on the DC Voltage bias applied to the MEMS varactor. The resonant null does not shift from the 4.85 GHz as expected from the modeling results. However, the resonant null decreases from a voltage gain magnitude of 0.51 at 0 VDC to 0.14 at 70 VDC. The expected pull-in voltage for the cantilevers was 65 VDC. The varactors were biased to a higher voltage to ensure measurements were obtained beyond the cantilever pull-in voltage. As the MEMS varactors are biased, the capacitance for each individual RF meta-atom becomes uniform and consistent across the four RF meta-atoms in the row. This uniform capacitance helps with the resonant null value by allowing the entire row to react at one frequency in the electromagnetic field spectrum. From the results obtained in the RF strip-line, the metamaterial structure can be built using the RF meta-atom that produced the most promising results.

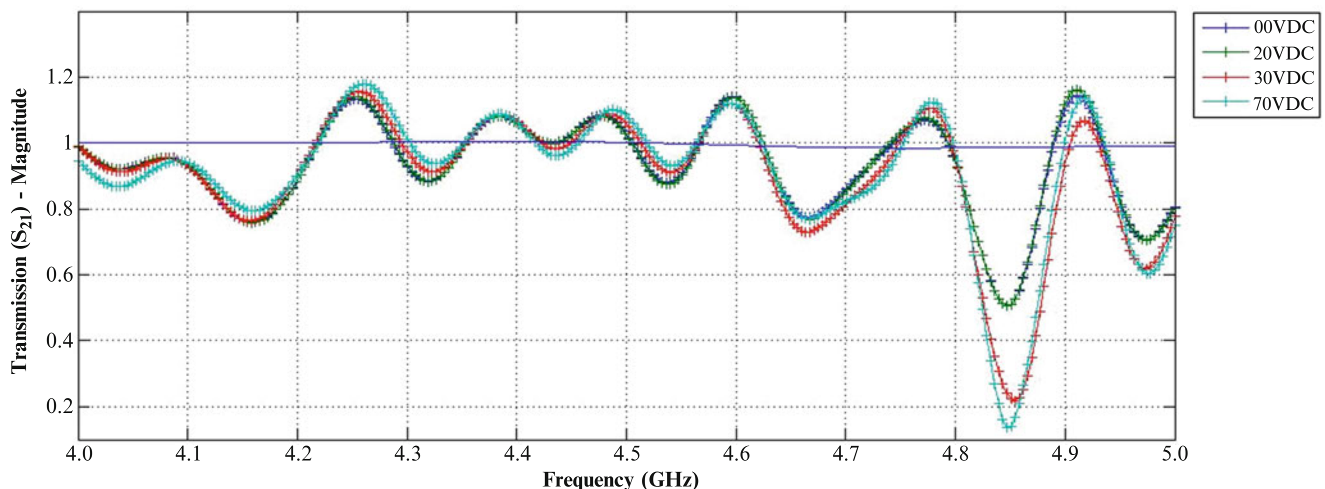

Fig. 7.5 RF transmission response measured for Design B. The meta-atom is biased at different voltage levels. At 4.85 GHz, the RF meta-atom increases the resonant null response based on the applied voltage level

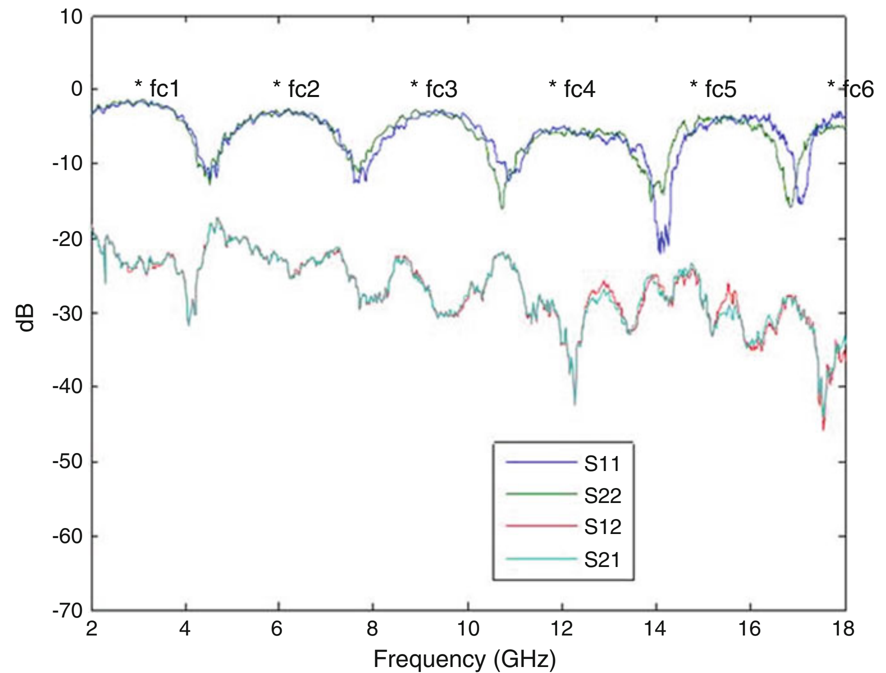

Fig. 7.6 RF measurement results for the RF testing system with focusing lenses. The s-parameters are obtained with a programmable network analyzer. Monopole antennas are used as sources to transmit and receive the RF signal [5]

The combined testing system was tested from 2 to 18 GHz for its response. The S-parameter results for the system are transmitted and received through two monopole antennas located behind the focusing lens. Figure 7.6 shows the results obtained with the use of a programmable network analyzer. The experimental results matched the CST Microwave Studio modeling results for the system as a parallel plate wave guide and a system with the focusing lenses.

7.6 Conclusion

This investigation into a frequency selective surface structure has provided valuable information into RF meta-atom designs and the combined testing system to use for experimental results. Using the MEMS varactors to adjust the capacitance of the individual RF meta-atoms proves to be a valuable method to create Frequency Selective Surfaces with a tunable response. The resonant frequency null definitely showed a change in the voltage gain response with biasing of the MEMS varactor. Conducting research on the integrated design, modeling, fabrication and testing for the RF meta-atom will definitely help to manufacture the larger metamaterial structure because of the repeatable fabrication for these structures. Having a method to test the metamaterial structure was also a part of the investigation. By developing the testing system, FSS testing can be accomplished and provide information into the characterization of these artificially made electromagnetic structures.

Acknowledgements The authors are thankful to AFIT's clean room support team of Mr. Richard Johnston and Mr. Thomas Stephenson for assistance during device fabrication.

References

1. Capolino F (2009) Applications of metamaterials. CRC Press, Boca Raton
2. Moore EA, Langley D, Jussaume ME, Rederus LA, Lundell CA, Coutu RA Jr, Collins PJ, Starman LA (2012) SRRs embedded with MEMS cantilevers to enable electrostatic tuning of the resonant frequency. Exp Mech 52(4):395–403. doi: 10.1007/s11340-011-9498-8
3. Coutu RA, Collins PJ, Moore EA, Langley D, Jussaume ME, Starman LA (2011) Electrostatically tunable meta-atoms integrated with in-situ fabricated MEMS cantilever beam arrays. IEEE/ASME J Microelectromech Syst 99:1–6
4. Langley D, Moore EA, Coutu RA Jr, Collins PJ (2011) MEMS integrated metamaterials with variable resonance operating at RF frequencies. In: Proceedings of the 2011 SEM annual conference and exposition on experimental and applied mechanics, Uncasville, CT, USA, 328, pp 1–8
5. Faris S (2012) Development of a radar-frequency metamaterial measurement and characterization apparatus. AFIT thesis (AFIT/GE/ENG/12-13)
6. www.coventor.com/coventorware.html

Chapter 8
Stress Characterization in Si/SiO_2 Spherical Shells Used in Micro-robotics

LaVern A. Starman and Vladimir Vasilyev

Abstract An in-depth parametric and stress analysis study was accomplished using CoventorWare™finite element method (FEM) modeling to evaluate 1–3 μm thick Si/SiO_2 layers which are being used to create spherical shells of 1.0 mm in diameter to be used as a baseline for realizing cubic millimeter micro-robotics. FEM was performed on spherical shells to optimize both the level of curvature of the petal designs which, once released, deflect upward to create one component of the fully self assembled spherical shell. In addition, FEM modeling was used to determine petal spacing in an effort to maximize the total functional surface area of the self-assembled spheres for future circuit integration and electrostatic actuation which will enhance shell movement. As expected, the radius of curvature of the petal is primarily based on the design of the petal, material thicknesses, and residual stresses in the structural layers. Four different petal designs were analyzed, modeled and fabricated to determine which petal design would likely satisfy the self assembly requirement and desired spherical shape. To fabricate the shells, both bulk and thin-film micromachining processes were performed on the silicon-on-insulator (SOI) wafer. To release the spherical shells from the substrate, a multistage wet and dry etching process was used. Once the petals are released, the petals curl up, self-assembling into spherical shells.

Keywords MEMS • Robotics • Self assembly • Silicon-on-insulator • Finite element modeling (FEM)

8.1 Introduction

Due to the small size of Micro-Electro-Mechanical Systems (MEMS) devices, the residual stress within the material layers after growth and fabrication can play a major role in the successful functionality and reliability of a device. In an effort to obtain robust and reliable micromechanical devices, it is essential to understand how the processing parameters affect the mechanical properties of individual and multilayered thin-film within MEMS devices. The mechanical properties of the structural layers, in particular the stress and stress gradients are very important for device performance. Residual stress in thin films often cause device failure due to out-of-plane curling, buckling, or fracture [1]. However, in our micro-robot design presented in this paper, we utilize the inherent residual stress between material layers to self-assemble the exoskeleton of a micro-robot upon release from the substrate to create spherical shells.

While the realization of micro-robotics has been a goal of researchers for several decades [2], it has proven to be extremely difficult to build systems that combine power collection, power storage, computation, sensing, and actuation in a compact package. Traditional MEMS approaches have tried to do this by first achieving the required functionality and then combining the pieces together to form a robot [3] and systems for the automated assembly of MEMS devices were previously demonstrated [4]. In this research effort, we're taking the opposite approach and focusing on realizing the structure first and then adding and integrating the functionality into the mechanical structure. This work was initiated by developing a CMOS compatible process for fabricating cubic millimeter structures. These structures will eventually integrate electrostatic electrodes for mobility purposes while enclosing a photovoltaic cell, capacitor, and processor. An artistic rendering of a spherical micro-robot consisting of an outer shell and an inner core containing the electrical

L.A. Starman (✉) • V. Vasilyev
Air Force Research Laboratory, Sensors Directorate, EO/IR Sensing Technology Branch (AFRL/RYDP),
2241 Avionics Cr, Wright-Patterson AFB, OH 45433, USA
e-mail: lavern.starman@wpafb.af.mil

G. Shaw III et al. (eds.), *MEMS and Nanotechnology, Volume 5: Proceedings of the 2013 Annual Conference on Experimental and Applied Mechanics*, Conference Proceedings of the Society for Experimental Mechanics Series,
DOI 10.1007/978-3-319-00780-9_8, © The Society for Experimental Mechanics, Inc. 2014

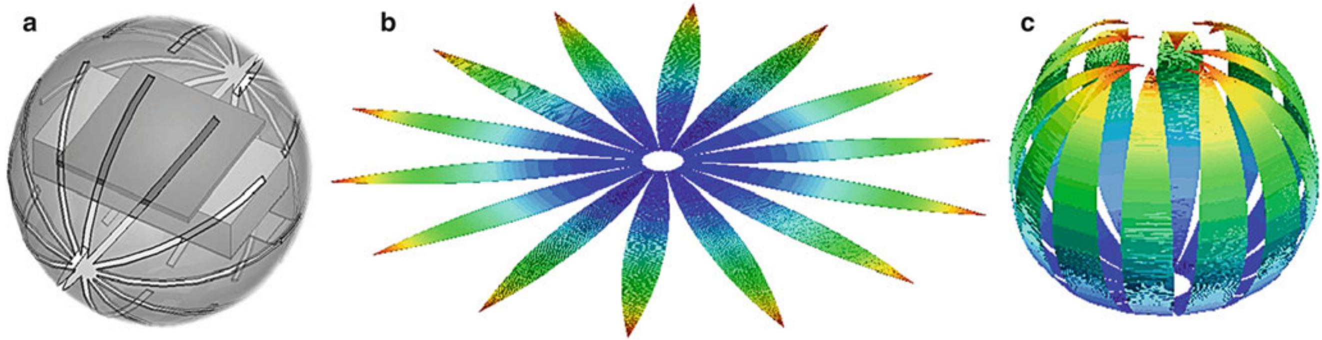

Fig. 8.1 (**a**) Artistic rendering of a spherical micro-robot consisting of an outer shell and an inner core containing the electrical control circuitry [5], (**b**) CoventorWare™ FEM layout for a single 14-petal sphere, and (**c**) a self-assembled 1-mm 14-petal sphere as illustrated in CoventorWare™

control circuitry is shown in Fig. 8.1a. A key goal of the spherical design is to integrate control circuitry into future petal designs; thus, it is critical to maximize the available surface area of the resultant micro-robotic spheroid to enable the greatest flexibility in circuit architecture [5]. An additional benefit for peak surface area utilization is to reduce the bias voltages necessary for locomotion which is critical since we will have limited power availability due to the small size. Presently, the design is based upon electrostatic actuation which directly correlates to the contact surface area: the larger the surface area, the lower the bias voltage required for movement.

To maximize the functional surface area of the enclosed sphere, the sphere was divided into 4-, 8-, 12- or 16-petals with petal widths ranging from 188 to 750 μm with all petal lengths set to 1,570 μm (equivalent to the circumference of a semicircle with a 1 mm diameter). The 2D 14-petal sphere layout shown in Fig. 8.1b is a CoventorWare™ finite element modeling (FEM) image of the unreleased petal sphere design. Based on the petal design, the structure can be essentially modeled as a fixed cantilever beam such that the free end of the beam can freely deflect out of plane, creating the exoskeleton or sphere as shown in Fig. 8.1c.

8.2 Analytical Modeling of Beam Deflection

A general analytical beam model was used to evaluate the radius of curvature, R, for a beam subjected to a bending moment, M, which can be calculated as

$$R = \frac{EI}{M}, \tag{8.1}$$

where E is Young's modulus for the material and I is the moment of inertia of the beam. For a multi-layer beam in which each layer has different residual stress and material properties, it is necessary to determine EI and M as the sum of the values for each layer. The value of EI can be calculated as

$$EI = EI_{eff} = \frac{w}{3}\sum_{l=1}^{N} E_l\left(t_l^3 + 3x_l^2 t_l + 3x_l t_l^2\right), \tag{8.2}$$

where the width, w is the same for all the layers; E_l is Young's modulus of layer l; t_l is the thickness of layer l; N is the number of layers; and x_l is the height of the bottom layer l relative to the bending axis [6]. The position of the bending axis in the layer stack is determined iteratively to minimize EI_{eff}. The bending moment is then calculated by assuming each layer has a uniform residual stress, σ_l, and summing up the bending moments from each layer as [6]

$$M = M_{eff} = \sum_{l=1}^{N} \frac{\sigma_l w}{2}\left(t_l^2 + 2x_l t_l\right). \tag{8.3}$$

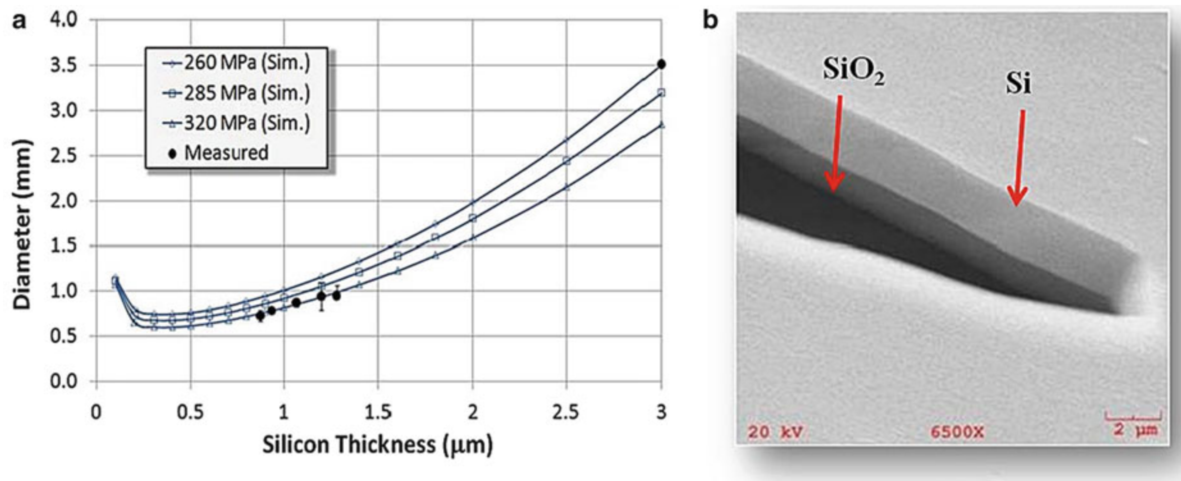

Fig. 8.2 (**a**) Calculated diameters compared with measured values for two layer shells having a young's modulus of silicon being 150 GPa and silicon dioxide being 39 GPa [6], and (**b**) SEM image of the two layers, Si and SiO_2 that form the shell

Therefore, for our two layer device design, since the compressive stress is significantly greater in the thermally grown SiO_2 layer when compared to the nearly stress free bulk Si layer. Thus, once the device is released, the SiO_2 stress will result in the structure bending upward, out of plane. Figure 8.2a illustrates an analytical solution to determine the sphere diameter based on a selected silicon layer thickness at three different SiO_2 residual stress levels. Figure 8.2b shows a scanning electron microscope (SEM) image of the stacked device layer.

8.3 Micro-robot Architecture and Design

There is a vast array of possible micro-robot designs which could be used for potential reconfigurable or programmable material applications. The end goal of this research is to develop a spherical micro-robot with a diameter of 1 mm that could serve as a basic unit for a programmable material [7]. The sphere designs selected for this effort are shown in Fig. 8.3 for the 4-, 8-, 12- and 16-petal designs. As stated earlier, some of the key design criteria for the final sphere were to maximize the total functional surface area of the structure while maintaining the ability for the petals to successfully self-assemble into a sphere.

In an attempt to maximize the useful surface area of the spheres, a generic sphere was equally partitioned into an equivalent number of petals for self-assembly. As observed in Table 1 of Fig. 8.4, the total surface area of the four different petal designs is all within approximately 4.1 %. This slight variation is primarily due to fabrication limitations in that approximately an 8 μm gap was established as a safe margin for petal spacing to account for any etching or bending deviations. The small gap enables each petal to act independently during the release and self-assembly process of the sphere such that for modeling purposes, a single petal can be modeled. This single petal model, due to symmetry, can represent the entire petal array as all petals should deflect identically following release. Due to this symmetry, this simplified single petal model will reduce simulation times, increase accuracy due to finer mesh grids, and enable advanced parametric studies for material and design parameter characterization.

A critical petal design criterion was the evaluation of the out of plane deflection. This out of plane deflection must be approximately 1,500 μm to allow for the petal tips to approximately touch during self-assembly, creating the sphere as shown in the CoventorWare™simulation in Fig. 8.1c. The material parameters for the silicon-on-insulator (SOI) substrate material used in the modeling and fabrication had a 1.0 μm thick silicon device layer and a 1.1 μm thick buried oxide layer. For the FEM models, the inherent compressive residual stress for the silicon device layer was set to 5 MPa [8] and the buried oxide layer was set to 280 MPa [9]. A single petal for each of the four designs was simulated and a 2D deflection curve was obtained. Figure 8.4b shows the deflection curve comparisons for the four petal designs for a selected global mesh size of 50 μm. As shown, the four-petal design has a deflection of only 800 μm which is far below the required level of deflection. The eight-petal design deflects approximately 1,000 μm and the 16-petal design reaches a deflection of around 1,200 μm. Based on the deflection results, the 12-petal design produces the greatest deflection of approximately 1,350 μm. The reduced deflection for

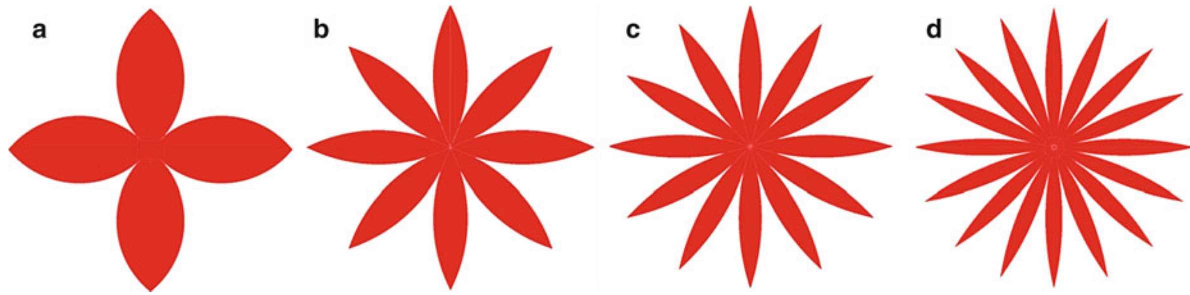

Fig. 8.3 Four proposed 2D patterns of 1 mm diameter sphere designs; (**a**) four-petal sphere, (**b**) eight-petal sphere, (**c**) 12-petal sphere, and (**d**) a 16-petal sphere

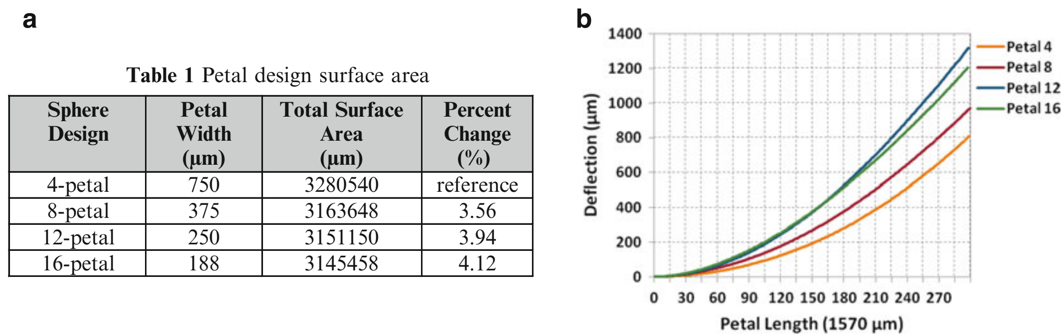

a

Table 1 Petal design surface area

Sphere Design	Petal Width (μm)	Total Surface Area (μm)	Percent Change (%)
4-petal	750	3280540	reference
8-petal	375	3163648	3.56
12-petal	250	3151150	3.94
16-petal	188	3145458	4.12

Fig. 8.4 Table 1 in (**a**) provides design parameters for each sphere petal, and (**b**) comparison of the peak deflections for the four different petal sphere designs using a 50 μm mesh. All deflection curves shown are for a silicon device layer of 1.0 μm, buried oxide layer 1.1 μm with an oxide stress value of 280 MPa [9]. As shown, the 12-petal design provides the greatest deflection for this design setting. **Please note**: each data point shown along the x-axis corresponds to roughly 5.25 μm as only 300 data points was collected over the 1,570 μm long petal

the four and eight petal designs is likely due to a slight deflection across the width of the petal, creating a slight fold along the petal edges which inhibits deflection. A good representative example of the across petal deflection is in the form of a sheet of paper. If you create a slight fold upward along the long edges of the paper, then try to bend up the far, free edge of the paper, the bending is significantly inhibited and it requires a lot more force to overcome this edge bending. Only a slight edge deflection significantly changes the bending moments about the long axis of the paper, reducing its peak deflection for a given force. From 2D extracted data for these two petals across the maximum width of the petal verifies this slight edge bending moment. As a result of the deflection curves shown in Fig. 8.3b, all subsequent FEM analysis presented in this paper will be focused on the 12- and 16-petal designs. Please note that each data point shown along the x-axis of all petal deflection plots throughout this paper corresponds to roughly 5.25 μm as only 300 data points were collected to cover the 1,570 μm long petal.

In Fig. 8.4b, the peak deflection for a 12-petal design is slightly less than our desired value of 1,500 μm. To verify this result, a mesh study was performed to validate the modeling results for the deflection curves. Due to the physical size of the petals, an initial 50 μm mesh grid was selected in an attempt to reduce simulation times. A single 12-petal design having a 20, 25, and 50 μm global mesh grid was selected to evaluate peak deflection. When comparing the peak deflection of the 20 μm mesh grid to the 50 μm mesh, the peak deflection increased from slightly over 1,400 μm to nearly 1,600 μm, or an 8.1 % increase in deflection. However, simulation times increased significantly from approximately 6 min to nearly 45 min for a single parameter model. By knowing the peak deflection for a finer mesh is approximately 150 μm greater, which exceeded our projected deflection value, all subsequent FEM modeling was accomplished using a 50 μm mesh grid to minimize simulation times.

8.4 Coventorware Modeling Analysis

When purchasing wafers, one can buy the SOI wafers with different buried oxide and silicon device layer thicknesses. Therefore, a series of parametric studies were performed to assess the impacts layer thicknesses and stress levels have on the peak out-of-plane deflection of the petals. Parametric studies were performed for varying oxide and silicon device layer

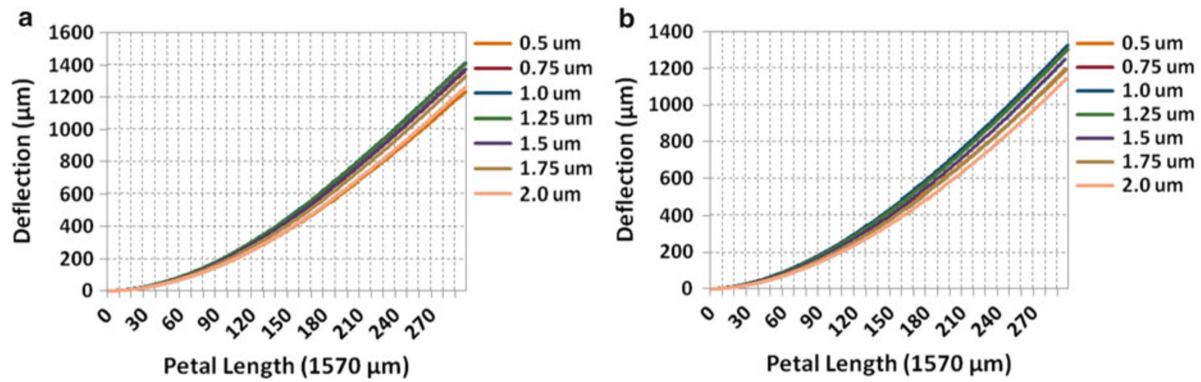

Fig. 8.5 Comparison of petal deflection with the buried oxide layer varying from 0.5 to 2.0 µm. The silicon device layer is set to 1.0 µm thick and the oxide stress is set to 320 MPa; (**a**) 12-petal sphere, (**b**) 16-petal sphere. As shown, the 12-petal sphere has a greater deflection by ~100 µm with both petals reaching maximum deflection when the buried oxide layer is 1 ± 0.25 µm or approximately equal to the silicon device layer thickness. **Note:** each data point along the x-axis relates to roughly 5.25 µm

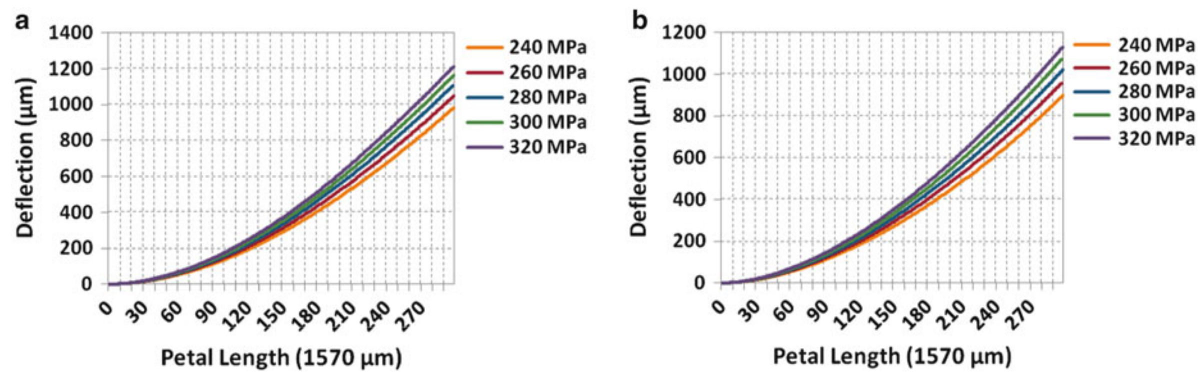

Fig. 8.6 Comparison of petal deflection for oxide stress levels varying from 240 to 320 MPa. The silicon device layer is set to 1.5 µm and the buried oxide layer is 1.1 µm thick; (**a**) 12-petal sphere, and (**b**) 16-petal sphere. As shown, the maximum deflection of the 12-petal sphere is ~100 µm more than the 16-petal sphere for all stress levels. **Please note**: each data point along the x-axis corresponds to roughly 5.25 µm as only 300 data points was collected over the 1,570 µm long petal

thicknesses in addition to varying the residual stress inherent in the buried oxide layer. One should note that the residual stress in the oxide layer tends to vary from 280 ± 40 MPa [9] depending on growth or deposition parameters. As shown in Fig. 8.4b, the 12- and 16-petal spheres provided the greatest out of plane deflections; thus, single petals for each sphere will be evaluated for all parametric studies presented.

(a) **Buried Oxide Modeling**

Since a typical SOI wafer can be purchased with the appropriate buried oxide thickness which will maximize petal deflection, this study evaluates the effects the oxide layer has on the overall operation and functionality of the self-assembled sphere. Thus, for the first modeling study, the silicon device layer thickness was set to 1.0 µm with the buried oxide stress level set to 320 MPa [9]. A parametric study was performed to vary the buried oxide layer thickness from 0.5 to 2.0 µm in increments of 0.25 µm. The resultant plots obtained for this parametric study are shown in Fig. 8.5 with the 12-petal sphere shown in Fig. 8.5a and the 16-petal sphere in Fig. 8.5b. As illustrated in both deflection plots, the peak deflection occurs when the oxide layer is 1 ± 0.25 µm or approximately equal to the silicon device layer thickness. If the oxide layer deviates from this optimal oxide thickness range, the peak deflection decreases. The peak deflection for the 12-petal sphere is approximately 100 µm more than the 16-petal sphere at the peak deflection point which occurs at the 1.25 µm oxide thickness level.

A second parametric study was performed with the silicon device layer set to 1.5 µm thick and the buried oxide layer was set to 1.1 µm thick. Although we do not have a significant amount of control over the various stress levels within the material layers from purchased SOI wafers, this study will illustrate the effects varying stress has on the overall deflection of the bilayer petals. The silicon residual stress level was set to 5 MPa and the buried oxide stress level was set to vary between 240 and320 MPa. As stated earlier, the residual stress in the buried oxide layer will dominate the overall operation of the petals

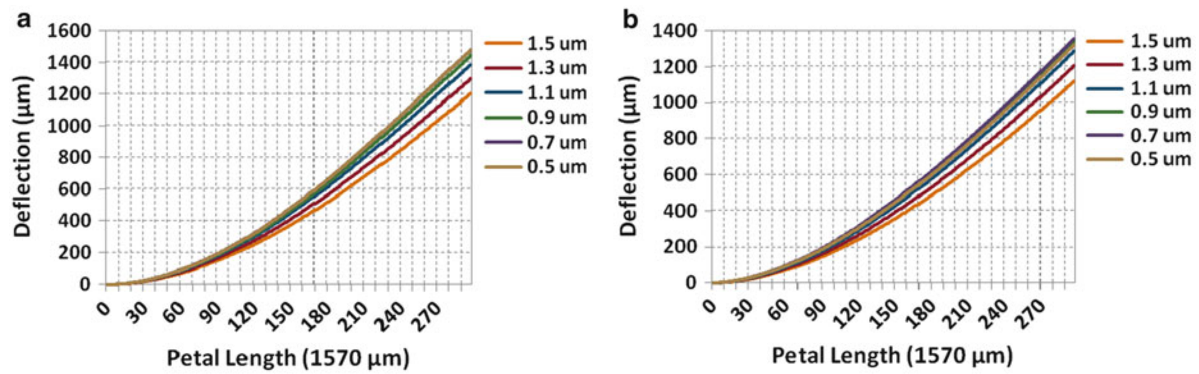

Fig. 8.7 Comparison of petal deflection with the silicon device layer varying from 0.5 to 1.5 µm. The buried oxide layer is set to 1.1 µm thick with a stress value of 320 MPa; (**a**) 12-petal sphere, and (**b**) 16-petal sphere. As shown, the 12-petal sphere's deflection is ~100–150 µm greater than the 16-petal sphere. In both petal designs, maximum deflection occurs when the silicon device layer is approximately 0.7 ±0.2 µm. **Please note**: each data point shown along the x-axis corresponds to roughly 5.25 µm as only 300 data points was collected over the 1,570 µm long petal

and predominantly helps dictate the peak deflection of the petals. As shown in Fig. 8.6, as the oxide stress increases, the deflection increases approximately 50 µm for every additional 20 MPa of stress added to the oxide layer. Again, the maximum deflection of the 12-petal sphere is ~100 µm more than the 16-petal sphere for all stress levels. One should note that the 1.5 µm thick silicon device layer reduced the peak deflection from the 1.0 µm thick silicon deflection curves by approximately 200 µm as shown in Fig. 8.4 for the 280 MPa stress value.

(b) **Silicon Device Layer Modeling**
The silicon device layer thickness is the primary layer which we have nearly full control over. We, the designer can dictate the thickness of this layer through purchasing the appropriate silicon device layer thickness or we have the ability to thin this layer if needed through chemical mechanical polishing (CMP). A parametric study was accomplished to vary the thickness of the silicon device layer from 0.5 to 1.5 µm with a stress value of 5 MPa [8] to evaluate output deflection changes based on this layer. The buried oxide layer for all simulations was set to be 1.1 µm thick at a residual stress value of 320 MPa. As shown in Fig. 8.7a, the 12-petal sphere's deflection is ~100 to 150 µm greater than the 16-petal sphere shown in Fig. 8.7b. For both petal designs, maximum deflection occurs when the silicon device layer is approximately 0.7 ± 0.2 µm. As shown in both Figs. 8.5 and 8.7, there is a limit reached at which time further thinning of either the oxide or silicon device layers do not significantly change the deflection of the petal. This is likely a result of physical material limitations due to a lack of remaining structural rigidity in the thinned layers.

(c) **Petal Modification**
As a result of the peak petal deflections shown in Fig. 8.4b for each sphere design, a slight modification to the petal width was performed in an attempt to alleviate any across petal curl. The petal designs are identical to previous models; however the peak width of the petal was reduced by 10 µm on each side (creating flat edges along the length of the petal) as shown in Fig. 8.8a for the 8- and 16-petal designs. The silicon device layer was set to be 1.5 µm thick and the buried oxide layer is 1.1 µm thick at a residual stress value of 320 MPa. As shown in Fig. 8.8b, the deflection of the modified 8-petal design increased approximately 170 µm as compared to the standard design. The modified 16-petal designs deflection increased approximately 300 µm over the initial 16-petal design. The increased deflection in the eight-petal design can easily be attributed to the reduced curl on the edges of the petal. However, the significant increase in deflection for the 16-petal design is not likely due to the reduced petal edge curl but rather the petal narrowing produces a more traditional, cantilever beam-like structure which typically produces improved pure out-of-plane bending.

8.5 Sphere Fabrication

For the current sphere designs, the fabrication is expected to be fairly straightforward. A single mask is needed to define the spheres. The flowchart shown in Fig. 8.9 illustrates the fabrication process. The SOI wafer shown in Fig. 8.8a has a Si device layer of 1.5 µm, a buried SiO_2 layer of 1.1 µm, and a substrate of 750 µm thickness. Figure 8.9b shows the first step in the fabrication process by spin casting a layer of PMGI at 4,000 RPMs, and a layer of Shipley 1813 photoresist. The 1813

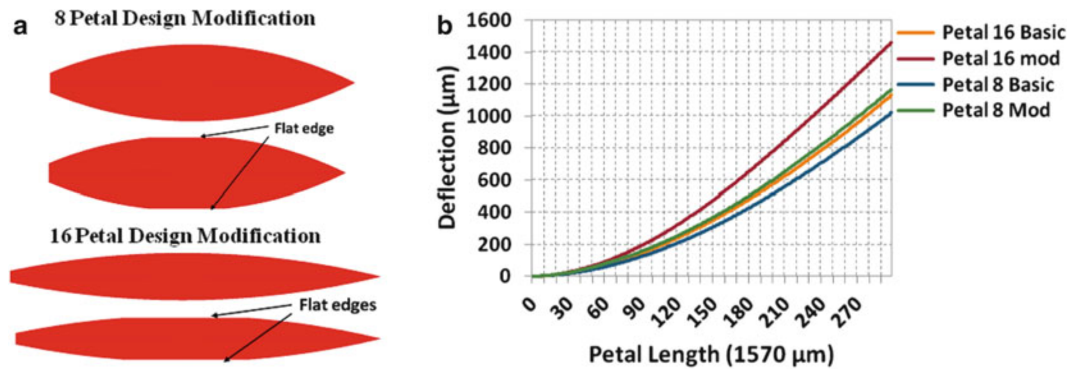

Fig. 8.8 (**a**) Sphere petals modified by reducing the width of the petal by 10 µm from each side of the petal, creating flat edges along the length of the petal (total width reduced by 20 µm), and (**b**) comparison of the simulated deflection curves for the modified petal designs to that of the initial petal designs having material parameters for the silicon device layer of 1.5 µm, buried oxide set to 1.1 µm with a stress value of 320 MPa. **Note:** each data point along the x-axis relates to roughly 5.25 µm

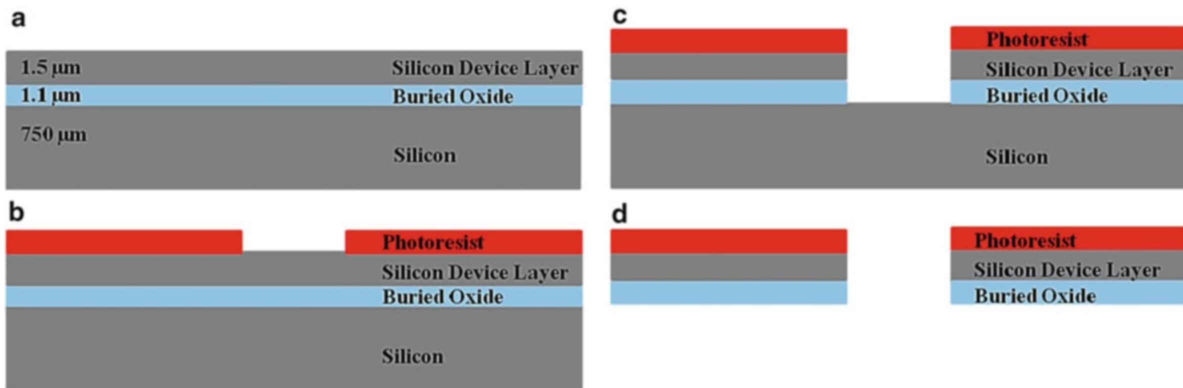

Fig. 8.9 Sphere fabrication flow chart, (**a**) standard SOI wafer, (**b**) spin on photoresist, pattern, and develop to create sphere pattern, (**c**) DRIE silicon device layer followed by RIE of the buried oxide layer, and (**d**) completely DRIE the silicon bulk substrate layer

photoresist is exposed to UV and then developed. Following development, the stacked resist is exposed to deep UV to pattern the PMGI layer and is again developed as illustrated in Fig. 8.9b. The 2.4 µm thick stacked layer of resist will serve as the mask for both the silicon device layer deep reactive ion etch (DRIE) and the oxide reactive ion etch (RIE) as shown in Fig. 8.9c. The DRIE silicon device layer etch was completed in 32 s which was immediately followed up with the RIE etch of the oxide layer and was completed in 22 min. Following the device and oxide layer etches, the top surface (device layer) had Shipley 1805 photoresist spun on at 4,000 RPMs to coat all sphere sidewalls. Following the 1805 bake, a layer of 9260 photoresist was spun on at 4,000 RPMs to serve as a protective mask for the sphere sidewalls and device layer during the substrate DRIE etch. As shown if Fig. 8.9d, the entire silicon substrate is removed via DRIE such that only the buried oxide and silicon device layers remain. During the DRIE backside etch, the buried oxide layer should act as a natural etch stop, thus preventing the inadvertent etching of the sphere layers. The final step to the process is to dissolve the photoresist in acetone and isopropyl to release the spheres followed by drying in ambient air.

This was the first attempt to fabricate the spheres using this simplified etching fabrication process and we encountered a few unforeseen problems. For one, the DRIE backside etch was too aggressive (etch rate was approximately 7–8 µm/min) such that it inadvertently etched the sphere layers. A slower etch recipe (etch rate of approximately 1–2 µm/min) will be used in all subsequent fabrication processes. A prior fabrication process involving a wet/dry etch combination was used to fabricate the initial spheres [6]. Figure 8.10 shows the 2D and post release results for three different, smaller sphere designs fabricated using our initial process. As shown, the spheres ranged from 0.5 to 0.775 mm in diameter with very promising results.

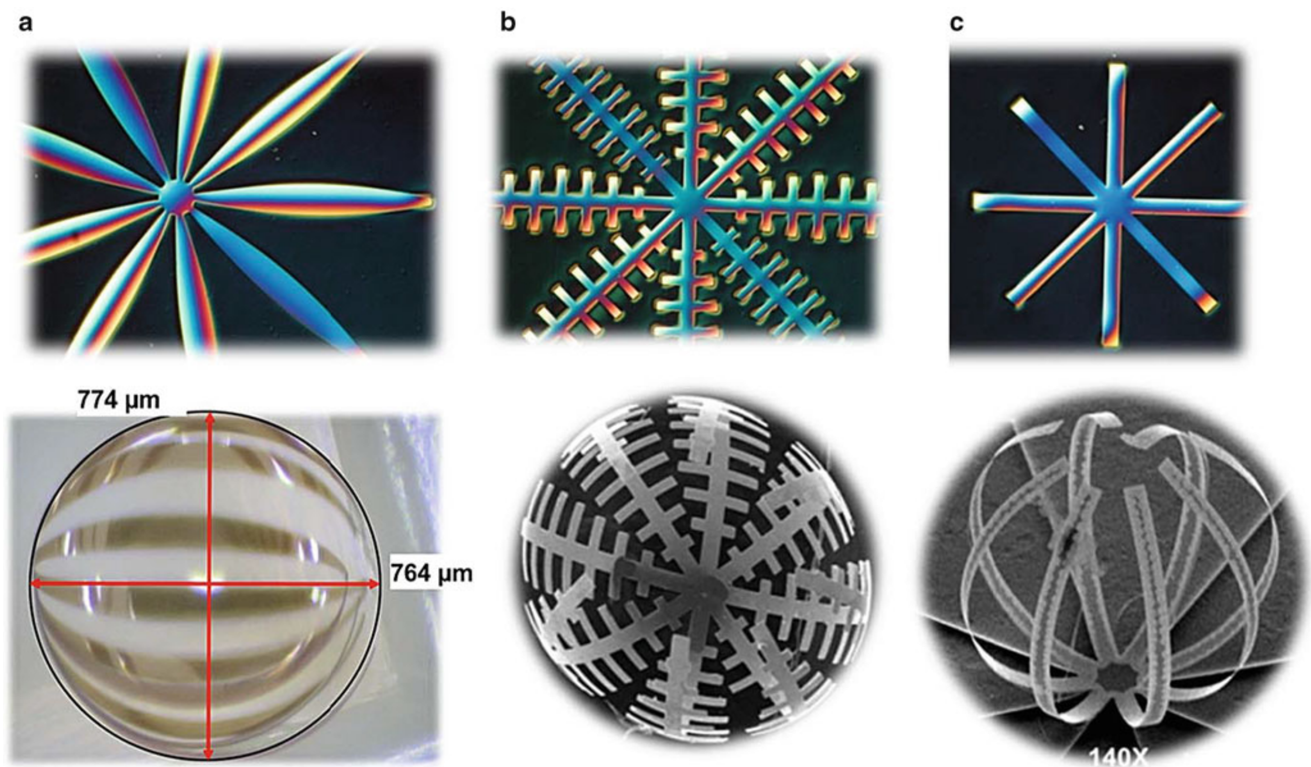

Fig. 8.10 Optical and scanning electron micrograph images of sub-mm^3 spheres fabricated in thin Si and SiO_2 layers with the *top images* showing the 2D fabricated structures while the *bottom images* illustrate the self-assembled spheres which ranged from 0.5 to 0.775 mm, (**a**) 9-petal pattern sphere with a diameter of approximately 775 μm [6], (**b**) an 8-petal rigid ribbon pattern sphere [5], and (**c**) an 8-petal ribbon pattern sphere [6]

8.6 Conclusions

The realization of micro-robotics has been a goal of researchers for several decades and in general, MEMS approaches have tried to first achieve the required functionality and then combine the various pieces together to form a robot. In this research effort, we took the opposite approach and focused on realizing possible shell structures first before we attempt to integrate functionality into the mechanical structures. In this paper, we designed, modeled and performed preliminary fabrication on four different petal structures made in Si-SiO_2, such that upon release will self-assemble into 1 mm^3 spherical shells. A series of parametric studies was performed on the petal designs by varying Si and SiO_2 layer thicknesses in addition to varying the residual stress in the oxide layer to determine which variables have the greatest impact in sphere self-assembly. Parametric FEM models performed using CoventorWare revealed that the optimal bending occurs approximately when the Si and SiO_2 layers are roughly the same thickness. As the thickness of either the Si or SiO_2 exceeds 1.5 μm, the deflection of the petal significantly decreases. Other features that inhibit petal bending include the physical size of the petal and lower residual stress levels within the oxide layer. Based off the FEM results, the 12- or 16-petal sphere with each layer of the stacked Si/SiO_2 layer being approximately 1 μm should self-assemble with the greatest reliability given the variability of the residual oxide stresses. An attempt was performed to simplify the multi-stage processing of the SOI micro shells performed previously using dry and wet etching steps to the DRIE process. As shown, the DRIE recipe needs to be optimized to achieve successful Si/SiO_2 bilayer 2D structures. This simplification might be critical in the eventual mass production of micro shells. Since the end goal of this work is to develop a spherical micro-robot with a diameter of 1.0 mm that could serve as the basic unit for programmable matter, the fabrication approach being developed will be suitable to the realization of a wide range of micro-robotic systems. Future research will consist of refining the fabrication of the spheres using DRIE, testing sphere rigidity, and to begin circuit integration into the petal structures.

Acknowledgements Support for this research is greatly appreciated with funded through the Air Force Office of Scientific Research (AFOSR) LRIR – 10RYO7COR Titled: "Programmable Reconfigurable Sensors"

References

1. Starman L, Coutu R Jr (2012) Stress monitoring of post-processed MEMS silicon microbridge structures using Raman spectroscopy. J Exp Mech 52(9):1341–1353
2. Feynman R (1992) There's plenty of room at the bottom. J Microelectromech Syst 1(1):60–66
3. Holler S, Flynn A, Bellow C, Pister K (2003) Solar powered 10 mg silicon robot. In: Proceedings of the IEEE international conference on micro electro mechanical systems, Kyoto, Japan, pp 706–711
4. Reid J, Bright V, Comtois J (1997) Automated assembly of flip-up micromirrors. In: Proceedings of international conference of solid-state sensors and actuators (Transducers 97), Chicago, IL, USA, vol 1, pp 347–350
5. Reid JR, Vasilyev V, Webster RT (2008) Building micro-robots: a path to sub-mm^3 autonomous systems. In: Proceedings of nanotech 2008, Boston
6. Vasilyev V, Reid JR, Webster RT (2008) Microfabrication of Si/SiO_2–spherical shells as a path to sub-mm^3 autonomous robotic systems. 2008 MRS proceedings, Boston, MA, USA, vol 1139, 1139-GG03-43. doi:10.1557/PROC-1139-GG03-43
7. Goldstein SC, Campbell JD, Mowry TC (2005) Invisible computing: programmable matter. Computer 38(6):99–101
8. Yang C, Mess F, Skenes K, Melkote S, Danyluk S (2013) On the residual stress and fracture strength of crystalline silicon wafers. Appl Phys Lett 102(2):021909
9. Kovacs GT (1998) Micromachined transducers sourcebook. McGraw Hill, Boston

Chapter 9
MEMS Cantilever Sensor for Photoacoustic Detection of Terahertz Radiation

Nathan E. Glauvitz, Ronald A. Coutu Jr., Michael Kistler, Ivan R. Medvedev, and Douglas T. Petkie

Abstract Cantilever structures have long been used in a variety of sensor and actuator applications. In this work, a Microelectromechanical system (MEMS) cantilever pressure sensor was designed, modelled, and fabricated to investigate the photoacoustic response of various gases to terahertz radiation. Cantilever design parameters of length, width, and thickness are investigated using CoventorWare finite element model software. Cantilever tip deflection and resonant frequencies of the beams are of particular interest in order to maximize the effectiveness of the sensor. A few select designs were then fabricated on the device layer of a silicon-on-insulator wafer which was used to create the physical structure of the cantilever. Fabricated devices will then be tested in a custom made vacuum test chamber where the amplitude modulated THz radiation excited acoustic waves in the chamber and cause the cantilever to deflect. To examine the induced deflection in the cantilever, a laser beam reflected off the tip of the cantilever back to a photodiode to analyze tip displacements caused from the photoacoustic effect. Initial test measurements are currently underway and initial data indicates a nearly linear response in signal amplitude from the photodiode which directly correlated to the gases absorption coefficients.

Keywords MEMS • Cantilever • Photoacoustics • Terahertz sensor • Spectroscopy

9.1 Introduction

Many techniques have been employed over the last several decades for photoacoustic detection of trace gases and molecular spectroscopy [1]. The photoacoustic effect is the result of molecules absorbing energy from an electromagnetic wave where the energy is then released through collisions with other molecules. When the radiation source is modulated and enough of the energy is absorbed by a gaseous species, an acoustic wave results. This pressure wave can then be detected by a cantilever or other pressure sensitive device. Several different sensor methods to pick up photoacoustic waves have been implemented over the years; among them are tuning fork detectors [2], membrane microphones [3], bridge [4], and cantilever designs [4–9]. In each instance, specific sensor designs are configured in order to be sensitive to the expected pressures conditions caused by the excitation radiation captured in the photoacoustic cell.

The first step to developing an adequate FEM model to predict cantilever behaviour in the photoacoustic chamber is to understand the range of anticipated pressures that could be encountered. Expected pressures generated in a PA cell are anticipated through the use of the ideal gas law and kinetic theory of gasses. For this PA analysis, the absorption cell is assumed to have a cylindrical shape with a characteristic length l and radius r. It is also assumed that the THz radiation beam energy from the source is uniformly distributed and that the radius of the beam closely matches to that of the chamber radius. The radiation power from the source that is inserted into the chamber is defined as P_s, while P_o is the amount of power that exits the chamber. Over long distances, molecular absorption of radiation is best described by Beer's absorption law but through a short chamber length l, the absorbed power ΔP follows the relationship

N.E. Glauvitz • R.A. Coutu Jr. (✉)
Air Force Institute of Technology, 2950 Hobson Way, Wright-Patterson AFB, Dayton, OH 45433, USA
e-mail: Ronald.Coutu@afit.edu

M. Kistler • I.R. Medvedev • D.T. Petkie
Wright State University, 3640 Colonel Glenn Hwy, Dayton, OH 45435, USA

G. Shaw III et al. (eds.), *MEMS and Nanotechnology, Volume 5: Proceedings of the 2013 Annual Conference on Experimental and Applied Mechanics*, Conference Proceedings of the Society for Experimental Mechanics Series,
DOI 10.1007/978-3-319-00780-9_9, © The Society for Experimental Mechanics, Inc. 2014

$$\Delta P = P_s - P_o = P_s p_x \alpha l \tag{9.1}$$

where α is the absorption coefficient and p_x is the partial pressure factor of the gas under investigation. When the THz radiation source is amplitude modulated on and off, the energy absorbed ΔE by the gas during each pulse is

$$\Delta E = \frac{\Delta P}{2f_m} \tag{9.2}$$

where ΔP is the power absorbed per cycle and $1/(2f_m)$ is the duration of time the radiation source is on per cycle. The amount of energy absorbed per pulse can also be described by the kinetic theory of gasses as

$$\Delta E = \frac{3}{2} N k_B \Delta T \tag{9.3}$$

where N is the number of molecules in the enclosed system, k_b is the Boltzmann constant, and ΔT is the induced temperature change. To determine the change in pressure Δp generated by a temperature increase of ΔT in a fixed volume V, the ideal gas law is used.

$$\Delta p = \frac{N}{V} k_B \Delta T \tag{9.4}$$

Substituting Eqs. 9.3 and 9.2, and then Eq. 9.1 into Eq. 9.4 yields an expression for the anticipated change in pressure Δp as function of several variables.

$$\Delta p = \frac{P_s p_x \alpha l}{3 V f_m} = \frac{P_s p_x \alpha}{3 \pi r^2 f_m} \tag{9.5}$$

Equation 9.5 describes the anticipated change in chamber pressure per cycle as a multivariable function of radiation source power (P_s), partial pressure factor of the gas (p_x), absorption coefficients (α), chamber radius (r), and the radiation modulation frequency (f_m). Based on these design space parameters, the anticipated changes in pressures could span a very large range. On the high end, changes in pressure could be in the tens of Pascal; while the low end of the pressure regime is 10^{-9} Pa or lower could be expected depending on the gas constituents and chamber conditions. With these anticipated photoacoustic conditions in mind, multiple cantilever designs were implemented and tested in the CoventorWare FEM software.

9.2 Cantilever Modelling

Traditional cantilever design parameters of length, width, and thickness were used to create designs sensitive to the lower end of the anticipated pressure spectrum. Cantilever spring constant as well as cantilever resonant frequencies are also of importance to the design. A common equation for the spring constant k of a cantilever beam is

$$k = \frac{2}{3} E_Y w \left(\frac{t}{L}\right)^3 \tag{9.6}$$

where E_Y is Young's modulus of the material, while the other parameters are the beam dimensions of length (L), width (w), and thickness (t). This equation generates two comments on potential beam designs. First, the stiffness of a cantilever scales linearly with changes in width and that it is a cubic function of the thickness over length ratio. Beam designs must take advantage of a small thickness to length ratio to reduce stiffness of the beam and allow greater deflection under small pressure loads. Due to the large span of anticipated pressure conditions, both static and resonant modes of cantilever deflection were studied in CoventorWare.

Cantilever designs from 3 to 9 mm long and widths of 1–5 mm were drawn and then imported into CoventorWare. Mesh quality analysis settings of from 1 mm down to 5 um blocks were tested to determine mesh quality and effect on displacement results. The mesh settings used a z-extruded parabolic brick mesh pattern. Tip displacement results for the

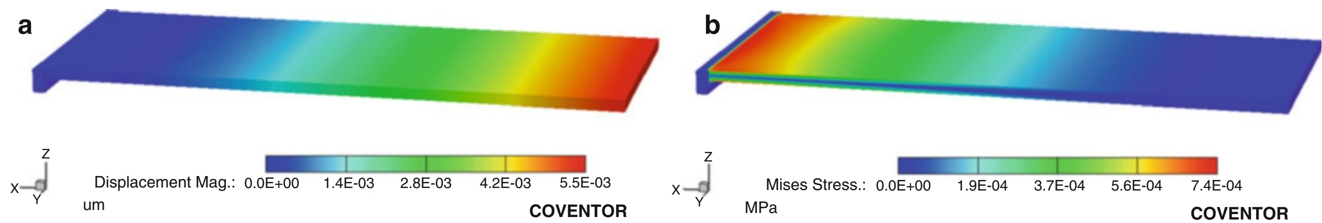

Fig. 9.1 CoventorWare FEM model of a 5 × 2 × 0.01 mm^3 cantilever under 1 mPa static load, (**a**) displays the resultant beam deflection and (**b**) the mises stress generated in the beam

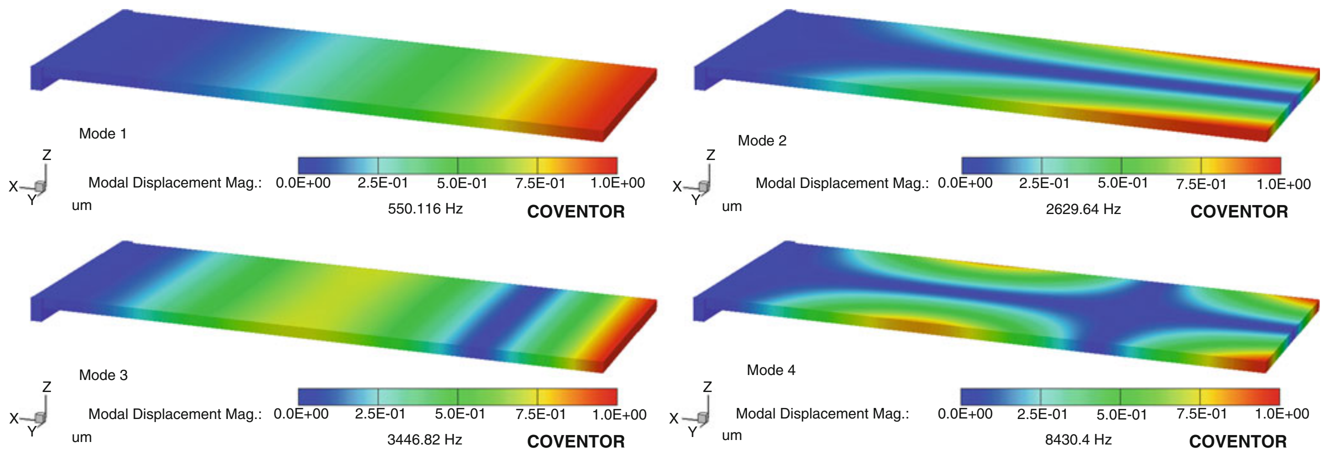

Fig. 9.2 Cantilever resonant mode shapes and frequencies for a 5 × 2 × 0.01 mm^3 cantilever due to a sinusoidal load

mesh patterns were within 0.2 % agreement of each other when a large 25 μm mesh and the smaller 5 μm mesh blocks were used. The larger 25 μm mesh size had a computation advantage, generating results 18 times faster than the finest mesh model. The larger mesh settings were shown to be satisfactory, static load analysis and harmonic modal analysis were performed on the cantilever beam designs. Static load simulations were accomplished to study the resultant cantilever bending shape and tips displacements. These static load conditions are representative of an operational test condition where the THz radiation could be modulated at a very low frequency.

Shown in Fig. 9.1a is the beam deflection and mises stress in Fig. 9.1b on a 5 × 2 × 0.01 mm^3 cantilever under a 1 mPa static pressure load. This beam configuration had a tip displacement of 5.5 nm and a maximum stress of 7.4E^{-4} MPa at the base of the beam. Beams modelled under lighter load conditions showed even less bending as the tip displacement scaled linearly with changes in load pressures.

A modal analysis was performed to determine the natural oscillation modes and at what frequencies they occurred for the cantilevers. The first resonant mode is desirable as it exhibits the greatest tip deflection at the lowest resonant frequency. All other higher order modes are undesirable since they experience much less tip deflection. Shown in Fig. 9.2 are the mode shape and frequency results for a 5 × 2 × 0.01 mm^3 cantilever subjected to a 1 mPa sinusoidal load. The second resonance is a torsional mode, third resonance is a small amplitude multi-peak longitudinal mode, while the fourth resonance is a combination longitudinal and torsional modes. A desirable beam design would have a large separation between the first and second modes of resonance to minimize the potential of exciting the torsional mode during testing in the photoacoustic chamber.

A summary of the first and second resonant frequency results is shown in Table 9.1 for each of the beam designs modeled. As the beam width increased, the second resonance mode moved significantly closer to the lower first resonant mode frequency. As the cantilever beam width increased, the first resonant mode increased only slightly. Based on these results, it is advantageous to select beam designs that have a narrow width since wider widths cause the second harmonic mode to shift down closer toward mode one.

The next examination performed was a harmonic modal analysis which computed the magnitude of cantilever tip deflection causes by a harmonic load applied to the surface of the cantilever as a function of frequency. In this method, a cantilever damping parameter is used and is defined as a fraction of the critical damping coefficient c_0

Table 9.1 Resonant frequency of modes 1 and 2 for the each beam design length and width for a 10 μm thick device

Width (mm) / Length (mm)	1		2		3		5	
	Mode 1 (Hz)	Mode 2 (Hz)	Mode 1 (Hz)	Mode 2 (Hz)	Mode 1 (Hz)	Mode 2 (Hz)	Mode 1 (Hz)	Mode 2 (Hz)
3	1,516.63	8,542.32	1,526.28	4,765.54	1,527.36	3,500.80		
5	549.92	3,445.98	550.12	2,629.64	550.25	1,869.13	550.40	1,261.26
7	280.67	1,758.70	280.76	1,759.10	280.93	1,264.61	280.90	830.15
9	169.83	1,064.09	169.86	1,064.13	169.91	953.96	169.96	614.70

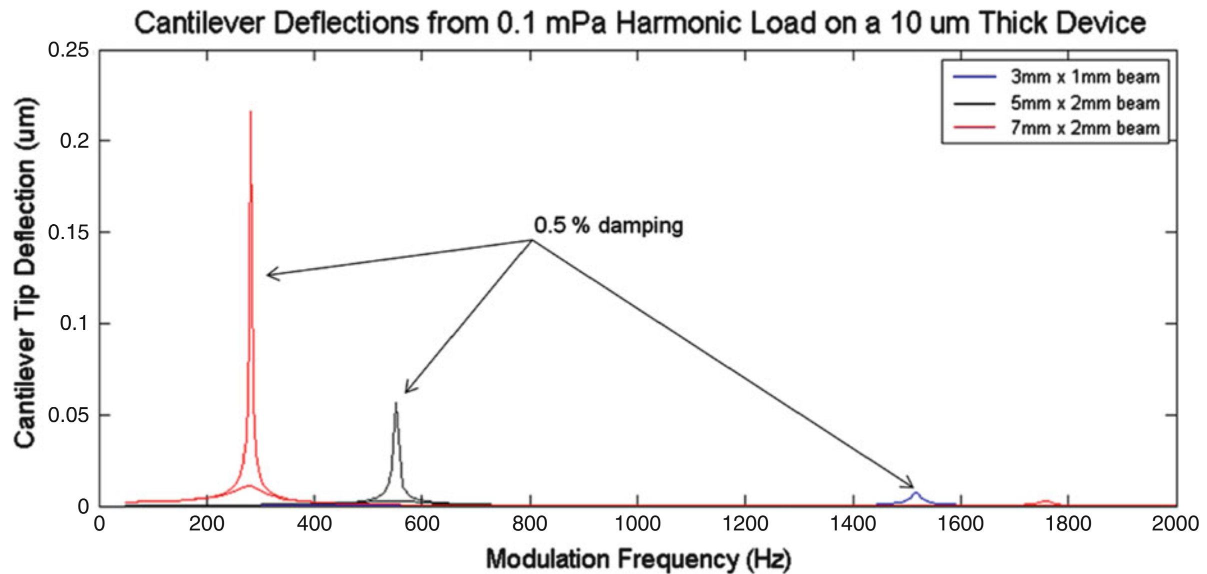

Fig. 9.3 Cantilever tip deflections for three cantilever designs under a 0.1 mPa harmonic load with 0.5 % damping highlighted by the arrows while a 10 % damping factor results is a very small deflection barely visible below the lesser damped curve

$$c_0 = 2\sqrt{mk} \tag{9.7}$$

where m is the mass of the beam and k is the spring constant. A series of percentages of the critical damping coefficient values were selected and tested to represent a range of possible pressure damping effects in the test chamber from atmospheric down to low vacuum conditions. Test conditions in the photoacoustic chamber are expected to operate in the 5–600 mtorr pressure range. To investigate damping effects, a 0.1 mPa sinusoidal load was applied to the cantilever beams and damping percentages from 10 % down to 0.5 % were simulated. Figure 9.3 illustrates the resulting tip deflections for three cantilever beam designs under the 0.1 mPa sinusoidal load utilizing 10 % and 0.5 % of the damping coefficients. It is clear that the tip deflection of the 0.5 % damped cases greatly exceeded that of the 10 % damped cases which are barely visible in the graph. The $3 \times 1 \times 0.01$ mm^3 cantilever beam illustrated by the blue line in Fig. 9.4, it had a maximum of 7 nm tip displacement at the first resonant frequency of 1,517 Hz with the 0.5 % damping coefficient. The next larger design graphed in Fig. 9.4 was the $5 \times 2 \times 0.01$ mm^3 cantilever illustrated with a black line had a maximum tip displacement of 56 nm at 550 Hz, for the 0.5 % damping condition. The final beam with a red line in Fig. 9.4 is a $7 \times 2 \times 0.01$ mm^3 cantilever. Under the same 0.5 % damping condition, it had a maximum tip displacement of 280 nm at 280 Hz modulation frequency. The second resonance mode was observed with the $7 \times 2 \times 0.01$ mm^3 cantilever shows a small peak on the graph as a 3 nm tip torsional displacement at 1,759 Hz.

Two factors were considered in selection of a beam design for fabrication, resonant frequency and tip displacement. A higher cantilever resonant frequency is advantageous because it would allow for faster data collection rates. While a counter argument is to select a reduced resonant frequency design due to Eq. 9.5, which shows the anticipated change in chamber pressure per cycle is inversely proportional to the modulation frequency. From the modeled beam designs, the $5 \times 2 \times 0.01$ mm^3 beam was selected for fabrication. This design was selected due to the moderately high resonant frequency and predicted tip deflections were adequate for low pressure loads.

9.3 Device Fabrication

Based on modal and static deflection results from the FEM model, the $5 \times 2 \times 0.01$ mm^3 cantilever beam design was fabricated out of the device layer of Ultrasil SOI (100) wafer using MEMS fabrication processes. The cantilever fabrication sequence, outlined in Fig. 9.4, began with a brief buffered oxide etch to remove the native oxide layer. Using the standard bi-layer photoresist lift-off technique in Fig. 9.4a, a reflective the metal layer of Ti/Au (200/1,000 Å) was deposited via electron beam evaporation at the tip of the cantilever. This small reflective area near the tip of the cantilever aided in HeNe laser alignment in the test chamber and provided the reflective surface necessary for the laser and photodiode measurements. In Fig. 9.4b, a patterned 2 μm layer of photoresist was then used to define the cantilever shape for the subsequent deep reactive ion etch (DRIE) through the device layer down to the buried oxide (BOX) of the SOI. With the cantilever pattern etched in the device layer it was then coated with a layer of PMGI to protect the silicon and gold surfaces during subsequent processing steps. To pattern the portion of the handle wafer below the cantilever for removal, the backside of the wafer was coated with a 20 μm layer SU-8 25 and exposed on a SUSS MAB-6 backside mask aligner. After the develop steps, the sample was hard baked on a covered hotplate at 110 °C for 1 h to further harden the SU-8.

Shown in Fig. 9.4c is the sample after a two step DRIE and then a reactive ion etch (RIE) through the backside of the handle wafer. It was found to be necessary to stop the backside DRIE process 20–30 μm short of the buried oxide layer, leaving a thin Si membrane to temporarily support the cantilever and BOX structure. Heat generated during the DRIE process caused portions of the PMGI protective layer to crack and resulted in non-uniform stresses between the device layer and the PMGI. Without the thin Si support layer, the residual stress between the device layer, BOX, and PMGI often caused fractures through the cantilever structure, ruining the device. The cantilever beams are extremely fragile during the fabrication process due to their large length to thickness ratio (L/t), which for these devices was 500/1. A successful processing method was developed where in the PMGI layer is stripped off and replaced by a layer of 1,818 which was applied at a low spin speed. The thicker resist layer was then bake for 5 min on a 100 °C hotplate. With a fresh PR coating to protect the device layer and provide some physical support for the device layer, the remaining thin Si membrane on the

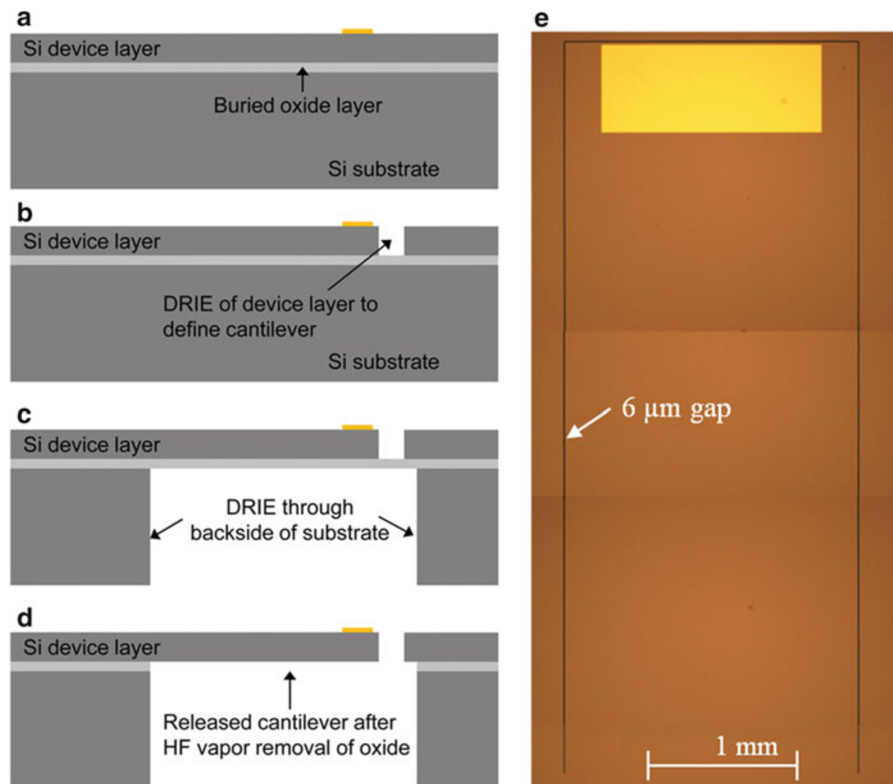

Fig. 9.4 Photoacoustic silicon cantilever fabrication process began with the (**a**) deposit Ti/Au for reflective surface, (**b**) etch device layer to define cantilever, (**c**) DRIE and RIE steps to etch through handle wafer, and (**d**) the removal of the exposed BOX with HF vapor. An optical image (**e**) of a fabricated $5 \times 2 \times 0.01$ mm^3 silicon cantilever shown in has Ti/Au reflective metal layer and a 6 μm gap etched through the device layer to define the cantilever beam

backside was removed in a RIE tool. This new PR protective layer proved essential in the fabrication process and greatly improved the sample yield. The process conditions used 30 sccm SF_6, 3 sccm O_2, 100 W RIE power, and a process pressure of 150 mTorr. This mild etch condition for the final etch allowed for a slow, uniform removal of the remaining Si that covered the BOX. The protective PR layer didn't experience any undesirable heating effects such as cracks, which were observed on samples if they were completely etched in the DRIE.

The final etch step in the fabrication process was the removal of the BOX layer with HF vapor, as illustrated in Fig. 9.4d. Sample were suspended over a 49 % hydrofluoric acid solution where the HF vapor then etched the exposed BOX layer over a period of several minutes. The protective PR on the device layer was then removed from the samples through a series of acetone soaks, a final dip in isopropanol, and allowed to air dry. An O_2 plasma ash at was performed for several minutes to remove any lingering PR from the cantilever surface and the narrow cantilever gap region to ensure the cantilever could oscillate unimpeded.

Using a single device layer etch mask designed with a 3 μm gap, multiple gap widths were achievable on different samples through varying the device layer etch conditions. A DRIE only etch of the 3 μm patterned slit produced the smallest gap, while a subsequent isotropic RIE etch on other samples allowed gaps up to 8 μm wide in this work. A completed $5 \times 2 \times 0.01\ mm^3$ silicon device is shown in Fig. 9.4e had a 6 μm gap etch through the device layer that defined the cantilever dimensions.

9.4 Conclusions

Photoacoustic detection of THz radiation for spectroscopy is a changeling and exciting area of research. In this work, a representative equation to anticipate photoacoustic pressures per radiation pulse was developed. Development of an expression for the expected changes in photoacoustic pressure was an important step to establish the load conditions that were applied to the modelled cantilever beams. MEMS cantilever sensors were then designed, modelled, and fabricated around the predicted pressure conditions in the photoacoustic chamber. The FEM solid model mesh parameters were investigated and it was found that the 25 μm extruded parabolic mesh displacement results differed from the finer mesh models by only 0.2 % which allowed the use of the larger mesh size and greatly reduced the required computational time. The FEM software models developed in this effort provide excellent insight into how the different cantilever beams would deflect under the both static and resonant modes of operation. MEMS fabrication processes and techniques were also refined to greatly increase sample yield for these large fragile high aspect ratio (L/t) cantilever devices.

Efforts are underway to optimize cantilever designs and photoacoustic signal analysis methods for the THz test chamber system. Photoacoustic test results from successful fabricated cantilever devices will be presented in future work. Data collections from experimental measurements on the fabricated cantilevers will then be used to refine the FEM load pressures and damping effects used to model the cantilever devices. The modelling results and fabrication techniques presented in this work directly contribute toward the overarching goal to create a compact photoacoustic detection method that is virtually independent of the absorption path length. This would be a significant advancement and greatly reduce the chamber size compared to traditional spectral detection techniques.

Acknowledgements The authors would like to thank the Air Force Research Laboratory (AFRL) Sensors and Air Vehicles Directorates for their helpful discussions, resources, and facility use. The authors also thank the technical support and dedicated work of AFIT's own cleanroom staff.

References

1. West GA, Barrett JJ, Siebert DR, Reddy KV (1983) Photoacoustic spectroscopy. Rev Sci Instrum 54(7):797–817, http://dx.doi.org/10.1063/1.1137483
2. Kosterev AA, Bakhirkin YA, Curl RF, Tittel FK (2002) Quartz-enhanced photoacoustic spectroscopy. Opt Lett 27:1902–1904
3. Krupnoz AF, Burenin AV (1976) New methods in submillimeter microwave spectroscopy. In: Rao KN (ed) Molecular spectroscopy: modern research. Academic Press, New York, pp 93–126
4. Ledermann N, Muralt P, Baborowski J, Forster M, Pellaux J (2004) Piezoelectric pb(zr x, ti 1− x)O 3 thin film cantilever and bridge acoustic sensors for miniaturized photoacoustic gas detectors. J Micromech Microeng 14(12):1650–1658, http://stacks.iop.org/0960-1317/14/i=12/a=008
5. Kuusela T, Peura J, Matveev BA, Remennyy MA, Stus' NM (2009) Photoacoustic gas detection using a cantilever microphone and III–V mid-IR LEDs. Vib Spectrosc 51(2):289–293

6. Kuusela T, Kauppinen J (2007) Photoacoustic gas analysis using interferometric cantilever microphone. Appl Spectrosc Rev 42(5):443–474, http://dx.doi.org/10.1080/00102200701421755
7. McNaghten E, Grant K, Parkes A, Martin P (2012) Simultaneous detection of trace gases using multiplexed tunable diode lasers and a photoacoustic cell containing a cantilever microphone. Appl Phy B Lasers Opt 107(3):861–871
8. Adamson BD, Sader JE, Bieske EJ (2009) Photoacoustic detection of gases using microcantilevers. J Appl Phys 106(11):114510, http://dx.doi.org/10.1063/1.3271157
9. Fonsen J, Koskinen V, Roth K, Kauppinen J (2009) Dual cantilever enhanced photoacoustic detector with pulsed broadband IR-source. Vib Spectrosc 50(2):214–217

Chapter 10
In-Plane MEMS Acoustic Emission Sensors Development and Experimental Characterization

Hossain Saboonchi and Didem Ozevin

Abstract Damage initiation and growth in materials releases elastic waves, which can be detected by surface mounted acoustic emission (AE) transducers. In this paper, new MEMS comb-drive AE transducers, responsive to in-plane motion, manufactured using electroplating technique for highly elevated microstructure geometries are presented. The transduction principle is capacitance change achieved by area/gap change in two separate designs. Mechanism of spring orientation, dimensions and mass have been selected in such a way that they satisfy three design criteria as the frequency range of 100–200 kHz, 2–30 pF capacitance and the functionality under atmospheric pressure. The challenge of coupling the microstructure vibration in out-of-plane and in-plane directions is addressed with differential mode approach and frequency domain responses. The squeeze film damping is reduced with 8 μm gap between moving electrodes so that the transducers are operational under atmospheric pressure. The directional independence of the transducers to two orthogonal directions is demonstrated using laser source as the excitation signal. The Nd: Yag Q switch laser has 3 mm beam diameter and is focused on the top and the edge of the transducer package. The results show a distinct output signal for in-plane and out-of-plane motions due to the directional sensitivity of the MEMS transducers.

Keywords MEMS • Acoustic emission • In-plane • Electroplating • Laser ultrasound

10.1 Introduction

Acoustic emission (AE) method relies on propagating stress waves due to newly formed damage surfaces. Conventional piezoelectric sensors have bulky geometry and are sensitive to the wave motion in thickness mode and tangential mode due to lateral deformation of the sensor geometry. Understanding the propagating wave direction through differentiating orthogonal wave motions can improve the source localization and characterization. The comb drive sensors have inter-digitized fingers formed by the stationary part known as stator and the moving part known as rotor [1]. Comb drive sensors created using Micro-Electro-Mechanical Systems (MEMS) can be designed to be sensitive to tangential wave motion with respect to the structure that the sensor is attached. Harris et al. [2] designed comb drive sensor using the surface micromachining method for detecting the in-plane motion. However, the sensor has coupled response for in-plane and out-of-plane motions. The unwanted out-of-plane motion dominated the sensor response. The surface micromachining method has the limited thickness as 2 μm, which limits the sufficient separation of the resonant frequency modes of in-plane and out-of-plane motions. The lateral instability of the comb drive is a known problem [3].

The metalMUMPs incorporates LIGA-like, thick metal electroplating and bulk/surface micromachining processes to develop thick metal layer. The process is available by Memscap Inc since 2003. The process has been implemented by several researchers in the literature. For instance, Tsai et al. [4] designed out-of-plane rotational platform using in-plane electrostatic comb drive actuators. Almeida [5] developed MEMS relay based on the comb drive electrostatic actuators. In this study, the AE sensors as receivers with the capacitance change as the transduction principle are manufactured using

H. Saboonchi • D. Ozevin (✉)
University of Illinois, Chicago, USA
e-mail: dozevin@uic.edu

G. Shaw III et al. (eds.), *MEMS and Nanotechnology, Volume 5: Proceedings of the 2013 Annual Conference on Experimental and Applied Mechanics*, Conference Proceedings of the Society for Experimental Mechanics Series,
DOI 10.1007/978-3-319-00780-9_10, © The Society for Experimental Mechanics, Inc. 2014

the metalMUMPs in order to separate two orthogonal wave motions in out-of-plane and in-plane directions. The sensors are numerically modeled to understand the fundamental mode shapes and frequencies and quantify the capacitance. The sensor characterization tests include capacitance and admittance measurements. The directional property of the sensors is identified using Nd: Yag Q-switched laser, which creates one directional source function.

10.2 Operational Principle and Design Properties

Capacitive sensing forms the transduction principle of the sensors. The capacitance change ΔC can be achieved via area change, gap change or dielectric change as shown in the equation below:

$$\frac{\Delta C}{C_o} = \frac{\Delta \varepsilon}{\varepsilon} + \frac{\Delta A}{A} - \frac{\Delta d}{d}$$

where ε is dielectric constant of the material between the electrodes, A is the overlap area of parallel plate capacitors, d is the gap between the capacitors. Any time dependent change in the equation causes capacitance change as dC/dt, which is recorded as current i when the parallel plate capacitors are connected to a DC bias source V_{DC} as:

$$i = V_{DC}\frac{dC}{dt}$$

The comb drive sensors are designed with two principles as area change and gap change in order to compare the response characteristics as signal to noise ratio and the separation of the intended in-plane motion and the unintended out-of-plane motion. Figure 10.1 describes the geometric variables of unit cells of two designs. For the area change design, Fig. 10.1a, the spring elements forming the stiffness of the dynamic system move in –x direction that causes the overlap area of stationary fingers and moving fingers change. The spring length and the mass width are varied to reach the target frequency in the range of 100–200 kHz. The vibration frequency of the fingers is designed as greater than 1 MHz; therefore, they stay stationary under the dynamic excitation, which does not include frequencies higher than 1 MHz. The dimensions of the unit cell gap 1 to gap 4, mass and spring elements are provided in Table 10.1. The area change design is configured such a way that the sensor can operate as differential mode in order to remove the effect of unintended out-of-plane motion. For the gap change design, Fig. 10.1b, the spring elements move in –y direction, which causes the changes of gap 1 and gap 2 shown in the figure. When the fingers move in –y direction, gap 1 decreases while gap 2 increases. The design has different gaps in order to prevent the cancellations.

Each unit cell is numerically modeled using Comsol Multiphysics program in order to determine the resonant frequencies and the static capacitance. For the frequency identification, the model is simulated using the eigenfrequency study. The geometries and material properties of the moving capacitance are modeled. Figure 10.2 shows the first mode shapes of the area change and gap change designs. The area change design has the first fundamental frequency at 105 kHz, the gap change design has the first fundamental frequency at 145 kHz. The cross sectional variables of the spring elements are as follows: height h as 20.5 μm and width b as 8 μm. The lateral resonance is proportional to $\sqrt{hb^3}$ while the transverse

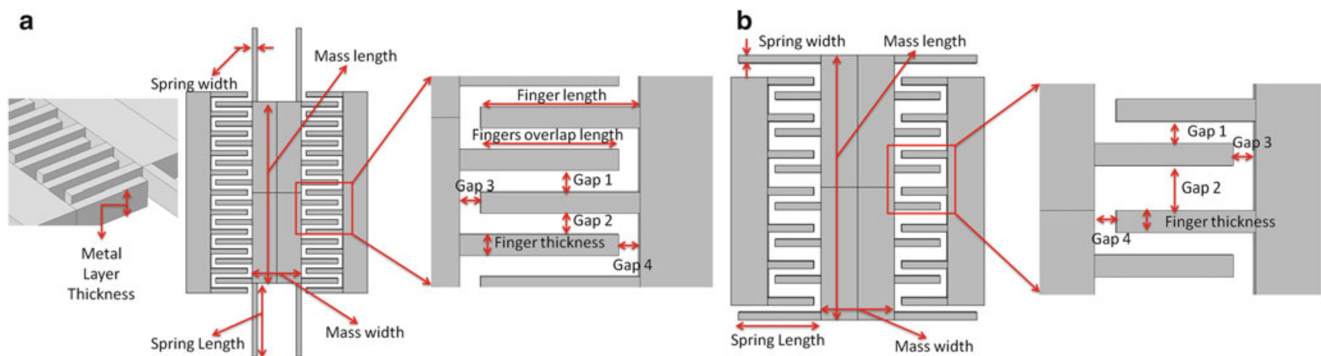

Fig. 10.1 The description of unit cell design for (**a**) area change, (**b**) gap change

Table 10.1 The description of unit cell design for area change and gap change

Sensor type	Mass		Spring		Gap				Fingers	
Units: [μm]	Width	Length	Width	Length	1	2	3	4	Thickness	Length
Area change	80	288	8	120	8	8	8	8	8	60
Gap change	72	296	8	120	8	16	8	8	8	60

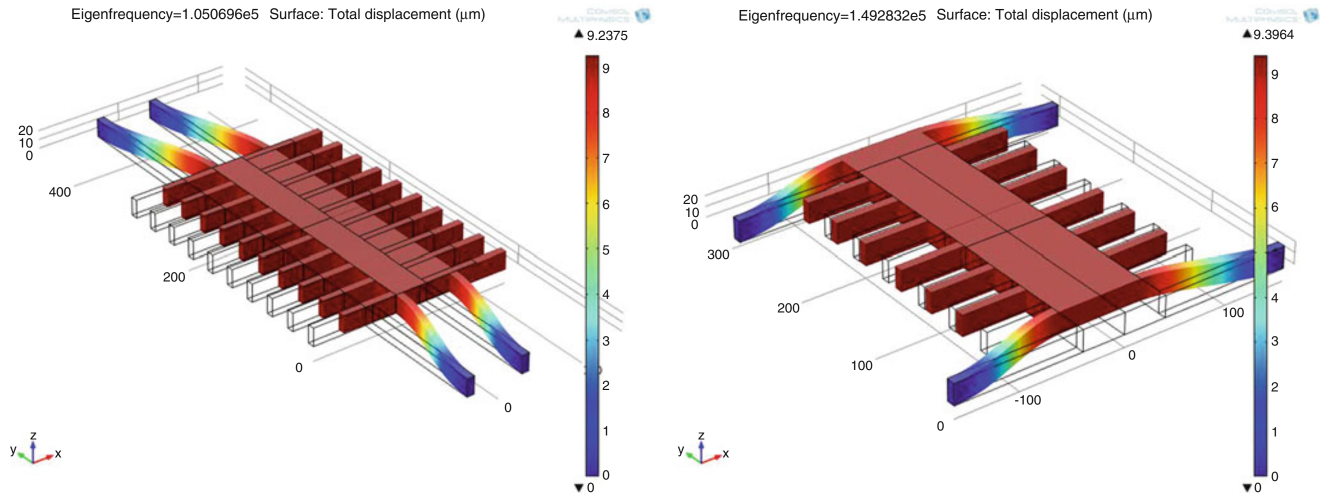

Fig. 10.2 Numerical simulations indicating the first resonate mode shapes and frequencies for area change and gap change designs

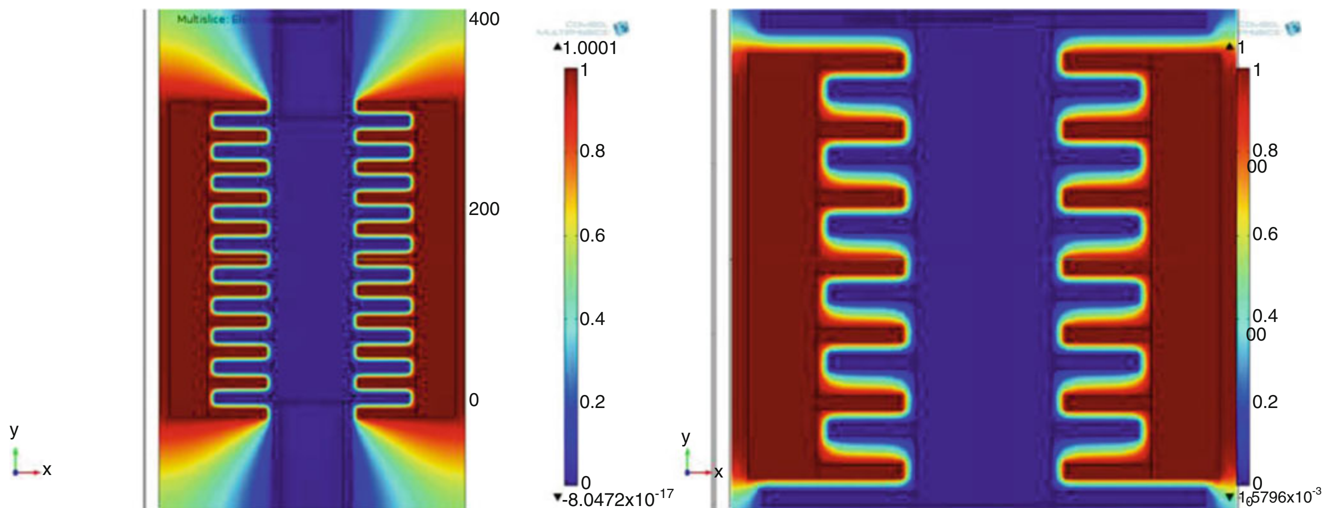

Fig. 10.3 Numerical simulations indicating the capacitance and fringe fields for area change and gap change designs

resonance is proporational to $\sqrt{bh^3}$. Therefore, the ratio of the frequencies of out-of-plane direction to in-plane direction is about 2.5. Theoretically, a narrowband filter would be sufficient to differentiate the motions in two directions.

To quantify the static capacitance of the designs, the stationary and moving electrodes are modeled as shown in Fig. 10.3. The electrodes are separated by air with the gaps given in Table 10.1. A box of air is formed around the geometry to create the electrical field and solve for the capacitance. 1 V_{DC} is applied to the stationary layer, which forms the ground; the moving layer is the terminal to measure the capacitance. 3D model includes the fringe fields as well as shown in the figure. The capacitances of the area change and the gap change designs are calculated as 2 pF (on each side) and 3 pF, respectively.

10.3 Manufacturing

The sensors are manufactured using MetalMUMPs, which is based on the electroplating technique to deposit 20 μm nickel layer and 0.5 μm gold layer. The sequence of the layers implemented in this study includes growth of silicon oxide (2 μm), deposition two layer of silicon nitride (0.35 μm each), deposition silicon oxide as the sacrificial layer (1.1 μm), deposition and formation of metal layer and finally release the metal layer. The thicknesses of the layers are controlled by the process while the planer views are controlled by the design. Figure 10.1 and Table 10.1 shows the dimensions of each design indicating the stationary and freely moving layers. The design is created using Cadence program and submitted for manufacturing. Figure 10.4 shows the SEM images of the sensors. Comparing the design and the final geometry indicates that the intended geometry is successfully manufactured.

10.4 Electromechanical Characterizations

The electromechanical characterization tests include capacitance measurement and impedance measurement using HP 4294A Impedance Analyzer. The capacitance curve is obtained through sweeping a range of DC voltages with 500 mV alternative voltage at 1 MHz. Figure 10.5 shows the C-V plots for area change and gap change sensors. While the

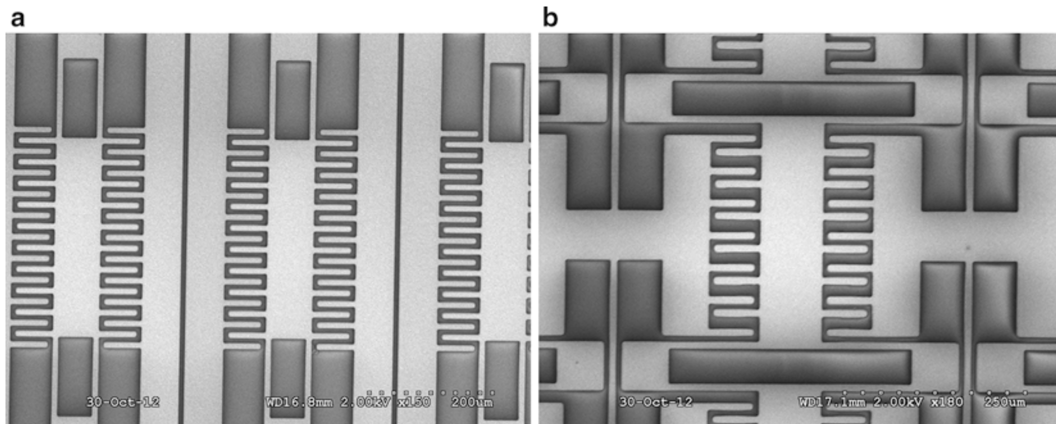

Fig. 10.4 SEM images of the sensors (**a**) area change, (**b**) gap change

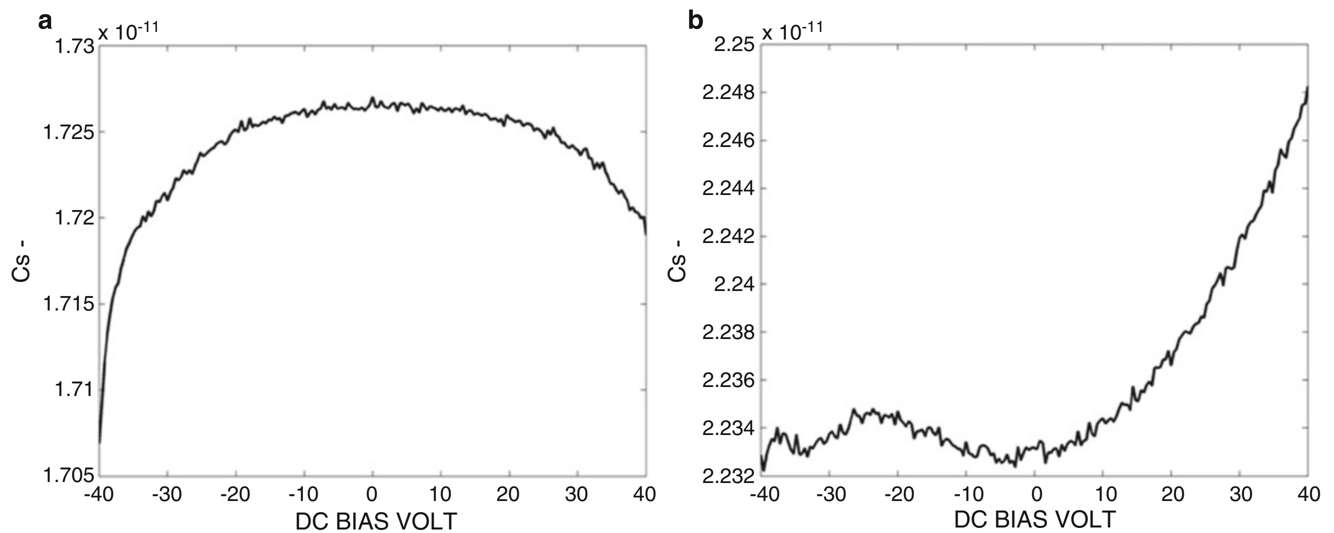

Fig. 10.5 C-V curve of sensors with the principle of (**a**) area change, (**b**) gap change

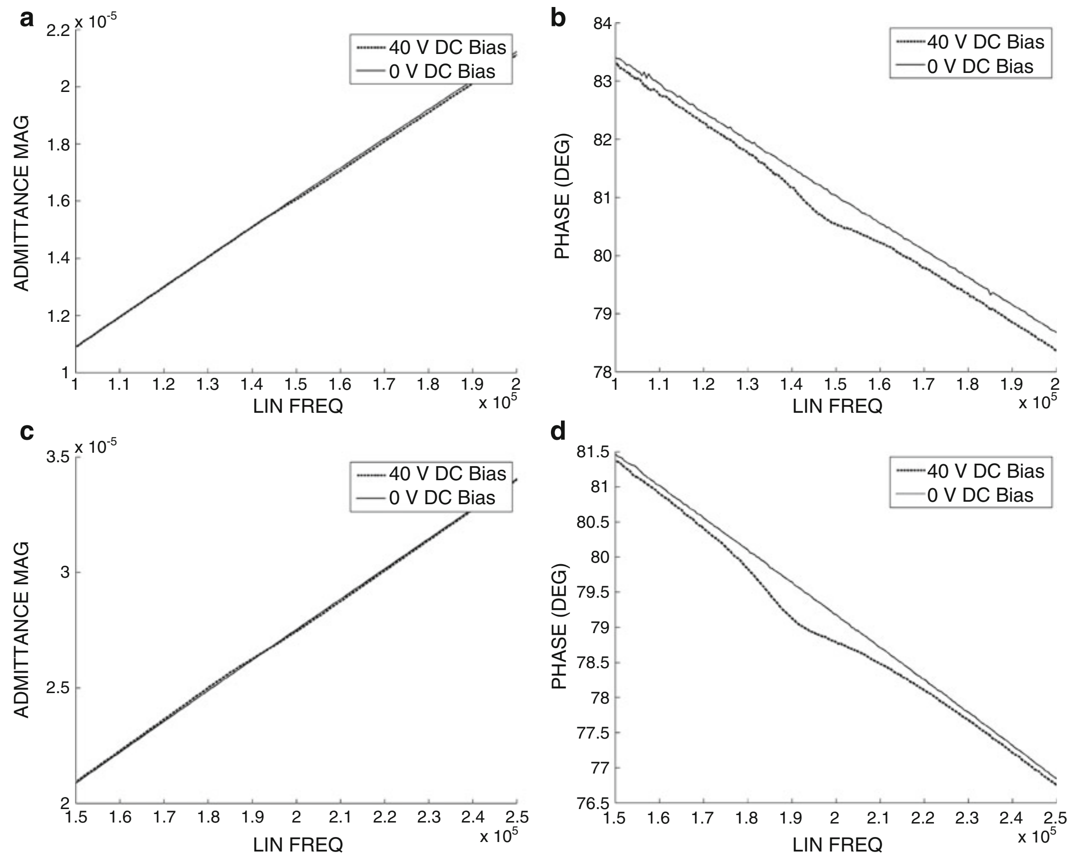

Fig. 10.6 Admittance plots of sensors with the principle of (**a**, **b**) area change, (**c**, **d**) gap change

capacitance sensors have parabolic relationship between capacitance and DC bias voltage, unexpected response is observed. There are two potential explanations for the C-V responses. The alternative voltage frequency is close to vibration frequency of the fingers, which may cause unexpected resonance of fingers. While the frequency is varied to be away from the resonance frequency of the fingers, the error in the capacitance measurement due to the limitation of the impedance analyzer becomes higher. The other reason may be because of parasitic displacement in the unintended direction at the out-of-plane direction [6]. The C-V behaviors of the sensors require further research.

The magnitude and phase plots of the admittance values for a range of frequencies are shown in Fig. 10.6. While the resonance is not clear in the magnitude plot, it is clearly seen in the phase plot. The resonance frequencies of the area change and gap change sensors are 150 and 190 kHz, respectively. The gap between the fingers is 8 μm; therefore, the squeeze film damping is significant when the sensor operates in atmospheric pressure. The numerical results are 105 and 145 kHz. The actual values are higher for both sensors. This may be because of variability in geometries, material properties and residual stress. Further, damping is not considered in the numerical models.

10.5 Directional Response with Laser Ultrasound

The isolation of the intended in-plane motion and the unintended out-of-plane motion is the critical design criterion of the sensor. Figure 10.7 shows the photograph of the experimental setup, which includes Nd: Yag Q-switched laser source, optical breadboard, mounting block and oscilloscope. The sensors are connected to 45 DC bias source using 9 V batteries. The orientation of the mounting block is changed in order to load the sensor in out-of-plane direction (z) and in-plane direction (x). The in-plane loading direction is y direction for the gap change design. The laser source creates a step load defined with Heaviside step function with 3 nsec rise time in orthogonal direction to the loading direction.

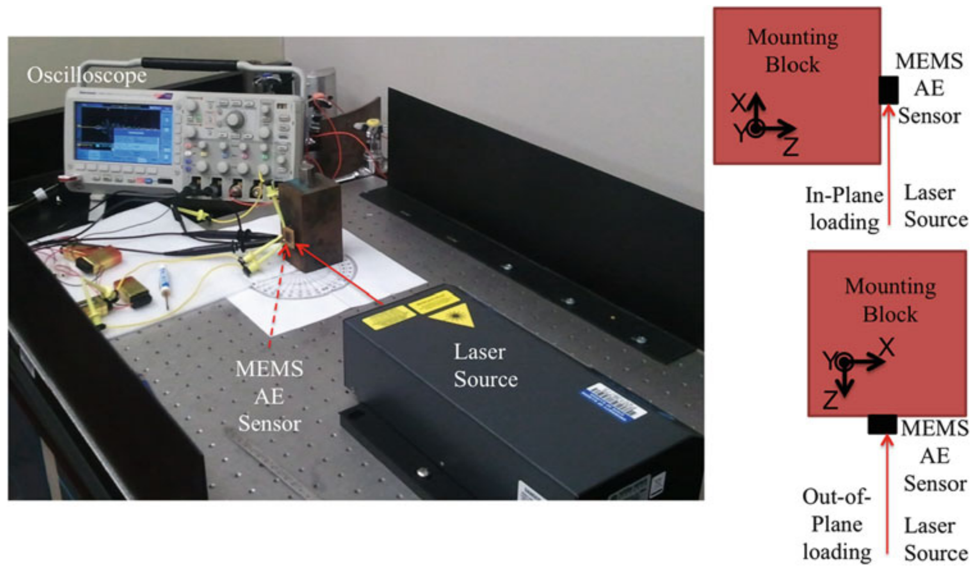

Fig. 10.7 The ultrasonic source generation with the Q-switched laser to study the directional dependence

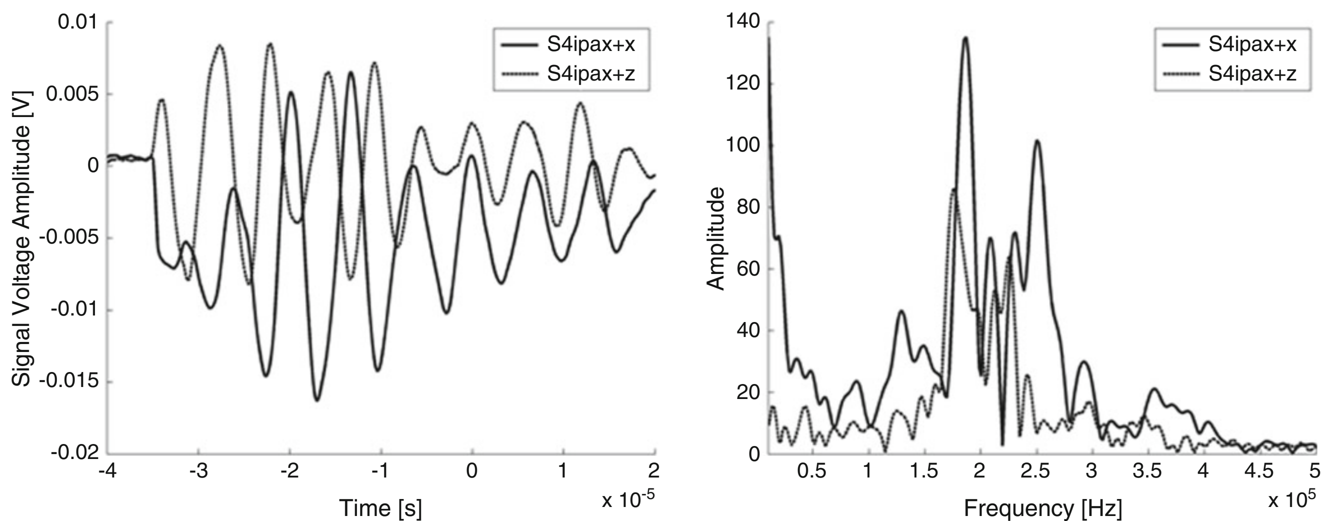

Fig. 10.8 Waveform histories and frequency spectra of the area change sensor for out-of-plane (z) and in-plane (x) directions

Figure 10.8 shows the waveforms and frequency spectra of the area change sensor when the sources are varied in z and x (intended) directions. The response in x direction has a sudden drop and then the sensor resonates. The initial displacement profile is similar to the theoretical response at the epicenter due to the laser source [7]. The initial displacement causes zero frequency, which is not observed for the z direction (unintended) excitation. The frequency bandwidth of 160–300 kHz is observed for both excitation directions. This may be because of high damping coefficient, which causes a wide bandwidth response.

Figure 10.9 shows the waveform histories and frequency spectra of the gap change sensor. The amplitude at the signal drop at the beginning of the waveform is smaller than that of the area change sensor; however, the overall maximum values are similar. There are several frequencies observed in the y direction excitation as compared to the z direction excitation such as 80, 150 kHz. The amplitude in the y direction is also higher than the amplitude in the z direction. While there are clear differences between the sensor response under the excitation sources at the intended (y) direction and the unintended (z) direction, a further study is needed to differentiate the responses.

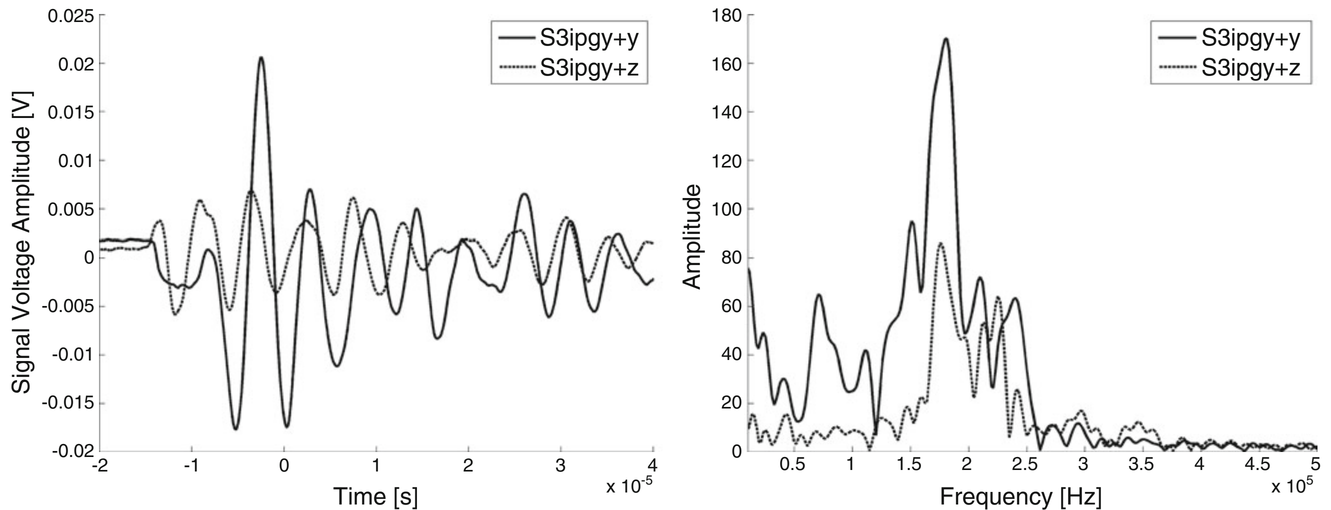

Fig. 10.9 Waveform histories and frequency spectra of the gap change sensor for out-of-plane (z) and in-plane (x) directions

10.6 Discussion and Conclusion

In this paper, in-plane AE sensors designed with the principles of capacitance change due to area and gap changes are introduced. The sensors are manufactured with MetalMUMPs to create higher aspect ratio geometry. Theoretically, the ratio of the resonant frequencies in out-of-plane and in-plane directions is 2.5. However, due to high damping coefficient, the damped response causes a wideband response, which makes differentiating the responses in the intended direction and the unintended direction difficult. The sensor has zero frequency component at the intended direction excitation due to the source function of the laser source (Heaviside step function). There are clear differences in waveform profile and amplitudes; however, differentiating the responses requires further research to implement the sensor in crack detection and localization studies.

References

1. Goravar S, Chandrasekaran S, Zribi A (2010) Probabilistic analysis of a comb-drive actuator. IEEE Sens J 10(4):877–882
2. Harris AW, Oppenheim IJ, Greve DW (2011) MEMS-based high-frequency vibration sensors. Smart Mater Struct 20(7):07501
3. Borovic B, Lewis FL, Liu AQ, Kolesar E S and Popa D (2006) The lateral instability problem in electrostatic comb drive actuators: modeling and feedback control. J Micromech Microeng 16(7):1233–1241
4. Tsai J et al (2009) An out-of-plane rotational platform with in-plane electrostatic combs made by the MetalMUMPs process. J Micromech Microeng 19(7):074007
5. Almeida L (2006) Experimental and Theoretical investigation of contact resistance and reliability of lateral contact type ohmic MEMS relays, MS Thesis Auburn University
6. Van Spengen WM, Heeres EC (2007) A method to extract the lateral and normal components of motion from the capacitance change of a moving MEMS comb drive. J Micromech Microeng 17(3):447–451
7. Scruby CB, Drain LE (1990) Laser ultrasonics techniques and applications. Taylor & Francis Ltd, London, UK

Chapter 11
New Insight into Pile-up in Thin Film Indentation

MariAnne Sullivan and Barton C. Prorok

Abstract This work builds involves leveraging our recent thin film mechanics model on the discontinuous transfer of strain from the film to the substrate. In applying this model with well-defined film and substrate properties we were able to decouple the effects of elastic modulus and Poisson's ratio mismatch in the indentation process. In doing so we identified new insight in the processes of pile-up and strong evidence suggested a dependence on film thickness and ratios of film/substrate of elastic modulus and Poisson's ratio. Atomic force microscopy was employed to characterize the degree of pile-up and correlate it with the above dependencies. We believe these efforts will enable the prediction of the degree of pile-up and subsequently the removal of its influence in measuring thin film behavior.

Keywords Pile-up • Sink-in • Nanoindentation • Thin film mechanics • Poisson's ratio

11.1 Introduction

Indentation of materials on a macro and micro scale have been a cornerstone of determining mechanical properties, such as hardness, of materials for the last century. During indentation, a tip with known geometric size and mechanical properties is pressed into a material. Once loading is complete, the hardness of the indented material is then calculated from the maximum load applied and the measured contact area from the remaining indent. As the experimentation method has progressed, there has been a desire to make smaller and less intrusive indents on smaller and smaller scales. Over the last few decades instrumented indentation on the nano-scale, nanoindentation, has gained attention as a method to extract the hardness and Young's modulus of a samples that require higher precision and much lower loads that can be applied by direct human interaction.

With nanoindentation came the possibility to indent on a sample that consists of a thin layer, or film, of one material on the surface of a different bulk material, or substrate. The interest in thin films comes from their use in a wide range of material applications such as optical coatings, very large-scale integrated circuits, anti-corrosion, anti-wear and fuel cells. Even when the applications are not centered on the mechanical behavior of the thin films, increasing their ability to withstand processing, and durability during their lifetime is still needed. One current shortcoming of nanoindenting thin films being widely researched is that as the film's thickness decreases, the substrate starts to play more of a role in the properties determined through indentation, even at very low penetration depths of the film. Recent authors [1–7] have developed theoretical models based on both experimental and finite element analysis that attempt to extract the mechanical properties of the film, independent of the substrate. While all of these models have their strengths, they also tend to only work for certain material combinations; such as compliant films on hard substrates, or hard films on compliant substrates.

The goal of this research is to thoroughly review one of the more recent models to of been developed that takes a new approach in describing the film and substrates composite behavior. This model, developed by Zhou et al. [6, 7] takes into account that the transfer of energy across the film-substrate interface is not linear, but actually discontinuous; allowing it to better describe the film's behavior for a broader range of material combinations. A group of materials were selected for their similar

M. Sullivan • B.C. Prorok (✉)
Department of Mechanical Engineering, Auburn University, Auburn, AL 36849, USA
e-mail: prorok@auburn.edu

G. Shaw III et al. (eds.), *MEMS and Nanotechnology, Volume 5: Proceedings of the 2013 Annual Conference on Experimental and Applied Mechanics*, Conference Proceedings of the Society for Experimental Mechanics Series,
DOI 10.1007/978-3-319-00780-9_11, © The Society for Experimental Mechanics, Inc. 2014

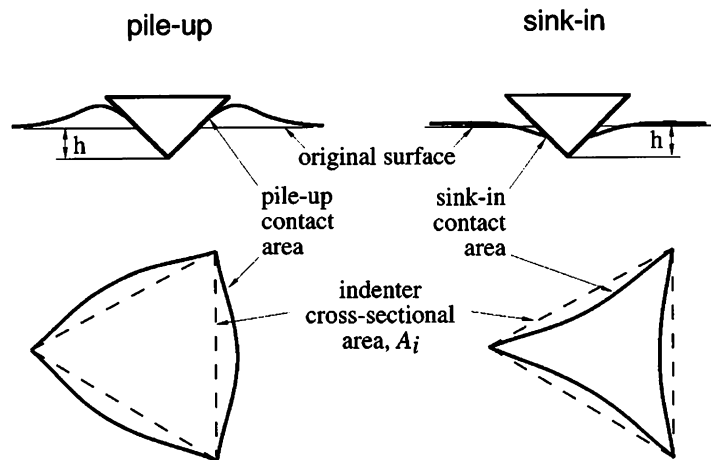

Fig. 11.1 Schematics of the pile-up and sink-in effect [8]

Poisson's ratio, but varying Young's modulus, to have a single thin film layer sputtered on them which also has a similar Poisson's ratio to the substrates. The samples were then nanoindented, comparing the Young's modulus verses indention depth to the behavior expected through the evaluated model.

One substantial challenge to nanoindentation is the difficulty in accurately measuring the contact area during displacement, due to how the material being indented can plastically deform around the indenter, causing a change in actual contact area between the sample and tip, also known as erroneous contact area. If the material is soft it will tend to pile-up around the indenter tip, causing an increase in contact area, leading to an overestimation of the material's modulus, and hardness, as there is more material providing elastic recovery. Harder materials have the tendency to translate their strain further away from the tip, allowing for a greater volume of material to distribute the deformation, causing the area around the tip to sink-in, reducing the contact area of the tip. The sink-in effect leads to an underestimation of the material's modulus, and hardness. A cross sectional schematic of both effects during indentation, and the resulting top-down view of the recovered material after unload is shown in Fig. 11.1 [8].

The goal of this research is to thoroughly review one of the more recent models to of been developed that takes a new approach in describing the film and substrates composite behavior. This model, developed by Zhou et al. [6, 7] takes into account that the transfer of energy across the film-substrate interface is not linear, but actually discontinuous; allowing it to better describe the film's behavior for a broader range of material combinations. A group of materials were selected for their similar Poisson's ratio, but varying Young's modulus, to have a single thin film layer sputtered on them which also has a similar Poisson's ratio to the substrates. The samples were then indented, comparing the Young's modulus verses indention depth to the behavior expected through the evaluated model. An interesting relationship was observed that may reveal new information about Pile-up and sink-in and methods to mitigate their effects.

11.2 Experimental Procedure

For this work, a platinum film was simultaneously deposited on several substrates to investigate the influence of pile-up and sink-in for different material combinations. Here the chosen materials all have identical Poisson's ratio but different elastic moduli. This enabled separation the Poisson's ratio effect on pile-up and sink-in. Table 11.1 lists the materials and properties employed.

The Pt film was simultaneously deposited onto the substrates by sputtering. A thin Ti film was forst deposited to aid in adhesion to the substrate. Table 11.2 lists the parameters employed.

The resulting platinum film was observed with SEM and found to have consistent coverage and excellent surface quality, shown in Fig. 11.2. Table 11.3 shows that using the profilometer, the film thickness of each film-substrate combination was measured in three locations and then averaged to determine the film thickness of 230 nm. As the platinum film had a good surface quality with no disproportionally large protrusions over the film's surface, this platinum film was determined to be the best candidate for indentations.

Table 11.1 Material selection for the films and substrates

Films			Substrates		
Material	E (GPa)	ν	Material	E (GPa)	ν
Al	70	0.35	In	11	0.44
Pt	168	0.36	Sn	50	0.36
			Al (100)	63–70	0.35
			Cu (100)	66–117	0.35
			Ti	116	0.32
			Pt	168	0.36
			Si	178	0.28
			Ta	186	0.34

Table 11.2 Sputtering parameters of 230 nm Pt film with Ti adhesion layer

Substrates	Al, Si, Cu, In, Sn, Pt, Ti, Ta	
Base pressure (Torr)	2.6×10^{-6}	
Magnetron type	DC	DC
Target material	Pt	Ti
Pre-sputtering power (W)	100	400
Pre-sputtering time (s)	15	25
Sputtering power (W)	100	400
Sputtering time (s)	800	25
Gas 1 (Ar) flow rate (sccm)	25	25
Gas 2 (O_2/N_2) flow rate (sccm)	0	0
Deposition pressure (mTorr)	4.7	4.7
Deposition temperature (°C)	23	23
Soak time (s)	0	0
Substrate holder rotation (%)	50	50
Ignition pressure (mTorr)	50	50
Expected film thickness (nm)	250	10
Actual film thickness (nm)	230	10

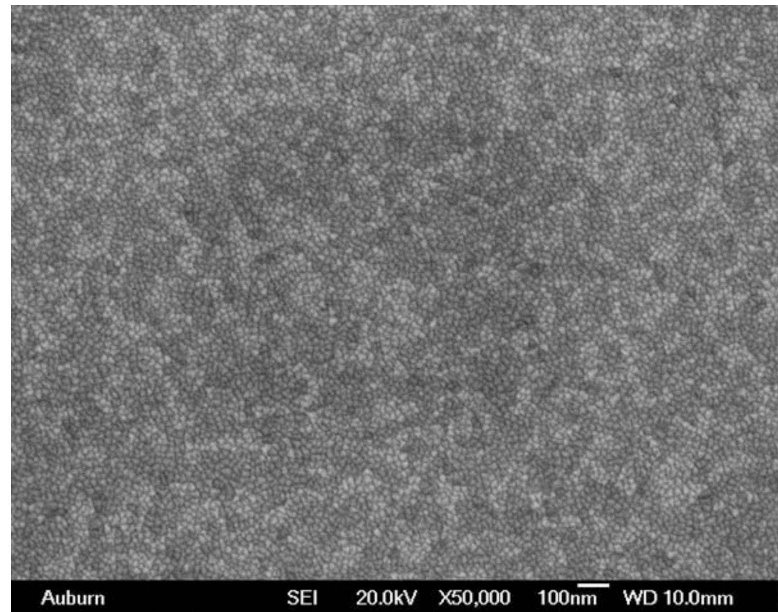

Fig. 11.2 Surface quality of platinum film

Table 11.3 Film thickness of sputtered platinum films

Substrate	Location 1 (nm)	Location 2 (nm)	Location 3 (nm)	Average (nm)
SiO_2	220	235	220	225
Si	235	236	231	234
Pt	210	235	214	220
Al	235	236	225	232
Ta	232	225	240	232
Ti	239	246	220	235
In	210	233	243	229
Sn	230	246	210	229
Cu	231	243	228	234

Each Substrate was indented to assess their material properties before the Pt film was deposited. Twenty five indents were made to determine an average value. The deposited PT film was than indented on each substrate using 25 indents per each film/substrate combination.

11.3 Results and Discussions

The indentation results of the Pt film on the various substrates are given in Fig. 11.3. The solid circles are the average experimental data while the solid squares are the elastic modulus of the film as extracted by the Zhou and Prorok model. This was performed for each film-substrate combination with the results given in Table 11.4.

The method indicates that the film properties can be extracted reliably. Probably the more interesting result is how the pile-up and sink-in differed from substrate to substrate. Figure 11.4 gives scanning electron microscopy images of each indent for the 230 nm thick Pt film at a maximum indent depth of 500 nm, or well past the film thickness.

Each substrate yielded a different degree of sink-in for the Pt film which can be isolated to the change in film/substrate elastic modulus ratio. Furthermore in most cases, even though the indent depth was twice the film thickness the indent never punched through the film (SI substrate the exception). Instead, the substrate was often the more compliant of the two in yielded significantly causing s strong degree of sink-in. Case-in-point, it was noticed that the residual indention in the Pt-In surface was much smaller than that of the other materials, so another micrograph at 1,000 magnification was taken, Fig. 11.5. In this micrograph there is a visible halo of deformation that spreads out wider than the readily identifiable indention shown in Fig. 11.5a. It is believed that since the film is so much stiffer, that as the tip pushes down on the film, a larger area of the film than that just below the tip begins to push down on the substrate; as demonstrated in Fig. 11.5b, c. Shortly after the tip contacts the film's surface, the film's modulus as calculated through the Z-P model starts to rise toward its correct value, but once the previously mechanism becomes dominate, there is more plastic deformation than expected, allowing for less elastic recovery, so the film's modulus starts to drop toward that of the substrate as the substrate becomes the driving force for elastic recovery.

11.4 Conclusions

Instrumented indentation testing was used with the continuous stiffness method in order to evaluate nine different substrates, with the same film. Once deposited, the platinum film was evaluated through SEM and was found that surface quality and consistency were ideal for nanoindentation. The experimental data from indenting these samples was then compared to the model, and the associated extracted film's Young's modulus and Poisson's ratio to see to what degree they remain constant through indentation. The Zhou-Prorok model is adept at predicting substrate effect behavior for plastically deforming substrates, when sink-in is the dominating factor of erroneous contact area, not pile-up.

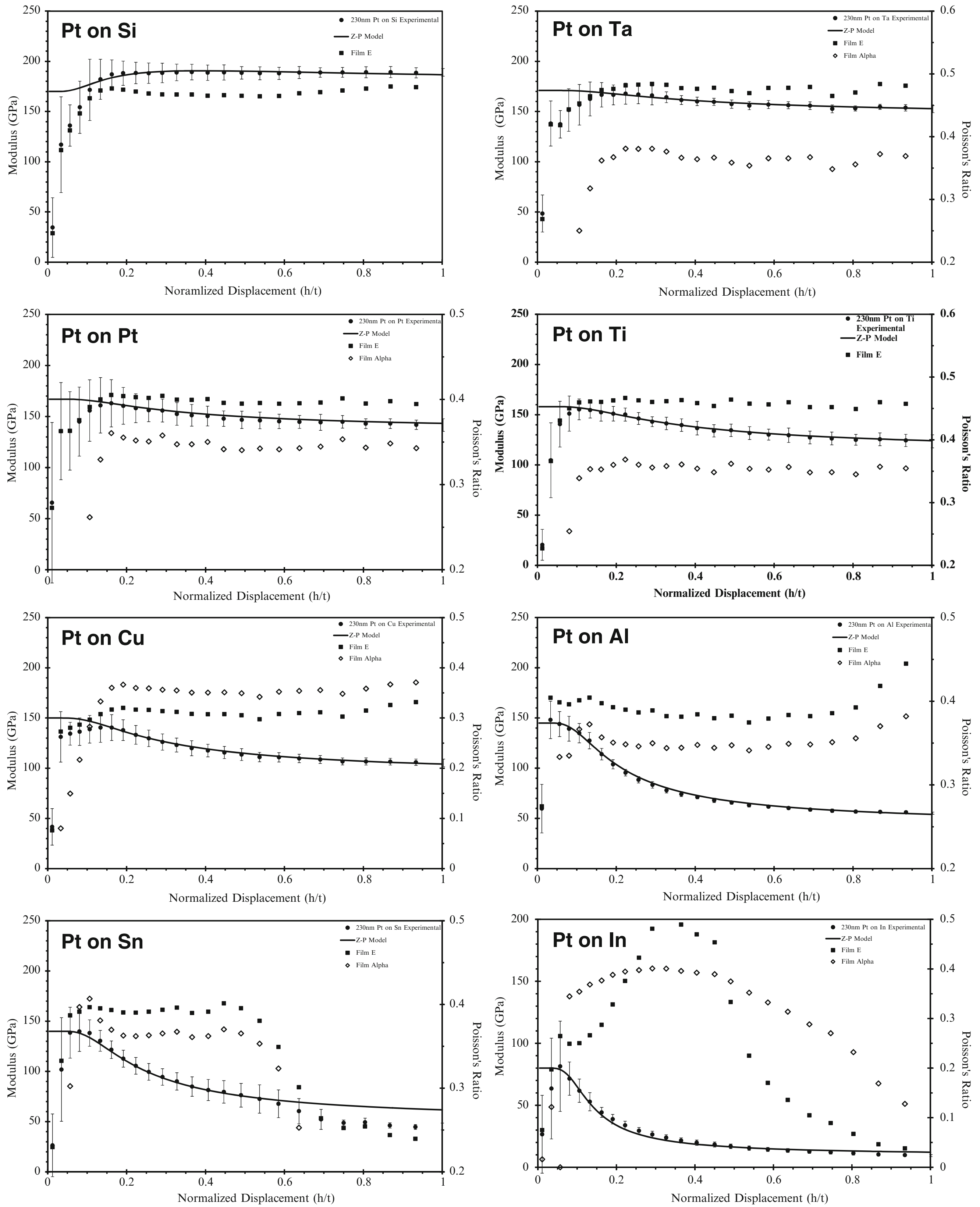

Fig. 11.3 Indentation results of a 230 nm Pt film on the substrates

Table 11.4 Determination of film properties on the various substrates

Substrate	$E'_{substrate}$	$\nu_{substrate}$	E'_{film}	ν_{film}
In	12	0.44	?	?
Sn	42	0.36	163 ± 5	0.36
Al	60	0.35	157 ± 7	0.35
Cu	100	0.35	158 ± 7	0.35
Ti	116	0.32	162 ± 2	0.35
Pt	168	0.36	167 ± 4	0.35
Ta	153	0.34	171 ± 7	0.36
Si	178	0.28	166 ± 2	0.36

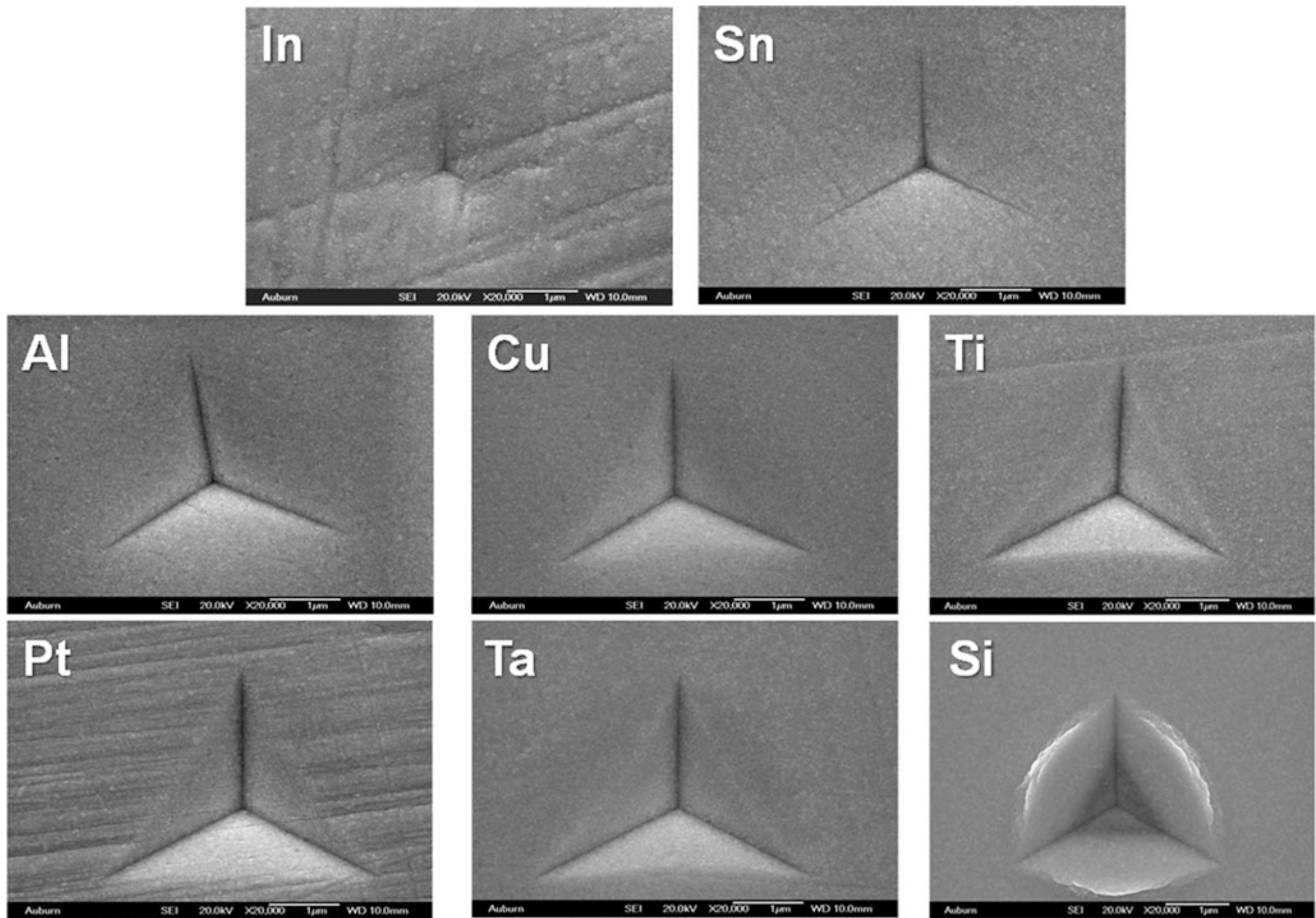

Fig. 11.4 Intents in the PT/substrate combinations for a 230 nm thick Pt film and a 500 nm maximum indent depth

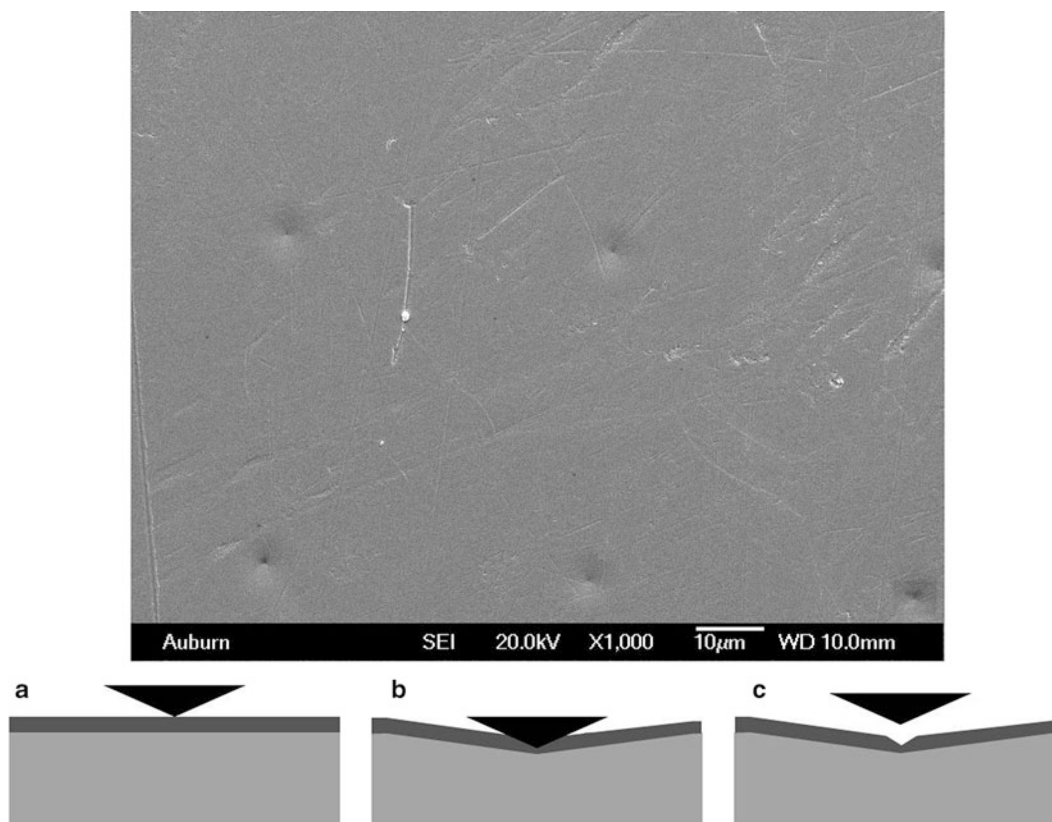

Fig. 11.5 Residual indents in an Pt/In film/substrate composite

References

1. Doerner MF, Nix WD (1986) A method for interpreting the data from depth-sensing indentation. J Mater Res 1:601–609
2. Hay J, Crawford B (2011) Measuring substrate-independent modulus of thin films. J Mater Res 26:727–738
3. King RB (1987) Elastic analysis of some punch problems for a layered medium. Int J Solid Struct 23:1657–1664
4. Pharr GM, Strader JH, Oliver WC (2009) Critical issues in making small-depth mechanical property measurements by nanoindentation with continuous stiffness measurement. J Mater Res 24:653–666
5. Saha R, Nix WD (2002) Effects of the substrate on the determination of thin film mechanical properties by nanoindentation. Acta Mater 50:23–38
6. Zhou B, Prorok BC (2009) A discontinuous elastic interface transfer model of thin film nanoindentation. Exp Mech 50:793–801
7. Zhou B, Prorok BC (2010) A new paradigm in thin film indentation. J Mater Res 25:1671–1678
8. McElhaney KW, Vlassak JJ, Nix WD (1998) Determination of indenter tip geometry and indentation contact area for depth-sensing indentation experiments. J Mater Res 13:7

Chapter 12
Mapping the Mechanical Properties of Alloyed Magnesium (AZ 61)

Jennifer Hay and Phillip Agee

Abstract In this work, an advanced form of nanoindentation is used to map the mechanical properties of AZ 61. The probed area includes both alpha (Mg-rich) and beta ($Al_{12}Mg_{17}$) phases. The measured moduli of the two phases compare well with expected values. The hardness of the beta phase is three times greater than that of the alpha phase. The hardness map reveals an area of intermediate hardness surrounding the beta phase. This zone is a mesophase which is chemically distinct and may influence the mechanical behavior of the alloy in unexpected ways.

Keywords Magnesium • Hardness • Elastic modulus • Mechanical-properties map • Mesophase

12.1 Introduction

Behind iron and aluminum, magnesium (Mg) is the third most common element used in engineered structures, because it is light-weight, stiff, and strong [1]. Alloying with aluminum can further improve stiffness and strength, although bulk mechanical properties depend strongly on chemical composition and thermo-mechanical history, insofar as these parameters affect microstructure. In this work, we use nanoindentation to determine the properties of individual phases within a popular magnesium alloy, AZ 61.

AZ 61 is a commercially available magnesium alloy which includes aluminum (nominally 6 %), zinc (nominally 1 %), and trace amounts of copper, silicon, and iron. The zinc and other trace elements have little effect on microstructure, and the Mg-Al phase diagram is employed to predict the constitution of slowly-cooled AZ 61 [2]. At 6 % Al, the Mg-Al phase diagram predicts the interaction of two phases: an α phase which is Mg-rich and a β phase comprising the intermetallic compound $Al_{12}Mg_{17}$. As the alloy cools from the liquid state, the α phase begins to solidify at about 620 °C. Solidification is complete at about 540 °C, and at this temperature, the material exists entirely in the α phase. Beginning around 300 °C, the β phase begins to precipitate and the mass fraction of this secondary phase continues to grow as the material continues to cool. At temperatures below 100 °C, the β phase accounts for about 15 % of the material [3].

In this work, we used nanoindentation to measure the elastic modulus and hardness of both phases of AZ 61. Our expectation is that the modulus for each phase should be close to that for the primary component. The primary component of the α phase is Mg, which has an elastic modulus of 45 GPa [1]; however, it should be remembered that at room temperature, the α phase includes 3 % of interstitial aluminum (by mass). Thus, we should not be surprised if the modulus of the α phase is slightly higher than 45 GPa. Zhang et al. calculated the elastic modulus of $Al_{12}Mg_{17}$ to be 78 GPa from first principles [4], so this value sets our expectations for the β phase of AZ 61.

In this work, we used an advanced form of nanoindentation called "Express Test" which performs one complete indentation cycle per second, including approach, contact detection, load, unload, and movement to the next indentation site [5]. This technology enabled us to quantitatively "map" both the elastic modulus (E) and the hardness (H) of a surface in a reasonable time. This feature is particularly beneficial for probing multi-phase metals such as AZ 61.

J. Hay (✉)
Agilent Technologies, Inc., Nano-Measurements Operation, 105 Meco Ln., Suite 200, Oak Ridge, TN 37830, United States
e-mail: jenny.hay@agilent.com

P. Agee
Agilent Technologies, Inc., Nano-Measurements Operation, 4330 West Chandler Blvd., Chandler, AZ 85226, United States

G. Shaw III et al. (eds.), *MEMS and Nanotechnology, Volume 5: Proceedings of the 2013 Annual Conference on Experimental and Applied Mechanics*, Conference Proceedings of the Society for Experimental Mechanics Series,
DOI 10.1007/978-3-319-00780-9_12, © The Society for Experimental Mechanics, Inc. 2014

12.2 Experimental Method

The sample of AZ 61 tested in this work was prepared by researchers at the Material Science and Engineering Department at Drexel University. AZ 61 chunks were purchased from Thixomat (Livonia, MI). The chunks were placed in alumina crucibles which were covered with alumina disks. Then the crucibles were placed in a vacuum furnace and were heated with a rate of 10 °C/min up to 750 °C and held for 1 h at the temperature after which the furnace was turned off and the samples were furnace cooled. To polish the surface, a section was cut from the sample, mounted, and rough ground with water using silicon carbide, beginning with 400-grit and finishing with 1,200-grit (US). The samples were polished using 6 and 1 μm diamond on a medium nap cloth with an alcohol-based extender.

Scanning electron microscopy was performed with the Agilent 8500 FE-SEM (Chandler, AZ). The prepared sample was fixed to an SEM stub with carbon tape and mounted onto the SEM sample stage. Imaging was performed with the slowest scan speed, in backscattered electron mode, with an accelerating voltage of 1 kV. The working distance was 2.2 mm.

All indentation testing was performed with an Agilent G200 NanoIndenter (Chandler, AZ) having Express Test, NanoVision, and a DCM II fitted with a Berkovich indenter. The test method "Express Test to a Force" was used to perform an array of 20 × 20 indents within a 50 × 50 μm area; thus, the separation between successive indents was about 2.5 μm (2,500 nm). The peak force for every indent was 4 mN; in the α phase, this force produced a peak displacement of about 380 nm; in the β phase, this force produced a peak displacement of about 240 nm. The total testing time for 400 indents was 15 min.

'Express Test' is the trade name for a specific option for the Agilent G200 NanoIndenter that allows rapid indentation. Although indents are performed rapidly (one per second), Young's modulus and hardness are obtained by analyzing the force-displacement data for each indentation according to established norms [6, 7]. Thus, these same measurements could be made by any commercially available instrument that conforms to ASTM E 2546–07 or ISO 14577 [8–11], although the required time would be much longer (on the order of hours, rather than minutes). To perform this work with another instrumented indentation system, the user would simply prescribe a similar array of 20 × 20 indents, each performed to a peak force of 4 mN, all within a 50 × 50 μm area.

12.3 Results and Discussion

The scanning-electron microscopic (SEM) image of Fig. 12.1 shows the microstructure of the AZ 61 surface as prepared for indentation. The α phase is darker and the precipitated β phase is lighter. From this image alone, one deduces that the β phase is harder, because scratches that span both phases are smaller in the β phase.

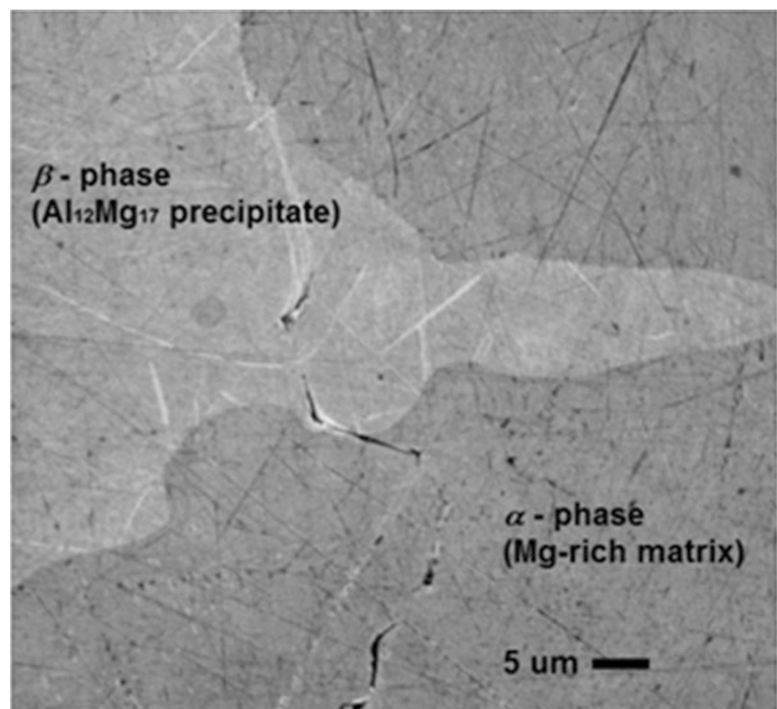

Fig. 12.1 Low-voltage, field-emission, scanning-electron-microscopy image of Mg AZ 61 as prepared for nanoindentation. Acquired in back-scattered electron (BSE) mode

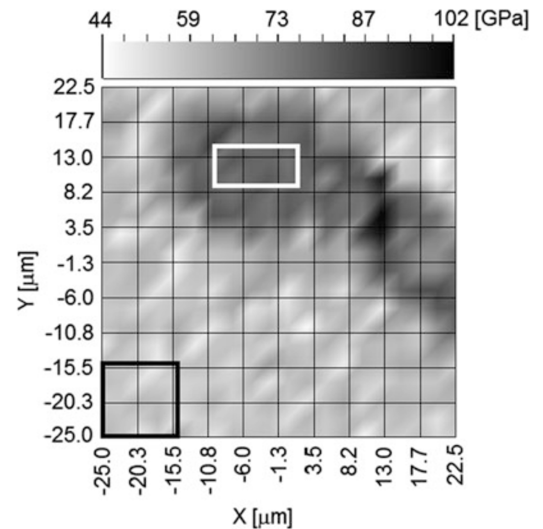

Fig. 12.2 Modulus map of two-phase Mg AZ 61. *Black rectangle* is in the primary α phase (Mg-rich). *White rectangle* is in the β phase ($Al_{12}Mg_{17}$). Image resolution is 20 × 20 pixels

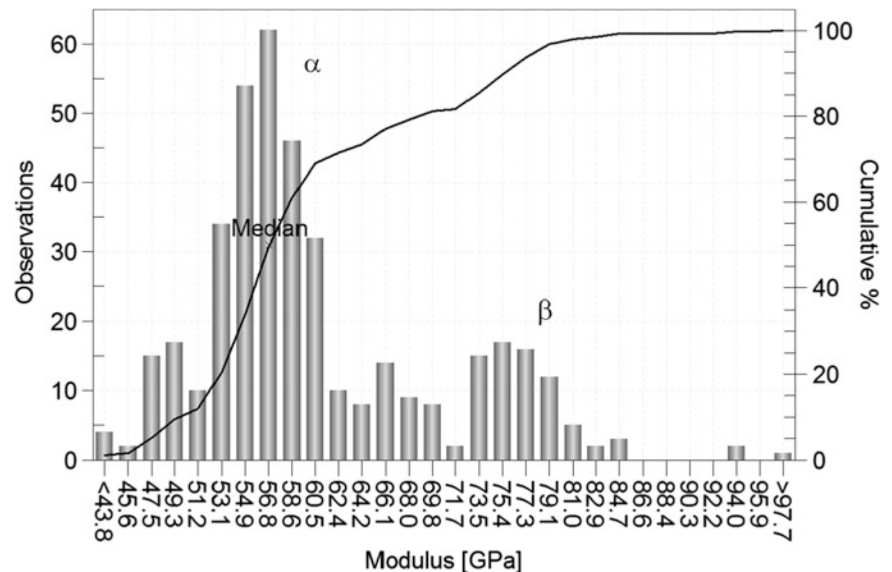

Fig. 12.3 Histogram of 400 modulus values

The indentation results are presented in Figs. 12.2, 12.3, 12.4 and 12.5. These four plots present results for the same 400 indents, but in various ways. Figure 12.2 is a map of elastic modulus (*E*); Fig. 12.3 presents the same modulus results, but in histogram form. Likewise, Fig. 12.4 is a map of hardness, and Fig. 12.5 presents the same hardness results, but in histogram form.

The mechanical-properties maps (Figs. 12.2 and 12.4) are 400-pixel (20 × 20) images, because each indentation generates the information content for one pixel. In order to calculate the properties of each phase independently, two rectangular domains were selected which were clearly in either one phase or the other. The rectangles in Figs. 12.2 and 12.4 identify these selected areas.

The black rectangles are in the primary α phase, which is the Mg with interstitial Al that constitutes about 92 % of the material. Within the area bound by the black rectangles, there are 25 indentations; the average elastic modulus for these indentations is $E = 54.9 \pm 3.3$ GPa, which is slightly higher than the modulus of pure Mg (45 GPa) [1]. The average hardness is $H = 1.35 \pm 0.05$ GPa.

The white rectangles are in the β phase, which is $Al_{12}Mg_{17}$. Within the area bound by the white rectangles, there are 15 indentations; the average elastic modulus for these indentations is 75.8 ± 3.3 GPa, which is consistent with the value predicted by Zhang (78 GPa) [4]. The average hardness is 4.3 ± 0.19 GPa, which is about three times greater than the hardness of the α phase. Table 12.1 summarizes the properties for each phase.

Surprisingly, the hardness image reveals a region around the β phase in which the hardness is lower than that of the β phase, but higher than that of the α phase. There are two reasonable explanations for this observation. First, the elevated

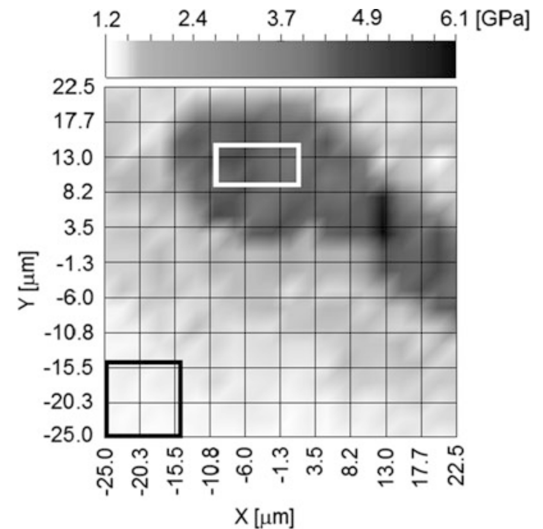

Fig. 12.4 Hardness map of two-phase Mg AZ 61. *Black rectangle* is in the primary α phase (Mg-rich). *White rectangle* is in the β phase ($Al_{12}Mg_{17}$). Image resolution is 20 × 20 pixels

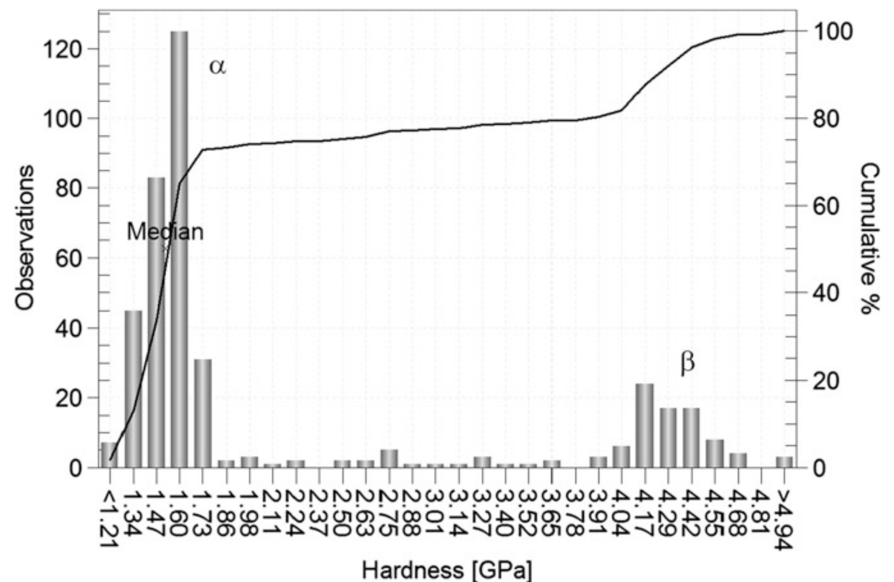

Fig. 12.5 Histogram of 400 hardness values

Table 12.1 Properties of magnesium AZ 61 constituents measured by nanoindentation at 4 mN

Material	N	*E* GPa	*H* GPa
α-phase (Mg-rich)	25	54.9[a] ± 3.3	1.35 ± 0.05
β-phase ($Al_{12}Mg_{17}$)	15	75.8[b] ± 3.3	4.30 ± 0.19

[a] *c.f.* the modulus of pure Mg (45 GPa) [1]
[b] *c.f.* the modulus of $Al_{12}Mg_{17}$ calculated by Zhang et al. (78 GPa) [4]

hardness of the material surrounding the β phase may be caused by (and reveal) α material immediately below the exposed surface. However, modulus is usually more sensitive to the influence of constraining material, and the modulus is uniform outside the β phase. It must be granted, however, that the difference in hardness between the two phases is much greater than the difference in modulus, so the hardness may manifest more constraint effect than modulus simply because there is a greater difference in hardness between the two phases.

The second (and more interesting) explanation is that the material around the β phase may be a true "mesophase" if it is chemically different than either α or β. More detailed analysis of the chemistry and microstructure of this region by means of energy dispersive x-ray spectroscopy (EDX), transmission electron spectroscopy (TEM), and focused-ion beam milling (FIB) may shed more light on this phenomenon.

12.4 Conclusions

In this work, the Express Test option for the Agilent G200 NanoIndenter was used to map out the mechanical properties of a magnesium alloy, AZ 61. The measured moduli of the α and β phases compared well with expected values. The hardness of the precipitate (β) phase was three times greater than that of the α phase. The hardness map revealed an area of intermediate hardness surrounding the β phase; more analysis is required to fully explain this phenomenon.

Acknowledgements The authors gratefully acknowledge Dr. Hamdallah Bearat of Arizona State University for the SEM images. The authors further acknowledge Mr. Babak Anasori and Dr. Michel Barsoum of the Materials Science and Engineering Department of Drexel University for providing the sample of AZ 61 tested in this work.

References

1. Magnesium. http://en.wikipedia.org/wiki/Magnesium. Accessed 9 July 2012
2. Fang C-f, Zhang X-g, Ji S-h, Jin J-z, Chang Y-b (2005) Microstructure and corrosion property of AZ61 magnesium alloy by electromagnetic stirring. Trans Non Ferrous Met Soc China 15(3):536–541
3. Shackelford JF (1988) Introduction to materials science for engineers, 2nd edn. Macmillan, New York
4. Zhang H, Shang SL, Wang Y, Saengdeejing A, Chen LQ, Liu ZK (2010) First-principles calculations of the elastic, phonon and thermodynamic properties of Al12Mg17. Acta Mater 58:4012–4018
5. Hay JL (2012) Revolutionary new agilent express test option for G200 nanoIndenters. http://cp.literature.agilent.com/litweb/pdf/5990-9948EN.pdf. Accessed 9 Apr 2012
6. Oliver WC, Pharr GM (1992) An improved technique for determining hardness and elastic-modulus using load and displacement sensing indentation experiments. J Mater Res 7(6):1564–1583
7. Hay JL (2009) Introduction to instrumented indentation testing. Exp Tech 33(6):66–72
8. ASTM E2546-07 (2007) Standard practice for instrumented indentation testing. http://www.astm.org/Standards/E2546.htm. Accessed 20 Mar 2013
9. ISO 14577–1:2002 (2002) Metallic materials – instrumented indentation test for hardness and material parameters – Part 1: test method. http://www.iso.org. Accessed 18 Nov 2004
10. ISO 14577–2:2002 (2002) Metallic materials – instrumented indentation test for hardness and material parameters – Part 2: verification and calibration of testing machines. http://www.iso.org. Accessed 18 Nov 2004
11. ISO 14577–3:2002 (2002) Metallic materials – instrumented indentation test for hardness and material parameters – Part 3: calibration of reference blocks. http://www.iso.org. Accessed 18 Nov 2004

Chapter 13
Temperature Dependent Micromechanical Testing on the Formation of Cu/Sn Intermetallic Thin Films

F.-C. Hsu, F.-C. Lu, C.-T. Huang, and M.-T. Lin

Abstract A temperature controlled tensile testing was performed to investigate the influence of external stress on the growth of an interfacial Cu-Sn IMC layer. The test specimens were prepared by depositing 25 μm layers of tin atop of copper substrate using electroplating. Samples were then clamped in a micromechanical testing apparatus integrated with a furnace. Experiments were carried out using load feedback control to provide constant load on the specimens with the stress level of 50, 100 and 150 MPa under constant temperature at 200 °C for 3–5 h annealing. Comparisons were made between samples undergoing stresses and those without stresses annealing. We observed the influence of stress levels and aging time on the formation of intermetallic compounds (IMC). Stress does influence the formation of Cu/Sn IMC. The thickness of IMC increased under stress. The growth rate of IMC was faster in stressed tin samples. Moreover, the formation of IMC micrographic structures under external stress differs considerably according to the level of stress.

Keywords Stress effect • Cu-Sn IMC • Tensile testing • Interdiffusion • High temperature tensile testing

13.1 Introduction

The fabrication of a dependable solder plays an important role in microelectronic packages due to its role on the interconnect joint of the microelectronic device packages. In practical, a microelectronics joint was generated from the formation of an inter-metallic compound at the interface between the solder and substrate materials such as Pb, Cu, Ag or Ni. Currently, the industry is facing an environmental demand for increased use of Pb-free solders [1]. Many of the leading solder alloy candidates for Pb-Sn solder replacement are based on the Sn -Cu system [2–4]. The primary concerns are the solderability and manufacturability using these Pb-free alloys. An understanding of reliability issues such as the microstructural evolution of a joint with time, temperature and stresses in as-prepared and aged joints has become an important need and the mechanical behaviors of Sn-based inter-metallics plays a significant role in determining the reliability of Pb-free solders [11–13].

In order to understand the stress effects on the solder reaction with Cu, especially during solid state aging, it is imperative to develop in-situ studies on the inter-metallic formation under stress. This study investigates the stress effect on the Sn-Cu interfacial reaction. Pure Cu plate was used as a sample substrate. Electroplated Sn film was deposited onto a Cu substrate as the sample [14, 15]. The sample was cut into a standard tensile specimen and placed inside a temperature controlled micro-tensile machine to exert tensile stress on the Sn-Cu films. The Sn-Cu interfacial reaction without the influence of stress was also studied as a reference for comparison.

F.-C. Hsu • F.-C. Lu • C.-T. Huang • M.-T. Lin (✉)
Graduate Institute of Precision Engineering, National Chung Hsing University, 250, Kuo-Kuang Rd., Taichung 40227, Taiwan, R.O.C.
e-mail: mingtlin@nchu.edu.tw

G. Shaw III et al. (eds.), *MEMS and Nanotechnology, Volume 5: Proceedings of the 2013 Annual Conference on Experimental and Applied Mechanics*, Conference Proceedings of the Society for Experimental Mechanics Series,
DOI 10.1007/978-3-319-00780-9_13, © The Society for Experimental Mechanics, Inc. 2014

13.2 Experimental Detail

The sample was fabricated on a conventional 99.99 microelectronics grade copper sheet with a thickness of 400 μm. After standard cleaning procedures, the samples exhibited uniformity prior to the experiments. Standard electroplating was used to deposit tin film on the copper substrate to a thickness of 25 μm. The samples were then cut into strips 90 mm in length and 5 mm in width.

The Hung Ta Instrument Co. HT-2402 tensile testing system was used with extensive modifications to make it suitable for elevated-temperature testing in the present study. The features of the testing system are detail in Figs. 13.1 and 13.2. As the primary goal was to investigate stress effect in intermetallic formation at elevated temperature, a major experimental concern was to limit thermal drift – and the associated thermally induced strains – in the system. To this end, the apparatus

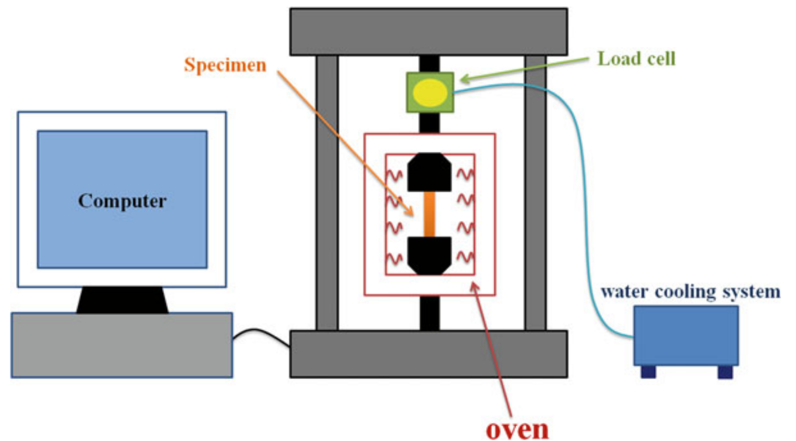

Fig. 13.1 Schematic view of the system

Fig. 13.2 Schematic image of the system

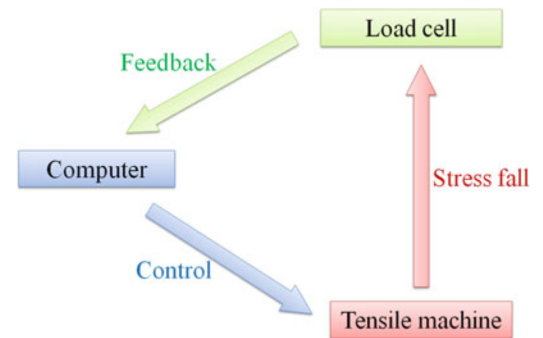

Fig. 13.3 Schematic of loading on a sample, it shows the feedback control of load if stress relaxation of the sample occurs during the experiment

Table 13.1 The parameters used to calculate stress values in the experiments

σ(MPa)	A(mm^2)	F(N)	Kgw
50	2.125	106.25	10.84
100	2.125	212.5	21.68
150	2.125	318.75	32.53

was mounted inside a temperature-controlled enclosure. This, and other features of the test system, made it possible to conduct elevated-temperature tests up to 200 °C with durations on the order of several days.

In preparation for mechanical testing, the samples were clamped into ceramic grips. The loading clamp was sufficiently aligned to accommodate four specimens simultaneously. Two unloaded control specimens were placed in close proximity to the loaded specimens in each run to account for variations in the experimental conditions from run to run. A typical test history involved constant strain rate straining to a predetermined stress level, a constant stress period duration with load feedback to eliminate stress relaxation effect, then constant strain unloading followed by a zero load hold period. Strain rates for the loading/unloading phases were 10 kgf/min.

In order to avoid creep or stress relaxation on the specimen, one program was executed to give tensile on the specimen by the actuator with constant load amplitude. At the same time, another program was performed to calculate the apparent stresses acquired from the data acquisition signals recorded from load cell to compare with the controlled stress signals and decided if it is necessary to adjust the actuator to maintain constant stress loading at all time (Fig. 13.3).

Test results were obtained for the same amounts of tensile stress with respect to the control. To apply greater stress effect on the Cu/Sn interface, we designed the experiment to provide stress values of 50, 100 and 150 MPa. Table 13.1 lists the parameters used to calculate stress values in the experiments.

After the samples were clamped, the furnace set to 200 °C was used to carry out the stressed aging procedure. Some samples were held without stress for as-soldered state testing. For the inter-metallic growth in this step, diffusion couples were annealed for times such that a copper-tin inter-metallic specimen could be formed. The annealing times were based on literature values for growth rates in diffusion couples [5, 6]. The diffusion process postulated in the literature [7] indicated that there are two major IMCs formed in Copper Tin annealing. Cu_6Sn_5 is formed through short time annealing and Cu_3Sn is formed through long time annealing.

Following aging, the samples were removed from the tensile testing system and mounted in epoxy resin for metallographical examination. The samples were ground and polished to expose cross-sections of the Sn/Cu interface. A high magnitude optical microscope was used to observe the formation of IMC at the Sn/Cu interface. Image processing was used to facilitate the measurement of areas in the cross-sections of the IMC resulting from the unevenness of the IMC layer along the interface and the linear length of the Cu/Sn interface. The thickness of IMC was determined by dividing the area by the linear length, as described in the literature [8, 9]. The reported thickness of the IMC is the average value of at least six measurements.

13.3 Results

Figure 13.4 shows optical micrographs of cross-sections of the Cu/Sn interface of sample after thermal aging at 200 °C for 72, 120 and 168 h with sample without stress, sample subjected to a 100 MPa tensile, sample subjected to a 150 MPa tensile stress. According to the elemental analysis results, two distinct phases were observed in all of the samples: the phase adjacent to the Cu side was identified as Cu_3Sn; the phase next to the Sn side was Cu_6Sn_5. This indicates that the applied

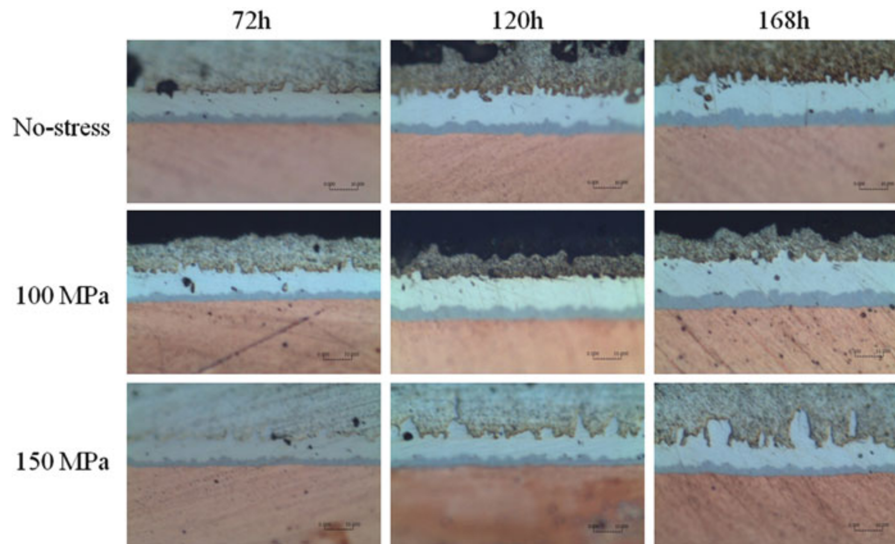

Fig. 13.4 Micrographs showing cross-sections of the Sn/Cu interface of sample after thermal aging at 200 °C for 72, 120 and 168 h with sample without stress, sample subjected to a 100 MPa tensile, sample subjected to a 150 MPa tensile stress

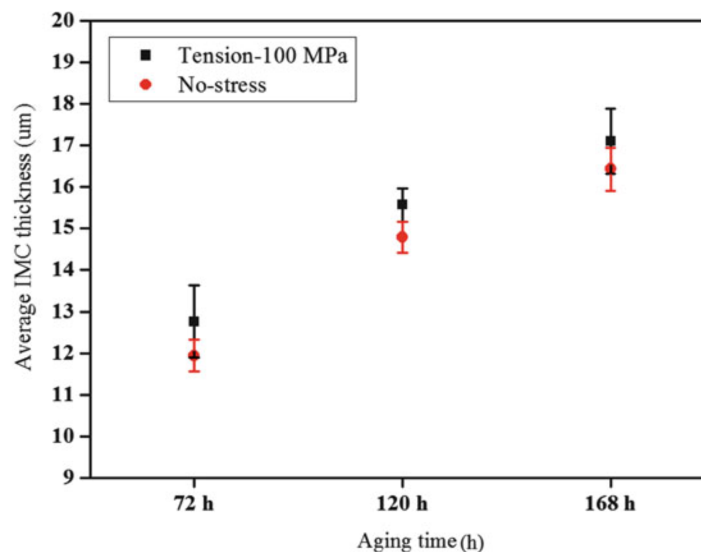

Fig. 13.5 Total thickness of Sn/Cu IMC sample versus aging times for stress of 100 MPa tensile and unloaded control

external stress, regardless of whether the stress state, had no influence on either type of IMC. However, the growth rates of IMC ($Cu_3Sn + Cu_6Sn_5$) were influenced by the applied stress. The thickness of the IMC film ($Cu_3Sn + Cu_6Sn_5$) differed among each of the cases. For example, the results of total thickness of IMC after thermal aging at 200 °C for 72 h under 100 MPa tension (12.77 μm) was thicker than in the sample with no stress (11.95 μm). The no stress samples in Fig. 13.4 show common scallops in the structure of the IMC while the sample under high stress (150 MPa) reveals considerable distortion. The samples submitted to high stress contain a large number of islands of needle-like columnar Cu/Sn IMC enclosed by continuous large planar Cu/Sn IMC.

Figure 13.5 shows the total thickness of the Sn/Cu IMC as a function of aging time at 200 °C under film stress of 100 MPa and unloaded. Table 13.2 summarizes the thickness of Sn/Cu IMC under all test conditions. The growth rate of the Sn/Cu IMC exhibited characteristics that under tension grew at a rate higher than that with no stress. Figure 13.6 shows the total thickness of Sn/Cu IMC as a function of aging time at 200 °C under film stress of 150 MPa and unloaded. The growth rate of the Sn/Cu exhibited characteristics similar to those observed in Fig. 13.5, in which the Sn/Cu IMC under tension grew more rapidly than in samples without stress. This indicates that tensile stress enhances the growth of the Sn/Cu IMC. In addition,

Table 13.2 Sn/Cu IMC thickness as s function of annealing time under tensile stress conditions (unit: μm)

Stress(MPa) \ Time(h)	72h	120h	168h
No-stress	11.945±0.383	14.782±0.378	16.425±0.517
100 MPa	12.766±0.86	15.559±0.407	17.102±0.779
150 MPa	13.787±0.631	16.033±0.407	18.816±0.577

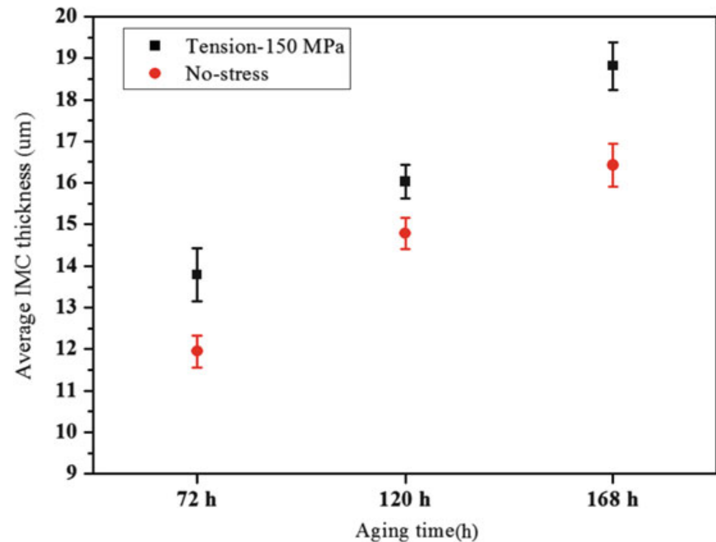

Fig. 13.6 Total thickness of Sn/Cu IMC sample versus aging times for stress of 150 MPa tensile and unloaded control

the overall IMC growth rates under higher stress samples exceed those of lower stress samples. Figure 13.7 illustrates the thickness of IMC samples as a function of film stress after thermal aging at 200 °C for 72 h. The error bars shown for each point indicate the minimum and maximum observed increase. The data points indicate mean values.

In almost every sample, tensile stress influenced the growth of Sn/Cu IMC. Interestingly, the enhancement of growth in IMCs is strong related with the increase of tensile stress. In the following, we discuss the diffusion behavior of components in the Sn/Cu interfacial reaction to gain a deeper understanding of the influence of external stress on IMC growth. During the isothermal aging of Cu and Sn films, Cu diffuses interstitially into Sn, leading to the assumption that Cu diffusion into Sn is the dominant process. Therefore, Cu is thought to be the faster diffusing species in Sn/Cu interfacial reactions [7, 10], and the growth of the Cu-Sn IMCs depends primarily upon Cu diffusion into Sn. Two major driving forces are involved in the diffusion behavior in the Sn/Cu interfacial reaction in the tested samples: (1) the typical concentration gradient and (2) the stress gradient. For samples without stress, the diffusion of Cu into Sn is driven only by the concentration gradient.

Because the participation of even higher stress in tin samples can create voids or defects in the solder matrix, it is not surprising to observe more distorted needle-like columnar islands in the samples under stress. The large number of distorted columnar islands in the samples under 150 MPa (Fig. 13.4) reveals that increased stress could be the driving force behind the outward diffusion of Cu into the solder. We observed this micrographic structure in the interfacial reaction of Sn/Cu samples subjected to a higher tensile stress. This leads us to believe that could create an inhomogeneous local strain field through the formation of voids or defects in the solder matrix. This phenomenon could be amplified through the application of external stress. As a result, we observed distorted needle-like columnar islands in the Cu/Sn IMC. Thus the diffusivity of Cu was increased since Cu diffusion in the tin lattice under tension was facilitated. As a result, the growth rate of IMC was also enhanced.

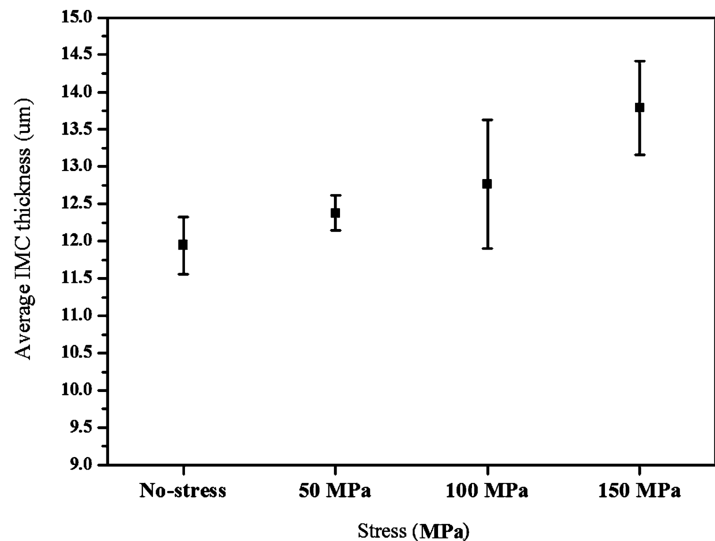

Fig. 13.7 Total thickness of Sn/Cu IMC sample versus stress of 50, 100 and 150 MPa after thermal aging at 200 °C for 72 h

13.4 Conclusions

In this paper, we reported on a temperature controlled micro-tensile measurement results of the stress effect related to interfacial Cu-Sn IMC layer growth. The proposed method allows interfacial Cu-Sn IMC layer growth observation under tension. The results indicated that tensile stress would affect Cu-Sn inter-metallic formation. We observed the influence of stress levels and aging time on the formation of intermetallic compounds (IMC). Stress does influence the formation of Cu/Sn IMC. The thickness of IMC increased under stress. The growth rate of IMC was faster in stressed tin samples. Moreover, the formation of IMC micrographic structures under external stress differs considerably according to the level of stress. The enhanced effect caused by the larger stress was somewhat more severe than that due to smaller tensile stress. We hypothesize that the observed IMC thickness increase is related to stress enhanced out-diffusion of Cu towards the solder and strain in the lattice at the diffusion interface.

References

1. Tu KN (1973) Interdiffusion and reaction in bimetallic Cu-Sn thin films. Acta Metall 21:347–354
2. Rymaszewski EJ, Tummala RR, Watari T (1997) Microelectronic packaging handbook, Part I, 2nd edn. Chapman and Hall, Springer US
3. Harper CA (2005) Electronic packaging and interconnection handbook. McGraw-Hill, New York
4. Zarrow P (1999) On the forefront: lead free: don't fight a fact, deal with it! Circ Assem 10:18–20
5. http://www.tycoelectronics.com/customersupport/rohssupportcenter/pdf/2010_CALCE_Tin_Whsker_Conference_TE.pdf
6. Snog JY, Jin Yu, Lee TY (2004) Effects of reactive diffusion on stress evolution in Cu–Sn films. Scripta Meterialia 51:167–170
7. Ngoh SL, Zhou1 W, Pang1 HL, Spowage AC, Shi XQ (2004) Effect of stress on interfacial intermetallic compound development of Sn-Ag-Cu Lead-free solder joint on Au/Ni/Cu substrate. Electronics packaging technology conference, Singapore
8. King-Ning Tu (2007) Solder joint technology. Springer, New York
9. http://www.tycoelectronics.com/customersupport/rohssupportcenter/pdf/tyco_electronics_hilty_ipc_Boston_2005.pdf
10. Huh JY, Moon SJ (2000) Effect of elastic stresses on solid-state amorphization of Zr/Co multilayers. Thin Solid Films 377–378:611–616
11. Mulugeta Abtew, Selvaduray G (2000) Lead-free solder in microelectronics. Mater Sci Eng 27:95–141
12. Daniel L, Wong CP (2009) Material for advanced packaging. Springer, New York
13. Görlich J, Schmitz G, Tu KN (2005) On the mechanism of the binary Cu/Sn solder reaction. J Appl Phys Lett 86:053106-1–053106-3
14. Kakeshita T, Shimizu K, Kawanaka R et al (1982) Grain size effect of electro-plated tin coatings on whisker growth. J Mater Sci 17:2560–2566
15. Lee Z, Lee DN (1998) Spontaneous growth mechanism of tin whisker. Acta Metal 46:3701–3714

Chapter 14
Molecular Interactions on $In_xGa_{1-x}N$

L.E. Bain, A.M. Hosalli, S.M. Bedair, T. Paskova, and A. Ivanisevic

Abstract Atomic force microscopy in solution offers a platform for assessing interactions on chemically modified surfaces. In this study a biologically relevant molecule, an amino acid, is adsorbed onto a compositionally varied semiconductor substrate. AFM is used to assess the effect of the substrate composition on the adhesion of the amino acid. We report adsorption of L-arginine to an indium-gallium-nitride (InGaN) substrate with a gradient of In:Ga composition. Data are collected above and below the isoelectric point of arginine to highlight the effect of protonation on the adhesive behavior across the InGaN. Characterization is also performed using X-ray photoelectron spectroscopy to establish the presence of amino acid on the surface and determine the general composition of a given region of the substrate both with and without amino acid. Combining these factors, we are able to better evaluate the significance of substrate properties in influencing the behavior of surface molecules. Determining the dynamics of amino acid behavior as a function of both the substrate and the environment provides new insight into the preparation of semiconductor materials for biological applications.

Keywords Amino acids • Atomic force microscopy • Composition gradient • Indium gallium nitride • X-ray photoelectron spectroscopy

14.1 Introduction

III-nitride semiconductors have drawn attention as candidates for multiple microelectronic applications due to their optical and electronic characteristics [1, 2]. GaN and GaN-based heterostructures have been of particular interest due to their noted biocompatibility and chemical stability [3, 4], while InN is of note due to its narrower band gap and high electron mobility for a III-V material [1, 5]. Ternary III-N materials also offer the advantage of a more tunable band gap by varying the elemental composition of the overall material [6]. These factors all suggest the potential of indium gallium nitride as a

L.E. Bain (✉)
UNC/NCSU Joint Department of Biomedical Engineering, NC State University, 911 Partners Way, Engineering Building 1, Raleigh, NC 27606, USA
e-mail: lebain@ncsu.edu

A.M. Hosalli • S.M. Bedair
Department of Electrical and Computer Engineering, NC State University, 911 Partners Way, Engineering Building 1, Raleigh, NC 27606, USA

T. Paskova
Department of Electrical and Computer Engineering, NC State University, 911 Partners Way, Engineering Building 1, Raleigh, NC 27606, USA

Department of Materials Science and Engineering, NC State University, 911 Partners Way, Engineering Building 1, Raleigh, NC 27606, USA

A. Ivanisevic
UNC/NCSU Joint Department of Biomedical Engineering, NC State University, 911 Partners Way, Engineering Building 1, Raleigh, NC 27606, USA

Department of Materials Science and Engineering, NC State University, 911 Partners Way, Engineering Building 1, Raleigh, NC 27606, USA

G. Shaw III et al. (eds.), *MEMS and Nanotechnology, Volume 5: Proceedings of the 2013 Annual Conference on Experimental and Applied Mechanics*, Conference Proceedings of the Society for Experimental Mechanics Series,
DOI 10.1007/978-3-319-00780-9_14, © The Society for Experimental Mechanics, Inc. 2014

candidate for designing chemical sensors and blue-violet LEDs. The band gap of the material may be tuned from the near-ultraviolet to near-infrared region by varying the ratio of indium to gallium, an effect that also produces a change in the optical properties of the substrate [2, 6].

In designing functional chemical interfaces, it is critical to have a sound understanding of surface chemistry and the interactions between the surface and environment [7–10]. This is of particular importance in developing biological interfaces, as the environment in biofluids is complex and consists of a wide variety of molecular species [11]. It is thus of interest to characterize the surface interactions between the inorganic materials and different molecules to better assess potential applications of different interfaces. While band gap tuning by varying material composition can be used to optimize a device for a specific application, it is vital to characterize how compositional changes influence the interactions between the semiconductor and its environment. Topography and surface chemistry can both play a significant role in dictating how these chemical interactions take place.

In this study we report the adhesive behavior of an amino acid (L-arginine) as a function of both amine group protonation and elemental composition of the underlying substrate. Emission band positions in PL spectra recorded at different spots were used to evaluate the In composition variation. Characterization techniques used to assess and evaluate the changes in amino acid adhesion include atomic force microscopy (AFM) in solution, and X-ray photoelectron spectroscopy (XPS.) The data presented suggest a change in adhesive behavior at different points on the substrate as well as a variation in arginine adsorption at different experimental conditions.

14.2 Experimental

Phosphate buffered saline (PBS) tablets, methanol, acetone, 37 % hydrochloric acid, and L-arginine were purchased from Sigma-Aldrich and used as received. PBS was prepared as instructed on the label, with one tablet producing 200 mL PBS.

14.2.1 $In_xGa_{1-x}N$

Thin InGaN film was grown by metal organic chemical vapor deposition (MOCVD) technique on a sapphire substrate. Conventional growth at 350 mtorr was performed using a low-temperature GaN buffer layer of about 100 nm thickness grown at 475 °C. Trimethylgallium (TMGa) and trimethylindium (TMIn) were used as III-group sources. Specific holder design and rotation variations were employed in order to achieve variable In concentration over the sample surface.

14.2.2 *Photoluminescence*

Photoluminescence (PL) measurements were carried out at room temperature with 325 nm excitation from cw He-Cd laser. The spectra were recorded with a 0.5 m monochromator, photomultiplier tube and standard lock-in amplifier technique in 350–650 nm spectral range.

14.2.3 *Surface Preparation*

The $In_xGa_{1-x}N$ was cleaved into several sections using a diamond scribe. Between each experiment, sections were sonicated in acetone, ethanol, and deionized water for 5 min, following by drying with nitrogen gas (N_2.) Following amino acid or PBS experiments, a 10 min soak in 80 °C deionized water was used to remove salt and amino acid from the surface. Subsequent removal of surface oxide included a 10 min etch in 37 % HCl. After this etch, samples were rinsed 3× with deionized water and dried with N_2. Samples were incubated in 1 mM amino acid in PBS of pH 6 (protonated) or pH 12 (non-protonated) overnight for experiments. Prior to analysis, samples were dried with N_2 gas.

14.2.4 AFM

Data were collected using the Asylum Research Cypher scanning probe microscope with Asylum silicon nitride probes (Model # TR800PSA.) Samples were mounted on AFM pucks using non-water soluble Crystalbond 509–3 adhesive (Ted Pella) to avoid adhesive dissolution and deposition on the surfaces during imaging in solution. For imaging in solution, sufficient pH-adjusted PBS (200–250 μL) was placed on the sample to avoid any droplet effects. $5 \times 5\ \mu m^2$ topography images were collected at representative points for each region of the substrate. Data analysis was performed using *Igor Pro* software. Force maps in solution were acquired using the same solution conditions. A 64×64 point map across a $1 \times 1\ \mu m^2$ area was constructed.

14.2.5 XPS

XPS data were collected using a Kratos Analytical Axis Ultra using a monochromated Al Kα source. High resolution spectra of Ga 2p and 3d, O 1 s, C 1 s, N 1 s, In 3d, and S 2p were collected at a 0° photoemission angle with a 20 eV pass energy. Survey scans (0–1200 eV) were also performed at 0° with pass energy 160 eV. Data analysis was performed using CasaXPS software, version 2.3.16. Charge shift was calibrated to the C 1 s peak (284.8 eV.) Peak fitting was performed using a summed Gaussian and Lorentzian shape with a subtracted Shirley background. The presented data were normalized prior to plotting to aid in visual comparison of the spectra and constituent peaks.

14.3 Results and Discussion

$In_xGa_{1-x}N$ features an optical gradient across the substrate as the ratio of In:Ga increases. While the gradient is a continuous feature, for ease of experiment repeatability distinct regions within the substrate have been designated. As seen in the schematic representation in Fig. 14.1a, “High In:Ga,” “Mid-High In:Ga,” “Mid-Low In:Ga,” and “Low In:Ga” regions have been designated. The variation of In:Ga ratio was confirmed by the shift of the emission band in the PL spectra recorded in four different regions across the sample surface of the InGaN layer (Fig. 14.2). According to In composition dependence of the band gap energy in the InGaN alloys with bowing parameter of 1.51 [12], we calculated the In composition in the different spots to vary from 29.2 % to 31.1 %. The sample dicing is also illustrated in Fig. 14.1a, indicating that the full range of accessible In:Ga ratios was included in both XPS and AFM data acquisition. Figure 14.1b illustrates the change in

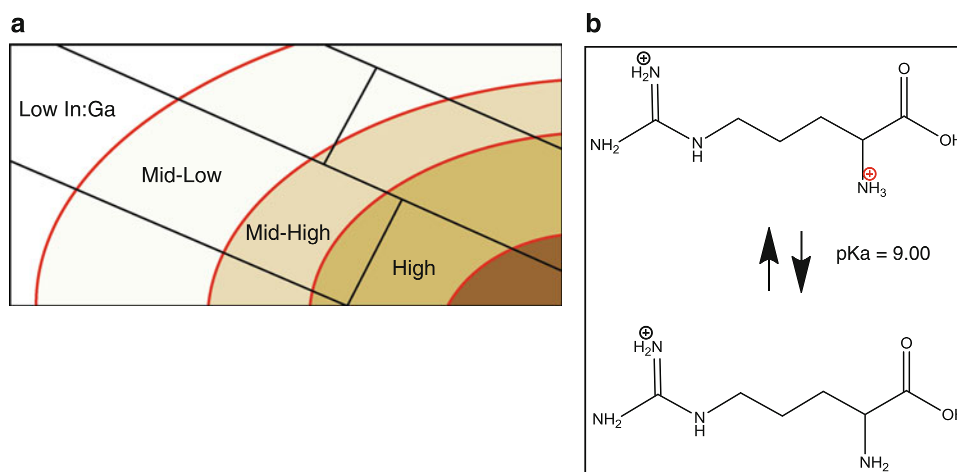

Fig. 14.1 (**a**) Schematic representation of InxGa1-xN substrate. Indium composition increases from top left to bottom right, producing a visible change in substrate hue and opacity. *Red lines* designate sample ‘regions,’ while *black lines* represent sample dicing. (**b**) Deprotonation of L-arginine occurs at pH = 9. At pH 6, the arginine population is predominantly protonated (*top* species); at pH 12, the population is largely deprotonated (*bottom*)

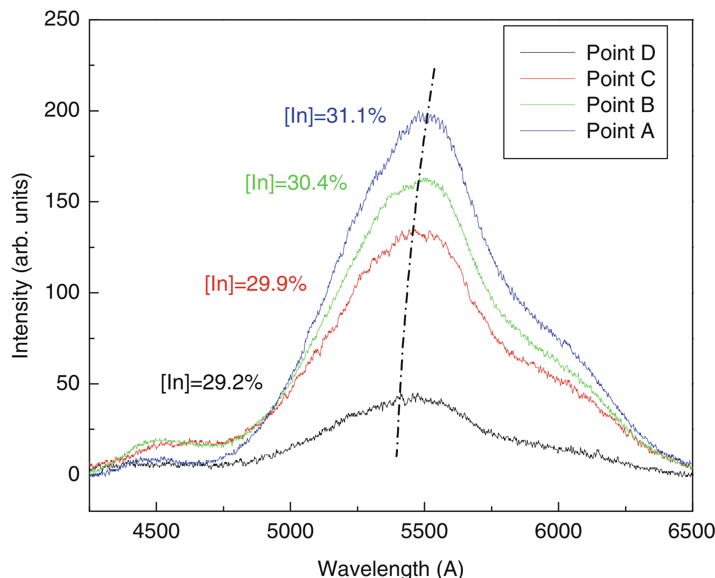

Fig. 14.2 Room temperature PL spectra recorded at four spots across the sample surface, showing a shift of the InGaN emission position

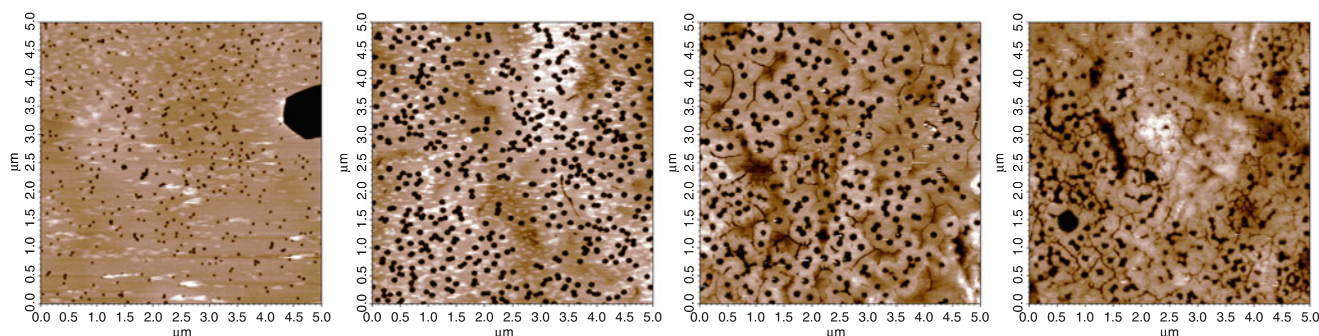

Fig. 14.3 Changes in topography as a function of substrate composition. The ratio of In:Ga increases from a through d, illustrating standard topographies in the low through high substrate regions. The hexagonal surface pits are indicative of defects in the underlying crystal lattice, and generally increase in size and decrease in density as the relative quantity of In is increased. (**a**) Features an abnormally large defect on the *right side* of the image; however, the *hexagonal outline* suggests that this is still crystallographic in nature. All images are 5 × 5 µm

arginine protonation as a function of pH. The pKa for the α-amine group is 9.00, while the pKa of the carboxyl group is 2.03 and the pKa of the guanidium cap is 12.10. Thus, the only significant chemical change expected between the pH 6 and pH 12 experiments is protonation of the α-amine.

Surface topography varies significantly as a function of elemental composition, as illustrated in Fig. 14.3. Previous studies have attributed surface defects to arise due to both threading and screw dislocations in $In_xGa_{1-x}N$ composites [13]. These hexagonal defects demonstrate the underlying wurtzite crystalline structure of the $In_xGa_{1-x}N$. The crystallographic pits vary in size and density as the material composition changes. This is particularly evident in the transition from the low In:Ga region to the mid-low In:Ga region. The diameter of the hexagonal pits increases with an increase in In, while pit density decreases. Further crystallographic surface features arise as In continues to increase, including the apparent formation of hexagonal 'leaves' (seen in Fig. 14.3c and d).

Following the adsorption of amino acid to the surface, a force-volume map was acquired to illustrate the surface structure and accompanying adhesion force of amino acid on the surface. Figure 14.4 provides the surface topography and corresponding force map. The crystallographic pits are still evident, as are the presence of white "clumps" of adsorbed arginine on the surface. White circles are used to illustrate the presence of increased adhesion at the arginine locations. While this change in adhesion is evident, the variation in arginine clustering is an interesting phenomenon paralleling that reported for adhesion of peptides to other semiconductor surfaces [14].

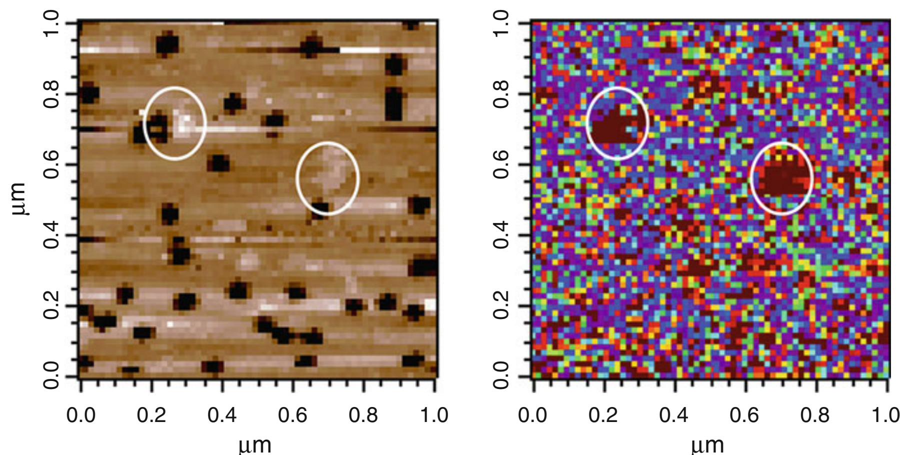

Fig. 14.4 Topography (*left*) and adhesion force map (*right*) of the low In:Ga region with pH 6 arginine. *White circles* highlight clumps of amino acid and the increased adhesion at these sites. Adhesion on the substrate surrounding arginine clusters is highly variable; however, adhesion is more consistent over these large clusters

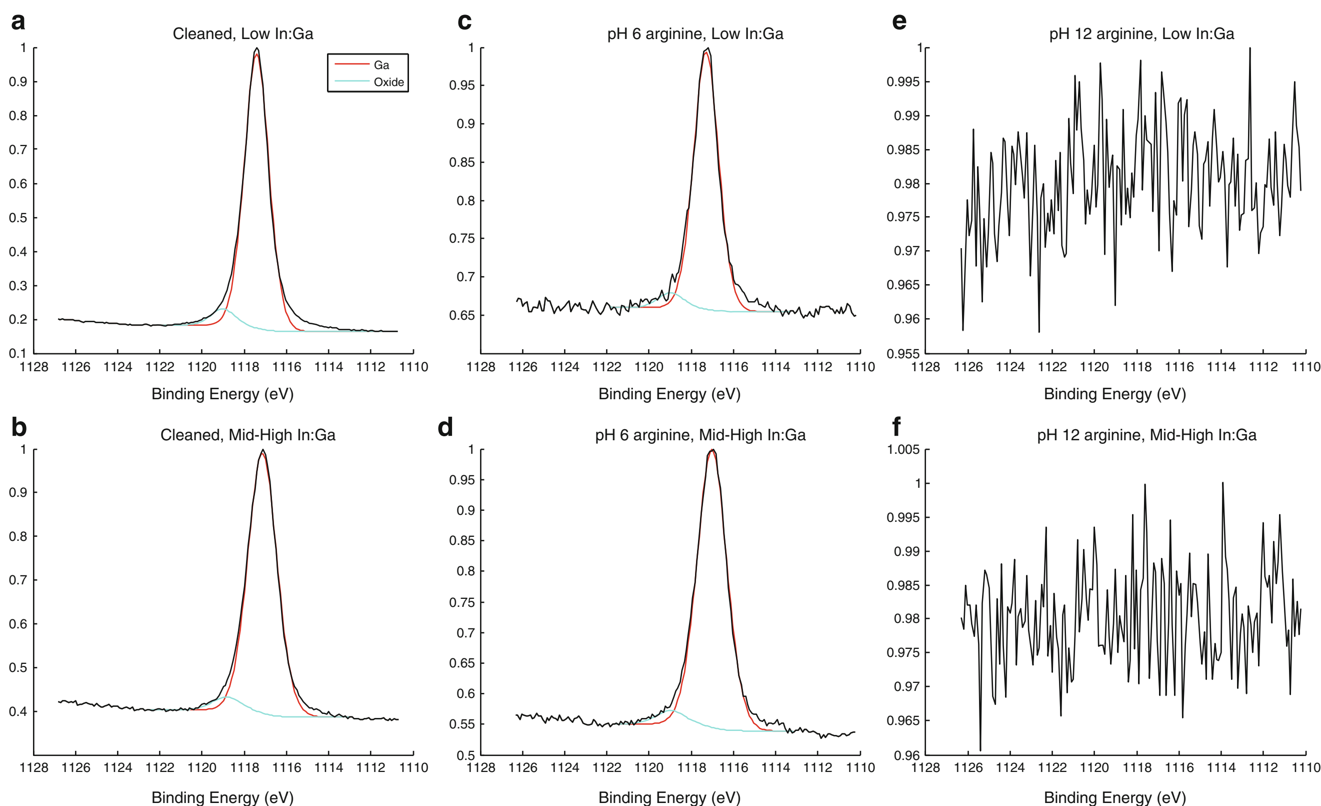

Fig. 14.5 Normalized Ga 2p XPS spectra for (**a-b**) cleaned, (**c-d**) pH 6 arginine, and (**e-f**) pH 12 arginine surface preparations. Low In:Ga regions (**a, c, e**) and high In:Ga regions (**b, d, f**) feature comparable surface characteristics at pH 6 and cleaned preparations, but the addition of arginine reduces the signal:noise ratio, and the drop in oxide contribution could be attributed to occlusion by the binding of positively charged arginine. Most notably, the pH 12 arginine case has no apparent peak, suggesting that the surface arginine multilayer is sufficient to prevent x-rays from reaching the substrate

Previously, clustering has been attributed to the interaction of polar side-chains with a polar semiconductor surface [14]. To better illustrate the relationship between charge effects and cluster formation, we acquired XPS data for substrates prepared above and below the protonation point of the α-amine on arginine. Ga 2p spectra are presented in Fig. 14.5, illustrating the relative contribution of gallium oxide. Table 14.1 summarizes data on the relative presence of indium,

Table 14.1 Surface atomic ratios of In, O, and C to Ga for different substrate locations and conditions

	Cleaned		pH 6 L-arginine	
Surface atomic ratio to Ga	High In:Ga	Low In:Ga	High In:Ga	Low In:Ga
In	0.34	0.08	0.43	0.17
O	0.39	0.30	3.62	30.67
C	1.61	0.60	2.61	15.27

oxygen, and carbon on the cleaned and pH 6 L-arginine surfaces, taken with respect to gallium composition. In this analysis, the Ga 2p spectrum at pH 12 is significant – the Ga peak is absent, indicating that surface species were present in sufficient volume to completely occlude the signal from the underlying substrate species. This suggests that there is a significant change in arginine behavior when in the deprotonated state, particularly in interactions with the underlying $In_xGa_{1-x}N$.

14.4 Conclusions

We find that adsorption of arginine to compositionally varied $In_xGa_{1-x}N$ yields clusters of amino acid on the surface rather than monolayer coverage. In addition the adhesion force of these clusters on a silicon nitride probe tip differs from the surrounding substrate. XPS confirms the presence of differing oxide levels at different positions on the substrate, as well as significant accumulation of arginine when adsorbed at pH 12. Thus, adsorption and adhesive behavior is shown to vary at different points on the $In_xGa_{1-x}N$ gradient substrate.

References

1. Davis RF (1991) III-V nitrides for electronic and optoelectronic applications. Proc IEEE 79(5):702–712
2. Ponce FA, Bour DP (1997) Nitride-based semiconductors for blue and green light-emitting devices. Nature 386:351–359
3. Jewett SA, Makowski MS, Andrews B, Manfra MJ, Ivanisevic A (2012) Gallium nitride is biocompatible and non-toxic before and after functionalization with peptides. Acta Biomater 8:728–733
4. Gupta S, Elias M, Wen X, Shapiro J, Brillson L, Lu W, Lee SC (2008) Detection of clinically relevant levels of protein analyte under physiologic buffer using planar field effect transistors. Biosens Bioelectron 24(4):505–511
5. Chin VWL, Tansley TL, Osotchan T (1994) Electron mobilities in gallium indium, and aluminum nitrides. J Appl Phys 75(11):7365–7372
6. Kuykendall T, Ulrich P, Aloni S, Yang P (2007) Complete composition tenability of InGaN nanowires using a combinatorial approach. Nat Mater 6:951–956
7. Cimalla I, Will F, Tonisch K, Niebelschütz M, Cimalla V, Lebedev V, Kittler G, Himmerlich M, Krischok S, Schaefer JA, Gebinoga M, Schober A, Friedrich T, Ambacher O (2007) AlGaN/GaN biosensor – effect of device processing steps on the surface properties and biocompatibility. Sens Actuators B 123:740–748
8. Chaniotakis N, Sofikiti N (2008) Novel semiconductor materials for the development of chemical sensors and biosensors: a review. Anal Chim Acta 615:1–9
9. Slavin JWJ, Jarori U, Zemlyanov D, Ivanisevic A (2009) Characterization of amino acid adlayers on InAs surfaces using X-ray photoelectron spectroscopy. J Electron Spectrosc Relat Phenom 172:47–53
10. Slavin JWJ, Zemlyanov D, Ivanisevic A (2009) Adsorption of amino acids on indium arsenide (100) surfaces: assessment of passivation capabilities. Surf Sci 603:907–911
11. Makowski MS, Ivanisevic A (2001) Molecular analysis of blood with micro-/nanoscale field-effect-transistor biosensors. Small 7(14): 1863–1875
12. César M, Ke Y, Ji W, Guo H, Mi Z (2011) Band gap of $In_xGa_{1-x}N$: a first principles analysis. Appl Phys Lett 98:202107–202109
13. Chen Z, Su LW, Shi JY, Wang XL, Tang CL, Gao P (2012) AFM application in III-nitride materials and devices. In Bellitto V (ed) Atomic force microscopy – imaging, measuring, and manipulating surfaces at the atomic scale. InTech, pp 189–208
14. Goede K, Grundmann M, Holland-Nell K, Beck-Sickinger AG (2006) Cluster properties of peptides on (100) semiconductor surfaces. Langmuir 22:8104–8108

Chapter 15
Timoshenko Beam Model for Lateral Vibration of Liquid-Phase Microcantilever-Based Sensors

Joshua A. Schultz, Stephen M. Heinrich, Fabien Josse, Isabelle Dufour, Nicholas J. Nigro, Luke A. Beardslee, and Oliver Brand

Abstract Dynamic-mode microcantilever-based devices are potentially well suited to biological and chemical sensing applications. However, when these applications involve liquid-phase detection, fluid-induced dissipative forces can significantly impair device performance. Recent experimental and analytical research has shown that higher in-fluid quality factors (Q) are achieved by exciting microcantilevers in the lateral flexural mode. However, experimental results show that, for microcantilevers having larger width-to-length ratios, the behaviors predicted by current analytical models differ from measurements. To more accurately model microcantilever resonant behavior in viscous fluids and to improve understanding of lateral-mode sensor performance, a new analytical model is developed, incorporating both viscous fluid effects and "Timoshenko beam" effects (shear deformation and rotatory inertia). Beam response is examined for two harmonic load types that simulate current actuation methods: tip force and support rotation. Results are expressed in terms of total beam displacement and beam displacement due solely to bending deformation, which correspond to current detection methods used with microcantilever-based devices (optical and piezoresistive detection, respectively). The influences of the shear, rotatory inertia, and fluid parameters, as well as the load/detection scheme, are investigated. Results indicate that load/detection type can impact the measured resonant characteristics and, thus, sensor performance, especially at larger values of fluid resistance.

Keywords Timoshenko beam • Microcantilever-based sensors • Quality factor • Resonant frequency • Fluid–solid interaction

15.1 Introduction

Chemical and biological sensing is a rapidly developing field, resulting in an ever-increasing presence of micro/nanoelectromechanical systems (MEMS/NEMS) in a variety of diagnostic, monitoring, and security applications. However, many of these applications require liquid-phase sensing, which poses significant challenges for dynamic-mode sensors due to the drastic reductions in resonant frequency (f_{res}) and quality factor (Q) that occur due to the liquid. To meet such challenges, recent research has explored the use of alternative vibrational modes of micro/nanocantilever devices in lieu of the fundamental transverse, or out-of-plane, flexural mode. In particular, advantages associated with the use of lateral

J.A. Schultz (✉) • S.M. Heinrich
Civil and Environmental Engineering, Marquette University, Milwaukee, WI 53233, USA
e-mail: joshua.schultz@outlook.com

F. Josse
Electrical and Computer Engineering, Marquette University, Milwaukee, WI 53233, USA

I. Dufour
Université de Bordeaux, CNRS, IMS Laboratory, Talence, France

N.J. Nigro
Mechanical Engineering, Marquette University, Milwaukee, WI 53233, USA

L.A. Beardslee • O. Brand
School of Electrical and Computer Engineering, Georgia Institute of Technology, Atlanta, GA 30332, USA

G. Shaw III et al. (eds.), *MEMS and Nanotechnology, Volume 5: Proceedings of the 2013 Annual Conference on Experimental and Applied Mechanics*, Conference Proceedings of the Society for Experimental Mechanics Series,
DOI 10.1007/978-3-319-00780-9_15, © The Society for Experimental Mechanics, Inc. 2014

(in-plane) flexural modes have been pursued [1–9]. These studies were motivated by the goal of reducing the detrimental effects of fluid damping and fluid inertia, thus providing higher resonant frequencies, f_{res}, and quality factors, Q, the latter corresponding to sharper resonance peaks. Such improvements in the resonant characteristics of the device translate into corresponding enhancements in sensor sensitivity and limit of detection, especially for liquid-phase detection [6, 10].

Some of the previously mentioned studies on the use of the in-plane flexural mode demonstrated both theoretically [3, 4, 8] and experimentally [5, 7] that the improvements in the in-liquid resonant characteristics will be most pronounced in microcantilevers that are relatively short and wide. However, the conclusions in the theoretical studies were based on Euler-Bernoulli beam models whose accuracy is known to deteriorate for short, wide beams deforming in the lateral mode due to the neglected "Timoshenko beam effects" of shear deformation and rotatory inertia. As these are exactly the geometries that show the most promise for lateral-mode, liquid-phase sensing, a strong motivation exists to generalize the previous Euler-Bernoulli modeling efforts to the realm of Timoshenko beam theory. Thus, the aim of the present paper is to present a Timoshenko beam model for a laterally vibrating microcantilever in the presence of a viscous fluid and to examine the theoretical beam response for two types of harmonic excitation that simulate current actuation methods: tip force and support rotation. Results will be expressed in terms of total beam displacement and beam displacement due solely to bending deformation, which correspond to current detection methods used with microcantilever-based devices (optical and piezoresistive detection, respectively). The influences of the shear, rotatory inertia, and fluid parameters, as well as the actuation/detection scheme, will be investigated.

15.2 Problem Statement

Consider a microcantilever beam immersed in a viscous fluid which experiences an in-plane flexural vibration. The effects of shear deformation and rotatory inertia in the beam ("Timoshenko beam effects") are to be included, as are the inertial and damping effects of the surrounding fluid. The geometric parameters (L, b, h) and material density and elastic moduli (ρ_b, E, G) of the cantilever are indicated in Fig. 15.1, as are the fluid's density and viscosity (ρ_f, η). The loading parameters for the two load cases to be considered are shown in Fig. 15.2.

Load Case I involves a harmonically varying imposed rotation at the supported end, with amplitude θ_0 and frequency ω. In Load Case II the beam is excited by a harmonically varying tip force of amplitude F_0 and frequency ω. These load cases are considered because they represent two of the more common actuation methods used in microcantilever-based sensing applications. Load Case I simulates an electrothermal excitation scheme [5], involving thermally induced longitudinal thermal strains at the extreme fibers near the support. Such a loading may be represented kinematically as an imposed harmonic rotation at the support [4]. Load Case II is chosen because a tip force loading may be induced via electromagnetic actuation methods, commonly used in dynamic-mode sensing applications. For each load case our focus will be on examining two particular response histories: the total displacement at the beam tip and the bending-deformation displacement at the beam tip, the latter being that portion of the total tip displacement which is due to bending deformation *only*. The total tip displacement is the relevant output signal if microcantilever response is monitored by optical (laser) methods, while the bending-deformation displacement of the tip as predicted by the model provides an indirect measure of the beam's bending strain, i.e., it will correspond to the output signal generated by piezoresistive elements that may be used to monitor beam response [5]. (This correlation is valid in the vicinity of a resonant peak since the vibrational shape due to bending

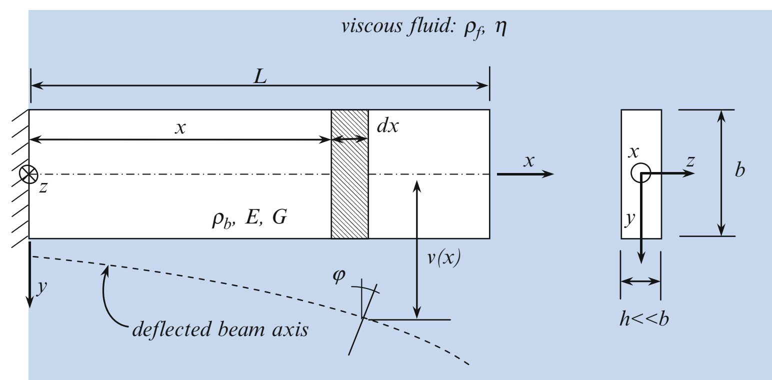

Fig. 15.1 Definitions of geometric and material parameters

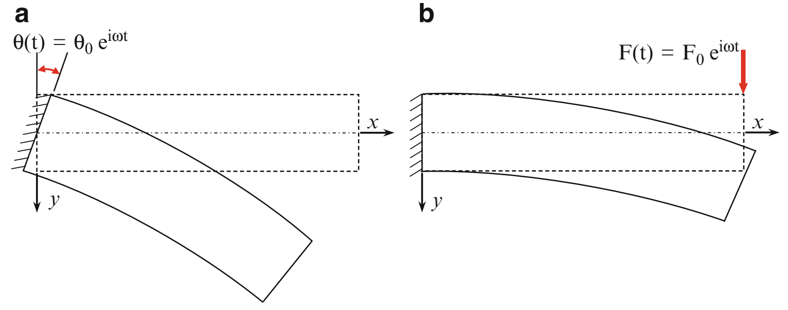

Fig. 15.2 (**a**) Load Case I – imposed harmonic support rotation; (**b**) Load Case II – imposed harmonic tip force

deformation is relatively constant.) Of particular interest are the resonant frequency, f_{res}, and the quality factor, Q, associated with viscous losses in the surrounding fluid. These may be correlated to sensor performance metrics, i.e., mass and chemical sensitivities and limit of detection.

15.3 Theoretical Model

To derive the Timoshenko beam model the following assumptions are made: (1) the beam is homogeneous, linear elastic, and isotropic; (2) deformations are small; (3) the beam is attached to a rigid support at one end (see left end in Figs. 15.1 and 15.2); (4) the cross section is relatively thin ($h << b$) so that the fluid resistance on the smaller faces is negligible; (5) the shear stress exerted by the fluid on the beam is modeled by local application of the solution of Stokes's second problem for harmonic, in-plane oscillations of an infinite rigid surface in contact with a viscous fluid [11]; (6) the viscous energy dissipation in the fluid is the dominant loss mechanism. In tandem assumptions 4 and 5 shall be referred to the assumption of "Stokes fluid resistance," as was the case in earlier Bernoulli-Euler models [3, 4].

The foregoing assumptions (and the consideration of loads as specified in Load Cases I and II) result in the following governing equations for the lateral vibration of a harmonically excited Timoshenko beam in a viscous fluid providing Stokes resistance:

$$\frac{\partial^2 \bar{v}}{\partial \xi^2} - \frac{\partial \varphi}{\partial \xi} - s^2 \lambda^3 (\lambda + \zeta) \frac{\partial^2 \bar{v}}{\partial \tau^2} - s^2 \lambda^3 \zeta \frac{\partial \bar{v}}{\partial \tau} = 0, \tag{15.1a}$$

$$s^2 \frac{\partial^2 \varphi}{\partial \xi^2} + \frac{\partial \bar{v}}{\partial \xi} - \varphi - r^2 s^2 \lambda^3 (\lambda + \zeta) \frac{\partial^2 \varphi}{\partial \tau^2} - r^2 s^2 \lambda^3 \zeta \frac{\partial \varphi}{\partial \tau} = 0, \tag{15.1b}$$

where $\bar{v} \equiv v/L$ is the dimensionless total deflection, φ represents the rotation of the beam cross section, $\xi \equiv x/L$ is a dimensionless spatial coordinate, and $\tau \equiv \omega t$ is dimensionless time. The "Timoshenko beam parameters," r and s, are defined as the rotational inertia parameter and the shear deformation parameter, respectively, via [12, 13]

$$r^2 \equiv \frac{I}{AL^2} = \frac{1}{12}\left(\frac{b}{L}\right)^2, \quad s^2 \equiv \frac{EI}{kAGL^2} = \frac{1}{12}\left(\frac{b}{L}\right)^2 \left(\frac{E}{kG}\right). \tag{15.2a, b}$$

where $A = bh$, $I = hb^3/12$, and $k = 5/6$ is the shear coefficient for a rectangular cross section. The dimensionless frequency and fluid resistance parameters, λ and ζ, are related to the fundamental system parameters by

$$\lambda \equiv \left(\frac{12\rho_b L^4 \omega^2}{Eb^2}\right)^{1/4}, \qquad \zeta \equiv \frac{L}{hb^{1/2}} \left(\frac{48{\rho_f}^2 \eta^2}{E{\rho_b}^3}\right)^{1/4}. \tag{15.3a, b}$$

The governing equations are accompanied by four boundary conditions (BCs). For Load Case I, the BCs are

$$\bar{v}(0,\tau) = 0, \quad \varphi(0,\tau) = \theta_0 e^{i\tau}, \quad \frac{\partial \varphi(1,\tau)}{\partial \xi} = 0, \quad \frac{\partial \bar{v}(1,\tau)}{\partial \xi} - \varphi(1,\tau) = 0, \tag{15.4a -- d}$$

while for Load Case II the following BCs apply:

$$\bar{v}(0,\tau)=0,\quad \varphi(0,\tau)=0,\quad \frac{\partial\varphi(1,\tau)}{\partial\xi}=0,\quad \frac{\partial\bar{v}(1,\tau)}{\partial\xi}-\varphi(1,\tau)=s^2\bar{F}_0e^{i\tau}; \qquad (15.5a\text{ -- }d)$$

where

$$\bar{F}_0\equiv F_0L^2/EI \qquad (15.6)$$

The boundary value problems (BVPs) to be solved consist of the governing equations, Eqs. 15.1a and 15.1b, and the corresponding set of BCs: Eq. 15.4a–d for Load Case I (harmonic support rotation) and Eq. 15.5a–d for Load Case II (harmonic tip force). These BVPs may be solved in analytical form, the details of which will not be presented here, but may be found in [14]. Once the solution for the beam response ($\bar{v}$ and φ) is obtained, any other field of interest may be derived. In particular, the beam displacement due to bending deformation, v_{B-D}, may be expressed in normalized form as

$$\bar{v}_{B-D}(\xi,\tau)\equiv\frac{v_{B-D}(\xi,\tau)}{L}=\begin{cases}\int_0^{\xi}\varphi(\xi',\tau)d\xi'-\theta_0\xi e^{i\tau}, & \text{Load Case I;}\\[2ex] \int_0^{\xi}\varphi(\xi',\tau)d\xi', & \text{Load Case II.}\end{cases} \qquad (15.7a,\ b)$$

Note that the final term in Eq. 15.7a, b is associated with removing the rigid-body rotation (see Fig. 15.2a) so that the result corresponds to the “bending-deformation displacement” that is associated only with bending strains that are being induced. The normalized shear displacement may be obtained for either load case by subtracting the bending displacement (including any rigid-body rotation) from the total displacement:

$$\bar{v}_S(\xi,\tau)\equiv\frac{v_S(\xi,\tau)}{L}=\bar{v}(\xi,\tau)-\int_0^{\xi}\varphi(\xi',\tau)d\xi'. \qquad (15.8)$$

15.4 Theoretical Results and Discussion

15.4.1 Frequency Spectra

The theoretical model may be used to generate frequency spectra, i.e., plots of the magnitude of the tip displacement amplitude versus the driving frequency for any output signal and for either load case (harmonic support rotation or tip force). In what follows the dynamic response of the beam will be characterized by three different output signals: D_T, D_{B-D}, and D_S, corresponding respectively to normalized values of total displacement at the beam tip (D_T) and the components of the tip displacement associated only with bending deformation (D_{B-D}) or shear deformation (D_S). Of primary interest are the resonant characteristics and not the entire frequency spectrum; however, for illustrative purposes we show some examples of frequency spectra in Fig. 15.3a, b for Load Cases I and II, respectively. These figures correspond to fixed values of $r = 0.2$ and $\zeta = 1$ while the value of the material parameter

$$e\equiv\sqrt{E/kG} \qquad (15.9)$$

is allowed to vary. Note that e corresponds to the relative size of the Young’s modulus to the shear modulus and thus larger values of e correspond to the material having an increased susceptibility to shear deformation (i.e., smaller values of the

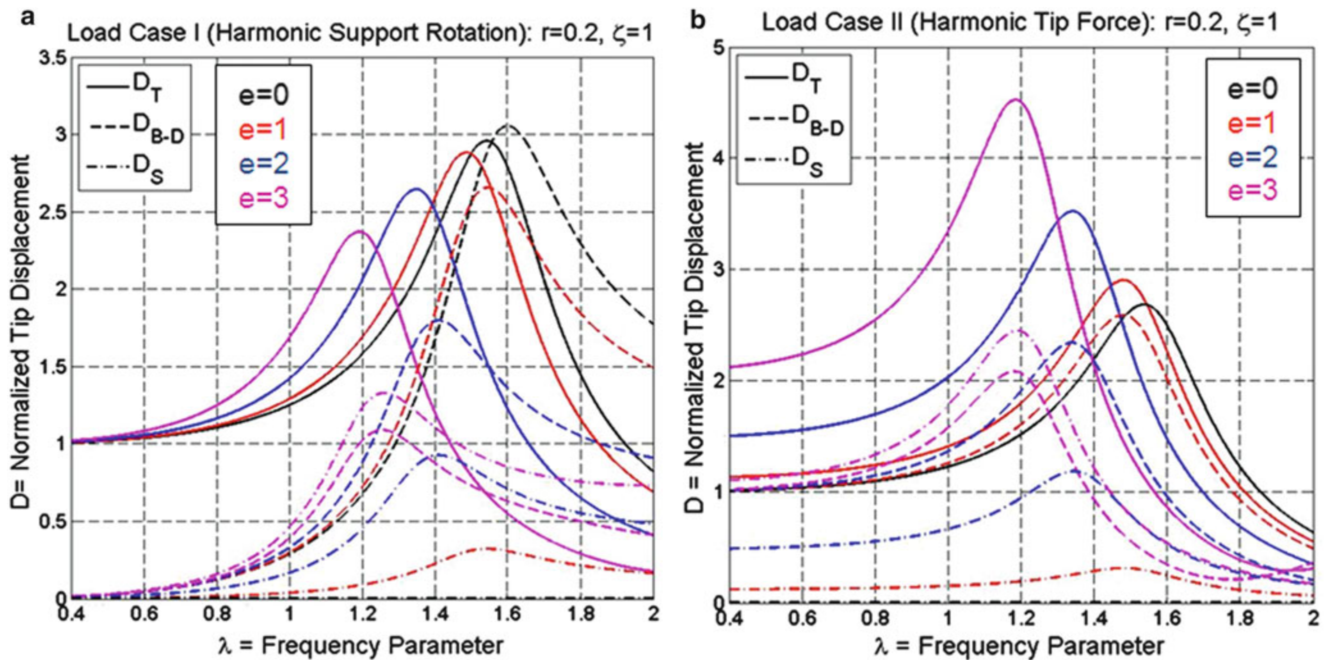

Fig. 15.3 Frequency spectra for a microcantilever beam vibrating laterally in a viscous fluid for the case $r = 0.2$, $\zeta = 1.0$, and $e = 0$ (*black*), 1 (*red*), 2 (*blue*), 3 (*magenta*) as detected by total, bending-deformation, and shear displacement at the tip: (**a**) Load Case I; (**b**) Load Case II (see online version for color figures)

shear modulus G). Since parameter e is independent of beam dimensions, we shall use it as a shear deformation parameter in place of parameter s $(= er)$ defined in Eq. 15.2a, b.

The plots of Fig. 15.3a, b indicate that an increase in e results in a decrease in the resonant frequency as would be detected by any of the signals, which is to be expected due to the increasing flexibility of the model for larger e values. For the case of harmonic support rotation (Fig. 15.3a) an increase in e causes a decrease in the resonant amplitude of the total tip displacement (D_T), while for the harmonic tip force case (Fig. 15.3b) the resonant amplitude increases with increasing e. However, if one considers the resonant amplitudes of the bending-deformation and shear portions of the tip displacement (D_{B-D} and D_S) as the value of e increases, one finds that the strength of the D_{B-D} signal at resonance decreases for both load cases, while the strength of the shear signal increases, as expected. Similar conclusions apply with respect to changes in the value of r, although the corresponding figures are not included here. For Load Case I it is interesting to note that the bending-deformation displacement signal yields a larger resonant amplitude than the total displacement signal. This is associated with "misalignment" of the resonant peaks of the three output signals in Fig. 15.3a, which is due to the fact that the total displacement becomes more out-of-phase with the bending-deformation and shear displacements (and the imposed support rotation) as ζ increases. The different resonant amplitudes of the various output signals could have important implications with regard to the appropriate design of detection schemes for these types of sensing devices. For example, a detection scheme based on monitoring of bending strain (e.g., via piezoresistors at the extreme fibers of the beam near the support) might only "see" a small portion of the deformation response if a significant amount of shear deformation is present. In such a case, one may wish to replace or supplement the bending-strain detection scheme with shear strain measurements near the neutral axis of the beam's cross section.

The numerical results to follow in the remaining sections of the paper will focus on the resonant frequency and quality factor of lateral-mode mirocantilevers in liquids. Theoretical values of these resonant quantities may easily be extracted from frequency response curves of the type shown in Fig. 15.3a, b. For microscale devices in liquids whose properties are on the same order as that of water, the fluid resistance parameter lies in the range $0 \leq \zeta \leq 0.2$, in which case the values of resonant frequency and quality factor are very insensitive to both the load case and the output signal employed. However, for other applications (either at the nanoscale or in fluids with higher viscosity and/or density) the fluid resistance parameter may be much larger. In these cases there may be noticeable differences in resonant characteristics of the output signals generated by the different loading/detection schemes, as is apparent in Fig. 15.3a, b for the case of $\zeta = 1$. In the results that follow such differences between the total and bending-deformation signals will be explored, but only Load Case I (harmonic support rotation) will be considered as it corresponds to the most common actuation method (electrothermal) used to date for lateral-mode microcantilevers. (Similar results may easily be generated for the tip force case.)

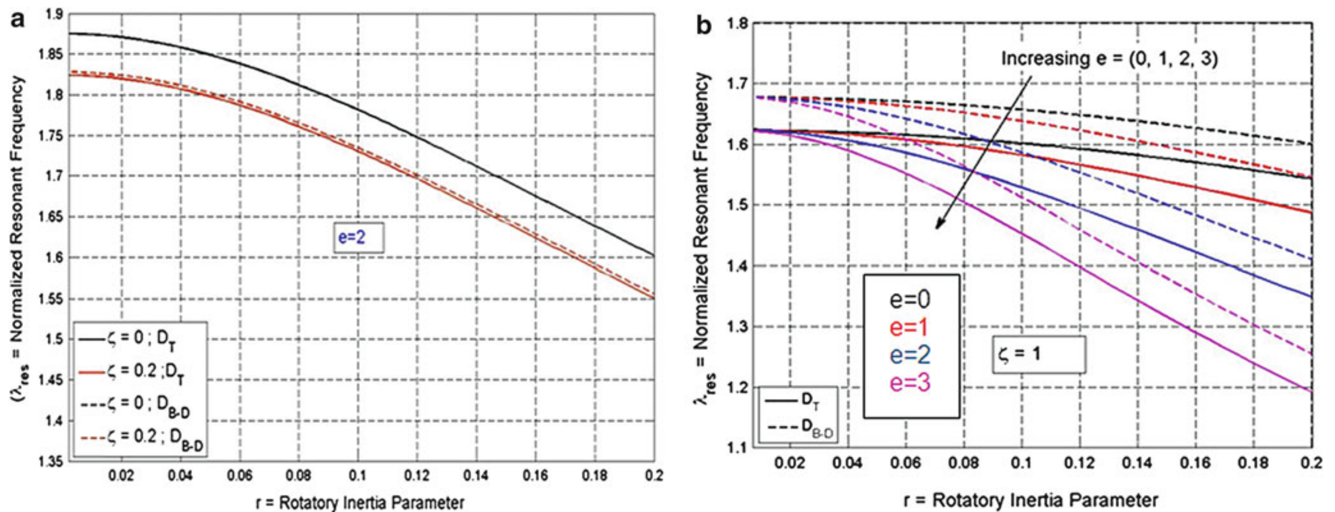

Fig. 15.4 Theoretical values of normalized resonant frequency of a microcantilever vibrating laterally in a viscous fluid as detected by total and bending-deformation tip displacements for Load Case I: (**a**) small fluid resistance results ($\zeta = 0$ and $\zeta = 0.2$); (**b**) large fluid resistance results ($\zeta = 1.0$) (see online version for color figures)

15.4.2 Resonant Frequency

The resonant frequency parameter, λ_{res}, for the first lateral mode is plotted in Fig. 15.4 for the case of harmonic support rotation. The figure shows the dependence of resonant frequency on the Timoshenko parameters, as characterized by the geometric parameter r and material parameter e. These resonant frequency values correspond to the first peaks of the frequency spectra for the total displacement and the bending-deformation displacement at the tip (curves of the type plotted in Fig. 15.3a). The ranges of parameters considered in Fig. 15.4 include practical values of microcantilever dimensions and material properties expected to be encountered in lateral-mode MEMS sensing applications, including those necessitating the incorporation of shear deformation and rotatory inertia effects (i.e., when b/L is *not* small relative to unity).

Figure 15.4 clearly illustrates several trends. First, there is an expected reduction in resonant frequency associated with an increase in the fluid resistance parameter. This may be interpreted as follows: for fixed cantilever dimensions the resonant frequency will decrease if the fluid density or viscosity is increased. Also observed in Fig. 15.4 is how higher levels of Timoshenko parameters – larger r and e values, corresponding to increased rotational inertia and decreased shear stiffness of the beam – will result in a reduction in resonant frequency. Over the range of Timoshenko and fluid parameters considered in Fig. 15.4, the maximum effect of r and e is to cause a reduction of 26 % in λ_{res} which, according to Eq. 15.3a, is equivalent to a decrease in the resonant frequency, ω_{res}, of 46 %. These reductions correspond to the D_T signal for the case of $r = 0.2$, $e = 3$ in Fig. 15.4b. If we consider the case $e = 2$, which corresponds to "textbook" values of moduli for silicon in the frame of reference of a standard (100) silicon wafer [15], i.e., $E = 169$ GPa, $G = 50.9$ GPa, and a shear coefficient of $k = 5/6$, Fig. 15.4b shows that the largest influence of the Timoshenko effects on the resonant frequency is a 17 % decrease in λ_{res} (31 % reduction in ω_{res}), which occurs at $r = 0.2$. Clearly, significant error may be introduced in the resonant frequency estimate if the Timoshenko effects are ignored in such cases. Finally, as a verification of the resonant frequency results, we find that the value in Fig. 15.4a for the case $r = \zeta = 0$ (i.e., the starting value of the upper curve) is given by $\lambda_{res} = 1.8751$, which agrees with the well-known eigenvalue for an Euler-Bernoulli beam in vacuum [16].

The effect of a larger value of fluid resistance parameter (associated with smaller beam dimensions and/or increased values of fluid properties) may be seen by comparing the curves in Fig. 15.4a (small ζ) to those in Fig. 15.4b (larger ζ). In particular we note that the sensitivity of the resonant frequency to the output signal is negligible in the former case but becomes much more pronounced in the latter case of $\zeta = 1$. We observe that for cases of larger values of fluid resistance parameter, monitoring the bending deformation of the beam actually results in a noticeably higher resonant frequency than if one tracks the total tip displacement. This result is related to the previously mentioned fact that the total displacement becomes more out-of-phase with the bending-deformation and shear displacements as ζ increases, and may have important implications in sensor applications as the mass sensitivity tends to be higher at larger values of resonant frequency.

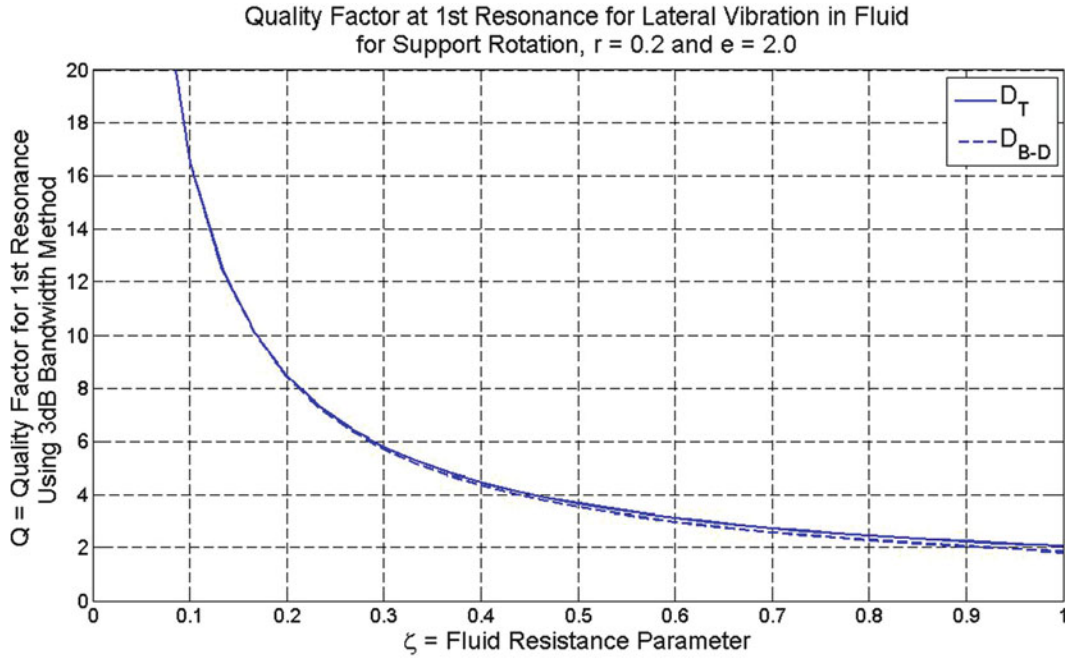

Fig. 15.5 Theoretical quality factor based on half-power (bandwidth) method at first resonance for fluid resistance values $\zeta \in [0,\ 1]$ and Timoshenko parameters $r = 0.2$ and $e = 2$ as detected by D_T and D_{B-D}

15.4.3 Quality Factor

Applying the half-power (bandwidth) method to the theoretical frequency spectra such as those shown in Fig. 15.3, one may obtain the quality factor for a range of fluid resistance and Timoshenko parameters. For example, the quality factor based on both the total tip displacement and the bending-deformation portion are plotted in Fig. 15.5 for the case of harmonic support rotation loading over the range $\zeta \in [0,\ 1]$. The figure is based on specified values of $r = 0.2$ (i.e., $b/L = 0.7$) and $e = 2$ (e.g., silicon). Clearly, there is a very strong impact of the fluid resistance parameter on the quality factor, with Q following what appears to be roughly an inverse relationship with ζ as was shown to be the case for a Bernoulli-Euler beam [3, 4]. Recalling the definition of ζ, the viscosity and density of the fluid participate to an equal extent in determining Q. Also apparent from Fig. 15.5 are the virtually identical results for Q as detected by the two types of output signals when ζ is small ($\zeta \leq 0.2$). However, at larger values of fluid resistance, the figure indicates a noticeable difference in the detected values of Q, with D_T yielding a quality factor that is 11 % higher than that based on the D_{B-D} signal at $\zeta = 1$.

Unlike the strong dependence of Q on ζ, the effect of increasing the Timoshenko parameter e from 0 to 3 (not shown here) results in a relatively modest 15 % reduction of the quality factor compared to the Bernoulli-Euler ($e = 0$) case, even for a relatively large value of r such as $r = 0.2$. Similarly, for a specified value of e between 0 and 3, changing r over the range 0–0.2 results in a modest reduction in Q that is no larger than 15 %. Thus, based on the observations here and in the previous section, the model indicates that the Timoshenko effects have a stronger impact on the resonant frequency than on the quality factor.

15.5 Comparisons with Experimental Data

In an attempt to validate the current model, the theoretical results were compared with experimental data for resonant frequency and quality factor for laterally excited microcantilevers in water. The beams were actuated electrothermally in a manner that may be modeled kinematically as an imposed support rotation as noted earlier. Details regarding device fabrication [5] and the testing procedure [7] are described elsewhere. Specimen geometries were grouped according to the nominal thicknesses of the Si substrate material, $h_{nom} = (5, 8, 12, 20)$ μm, and within each thickness set the length and width dimensions were as follows: $L = (200, 400, 600, 800, 1000)$ μm, $b = (45, 60, 75, 90)$ μm. For all of the theoretical calculations, estimates of the total thickness (Si plus several passivation layers) were used in lieu of the nominal silicon thicknesses.

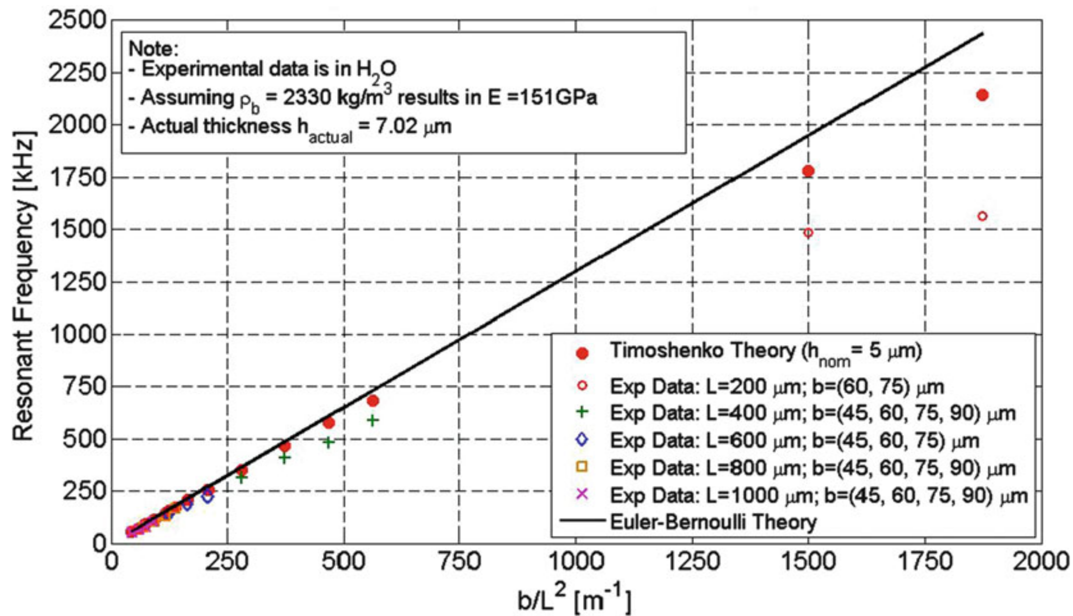

Fig. 15.6 Comparison of current in-fluid, Timoshenko model to experimental resonant frequency for first lateral flexural mode, nominal thickness 5 μm using $C1 = 2.3240$ km/s and $C2 = 2$

To generate theoretical results it was necessary to also specify numerical values of the following material parameters: $C1 \equiv \sqrt{E/12\rho_b}$ and $C2 \equiv e = \sqrt{E/kG}$. Due to the composite nature of the fabricated cantilevers (Si substrate plus several passivation layers), it is difficult to prescribe specific values of the effective Young's modulus E or shear modulus G a priori. Therefore, the values of the $C1$ parameter (for each thickness set) were determined by fitting the *in-vacuum* results of the present model to *in-air* experimental frequency data (assuming that the air resistance has a negligible impact on the f_{res}). The *same* values of $C1$ were then used in making the comparison between the *in-water* results of the present model and the *in-water* experimental data, which is the comparison of main interest in this study. A similar approach may have been utilized to obtain best-fit $C2$ values by fitting the in-air frequency data; however, this would possibly result in "overfitting" the model to the data. To avoid this situation and thereby provide a more objective means of validating the model, the previously mentioned "textbook" value of $C2 = 2$ was used, as this corresponds to the orientation of the Si microbeams used. Note that the $C1$ value is associated with the initial slope of the resonant frequency vs. b/L^2 curves, while the $C2$ value corresponds to the degree of curvature of these curves (i.e., departure from linearity) at larger values of b/L^2. In all calculations for the in-water case, the fluid properties were specified as $\rho_f = 1{,}000$ kg/m^3 and $\eta = 0.001$ Pa·s in the model.

A sample of the theory vs. experimental data comparisons is shown in Fig. 15.6 for the resonant frequency for the first lateral mode. Only the comparison for the nominal thickness of 5 μm is included here (total thickness = 7.02 μm when passivation layers are included), but similar trends apply to the other thicknesses [14]. The comparison of resonant frequencies in Fig. 15.6 indicates that the model is able to simulate qualitatively the softening trend of the experimental data for the shorter, wider beams (larger b/L^2 values) for which the Timoshenko beam effects (shear deformation and rotatory inertia) are expected to be more pronounced. However, from a quantitative perspective the model underestimates the departure from the linear Bernoulli-Euler results, indicating that (a) the actual value of $C2$ is much larger than the specified value of 2, possibly due to the composite nature of the microstructure or imperfect bonding between layers, and/or (b) an additional softening effect is being neglected in the present model. With regard to the latter possibility, the most likely candidate would be the finite support compliance that is ignored in the present model which assumes a rigid support. As the beam becomes shorter and wider, not only do the Timoshenko beam effects become more important, but the flexural stiffness of the beam becomes relatively large in comparison with the rotational stiffness of the support. As a result, there is a greater likelihood that the support will elastically deform during the vibration and that this will introduce an additional softening effect leading to even lower resonant frequencies such as those indicated by the data in Fig. 15.6. (This effect is currently being incorporated into the present Timoshenko beam model via an appropriate modification of the boundary conditions.)

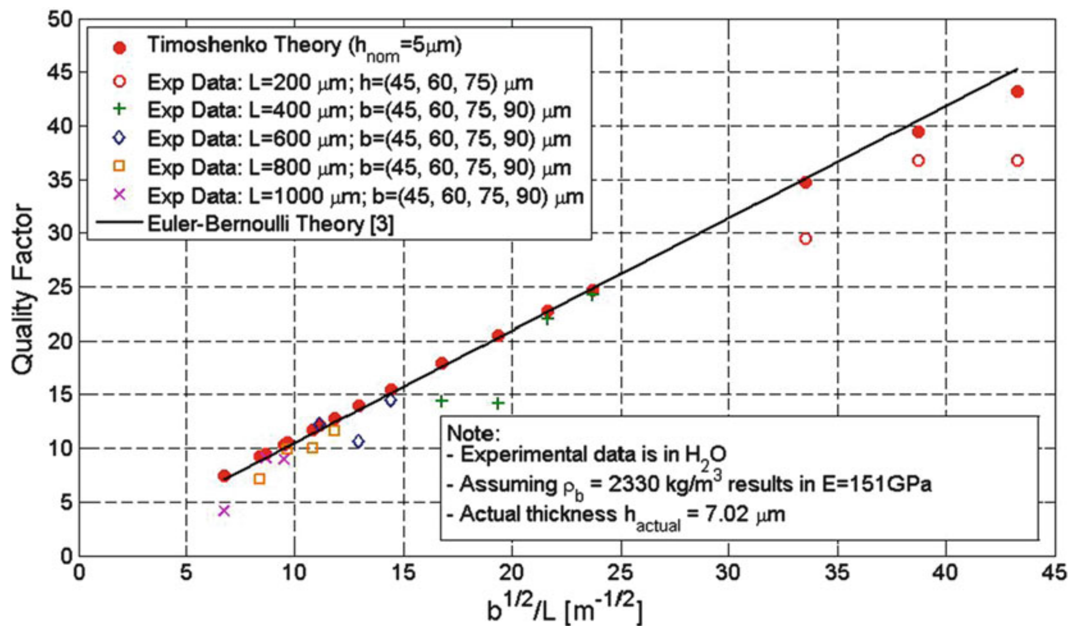

Fig. 15.7 Comparison of current in-fluid, Timoshenko model to experimental [7] quality factor for first lateral flexural mode, nominal thickness 5 μm using $C1 = 2.3240$ km/s and $C2 = 2$

In Fig. 15.7 the comparison of theoretical results vs. experimental data is shown for the quality factor at the first resonance peak. Again, the comparison is shown only for the 5 μm nominal thickness specimens, but similar trends apply to the other thicknesses [14]. As was the case in the frequency comparison, the model is able to simulate qualitatively the softening trend of the experimental Q data for the shorter, wider beams (larger $b^{1/2}/L$ values) due to higher levels of shear deformation and rotatory inertia, but quantitatively the predicted Q values still remain larger than the experimental values. Possible reasons for this include those that were previously noted for the frequency comparison. Figure 15.7 also indicates that the theoretical results for Q slightly overestimate the data even for the more slender specimens, indicating that the Stokes fluid resistance model is slightly underestimating the fluid damping and thereby giving a reasonable upper-bound estimate of the actual quality factor. As expected, the assumption of Stokes resistance yields reasonable estimates of Q for the thinner beams (in this case those with nominal thicknesses of 5 and 8 μm), but leads to a significant overestimation of Q for the thicker specimens (nominal thicknesses of 12 and 20 μm). We note that the departure of the experimental Q data from the linearity implied by Bernoulli-Euler theory is not as strong as that associated with the resonant frequency (compare Figs. 15.6 and 15.7), and the theoretical model shows a similar trend in this respect.

15.6 Summary and Conclusions

An analytical Timoshenko beam model that incorporates fluid effects via a Stokes-type fluid resistance assumption has been presented. The theoretical results for resonant frequency and quality factor have been shown to depend on the loading type and detection scheme for higher values of the fluid resistance parameter. Notably, the quality factor obtained from the total tip displacement was found to be higher than that associated with monitoring the bending deformation response (analogous to measuring flexural strains near the support). Comparisons between the analytical results and experimental data indicated that the analytical model provides an improvement over the Bernoulli-Euler theory and yields the same qualitative trends exhibited by the data. These comparisons indicate that the quantitative results of the model, which provide reasonable estimates to the data in many cases, may be further improved by incorporating support compliance effects into the Timoshenko beam model presented in the present work.

Acknowledgments This work is supported in part by NSF Grant Nos. ECCS-0824017, ECCS-1128992, and ECCS-1128554, and the Graduate School of Marquette University.

References

1. Sharos LB, Raman A, Crittenden S, Reifenberger R (2004) Enhanced mass sensing using torsional and lateral resonances in microcantilevers. Appl Phys Lett 84:4638–4640
2. Dufour I, Josse F, Heinrich S (2007) Theoretical analysis of strong-axis bending mode vibrations for resonant microcantilever (bio)chemical sensors in gas or liquid phase. J Microelectromech Syst 16:44–49
3. Heinrich SM, Maharjan R, Beardslee L, Brand O, Dufour I, Josse F (2010) An analytical model for in-plane flexural vibrations of thin cantilever-based sensors in viscous fluids: applications to chemical sensing in liquids. In: Proceedings, international workshop on nanomechanical cantilever sensors, Banff, 2 pp, 26–28 May 2010
4. Heinrich SM, Maharjan R, Dufour I, Josse F, Beardslee LA, Brand O (2010) An analytical model of a thermally excited microcantilever vibrating laterally in a viscous fluid. In: Proceedings, IEEE sensors 2010 conference, Waikoloa, pp 1399–1404, 1–4 Nov 2010
5. Beardslee L, Addous A, Heinrich S, Josse F, Dufour I, Brand O (2010) Thermal excitation and piezoresistive detection of cantilever in-plane resonance modes for sensing applications. J Microelectromech Syst 19:1015–1017
6. Beardslee LA, Demirci KS, Luzinova Y, Mizaikoff B, Heinrich SM, Josse F, Brand O (2010) Liquid-phase chemical sensing using lateral mode resonant cantilevers. Anal Chem 82:7542–7549
7. Beardslee LA, Josse F, Heinrich SM, Dufour I, Brand O (2012) Geometrical considerations for the design of liquid-phase biochemical sensors using a cantilever's fundamental in-plane mode. Sens Actuators B 164:7–14
8. Cox R, Josse F, Heinrich S, Brand O, Dufour I (2012) Characteristics of laterally vibrating resonant microcantilevers in viscous liquid media. J Appl Phys 111:014907–014914
9. Dufour I, Josse F, Heinrich S, Lucat C, Ayela C, Menil F, Brand O (2012) Unconventional uses of microcantilevers as chemical sensors in gas and liquid media. Sens Actuators B 170:115–121
10. Cox R, Josse F, Wenzel M, Heinrich SM, Dufour I (2008) A generalized model of resonant polymer-coated microcantilevers in viscous liquid media. Anal Chem 80:5760–5767
11. Stokes G (1851) On the effects of the internal friction of fluids on the motion of pendulums. Trans Camb Philos Soc 9:8–106
12. Timoshenko S, Young DH (1955) Vibration problems in engineering, 3rd edn. Van Nostrand, New York, USA
13. Huang TC (1961) The effect of rotatory inertia and of shear deformation on the frequency and normal mode equations of uniform beams with simple end conditions. J Appl Mech 28:579–584
14. Schultz J (2012) Lateral-mode vibration of microcantilever-based sensors in viscous fluids using Timoshenko beam theory. Ph.D. dissertation, Marquette University
15. Hopcroft M, Nix W, Kenny T (2010) What is the Young's modulus of silicon? J Microelectromech Syst 19:229–238
16. Clough RW, Penzien J (1993) Dynamics of structures, 2nd edn. McGraw-Hill, New York, USA

Chapter 16
Improvement in Uncertainty of Tuning Fork-Based Force Sensor Stiffness Calibration via the Indentation Method Using Direct Determination of Contact and Machine Compliance

Gordon A. Shaw

Abstract Noncontact-atomic force microscopy (NCAFM) combines atomic resolution imaging with the ability to measure forces at the atomic scale. Despite burgeoning applications for this method to measure force at the atomic scale, the metrology necessary to interpret the frequency shifts occurring in NCAFM sensors from tip-sample interactions is still in a very early stage of development. A key parameter in this measurement is the stiffness of the sensor being used in the measurement. Here we outline an improvement in the procedure for measuring the spring constant of a tuning fork-type sensor using an instrumented indenter. Instead of using models and materials properties to estimate the effect of contact and machine compliance, these quantities are directly measured by indenting the base of the tuning fork. This decreases the uncertainty in the measurement by nearly a factor of two.

Keywords Atomic force microscopy • Nanotechnology • Force • Metrology • Calibration

16.1 Introduction

NCAFM has been used to quantitatively measure atomic-scale force between the atoms on a surface and a sharp probe tip [1–3]. The force sensors used for this work are typically cantilever structures, and they are used as dynamic force sensors. In a frequency-modulated force measurement, a phase-locked loop is used to monitor the frequency of the resonant cantilever structure (typically at its first resonant frequency). As the sharp tip at the end of the force sensor interacts with a surface, this frequency shifts. The frequency shift can be converted to force using the Sader-Jarvis inversion algorithm [4],

$$F(z) = 2k\int_z^\infty \left(1 + \frac{a^{1/2}}{8[\pi(t-z)]^{1/2}}\right)\Omega(t) - \frac{a^{3/2}}{[2(t-z)]^{1/2}}\frac{d\Omega(t)}{dt}dt \qquad (16.1)$$

where k is the sensor spring constant, a is vibration amplitude, z is distance of closest approach between the tip and surface, and $\Omega(t) = \omega/\omega_0$ such that ω is probe resonant frequency near the surface at non-negligible tip-sample force, $F(z)$, and ω_0 is probe resonant frequency far from the surface at $F(z) = 0$.

All of the terms enumerated above are subject to uncertainty. The spring constant of the sensor in particular has been the subject of several inquiries [5–8]. One method that has been used to determine sensor stiffness is the indentation method [6]. In this method, the sensor stiffness was measured directly by applying a known force and measuring resulting displacement of a sharp indenter tip in contact with a tuning fork sensor at a particular location along the longitudinal axis of the cantilevered tuning fork, as shown in Fig. 16.1. The static tuning fork stiffness at the test location can be calculated with

$$k_{corr} = \cos^{-2}\theta\left(k_T^{-1} - k_c^{-1} - k_m^{-1}\right)^{-1} \qquad (16.2)$$

G.A. Shaw (✉)
Physical Measurement Laboratory, Mass and Force Group, U.S. National Institute of Standards and Technology, Gaithersburg, MD, USA
e-mail: gordon.shaw@nist.gov

G. Shaw III et al. (eds.), *MEMS and Nanotechnology, Volume 5: Proceedings of the 2013 Annual Conference on Experimental and Applied Mechanics*, Conference Proceedings of the Society for Experimental Mechanics Series,
DOI 10.1007/978-3-319-00780-9_16, © The Society for Experimental Mechanics, Inc. 2014

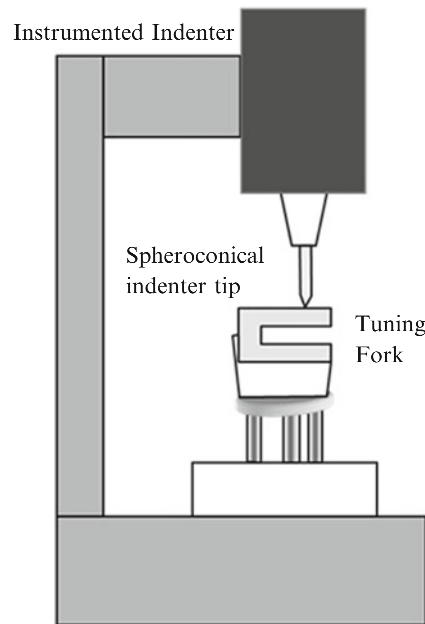

Fig. 16.1 Schematic of instrumented indentation testing of a cantilevered tuning fork spring constant

where θ is the angle of repose of the cantilevered tuning fork, k_T is the indentation stiffness, measured as the slope of the force displacement curve generated while the indenter is in contact with the tuning fork at the test location, k_c is indenter tip-tuning fork surface contact stiffness, and k_m is machine stiffness, including the stiffness of the indenter apparatus, and the test fixture that holds the tuning fork.

Previously, the k_m and k_c were estimated using materials properties and a model based on simplified contact mechanics [6]. Because of the range of literature values for the material properties used in the calculation, this limited relative combined standard uncertainty of the measurement to around 10 %. Improved uncertainty can be obtained by directly measuring the combined contact and machine stiffness by pressing on the base of the tuning fork with the indenter. Because the base is made of the same gold-coated quartz material as the cantilevered tuning fork, the contact compliance should be similar, barring material inhomogeneities.

16.2 Experimental Method

The tuning fork used in the experimental work was attached to a piece of ceramic on a tripod-style holder from Omicron*. The tuning fork was attached using Torr Seal adhesive by its bottom tine only. This results in the top tine acting as a cantilevered elastic element (i.e., a qPlus-style sensor) at a 5° angle of repose. The tuning fork assembly was then placed under an instrumented indenter with a spheroconical diamond tip ($r_c \cong 20$ μm). A proximal microscope and optically encoded stage were used to position the indenter tip at the base of the tuning fork. After the application of a 10 μN preload, the force applied by the indenter was increased to 2,000 μN, and then ramped between 1,000 and 2,000 μN five times while displacement of the indenter tip was simultaneously recorded. The experiment was also carried out at approximately 150 μm from the free end of the tuning fork.

16.3 Results

Representative results are shown in Fig. 16.2. A Hertzian contact model is used for comparison to calculate the theoretical force-displacement behavior of the contact between an elastic half space and rigid indenter using [9]

$$\partial = \left(\frac{9F^2}{16R_cE^2}\right) \tag{16.3}$$

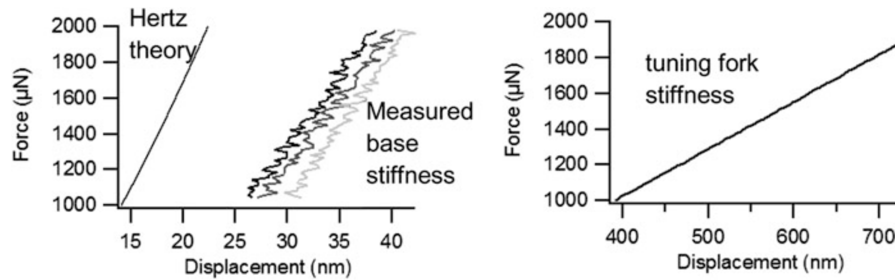

Fig. 16.2 Indentation force-displacement measurements conducted at the tuning fork base (*left*) and near the tuning fork free end (*right*)

where F is force applied by the indenter tip, and E is the Young's modulus of Gold, which is taken as the bulk value of 78 GPa [10] although indentation experiments on gold nanowires have indicated values as high as 119 GPa [11]. From this approximation, the contact stiffness over the force range used is calculated to be approximately 10^5 N/m. The theoretical Force displacement behavior is shown in Fig. 16.2, and indicates that the maximum deviation of contact stiffness from the stiffness at the midpoint is approximately 10 % of the stiffness at the midpoint force (1,500 μN.) The experimentally measured stiffness at the base of the tuning fork is calculated using a linear least squares fit of the force displacement data. The average of the three locations tested yields a stiffness of 80 $\pm$ 0.4 kN/m, where uncertainty is calculated as the standard deviation of the three separately determined stiffness values.

A value of stiffness slightly lower than the Hertz prediction is expected for two different reasons in this case. First, there is an additional machine stiffness, k_m, in series with the contact stiffness, which is expected to be approximately 2 $\times$ 10^6 N/m. This has the effect of lowering the stiffness measured by the indenter at the base of the tuning fork by approximately 5 % relative to the stiffness value that would be present with an infinitely stiff machine. It is important to note the fact that the indenter measures the combined effects of these two stiffnesses does not affect the calibration of the tuning fork spring constant because, as is shown in Eq. 16.1, both k_c and k_m can be subtracted simultaneously from the measured stiffness. Second, the surface of the tuning fork is not flat, but has peaked ridges as a result of its manufacturing process. The presence of surface structure serves to reduce the contact area relative to that of the Hertz prediction, resulting in a slightly lowered contact stiffness. Although exact quantification of this effect is difficult, the standard deviation of the stiffness measured in the three different test locations indicates a maximum relative contribution of approximately 5 % to the stiffness in this case. In the indentation testing of other tuning forks, the spread of the stiffness measured at the tuning fork base has been observed to be as high as 20 %. Thus, the effect of surface topography in this case appears to be the dominant uncertainty in determining the combined effect of machine and contact stiffness.

16.4 Discussion

Despite the relatively high uncertainty in measuring the combined effects of k_c and k_m, the effect on total uncertainty is mitigated by the fact that the free end of the tuning fork is much less stiff than the contact or machine. Figure 16.2 shows representative data from an indentation performed near the free end of the tuning fork; stiffness was 2.536 $\pm$ 0.001 kN/m at the point tested. The uncertainty of this measurement is a statistical uncertainty calculated from the standard deviation of the slopes of the force-displacement data from five load-unload cycles used for indentation testing at this particular location, and does not include other important systematic uncertainties discussed in other work [6]. Even a 20 % uncertainty in the combined contact and machine compliance results in 0.8 % contribution to uncertainty in the stiffness of the tuning fork at that test point. The subtraction of the contact and machine stiffness, and correction for sensor angle of repose as per Eq. 16.2 results in a tuning fork stiffness of 2.639 $\pm$ 0.004 kN/m, where the uncertainty reflects the quadrature sum of the statistical uncertainty described above and the uncertainty from the direct measurement of k_c and k_m. The 4 % uncertainty measured during the mechanical testing of this sensor's base adds only 0.1 % to the final uncertainty. This approach represents a marked improvement from previous methods where the uncertainty in tuning fork sensor spring constant from contact and base stiffness was around 5 % [6]. In addition, it allows the separation of the effect of the method of attachment of the tuning fork from the tuning fork spring constant measurement. This may provide some additional information, since it has been shown that the specifics of the method used to glue the tuning fork to its ceramic mount can be important for quantifying the sensor stiffness [7].

16.5 Conclusion

A new method has been outlined for determining the combined effect of contact and machine stiffness on tuning fork-type force sensor spring constant calibration by instrumented indentation. By testing indentation stiffness at the base of the tuning fork, uncertainty in the measured spring constant can be improved substantially. Although this study focuses on qPlus-type sensors, the indentation method described here could be used in the examination of any cantilevered elastic structure.

Disclaimer This article is authored by employees of the U.S. federal government, and is not subject to copyright. Commercial equipment and materials are identified in order to adequately specify certain procedures. In no case does such identification imply recommendation or endorsement by the National Institute of Standards and Technology, nor does it imply that the materials or equipment identified are necessarily the best available for the purpose.

References

1. Giessibl FJ, Hembacher S, Bielefeldt H, Mannhart J (2000) Subatomic features on the Silicon (111)-(7x7) surface observed by atomic force microscopy. Science 289:422–425
2. Ternes M, Lutz CP, Hirjibehedin CF, Giessibl FJ, Heinrich AJ (2008) The force needed to move an atom on a surface. Science 319:1066–1069
3. Sweetman A, Jarvis S, Danza R, Bamidele J, Gangopadhyay S, Shaw GA, Kantorovich L, Moriarty P (2011) Toggling bistable atoms via mechanical switching of bond angle. Phys Rev Lett 106:136101
4. Sader JE, Jarvis SP (2004) Accurate formulas for interaction force and energy in frequency modulation force spectroscopy. Appl Phys Lett 84:1801–1803
5. Simon GH, Heyde M, Rust H-P (2007) Recipes for cantilever parameter determination in dynamic force spectroscopy: spring constant and amplitude. Nanotechnology 18:22503
6. Shaw GA, Pratt JR, Jabbour ZJ (2011) Small mass measurements for tuning fork-based atomic force microscope cantilever spring constant calibration. MEMS and Nanotechnology, vol 2. In: Proceedings of the 2010 annual conference on experimental and applied mechanics. Springer, New York, pp 4956–4965
7. van Vörden D, Lange M, Schmuck M, Schmidt N, Möller R (2012) Spring constant of a tuning fork sensor for dynamic force microscopy. Beilstein J Nanotechnol 3:809–816
8. Berger J, Švec M, Müller M, Ledinský M, Fejfar A, Jelínek P, Majzik Z (2003) Characterization of the mechanical properties of qPlus sensors. Beilstein J Nanotechnol 4:1–9
9. Johnson KL (2001) Contact mechanics. Cambridge University Press, Cambridge
10. Tables of physical & chemical constants (16th edn, 1995). 2.2.2 Elasticities and strengths. Kaye & Laby Online. Version 1.0, 2005
11. Li X, Nardi P, Baek CW, Kim J-M, Kim Y-K (2005) Direct nanomechanical machining of gold nanowires using a nanoindenter and an atomic force microscope. J Micromech Microeng 15:551–556

Chapter 17
Flexible Terahertz Metamaterials for Frequency Selective Surfaces

J.A. Deibel, H.R. Jones, A. Fosnight, R. Shaver, E. Best, D. Langley, L.A. Starman, and R.A. Coutu

Abstract While recent years have seen great advances in the generation, detection, and application of terahertz frequency radiation, this region of the electromagnetic spectrum still suffers from a lack of efficient and effective frequency specific optical components. While such terahertz devices do exist, they are often limited by the materials they are based on and a lack of frequency selectivity and tunability. Metamaterial devices can provide frequency resonant behavior in the form of transmissive and reflective filters. Such a frequency selective surface can also be made tunable via the use of a flexible substrate. In this talk, we will highlight work involving the design, fabrication, and characterization of terahertz metamaterial devices based on flexible substrates. Finite element method simulations have been utilized to design a split-ring resonator (SRR) structure on a flexible SU8 polymer substrate with a targeted 250 GHz resonant response. Multiple configurations of SRR arrays have been fabricated on free standing SU8 substrates. These devices have subsequently been characterized using terahertz time-domain spectroscopy and imaging systems. The metamaterial devices have shown selective transmission and reflection over a narrow range of frequencies near the targeted resonance at 250 GHz. Details of both the design, fabrication, and characterization will be discussed.

Keywords Terahertz • Metamaterials • Filters • Polymer • Flexible

17.1 Introduction

The terahertz "gap" of the electromagnetic spectrum (0.1–10 THz) effectively bridges the electronic and optical parts of the spectrum. Recent years have seen rapid growth in this field due to advances in source and detector technology thereby accelerating application science and development. A variety of methods, both optical and electronic, exist for both the generation and detection of terahertz radiation [1–4]. The interest in THz radiation derives from the unique properties that many substances exhibit at these frequencies. Most dielectric materials are transparent to THz radiation, while metals are opaque. Many solids, liquids, and gases exhibit unique spectroscopic "fingerprints" at THz frequencies. Terahertz time-domain spectroscopy (THz-TDS), with its broad fractional bandwidth and sub-picosecond time resolution offers an effective method of characterizing the frequency dependent absorption, refractive index, conductivity, and other parameters of a variety of materials [1, 5]. Demonstrated application areas for THz imaging and spectroscopy include security [6], semiconductor spectroscopy [7], and imaging and diagnostics [8]. Despite the promises offered by terahertz technology, its use in real-world applications has been quite limited. One limiting factor has been a lack of compact and efficient sources and detectors, but significant advances have been made in recent years [9–12]. Another significant issue is the lack of suitable optical components to manipulate and control THz light. For instance, polarization, filtering, and focusing optics are

J.A. Deibel • H.R. Jones • A. Fosnight • R. Shaver • E. Best
Department of Physics and Engineering Physics Program, Wright State University, 3640 Colonel Glenn Highway, Dayton, OH 45435, USA

D. Langley • L.A. Starman • R.A. Coutu (✉)
Department of Electrical and Computer Engineering, Air Force Institute of Technology, 2950 Hobson Way, Wright-Patterson AFB, OH 45433, USA
e-mail: Ronald.Coutu@afit.edu

G. Shaw III et al. (eds.), *MEMS and Nanotechnology, Volume 5: Proceedings of the 2013 Annual Conference on Experimental and Applied Mechanics*, Conference Proceedings of the Society for Experimental Mechanics Series,
DOI 10.1007/978-3-319-00780-9_17, © The Society for Experimental Mechanics, Inc. 2014

readily available for purchase in many of the other regions in the electromagnetic spectrum while the situation in the THz spectral range is exactly opposite of this, severely limiting the ability to create systems to address specific applications.

Recent work has shown that THz technology and application development can be advanced via the creation of optical components based on low-loss metamaterial devices [13–15]. Metamaterial based devices are being developed for uses in many areas of the electromagnetic spectrum spanning from the microwave to even the visible. The end goals of this work include the development of high-precision filters, "super lenses", frequency-selective surfaces, and possibly cloaking technology. Metamaterials are composite-based devices that are often designed to affect a resonant response at a specified frequency. The device is designed such that, at this resonant frequency, an important parameter, such as refractive index, exhibits behavior normally un-observable using traditional materials or devices. For example, metamaterials have been used to demonstrate negative indices of refraction and sub-diffraction limited focusing. A common approach for realizing metamaterial devices utilizes metallized split ring resonator (SRR) arrays on dielectric substrates. This paper highlights ongoing work in which split-ring resonator (SRR) structures have been fabricated on flexible SU8 polymer substrates. The notion of utilizing a flexible substrate allows for both easier application integration and possible bending-based tuning of the frequency response [16, 17]. Prior to fabrication, the array structures and patterning were optimized using finite element method simulations. Initial characterization of these devices has been performed using terahertz time-domain spectroscopy and imaging. The metamaterial devices have shown selective transmission and reflection over a narrow range of frequencies near the targeted resonance at 250 GHz. Details of both the design, fabrication, and characterization will be discussed.

17.2 Design and Fabrication

The type of sub-wavelength structure that was utilized in the device designs presented herein utilized differing patterns of arrayed split ring resonator structures. This approach has been a basis of much previous work since first proposed by John Pendry in 1999 [18]. In this approach, the array of SRRs collectively responds to the incident radiation. SRRs also have a fixed narrow resonant frequency response based on the capacitance and the self- inductance of the SRR structure. With this approach, the magnetic field component of the incident electromagnetic wave induces a current in the place of the SRR (Fig. 17.1). This results in the performance of SRR-based metamaterial devices being strongly dependent on the angle of incidence and also non-resonant at normal incidence. The electric field component of the incident radiation also initiates a response in the SRR structure via the creation of a coupling response of the surface plasmons. This coupling is polarization dependent.

The two main contributing factors to the resonant response are the capacitance and self-inductance of the SRR structure. Device dimensions were based on the target frequency of 250 GHz as shown in Eq. 17.1,

$$\omega_o = \frac{1}{\sqrt{LC}} \tag{17.1}$$

where L is the metal inductance C is the overall capacitance. The gap in the SRR structure produces the largest capacitance and therefore is the only capacitance considered [18]. The inductance and the gap capacitance are given by Eqs. 17.2 and 17.3, respectively

$$L = \mu_o \left(\frac{\ell^2}{t} \right) \tag{17.2}$$

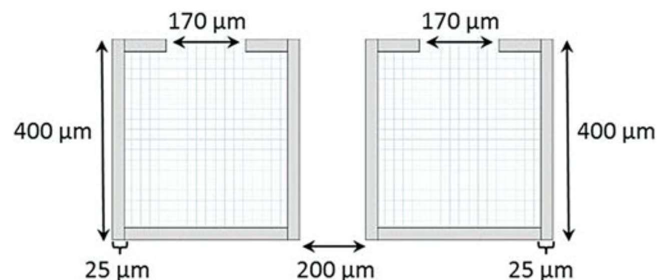

Fig. 17.1 A schematic of a top down view of two SRRs with dimensions indicated

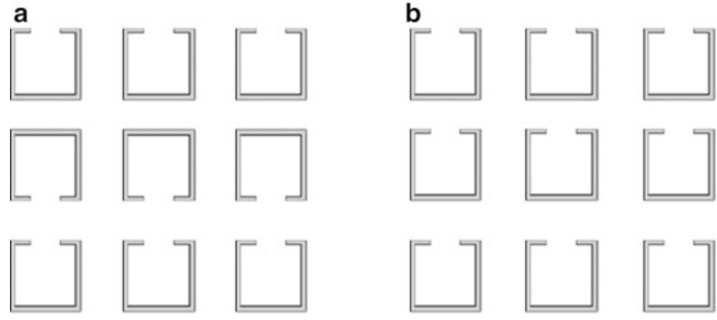

Fig. 17.2 (**a**) Pattern 1, gaps are "facing" each other. (**b**) Pattern 2, homogenously orientated

$$C = \varepsilon_o \varepsilon_r \left(\frac{wt}{g} \right) \tag{17.3}$$

where μ_o is the vacuum permeability, ℓ is the length of the side of the SRR, t is the thickness of the gold trace, ε_o is permittivity of free space, ε_r is the relative permittivity, w is the width of the gold trace, and g is the gap separation (Fig. 17.1). The parameter having the greatest effect on the resonant frequency is the length of the SRR.

A layout of the SRR structures and their dimensions are shown in Fig. 17.1. The SRRs have a square shape with a height and length of 400 μm with 200 μm spacing between them. The width of the gold trace is 25 μm. The capacitive gap opening is 170 μm, such that the length of the gold trace on either side of the gap is 90 μm.

Neighboring SRRs can be subject to responses from the incident electromagnetic field, thus the way that SRRs are arrayed is a contributing factor to the device's response. Two separate configurations for the SRR patterns were established. Pattern 1 consists of SRRs where the gaps are "facing" each other (Fig. 17.2a). Pattern 2 consists of all SRRs being equally spaced and homogenously orientated (Fig. 17.2b). These array patterns as well as the actual SRR device parameters were simulated and verified using a commercial electromagnetics finite element method solver, Comsol Multiphysics. Length constraints of this paper prevent inclusion of the simulation details and results.

Surface micromachining processes are used to fabricate the flexible THz metamaterial design. The fabrication process begins with a carrier wafer. On the carrier wafer, three layers of Omni Coat are spun on at 500 rpm and hard baked at 200 °C for 1 min. The Omni Coat serves as an adhesion layer and liftoff layer for the flexible substrate made from SU-8 2025 photoresist. The SU-8 2025 photoresist is coated and slowly spun on the adhesion layer at 500 rpm for 60 s. The SU-8 2025 photoresist is baked using a two step process to prevent thermal shock. The first bake occurs at 65 °C for 3 min and a second bake at 95 °C for 20 min. Following this baking process, the SU-8 2025 is exposed using a ultraviolet light flood exposure process for 40 s. Another baking cycle is performed to hard bake the photoresist starting with a 65 °C bake for 1 min and 95 °C bake for 5 min. The wafer is the sputter coated with titanium and gold to create the SRRs. The sputtered metals are coated with 1818 photoresist to pattern the SRRs. The 1818 photoresist serves as a etch blocking mask to define the SRRs. The gold layer is etched with potassium iodine etchant for 2 min. The titanium layer is etched with buffered oxide etchant for 30 s. After the SRRs are defined, the SU-8 2025 is submerged in acetone to liftoff the flexible substrate.

17.3 Characterization

A fiber-coupled terahertz time-domain system (Teraview) is being used to perform multiple characterization tests of the metamaterial devices. These include terahertz imaging of the devices as well as angular dependent transmission and reflection measurements. An additional, yet very important test parameter is analyzing the device response as a function of the polarization orientation.

THz time-domain images are acquired using a commercial system manufactured by Teraview. Ultrafast laser pulses with an 800 nm center wavelength and 100 fs pulse width trigger a fiber-coupled GaAs photoconductive antenna (PCA). Collimated THz light from the PC antenna transmitter is focused via a 50 mm focal length lens (f# = 2) onto the samples at a near-normal incident angle. The reflected radiation is detected by a PCA receiver module, based on LT-GaAs, with an identical lens configuration. When the system is optimized and calibrated using a metal sample target, the typical bandwidth of a detected THz pulse exceeds 3 THz. The constructed image can be based on the pixel to pixel change in amplitude of the

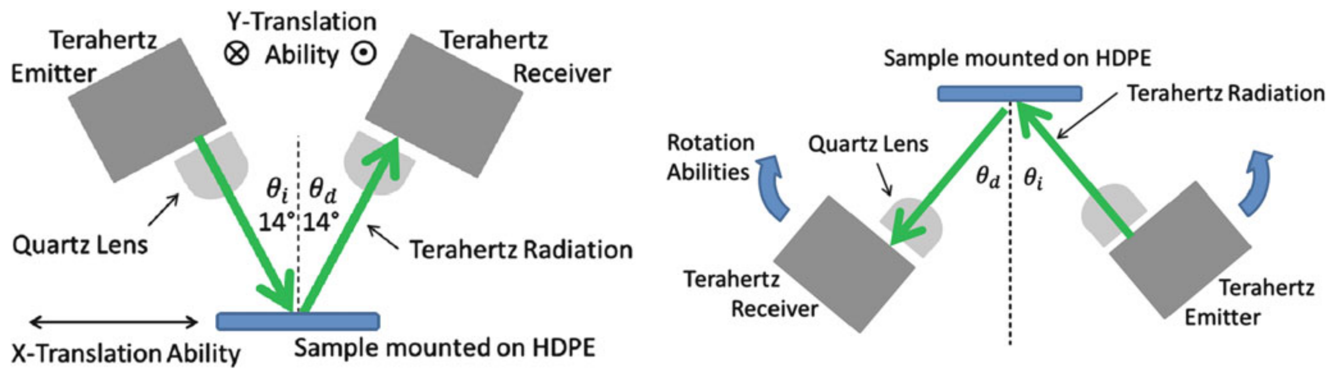

Fig. 17.3 Terahertz time domain spectroscopy imaging and reflection characterization schematics

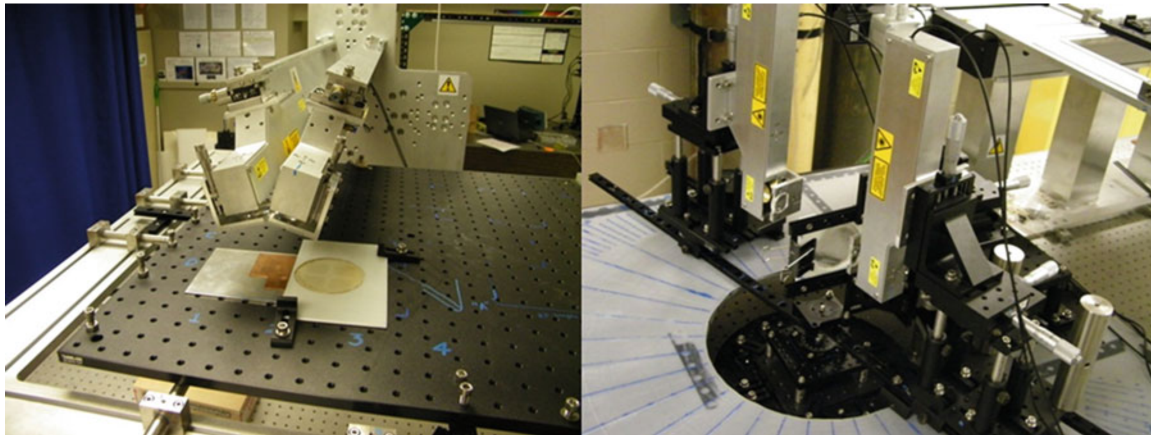

Fig. 17.4 Terahertz time domain spectroscopy imaging and reflection characterization setups

time-domain pulse or the change in the spectral amplitude at a specified frequency or range of frequencies. Such images essentially map the spatial dependence of a sample's absorption/conductivity properties.

Angular-dependent, reflection-based, THz time-domain measurements are also being taken using the same fiber-coupled THz time-domain spectroscopy system (Fig. 17.3). The devices are placed at the focal plane of the incident THz radiation and the angle of incidence (θ_i) was measured relative to the surface normal. A similar setup is being used to perform transmission measurements. Figure 17.4 shows pictures of the two of the characterization setups.

17.4 Results

Preliminary characterization measurements indicate that the devices are exhibiting the desired resonant response at frequencies near the design target of 250 GHz. Figure 17.5 shows the relative reflectivity for one device pattern as a function of incident angle. This data is for a non-alternating SRR patterned array in which the polarization of the incident beam is parallel to the length of the SRR gap. The data as presented is arrived at in the follow manner. For each angle of incidence, two time-domain waveforms are captured. One is from reflecting the beam from the actual device array while the other comes from reflecting the beam off of the bare SU8 substrate which provides a reference. The spectral amplitude is then computed using fast-fourier transforms and the sample spectrum is divided by the reference to yield the "relative reflectivity." It should be said that if these measurements were performed on a bulk metal surface, the bandwidth of the measurement would span from 100 GHz to 3 THz. It can be seen in the data presented here that the metamaterial device is acting as a frequency selective mirror in which only light near 250 GHz is reflected.

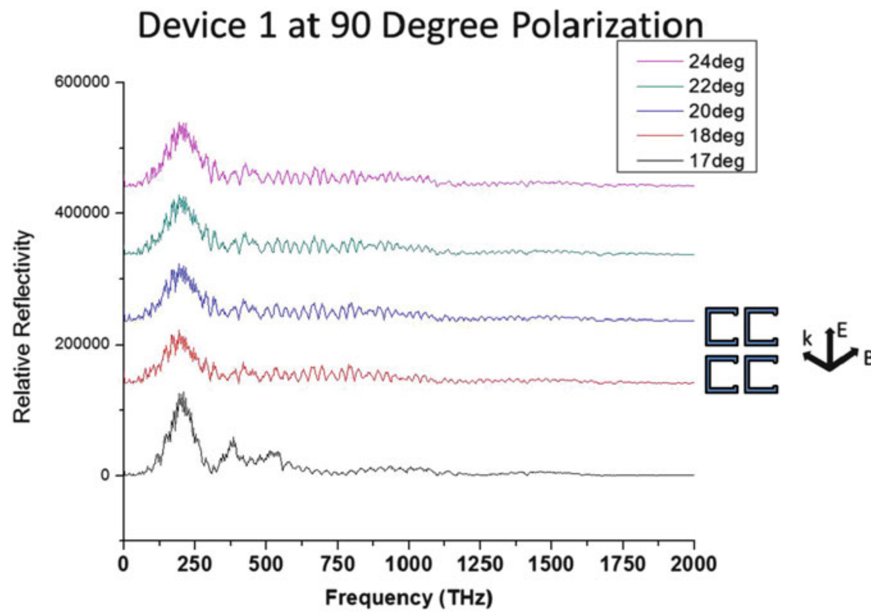

Fig. 17.5 Relative reflectivity measurements as a function of incident angle

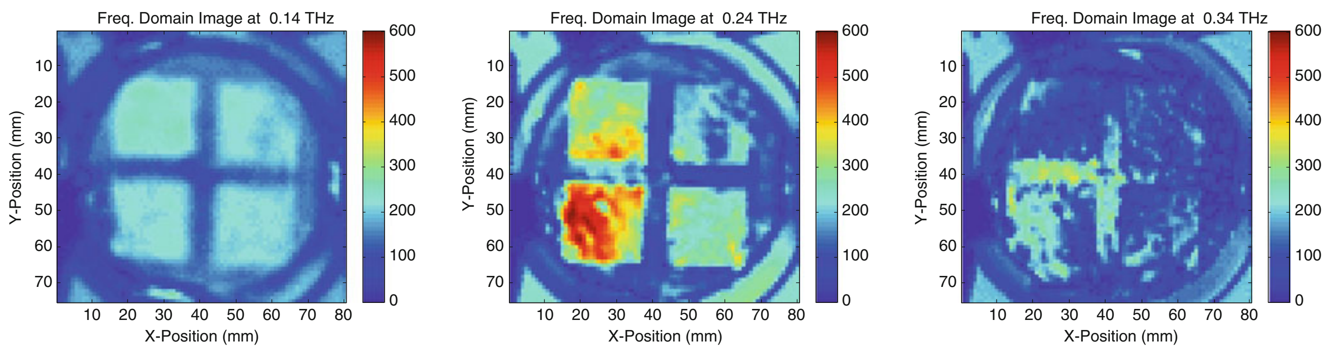

Fig. 17.6 THz Imaging measurements of the metamaterial devices at 0.14, 0.24, and 0.34 THz

Figure 17.6 shows early imaging results performed on a SU8 substrate containing four types of metamaterial devices. Each square consists of a pattern SRR array structure. The images are derived from the time-domain data. Each image is from the same data set but based on a different spectral amplitude, namely 140, 240, and 340 GHz. The amplitude scales are identical for each picture, thus showing that the reflected signal intensity from at least two of the SRR arrays is higher at 240 GHz than other frequencies, indicative of the desired resonant response.

17.5 Summary

Metamaterial devices based on a split ring resonator geometry have been fabricated as array patterns on flexible SU8 substrates. The device geometries as well as the array patterns were arrived at following finite element method simulations. Initial characterization efforts indicate that the devices are showing resonant responses in the vicinity of the targeted frequency of 250 GHz. Continuing work will include detailed characterization of the incident angle and polarization dependence. Future work will also include analyzing the resonant response as a function of substrate tension/bending.

References

1. Mittleman DM (2002) Sensing with terahertz radiation. In: Book sensing with terahertz radiation, Springer-Verlag, New York, NY, USA
2. Allen J, Jones B, Martin M, Taylor T, Allen M, Smith T, Nelson K, Mittleman D, Williams G, Norris T, Crowe T, Parks B, Hu Q, Kono J, Sherwin MA, Carr L, Bucksbaum PH, Zhang XC, Leemans W, Biedron S, Heyman J, Basov D, Orenstein J, Rangan C, Siegel P, Averitt R, Austin B, Tom H, Brunel L, Unterrainer K, Mihaly L, Zimdars D, Wilke I, Van der Meer L, Heinz T, Shan J, Jepsen P, Schmuttenmaer CA, Chamberlain M, DeLucia F, Noordham B, Cheville A, Markelz A, Plancken P, Citrin D, Grundfest W, Heilweil T, Kaind R, Wallace V (2004) DOE-NSF-NIH workshop on opportunities in THz science. In: Book DOE-NSF-NIH workshop on opportunities in THz science. Dept of Energy; Office of Science, 12–14 Feb 2004
3. Ferguson B, Zhang XC (2002) Materials for terahertz science and technology. Nat Mater 1(1):26–33
4. Siegel PH (2002) Terahertz technology. IEEE Trans Microw Theory Tech 50(3):910–928
5. Grischkowsky D, Keiding SR, Exter M, Fattinger C (1990) Far-infrared time-domain spectroscopy with terahertz beams of dielectrics and semiconductors. J Opt Soc Am B 7(10):2006–2015
6. Kawase K, Ogawa Y, Watanabe Y (2003) Non-destructive terahertz imaging of illicit drugs using spectral fingerprints. Opt Express 11 (20):2549–2554
7. Mittleman DM, Cunningham J, Neelamani R, Geva M (1997) Non-contact semiconductor wafer characterization with the terahertz hall effect. Appl Phys Lett 71:16–18
8. Zimdars D, White J, Stuk G, Chernovsky A, Fichter G, Williamson SL (2006) Large area terahertz imaging and non-destructive evaluation applications. Insight Non-Destruct Test Cond Monit 48(9):537–539
9. Crowe TW, Porterfield DW, Hesler JL, Bishop WL, Kurtz DS, Hui K (2005) Terahertz sources and detectors. In: Hwu RJ, Woolard DL, Rosker MJ (eds) Terahertz for military and security applications Iii. Spie-Int Soc Optical Engineering, Grenoble, France, pp 271–280
10. Lee AWM, Hu Q (2005) Real-time, continuous-wave terahertz imaging by use of a microbolometer focal-plane array. Opt Lett 30 (19):2563–2565
11. Saeedkia D, Safavi-Naeini S (2008) Terahertz photonics: optoelectronic techniques for generation and detection of terahertz waves. J Lightwave Technol 26(13–16):2409–2423
12. Belkin MA, Wang QJ, Pflugl C, Belyanin A, Khanna SP, Davies AG, Linfield EH, Capasso F (2009) High-temperature operation of terahertz quantum cascade laser sources. IEEE J Sel Top Quantum Electron 15(3):952–967
13. Neu J, Krolla B, Paul O, Reinhard B, Beigang R, Rahm M (2010) Metamaterial-based gradient index lens with strong focusing in the THz frequency range. Opt Express 18(26):27748–27757
14. Peralta XG, Smirnova EI, Azad AK, Chen H-T, Taylor AJ, Brener I, O'Hara JF (2009) Metamaterials for THz polarimetric devices. Opt Express 17(2):773–783
15. Peralta XG, Wanke MC, Brener I, Waldman J, Goodhue WD, Lic J, Azad AK, Chen HT, Taylor AJ, O'Hara JF (2010) Metamaterial based devices for terahertz imaging. In: Jansen ED, Thomas RJ (eds) Optical interactions with tissues and cells Xxi. Spie-Int Soc Optical Engineering, San Francisco, CA, USA
16. Azad AK, Chen HT, Lu X, Gu J, Weiss-Bernstein NR, Akhadov E, Taylor AJ, Zhang W, O'Hara JF (2009) Flexible quasi-three-dimensional terahertz electric metamaterials. Terahertz Sci Technol 2(1):15–22
17. Hu T et al (2008) Terahertz metamaterials on free-standing highly-flexible polyimide substrates. J Phys D: Appl Phys 41(23):232004
18. Pendry JB, Holden AJ, Robbins DJ, Stewart WJ (1999) Magnetism from conductors and enhanced nonlinear phenomena. IEEE Trans Microw Theory Tech 47(11):2075–2084